Active matter and complex environments

Inaugural-Dissertation

zur Erlangung des Doktorgrades
der Mathematisch-Naturwissenschaftlichen Fakultät
der Heinrich-Heine-Universität Düsseldorf

vorgelegt von

Davide Breoni
aus Verona, Italien

Düsseldorf, November 2023

aus dem Institut für Theoretische Physik II: Weiche Materie
der Heinrich-Heine-Universität Düsseldorf

Gedruckt mit der Genehmigung der
Mathematisch-Naturwissenschaftlichen Fakultät der
Heinrich-Heine-Universität Düsseldorf

Referent: Prof. Dr. Hartmut Löwen

Korreferent: Juniorprof. Dr. Ivo Buttinoni

Tag der mündlichen Prüfung: 26/01/2024

Abstract

One of the most puzzling mysteries in science is the spontaneous formation of extremely complex structures out of the simple and chaotic system that was Earth around four billion years ago: life [1,2]. At a first sight, in fact, the second principle of thermodynamics, demanding a continuous increase in the entropy, would only allow for complexity to fade away over time [3]. What this does not consider though, is that Earth is not a closed system, as it constantly absorbs and dissipates light. Since living beings, unceasingly requiring energy to remain alive and eventually procreate, are much more efficient than dead matter at dissipating this flow of energy and producing entropy, they can justify their complexity [4]. The constant hunger for energy makes it necessary for living creatures to learn to navigate any kind of complex environment. Most surroundings, in fact, feature very disordered landscapes of obstacles, sources of food, friendly species and unfriendly ones [5–7]. The smartest beings even manage to use and modify the environment itself to their advantage, as do for example hermit crabs when they use shells they scavenge as protection [8] or humans whenever they try to improve their well-being, bringing complexity and the production of entropy to even higher degrees [4].

This thesis draws inspiration from the intrinsic connection between life and disorder, and investigates the behavior of *active matter* [9] in disordered and complex landscapes [10]. Active matter, the field that studies what moves or does work by consuming an external source of energy [11, 12], is well suited for the study of living systems. It allows, for example, to use artificial active systems of self-propelled particles, relatively easy to tune and measure, as toy-models that can give us important insight on the much more complex living active matter. In particular, colloidal active particles such as the *Janus particles* [13, 14] provide some of the simplest examples of active matter, and can be effectively modeled by well-established frameworks such as the *Active Brownian Particle* (ABP) [10, 15, 16]. Indeed, in my first publication, **P1**, I study how ABPs move in disordered fields of both potential and motility (i.e. active speed), especially inquiring how disorder affects their short-time behavior. As a follow up, in **P5** I use ABPs to model and analyze the motion and collective behavior of real Janus active particles immersed in a light-induced motility field, finding the differences that occur as the motility field becomes more or less disordered. Chapter 1 of this thesis gives a broad introduction on the ABP and related models (Sec.1.1.1), disordered noise fields (Sec.1.1.2), how to calculate the *Mean Squared Displacement* (MSD) of active particles in a disordered field (Sec.1.2) and the basic mechanism behind the experimental setup

of **P5** (Sec.1.3).

The complexity of an environment can also come from the thermal bath: its properties can in fact depend on local variables, in the form, for example, of a temperature gradient [17,18], a medium which friction coefficient is space-dependent [19, 20] or anisotropic [21, 22] or Brownian ratchets and heat engines [23–25], which extract work from a system with an asymmetric potential by modulating the diffusion coefficient over time. The second and third publications deal with this kind of environment, studying respectively how a friction landscape can activate a passive Brownian particle (**P2**) and how the long-time diffusion and drifting speed of a passive particle in a tilted periodic potential can be enhanced by modulating the temperature as a function of space (**P3**). Since varying the background noise properties over space or time incurs in issues such as the *Itô/Stratonovich problem* [26–28], Sec.1.1.3 offers an overview on this subject.

Finally, interacting with others provides a source of complexity which is ubiquitous in nature and fundamental to the fascinating collective phenomena shown by active matter: we list for example schools of fishes [29], herds of sheep [30], bird flocks [31], cellular organization in bacteria colonies [32, 33] and multicellular organisms [34] or cluster formation in colloidal active particles [35, 36]. On this topic we can find **P4**, which studies how different and interacting populations of bacteria can form interesting structures, and **P6**, which instead focuses on large systems of entangled polymers and how activity affects their rheology. A short introduction on the *Fokker-Planck* formulation of stochastic equations [37], used to study the system of **P4**, can be found in Sec.1.1.4, while Chapter 2 is completely dedicated to the concepts of polymer physics necessary to appreciate **P6**.

Eidesstattliche Versicherung

Ich versichere an Eides Statt, dass die Dissertation von mir selbständig und ohne unzulässige fremde Hilfe unter Beachtung der „Grundsätze zur Sicherung guter wissenschaftlicher Praxis an der Heinrich-Heine-Universität Düsseldorf“ erstellt worden ist.

Düsseldorf, _____ _____

Preface

The content of this dissertation is based on articles that I co-authored, and that have been published in / submitted to peer-reviewed scientific journals. These articles are reproduced in Chapter 3 and are listed in the following (in chronological order):

- **P1** D. Breoni, M. Schmiedeberg and H. Löwen, *Active Brownian and inertial particles in disordered environments: Short-time expansion of the mean-square displacement*, Physical Review E **102**, 062604 (2020).
- **P2** D. Breoni, R. Blossey, and H. Löwen, *Active noise-driven particles under space-dependent friction in one dimension*, Physical Review E **103**, 052602 (2021).
- **P3** D. Breoni, R. Blossey, and H. Löwen, *Brownian particles driven by spatially periodic noise*, The European Physical Journal E **45**, 18 (2022).
- **P4** D. Breoni, F. J. Schwarzendahl R. Blossey, and H. Löwen, *A one-dimensional three-state run-and-tumble model with a "cell cycle"*, The European Physical Journal E **45**, 83 (2022).
- **P5** G. Jacucci D. Breoni, S. Heijnen J. Palomo P. Jones H. Löwen G. Volpe S. Gigan *Patchy landscapes promote stability of small groups*, arXiv:2310.01620 [cond-mat.soft] (2023).
- **P6** D. Breoni C. Kurzthaler B. Liebchen H. Löwen S. Mandal, *Giant Activity-Induced Stress Plateau in Entangled Polymer Solutions*, arXiv:2310.02929 [cond-mat.soft] (2023).

My contributions to these scientific articles are specified in Chapter 3.

Acknowledgments

I would like take this opportunity to thank all the people that accompanied me during the time of my doctorate and that made the production of this dissertation possible.
First of all, I thank my supervisor Prof. Dr. Hartmut Löwen. He transferred to me his passion and scientific knowledge by introducing me to the world of active matter, helping me whenever needed with discussions and support and being overall an exemplary supervisor.
I am grateful also to all the collaborators that made this project possible. I would like in particular to thank Prof. Dr. Ralf Blossey for his biological knowledge and ideas, fundamental for the production of three of my publications, Dr. Lorenzo Caprini for helping whenever I was stuck with a project and sharing his boundless knowledge of active matter and carbonara, Dr. Fabian Schwarzendahl for introducing me to a variety of topics, among which the intermediate scattering function and dad jokes, and finally Dr. Gianni Jacucci, thanks to whom a summer school produced a project worthy of the Mona Lisa.
I thank all the TP2 colleagues that accompanied me through the years, and especially Dr. Paul Monderkamp, whose energy made the office a really comfortable and welcoming place, Dr. Alexander Sprenger, who unlocked my artistic side and passed his passion for Mensa soups onto me, and Marcel Funk, without whom the office would have been much less lively. Among my colleagues, I would also like to thank all the members of the ITN project, for all the scientific and less scientific discussions we had during our meetings, and especially Gülce Bayram, who during her time in Düsseldorf became an unofficial TP2 member.
I express my gratitude next to all the friends I made and kept during the years: Lodovico, Michele, Luca, Olga, Regina, Doris, Sara, Sebastiano, Veronica, Giulia, Enes, Jane, Mirko, Valentina and Serji, who made these years truly enjoyable.
I would like to extend special thanks again to Dr. Lorenzo Caprini and Dr. Paul Monderkamp for reviewing this thesis and sharing their invaluable feedback.
Finally, I thank my family for providing me with everything I needed to reach this point of my life, and especially the food.

Contents

Chapter 1

Spherical active particles in complex environments

This chapter gives an overview on the modeling of active matter and complex environments, with a focus on simple spherical particles. I explain here the main notions underlying publications **P1**–**P5**: in Sec.1.1 I discuss the *active Brownian particle* (ABP) and similar models, used throughout most of my publications, and how to model a complex environment. In Sec.1.2 I explain how to derive the *mean squared displacement* (MSD) in various situations, and finally in Sec.1.3 there is a shift of focus from theory to experiments with an overview on *Janus particles* in *speckle light fields* and how to model them.

1.1 Modelling active matter and complex environments

The field of active matter is a relatively young one, dealing with materials that can consume energy from their environment in order to move autonomously or more generally, to produce work [9]. Since these kinds of systems require a constant energy intake to sustain themselves, they can only be studied in the frame of nonequilibrium physics [38, 39], leading to fascinating effects and behaviors that are not present in equilibrium, above all their collective behaviors [31, 40] (see for example Fig. 1.1).

Examples of active matter can be found everywhere around us, from birds flying in flocks [41] to bacteria forming biofilms [42], to human crowds [43]. All the cited examples are not casually chosen from the living world, as active matter can be seen as the strongest link between physics and biology: in fact, life can only thrive out of equilibrium. This is not to say that active matter can only describe living beings, as in fact much of the scientific effort in this field consists in creating machines from the macro- to the micro-scale which are active and can therefore perform directed motion and show interesting behaviors such as cluster formation [35] and flocking [44], with the aim of one day being able to perform complex tasks like

targeted drug delivery or assistance to people in dangerous environments.

Over the years, several different models have been proposed for active matter. In order to describe flocking, and hence self-aligning active particles, two very influential models have been introduced: the Vicsek model [40, 45], which is a stochastic particle-based model, where self moving particles are equipped with an aligning interaction, and the Toner-Tu model [46,47], that instead is a macroscopic theory which deals with fields of velocity, polarity and nematics. In the case of non-aligning active particles, fundamental models are instead the Active Brownian Particle (ABP) [10,15,16], which models the motion of active particles by adding a self-propelling term to the Brownian equations of motion, the Ornstein-Uhlenbeck model [48–50], where activity is implemented as a colored noise term, and the run-and-tumble model [51, 52], where particles move ballistically and change direction randomly with a certain rate in time.

It is uncommon to encounter perfectly homogeneous and simple environments in nature, as almost all surroundings present complexities and randomness in their conformation: from disordered landscapes, such as the soil [53] or the inside of a cell [54], to responsive non-Newtonian media [55], to gradients of temperature [56–59], viscosity [60] and many others. Complex environments are especially crucial in the case of active matter, as activity requires a constant flow of energy in the system: the energy present in the environment is consumed by the active agents, which by doing so modify their surroundings in a complex and dynamical way. This is true, both for living beings consuming the food resources of a certain area and for inanimate active particles burning through their fuel (such as, for example, Oxygen peroxide for Pt-Au Janus particles [61]).

Since publications **P1** and **P5** deal with different variations of the ABP model, I will explain its basics in detail in Sec.1.1.1, while in Sec.1.1.2 I will instead discuss the properties of a disordered field and how it can be modeled. Sec.1.1.3 concerns friction and thermal landscapes (that can be found respectively in **P2** and **P3**) and the related issue of multiplicative noise. Lastly, Sec.1.1.4 discusses the *Fokker-Planck* formulation of stochastic processes and how it can be used to model systems with various populations interacting with each other and themselves, as is done in **P4**.

1.1.1 The active Langevin/Brownian particle model

A large variety of experiments involving active matter are focused on colloids [62,63] (e.g. Fig.1.2a), that are either microscopic particles or droplets suspended in a fluid, where the molecules that make up the fluid are much smaller than the particles or droplets in question. At the micro-scale, although the single molecules of the medium are quite small, their collisions with the colloid give it small kicks, leading to the typical jiggling motion first described by Robert Brown in 1827 for a pollen particle in water [64]. The Langevin model takes these kicks into

Figure 1.1: Many active matter systems feature behavioral patterns, such as clustering, as displayed by this community of pigeons. In this example, the pigeons are possibly driven by a common food source, or shelter (photo taken by me).

account in a coarse-grained way by adding a noise term to the classic Newtonian equations [65,66]. As this framework, and especially its counterpart with no inertial term, the Brownian model [67, 68], proved very reliable to study colloids, this project features extensively them and their active versions: the active Langevin particle and active Brownian particle (ABP) models.

The Langevin model

Starting from the Langevin model, the equation of motion is the following:

$$m\ddot{\mathbf{r}}(t) + \gamma\dot{\mathbf{r}}(t) = -\nabla(U(\mathbf{r}(t))) + \mathbf{f}(t), \tag{1.1}$$

where $\mathbf{r}$ is the position of the particle, m is its mass, t is time, γ is the friction coefficient, U is an external potential and $\mathbf{f}$ is a random force that represents all the kicks given by small elements of the bath to our particle. As the bath is assumed to have no memory, the random force can be modeled by Gaussian white noise, which variance is derived from the fluctuation-dissipation theorem:

$$\begin{aligned} \langle \mathbf{f}(t) \rangle &= 0, \\ \langle f_\alpha(t) f_\beta(t') \rangle &= 2\gamma k_B T \delta_{\alpha,\beta} \delta(t - t'), \end{aligned} \tag{1.2}$$

where $\langle \cdot \rangle$ is the thermal noise average, α and β are components, k_B is Boltzmann's constant, T is the solvent temperature.

The Brownian model

A main feature of the Langevin model, is that it considers particles with finite mass. This is an important assumption at relatively large scales, where the *Reynolds number* of the medium, measuring the ratio between inertial and viscous forces [69], is very large and the full Navier-Stokes equations must be used to describe the fluid. This changes though when we move to smaller scales: as mass scales with the cube of the typical particle size and its surface with the square, at the micro-scale the effects of inertia (related to mass) become negligible with respect to those of friction (related to surface). Because of this, the most used model to describe colloids at the micro-scale is not the Langevin model, but a variant of it, the Brownian model, where the mass has been set to zero:

$$\gamma\dot{\mathbf{r}}(t) = -\nabla(U(\mathbf{r}(t))) + \mathbf{f}(t). \tag{1.3}$$

The limit in which friction dominates over inertia is called *overdamped* regime, in contrast to the *underdamped* regime more typical of larger length scales.

The ABP model

We now introduce activity to the Brownian model. We are not interested in modeling the specific propulsion mechanism of the active particle: the two main properties of self-propelled particles that we need to capture are *constant swim velocity* and *persistence*, i.e. the ability of active particles to perform directed motion consistently in the same direction for a certain *persistence time*. The ABP models these properties by introducing an orientation to the particle, $\mathbf{n}$, in which direction our particle pushes itself with speed v_0 [15, 70]. The orientation evolves stochastically thanks to the fluctuations of the thermal bath, while being independent of the motion of the particle. The equations of motion for the ABP model in 2D are:

$$\begin{aligned} \gamma\dot{\mathbf{r}}(t) &= \gamma v_0 \mathbf{n}(\phi(t)) - \nabla(U(\mathbf{r}(t))) + \mathbf{f}(t), \\ \beta\dot{\phi}(t) &= f_r(t), \end{aligned} \tag{1.4}$$

where $\mathbf{n} = (\cos(\phi), \sin(\phi))$, β is the rotational friction coefficient and the rotational random force f_r is white noise with

$$\begin{aligned} \langle f_r(t)\rangle &= 0, \\ \langle f_r(t) f_r(t')\rangle &= 2\beta k_B T \delta(t-t'), \end{aligned} \tag{1.5}$$

independent from the traslational random force $\mathbf{f}$.

As this work only discusses this model in reference to spherical particles, it is worth mentioning that in this case Stokes' law yields a relationship between γ, β

and the viscosity of the medium η_m [62]:

$$\begin{aligned} \gamma &= 3\pi\eta_m d, \\ \beta &= \pi\eta_m d^3, \end{aligned} \tag{1.6}$$

where d is the diameter of the particle.

The active Langevin model

Finally, as this project does not aim to only be relevant for colloids, a model which is capable of describing both activity and inertia is necessary. Macroscopic active particles, in fact, show behaviors that cannot be explained by the ABP model, such as inertial delays and different collective behaviors [71–73], see Fig.1.2b). The most straightforward way of implementing such a model is to go back to the initial Langevin model and extend it to also include activity, in a similar way to how the ABP model includes it [74]:

$$\begin{aligned} m\ddot{\mathbf{r}}(t) + \gamma\dot{\mathbf{r}}(t) &= \gamma v_0 \mathbf{n}(\phi(t)) - \nabla(U(\mathbf{r}(t))) + \mathbf{f}(t), \\ \beta\dot{\phi}(t) &= f_r(t). \end{aligned} \tag{1.7}$$

This model can be expanded to include further effects as rotational inertia, mass variations and more [22], but in this project only simple constant-mass point-like particles are treated.

1.1.2 Disordered fields

Disordered fields are one of the main subjects of this project, and were studied in publications **P1** and **P5**. They are of great interest to active matter research, as some of the most sought-after goals revolve around active matter navigating around unknown obstacles, for example when delivering drugs within the human body or when reaching a certain target location in harsh terrain. The effects of disordered fields on active matter have for this reason been an important subject of research [10, 75], showing how disorder can affect diffusion [76–78], flocking [79, 80], crowds [81] and phase separation [82]. A disordered landscape can be realized in a variety of ways, for example by setting obstacles on the substrate [83–87], letting particles move through porous media [53, 88] or using light speckle fields [89–91]. This section discusses the two methods of modeling a random employed in my publications.

Fourier series with randomly distributed modes

A very general way to define a disordered field, used in **P1**, is by the means of a Fourier decomposition where the mode amplitudes $\epsilon_{i,j}^{(\alpha)}$ are randomly distributed

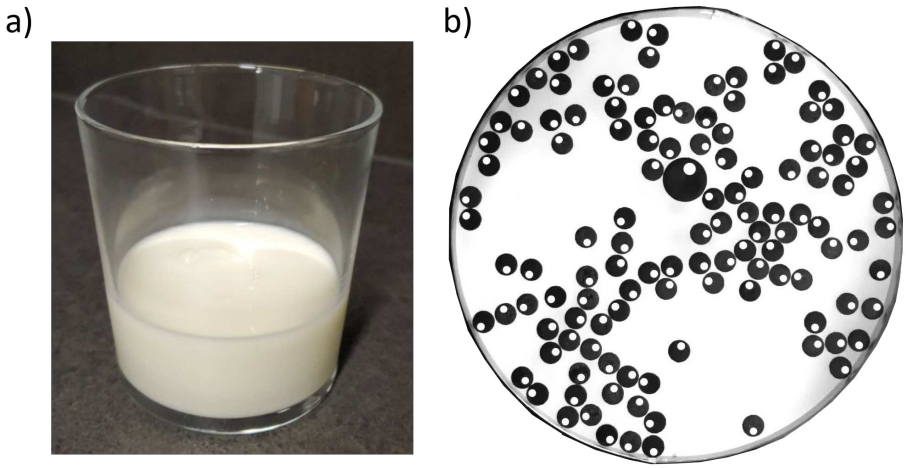

Figure 1.2: a) Milk is a very common example of a colloidal emulsion featuring proteins and small fat droplets suspended in water. The scattering of light provided by the droplets gives milk its typical white color (picture provided by Regina Rusch). b) Macroscopic system with a passive Brownian particle (the larger one) in a bath of active Brownian particles (called *vibrobots*, see [73]). These particles are on the length scale of centimeters, and the friction of the air and floor are not sufficient to completely suppress inertial effects. The Langevin/active Langevin model is well suited to describe systems such as this one (photo provided by Lorenzo Caprini).

(here in 2D):

$$M(\mathbf{r}) = \sum_{i,j=-\infty}^{\infty} \left[\epsilon_{ij}^{(1)} \cos(k_i x + k_j y) + \epsilon_{ij}^{(2)} \sin(k_i x + k_j y) \right], \tag{1.8}$$

where $k_n = \frac{2\pi}{L} n$ and L denotes an arbitrarily large periodicity. We further assume that the amplitudes are independent with respect to each other, Gaussian distributed and isotropic:

$$\overline{\epsilon_{ij}^{(\alpha)}} = 0, \quad \overline{\epsilon_{ij}^{(\alpha)} \epsilon_{mn}^{(\beta)}} = \epsilon_{i^2+j^2}^2 \delta_{im} \delta_{jn} \delta_{\alpha\beta}, \tag{1.9}$$

where $\overline{(\cdot)}$ is the average over disorder. By tuning how the noise amplitude $\epsilon_{i^2+j^2}^2$ varies as a function of the modes, we can create random fields with different properties, as we can give more or less importance to different length scales. Fig.1.3a) shows as example a random field where $\epsilon_{i^2+j^2}^2$ decays as $i^2 + j^2$ grows, giving more importance to larger length scales. In b) we can see its spatial autocorrelation $\langle\langle I(\mathbf{r}) I(\mathbf{r}')\rangle\rangle$, where I is the intensity of the field and $\langle\langle\cdot\rangle\rangle$ is the spatial average, while figure c) shows the intensity distribution.

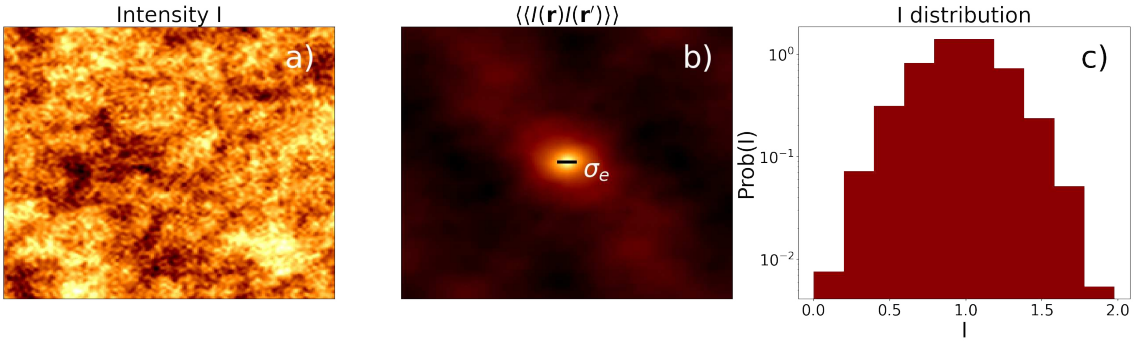

Figure 1.3: Figure a) shows a random map, b) its autocorrelation and the autocorrelation length σ_e and finally c) its intensity distribution.

Fourier transform of white noise

Speckle fields are particular type of disordered field, where a low-intensity background is disseminated with high-intensity areas, called *grains* or *speckles*, which are scattered in a disordered manner. Such fields can be easily produced in a laboratory by filtering a coherent light wave with some disordered medium [92, 93], as for example a simple sheet of paper. The resulting light field can then provide a complex environment for active colloids, which acts as either a potential [94, 95] or motility [96, 97] landscape based on the properties of the colloids and the light

intensity. In publication **P5** a light speckle field of this kind is used to provide a random motility field to active Janus particles.

One way to mathematically model a speckle pattern is related to the aforementioned light fields. As light scatters through the particles in the filter, it interferes with itself multiple times, resulting in a pattern that corresponds to the *structure factor* [98] of the filter, i.e. the Fourier transform of its spatial composition. As the filter is specifically chosen to be disordered, the distribution of its components can be seen as simple white noise. Summarizing this process, one can numerically produce a speckle field by applying the Fourier transform to a white noise map, as is shown in Fig.1.4a). These fields possess two main properties: firstly, their spatial autocorrelation function $\langle\langle I(\mathbf{r})I(\mathbf{r}')\rangle\rangle$ clearly defines a specific autocorrelation length, or *grain size*, σ_e (Fig.1.4b)), and secondly, their intensity distribution decays exponentially (Fig.1.4c)).

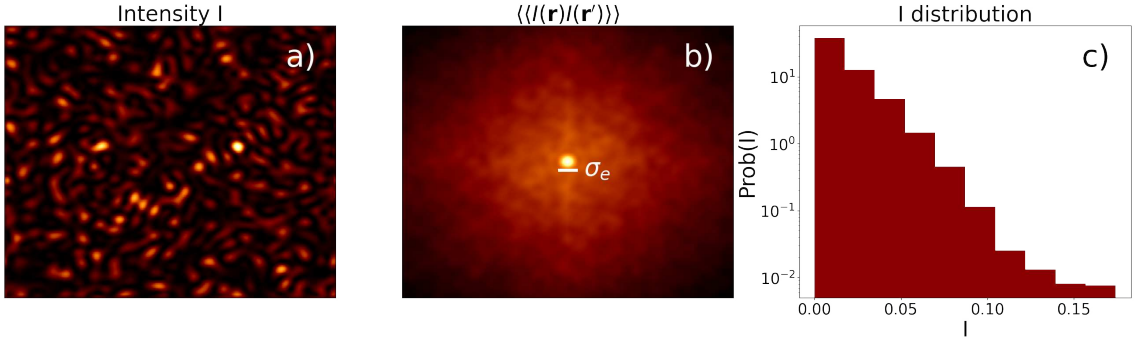

Figure 1.4: Figure a) shows a typical example of speckle field, b) its autocorrelation and the corresponding grain size σ_e and finally c) its exponentially decaying intensity distribution.

1.1.3 Multiplicative noise landscapes

In order to produce an even more complex and interesting environment for our particles to move into, we might want to further introduce a friction gradient (see publication **P2**) or a temperature field (**P3**). By doing so we run though into a new problem: we are introducing multiplicative noise into the system [27, 37].

Additive and multiplicative noise

We can write a generic stochastic equation for the real vector $\mathbf{r}$ in the form:

$$\dot{\mathbf{r}} = \mathbf{b}(\mathbf{r}, t) + \boldsymbol{\sigma}(\mathbf{r}, t) \cdot \boldsymbol{\eta}(t), \tag{1.10}$$

where $\boldsymbol{\eta}$ is a white noise vector, with $\langle \eta_i(t) \rangle = 0$ and $\langle \eta_i(t)\eta_j(t') \rangle = \delta_{i,j}\delta(t-t')$, $\mathbf{b}$ is a function that returns a vector and $\boldsymbol{\sigma}$ returns a matrix. If $\boldsymbol{\sigma}$ is constant, the noise $\boldsymbol{\eta}$ is considered *additive*, meaning that fluctuations are simply added to the equation and their strength does not depend on the state of the system. The models described in Sec.1.1.1 only consider systems of this kind, as we could for example write for the translational noise $\mathbf{f} = \boldsymbol{\sigma} \cdot \boldsymbol{\eta}$, where $\boldsymbol{\sigma} = \sqrt{2\gamma k_B T}\mathbb{I}$ and $\mathbb{I}$ is the identity matrix. The more general case where $\boldsymbol{\sigma}$ is not constant, and hence the strength of noise depends on the system variables, is called *multiplicative* noise and gives rise to a series of issues that will shortly be discussed.

The Itô/Stratonovich problem

As white noise is delta-correlated in time, Eq.(1.10) is not completely mathematically defined. It helps to consider, instead of the noise itself $\boldsymbol{\eta}$, the Wiener process that it generates $\mathbf{W}(t) = \int_0^t \boldsymbol{\eta}(t')\mathrm{d}t'$ and to rewrite the equation as

$$\mathbf{dr} = \mathbf{b}(\mathbf{r}, t)\mathrm{d}t + \boldsymbol{\sigma}(\mathbf{r}, t) \cdot \mathbf{dW}, \tag{1.11}$$

where, since the noise components η_i are Gaussian distributed and delta correlated, the increments $\mathrm{d}W_i$ are Gaussian distributed with variance $\mathrm{d}t$ and independent of the increments in others intervals of time [99]. If we attempt to integrate this set of equations with a Riemann integral, we immediately run into the problem that $\mathbf{W}$ is never differentiable, rendering the integral a purely formal expression. What we can instead do is to use the Stieltjes integral definition, for which:

$$\int_{t_0}^{t} f(t')\mathrm{d}g(t') = \lim_{n\to\infty} \sum_{i}^{n} f(\hat{t}_l)[g(t_l) - g(t_{l-1})], \tag{1.12}$$

where f and g are real functions of t and $t_{l-1} \leq \hat{t}_l \leq t_l$. If g is differentiable, the limit will always converge to the same value for any $\hat{t}_l$, but if g is not, the choice of $\hat{t}_l$ becomes relevant. For example, if we take both $f = W(t)$ and $g = W(t)$, where W is a Wiener process, the mean value of the integral $\int_0^t W(t)\mathrm{d}W$ will depend heavily on where we choose to evaluate the integrating function:

$$\begin{aligned}
&\lim_{n\to\infty} \sum_{l}^{n} \langle W(t_l)[W(t_l) - W(t_{l-1})] \rangle = \lim_{n\to\infty} \sum_{l}^{n} \langle [W(t_l) - W(t_{l-1})]^2 \rangle = t, \\
&\lim_{n\to\infty} \sum_{l}^{n} \langle W(t_{l-1})[W(t_l) - W(t_{l-1})] \rangle = \lim_{n\to\infty} \sum_{l}^{n} \langle W(t_{l-1}) \rangle \langle [W(t_l) - W(t_{l-1})] \rangle = 0,
\end{aligned} \tag{1.13}$$

where the independence of disjointed Wiener increments and the variance of a Wiener increment were used. Given this ambiguity in the definition of a Stieltjes

integral, it becomes always necessary to specify where the integrating function f is evaluated. The two most common conventions regarding this specification are $f(\hat{t}_l) = f(t_{l-l})$, or *Itô* convention, and $f(\hat{t}_l) = (f(t_l) + f(t_{l-1}))/2$, or *Stratonovich* convention. The Itô convention reflects well causality, as the noise is here a consequence of the state of the system, and is also good for performing numerical simulations, since the prefactor of the noise is usually calculated from the state of the system at the beginning of each time step. The trade-off is that the usual integration and differentiation laws, such as Leibniz's chain rule, do not apply (see for example Itô's lemma [100]). The Stratonovich convention, on the other hand, has the advantage of preserving the classical differentiation rules at the cost of an additional drift term:

$$\begin{aligned} \mathrm{d}r_i &= b_i \, \mathrm{d}t + \sigma_{ij}\mathrm{d}W_j \quad \text{(Itô)}, \\ \mathrm{d}r_i &= \left(b_i - \frac{1}{2}\sigma_{kj}\frac{\partial}{\partial x_k}\sigma_{ij} \right) \mathrm{d}t + \sigma_{ij}\mathrm{d}\tilde{W}_j \quad \text{(Stratonovich)}, \end{aligned} \tag{1.14}$$

where the noise term $\mathrm{d}\tilde{W}_j$ is interpreted in the Stratonovich sense and repeated indexes imply sums. For example, the simple diffusive equation in the Itô sense

$$\mathrm{d}x = \sqrt{2D(x)}\mathrm{d}W \quad \text{(Itô)}, \tag{1.15}$$

where $D(x)$ is a real positive function, transforms into

$$\mathrm{d}x = -\frac{1}{2}\frac{\partial D(x)}{\partial x}\mathrm{d}t + \sqrt{2D(x)}\mathrm{d}\tilde{W} \quad \text{(Stratonovich)}. \tag{1.16}$$

As the friction γ and the temperature T are fundamental properties of the thermal bath where our particles move, they directly affect the intensity of the random forces. It is fundamental then, when studying systems in which these quantities are a function of time or position, to always keep in mind the convention used and the relative properties.

1.1.4 Landscapes of different and interacting populations

Finally, we also want to model the differentiation of particles into populations and their ability to interact. In active matter, different populations can model for example competition among cells [101], predator-prey behaviors [102, 103], run-and-tumble motion [51, 52, 104], and the life cycle of cells [105]. Here, the complexity of the landscape is not a field imposed on the particles, but an emergent feature of the collective behavior of the particles themselves. In order to study such systems we now change our prospective, instead of using Langevin equations we describe our stochastic processes via probability distribution functions and the *Fokker-Planck* equation [37]. Starting from a stochastic equation for a certain variable $\mathbf{r}$ it is

always possible to write a partial differential equation for its probability distribution which describes the same system. In the case of an equation with both drift and diffusion, such as Eqs.(1.14), the corresponding Fokker-Planck equation is

$$\frac{\partial}{\partial t}P(\mathbf{r},t) = -\frac{\partial}{\partial r_i}\left[b_i P(\mathbf{r},t)\right] + \frac{1}{2}\frac{\partial^2}{\partial r_i \partial r_j}\left[\sigma_{ik}\sigma_{jk}P(\mathbf{r},t)\right]. \tag{1.17}$$

We now want to extend these equations to reflect the existence of various interacting populations. We consider a simplified version of the system studied in publication **P4**: a 1D system with two active particle populations, one described by the spatial density $\rho_+(x,t)$ moving with speed v_0 towards the right, and the other defined as $\rho_-(x,t)$ going at the same speed but in opposite direction, both subject to a constant diffusion coefficient D:

$$\begin{aligned}\partial_t\rho_+ &= -v_0\partial_x\rho_+ + D\partial_x^2\rho_+,\\ \partial_t\rho_- &= v_0\partial_x\rho_- + D\partial_x^2\rho_-.\end{aligned} \tag{1.18}$$

Please note that as these equations handle spatial densities, and not probability densities, they are not technically Fokker-Planck equations, although the only difference is that the integral over these densities does not converge to one, but to the total number of particles. Eqs.(1.18) are quite unremarkable, as they describe two populations that do not interact with themselves or each other. To make things more interesting we can include the population exchange rates $\lambda_\pm$ for particles going from $\rho_\mp$ to $\rho_\pm$:

$$\begin{aligned}\partial_t\rho_+ &= +\lambda_-\rho_- - v_0\partial_x\rho_+ + D\partial_x^2\rho_+ - \lambda_+\rho_+,\\ \partial_t\rho_- &= +\lambda_+\rho_+ + v_0\partial_x\rho_- + D\partial_x^2\rho_- - \lambda_-\rho_-.\end{aligned} \tag{1.19}$$

These equations now describe run-and tumble motion in 1D, i.e. active particles that can change their direction of motion with a certain rate [51, 52]. Lastly, interactions can be included as nonlinear terms in the population densities. We can for example include attraction among opposite-sign populations κ_a and repulsion among same-sign populations κ_r:

$$\begin{aligned}\partial_t\rho_+ &= +\lambda_-\rho_- - v_0\partial_x\rho_+ + D\partial_x^2\rho_+ - \lambda_+\rho_+ + \kappa_a\partial_x(\partial_x(\rho_-)\rho_+) - \kappa_r\partial_x(\partial_x(\rho_+)\rho_+),\\ \partial_t\rho_- &= +\lambda_+\rho_+ + v_0\partial_x\rho_- + D\partial_x^2\rho_- - \lambda_-\rho_- + \kappa_a\partial_x(\partial_x(\rho_+)\rho_-) - \kappa_r\partial_x(\partial_x(\rho_-)\rho_-).\end{aligned} \tag{1.20}$$

Nonlinear systems such as this one yield much richer results than linear ones, as they can model collective and emergent behaviors. The downside is that in most cases they cannot be exactly solved without the heavy use of approximations. One method that can reliably yield information on these systems is *linear stability theory* [106], which, by linearizing the equations around a certain state of the system, can tell us whether that state is stable or not.

1.2 Mean squared displacement

After choosing a model that can well represent our system, the next step is to decide what quantities to measure in order to yield the most insight out of it. The observables of reference for this chapter are the *mean displacement* (MD) of the particle and more importantly its *mean squared displacement* (MSD). These quantities can give us an idea respectively of how symmetric and persistent the trajectory of a particle is and how far it moves on average after a certain time t. They are defined as

$$\begin{aligned} \text{MD} &= \langle \mathbf{r}(t) - \mathbf{r}(0) \rangle, \\ \text{MSD} &= \langle (\mathbf{r}(t) - \mathbf{r}(0))^2 \rangle, \end{aligned} \tag{1.21}$$

where $\langle \cdot \rangle$ is the thermal average and $\mathbf{r}$ is the position. In the Fokker-Planck representation of our stochastic equations of motion, they would be the first two moments of the probability density function of the position (more on that in Sec.1.2.3).

We can learn a lot about the motion of a particle from the behavior of its MD and MSD, and more specifically from how they grow with time. Let us for example calculate the MD and MSD of a free non-stochastic particle with initial velocity $\mathbf{v}_0$ and initial position $\mathbf{r}(0) = 0$:

$$\begin{aligned} \langle \mathbf{r}(t) - \mathbf{r}(0) \rangle &= \mathbf{r}(t) = \mathbf{v}_0 t, \\ \langle (\mathbf{r}(t) - \mathbf{r}(0))^2 \rangle &= \mathbf{r}(t)^2 = |\mathbf{v}_0|^2 t^2. \end{aligned} \tag{1.22}$$

This simple calculation shows how a particle undergoing *ballistic motion* features an MD that grows linearly with time and an MSD which grows quadratically. As much as this result is trivial, a stable t^2 regime in the MSD is a very strong indication that in that time frame the system is performing ballistic motion. Another thing to notice is that if we assume a uniformly random initial orientation for the ballistic particle of Eqs.(1.22) and we average over the initial conditions, its MSD will not change, while its MD will average to zero. In fact, being an even function of the position, the MSD is much more resilient to averaging, both with respect to initial conditions and thermal noise, and will always yield more reliable information on the motion of a particle. Because of this, going forward more focus will be put on the MSD.

Let us now consider another example: the free Brownian particle. This case is not as straightforward as the previous one, as we are now considering stochastic trajectories and must average over noise. First of all we solve the Brownian differential equations (Eq.(1.3), setting $U = 0$ and $\mathbf{r}(0) = 0$) formally:

$$\mathbf{r}(t) = \frac{1}{\gamma} \int_0^t \mathbf{f}(t') dt'. \tag{1.23}$$

We then substitute $\mathbf{r}(t)$ in the MSD obtaining:

$$\begin{aligned}\langle \mathbf{r}(t)^2 \rangle &= \frac{1}{\gamma^2}\int_0^t\int_0^t \langle \mathbf{f}(t')\mathbf{f}(t'')\rangle \mathrm{d}t'\mathrm{d}t'' = \frac{1}{\gamma^2}\int_0^t\int_0^t 2d_f\gamma k_B T\delta(t'-t'')\mathrm{d}t'\mathrm{d}t'' \\ &= \frac{2d_f k_B T}{\gamma}\int_0^t \mathrm{d}t' = \frac{2d_f k_B T}{\gamma}t, \end{aligned} \tag{1.24}$$

where d_f is the number of dimensions and the fluctuation-dissipation theorem was used, Eq.(1.2). We further define the *diffusion coefficient* $D = \frac{k_B T}{\gamma}$, which allows us to simplify the final result:

$$\langle \mathbf{r}(t)^2 \rangle = 2d_f D t. \tag{1.25}$$

This calculation shows that the MSD of a particle undergoing *diffusive motion* grows linearly with time.

Knowing now that a linear regime of the MSD in time signifies diffusive motion and that a quadratic one indicates ballistic motion, we have the basic tools to understand the kinematic behavior of most stochastic systems by simply looking at their MSD.

1.2.1 The MSD and MD of an active particle

Mean squared displacement - overdamped

By introducing activity to the Brownian model, the ABP model showcases a variety of behaviors that are perfectly captured by its MSD [70]. Let us start the calculation from the formal solution of the 2D ABP model in Eq.(1.4), where $U = 0$, $\mathbf{r}(0) = 0$ and $\phi(0) \equiv \phi_0$:

$$\begin{aligned}\mathbf{r}(t) &= \frac{1}{\gamma}\int_0^t \mathbf{f}(t')\mathrm{d}t' + v_0\int_0^t \mathbf{n}(\phi(t'))\mathrm{d}t', \\ \phi(t) &= \phi_0 + \frac{1}{\beta}\int_0^t f_r(t')\mathrm{d}t'. \end{aligned} \tag{1.26}$$

When substituting into the MSD, this yields

$$\begin{aligned}\langle \mathbf{r}(t)^2 \rangle &= 4Dt + \frac{2v_0}{\gamma}\int_0^t\int_0^t \langle \mathbf{f}(t')\mathbf{n}(\phi(t''))\rangle \mathrm{d}t'\mathrm{d}t'' \\ &\quad + v_0^2\int_0^t\int_0^t \langle \mathbf{n}(\phi(t'))\mathbf{n}(\phi(t''))\rangle \mathrm{d}t'\mathrm{d}t'', \end{aligned} \tag{1.27}$$

where in the first term the result for a free Brownian Particle in 2D, Eq.(1.24), was used. Since $\mathbf{n}$ is only a function of ϕ, which in turn is only a function of the

random force f_r, and f_r is assumed to be independent from $\mathbf{f}$, in the mixed term we have

$$\langle \mathbf{f}(t')\mathbf{n}(\phi(t''))\rangle = \langle \mathbf{f}(t')\rangle\langle \mathbf{n}(\phi(t''))\rangle = 0, \tag{1.28}$$

as $\mathbf{f}(t')$ is white noise. In order to compute the last term of Eq.(1.27), which is purely active, we must know how ϕ is distributed. Since ϕ is a linear distribution of Gaussian variables, in this case f_r, Wick's theorem ensures that ϕ is Gaussian too [107, 108]. As a consequence, the probability distribution of ϕ is the following:

$$P(\phi, t) = \sqrt{\frac{\beta}{4\pi k_B T t}} \exp\left(-\frac{\beta(\phi-\phi_0)^2}{4k_B T t}\right). \tag{1.29}$$

We simplify the notation by defining the rotational diffusion constant $D_r = \frac{k_B T}{\beta}$. Knowing the distribution of ϕ we can calculate the average $\langle \mathbf{n}(\phi(t'))\mathbf{n}(\phi(t''))\rangle = \langle \cos(\phi')\cos(\phi'')\rangle + \langle \sin(\phi')\sin(\phi'')\rangle$, where $\phi' \equiv \phi(t')$ and $\phi'' \equiv \phi(t'')$. Focusing on the cosine term, we have [107]:

$$\langle \cos(\phi')\cos(\phi'')\rangle_{t'>t''} = \int\int \cos(\phi')\cos(\phi'')\frac{\mathrm{e}^{-\frac{(\phi'-\phi'')^2}{4D_r(t'-t'')}}}{2\sqrt{\pi D_r}} P(\phi'', t'')\mathrm{d}\phi'\mathrm{d}\phi''. \tag{1.30}$$

Solving the integral of Eq.(1.30) we obtain

$$\langle \cos(\phi')\cos(\phi'')\rangle_{t'>t''} = \frac{1}{2}\mathrm{e}^{-D_r(t'-t'')}\left[1+\cos(2\phi_0)\mathrm{e}^{-4D_r t''}\right], \tag{1.31}$$

which, when summed to the similarly obtained sine term and integrated into Eq.(1.27), yields the following MSD:

$$\langle \mathbf{r}(t)^2\rangle = 4Dt + 2v_0^2\int_0^t\int_0^{t'} \mathrm{e}^{-D_r(t'-t'')}\mathrm{d}t'\mathrm{d}t'' = 4Dt + 2\frac{v_0^2}{D_r^2}\left(D_r t + \mathrm{e}^{-D_r t} - 1\right). \tag{1.32}$$

The various regimes of the MSD become evident when we plot it in a log-log scale, as can be seen in Fig.1.5 a). The particle undergoes three major regimes: first a diffusive behaviour with diffusion constant D as the particle feels the effects of traslational noise, then a ballistic regime in which the particle moves at speed v_0 that encapsulate its active directed motion, and finally another diffusive regime with effective diffusion constant $D_{eff} = D + \frac{v_0^2}{2D_r}$ where the orientation of the particle starts changing randomly because of the rotational noise. The relative importance of the ballistic regime with respect to the diffusive ones is given by the Péclet number, defined here as [10]

$$\mathrm{Pe} = \frac{v_0}{\sqrt{DD_r}}. \tag{1.33}$$

It is possible to know exactly when the system goes from one behavior to the next by mathematically calculating the intersection of the various regimes in time. These intersections are defined as *crossing times*, and in the case of the ABP there are two of them: at time

$$t_1^c = \frac{4D}{v_0^2} \tag{1.34}$$

the particle starts moving ballistically and at time

$$t_2^c = \frac{4D}{v_0^2} + 2D_r^{-1} \tag{1.35}$$

we begin to see the final diffusive regime.

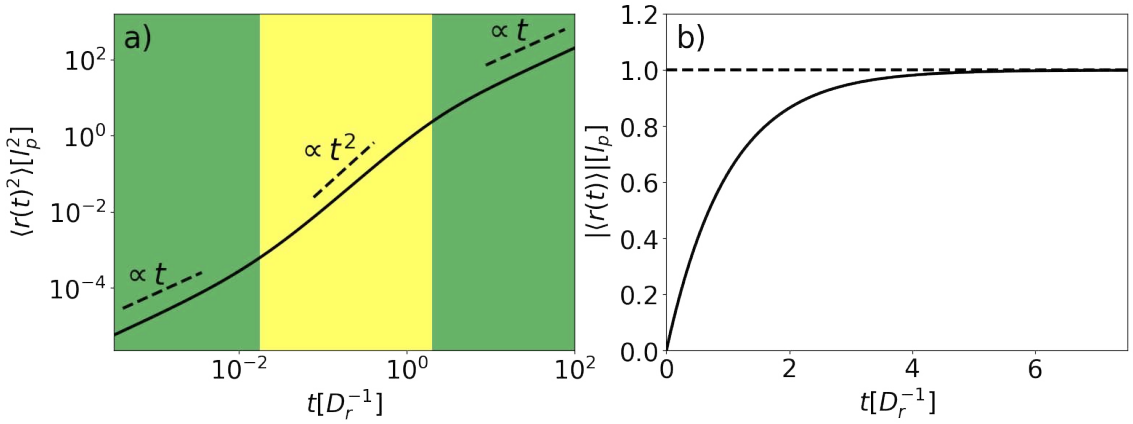

Figure 1.5: a) Typical MSD of an active Brownian particle. There are three distinctive regimes: diffusive, ballistic and diffusive again. b) Modulus of the mean displacement of an ABP, closing in on the persistence length l_p as time grows.

Mean displacement - overdamped

Differently from the passive Brownian case, where the MD inevitably averages to zero, calculating the Mean displacement for an active Brownian particle can give us some interesting insight in the system. The calculation is more straightforward than that of the MSD and yields:

$$\langle \mathbf{r}(t)\rangle = v_0\mathbf{n}(\phi_0)\int_0^t \mathrm{e}^{-D_r t'}\mathrm{d}t' = \frac{v_0\mathbf{n}(\phi_0)}{D_r}\left(1-\mathrm{e}^{-D_r t}\right). \tag{1.36}$$

We see that in the long time limit $t \to \infty$, the MD reduces to $v_0\mathbf{n}(\phi_0)/D_r$, meaning that ABPs will on average keep their initial directed motion for a *persistence length* $l_p = \frac{v_0}{D_r}$, before changing their orientation. In Fig.1.5 b) we see how the MD goes exponentially close to l_p.

Mean squared displacement - underdamped

In virtue of its inertia, the motion of an underdamped particle is dominated at short times by its initial speed. The MSD of an underdamped active particle in its stationary state is [74]:

$$\langle \mathbf{r}(t)^2 \rangle = 2\frac{m}{\gamma}\left(D + \frac{v_0^2}{D_r}\frac{1}{1-1/\alpha^2}\right)\left[\frac{t\gamma}{m} + \mathrm{e}^{-t\gamma/m} - 1\right] + 2\frac{v_0^2}{D_r^2}\frac{1}{1-\alpha^2}\left[D_r t + \mathrm{e}^{-D_r t} - 1\right]. \tag{1.37}$$

where the ratio $\alpha = \frac{mD_r}{\gamma}$ indicates how relevant inertia is in the system. By plotting a typical example of such MSD in Fig.1.6, we find how a new initial $\propto t^2$ regime appears, related to the average particle speed in the stationary state.

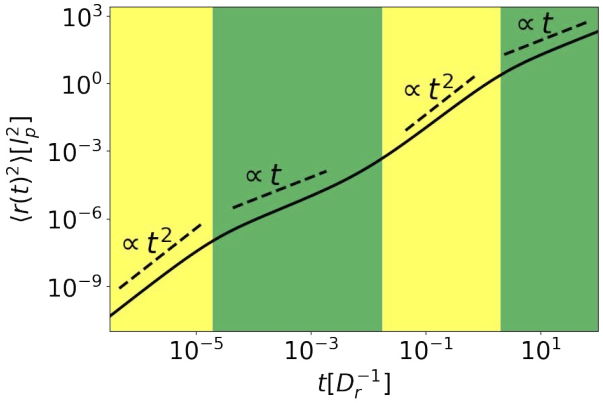

Figure 1.6: Typical MSD of an active Langevin particle. With respect to the overdamped case, we have now an additional initial ballistic regime, for a total of four: ballistic, diffusive, ballistic and diffusive again.

1.2.2 Short-time MSD in complex environments

This section goes through the basic procedure behind the calculations of the short-time MSD in publications **P1** and **P2**, also explained in the Appendix of **P1**. We consider for this example a 2D overdamped active particle (Eq.1.4) in a disordered potential field $U(\mathbf{r})$, in the form of Eq.(1.8).

Taylor approximation of the field

The first step necessary to approach this problem is to Taylor expand the external random forces $\mathbf{F} \equiv -\nabla U$ around the initial position of the particle $\mathbf{r}_0$:

$$\mathbf{F}(\mathbf{r}(t)) = \sum_{n_x=0}^{\infty}\sum_{n_y=0}^{\infty}\frac{(x(t)-x_0)^{n_x}(y(t)-y_0)^{n_y}}{n_x! n_y!}\left(\frac{\partial^{n_x+n_y}\mathbf{F}}{\partial x^{n_x}\partial y^{n_y}}\right)(\mathbf{r}_0) \tag{1.38}$$

and to approximate this expansion to first order:

$$\mathbf{F}(\mathbf{r}(t)) \simeq \mathbf{F}(\mathbf{r}_0) + \begin{pmatrix} (x-x_0)F_x^x(\mathbf{r}_0) \\ (y-y_0)F_y^y(\mathbf{r}_0) \end{pmatrix}, \tag{1.39}$$

where a subscript to F signifies a force component and a superscript denotes a partial derivative. This approximated system is that of an active particle influenced by two independent Brownian oscillators along the x and y directions, which is analytically solvable [109].

Short-time MSD of the active Brownian oscillator

Let us calculate the harmonic oscillator MSD for short times. After the field approximation, the equation of motion in the x direction becomes:

$$\gamma \dot{x}_B = f_x(t) + \gamma v_0 \cos(\phi(t)) + F_x(\mathbf{r}_0) + F_x^x(\mathbf{r}_0)(x_B(t) - x_0), \tag{1.40}$$

which formal solution is

$$\begin{aligned} x_B(t) &= x_0 + \frac{F_x(\mathbf{r}_0)}{F_x^x(\mathbf{r}_0)}\left(e^{\frac{1}{\gamma}F_x^x(\mathbf{r}_0)t} - 1\right) + \frac{1}{\gamma}\int_0^t e^{\frac{1}{\gamma}F_x^x(\mathbf{r}_0)(t-t')} f_x(t')\mathrm{d}t' \\ &\quad + v_0 \int_0^t e^{\frac{1}{\gamma}F_x^x(\mathbf{r}_0)(t-t')} \cos(\phi(t'))\mathrm{d}t' \\ &\equiv x_0 + x_a(t) + x_b(t) + x_c(t), \end{aligned} \tag{1.41}$$

where

$$\phi(t) = \frac{1}{\beta}\int_0^t f_r(t')\mathrm{d}t'. \tag{1.42}$$

The mean square displacement up to order t^4 in time in the x direction is then

$$\begin{aligned} \mathrm{MSD}_{xB}(t) &= \left\langle \overline{\langle (x_a(t) + x_b(t) + x_c(t))^2 \rangle} \right\rangle_r \\ &= 2Dt + \left(\frac{\widehat{F_x^2}}{\gamma^2} + \frac{v_0^2}{2}\right)t^2 + \frac{1}{6}\left(8D\frac{\widehat{F_x^{x2}}}{\gamma^2} - D_R v_0^2\right)t^3 \\ &\quad + \frac{1}{24}\left(14\frac{\widehat{F_x^2 F_x^{x2}}}{\gamma^4} + 7\frac{\widehat{F_x^{x2}}}{\gamma^2}v_0^2 + D_R^2 v_0^2\right)t^4 + \mathcal{O}(t^5), \end{aligned} \tag{1.43}$$

where $\langle\cdot\rangle_r$ is the average over the initial conditions, $\overline{(\cdot)}$ the average over disorder, $\langle\cdot\rangle$ the thermal average and $\widehat{(\cdot)}$ represents both the averages over disorder and initial conditions. We notice that Eq.(1.43) contains both a $\propto t^3$ and a $\propto t^4$ term, which are the lowest order terms where the configuration of the force field appears (i.e. the force derivatives), and are neither ballistic nor diffusive. The t^4 term in the

MSD, in fact, indicates an acceleration, while in this case the t^3 term is a complex mixture of acceleration and diffusion. In order to ascertain if these are real regimes, one must calculate the crossing times between the various order, and if a high order crossing time (for example between order t^3 and t^4) is smaller than a lower order one (for example between order t^2 and t^3), the orders between these crossing times do not constitute regimes (in this case, t^3 would not be a regime). In publication **P1**, we find for example that an ABP in such a disordered potential landscape does not feature real t^3 and t^4 regimes, while an active Langevin particle does.

Perturbative terms

Referring to the simpler active Brownian oscillator, the MSD calculated in Eq.(1.43) does not consider any terms of order higher than the first derivative in the forces expansion of Eq.(1.38). The contribution of higher order derivatives can be calculated starting from the oscillator solution $x_B(t)$ and adding to it a small perturbation term $h_x^{(1)}(t)$. We want to find

$$x(t) = x_B(t) + h_x^{(1)}(t) \tag{1.44}$$

such that:

$$\begin{aligned}\gamma\dot{x}_B(t) + \gamma\dot{h}_1(t) &= f_x(t) + \gamma v_0\cos(\phi(t)) \\ &+ \sum_{n_x=0}^{4}\sum_{n_y=0}^{4}\frac{(x_B(t)+h_x^{(1)}-x_0)^{n_x}(y_B(t)+h_y^{(1)}-y_0)^{n_y}}{n_x!n_y!}\left(\frac{\partial^{n_x+n_y}F_x}{\partial x^{n_x}\partial y^{n_y}}\right)(\mathbf{r}_0),\end{aligned} \tag{1.45}$$

where we considered all the terms in Eq.(1.38) for which $n_x + n_y \leq 4$. The result for a small perturbation $h_x^{(1)}(t)$ is:

$$\begin{aligned}\gamma h_x^{(1)}(t) \simeq \int_0^t \Big[&F_x^y(\mathbf{r}_0)\Delta y_B(t') \\ &+ \frac{1}{2}F_x^{xx}(\mathbf{r}_0)\Delta x_B^2(t') + F_x^{xy}(\mathbf{r}_0)\Delta x_B(t')\Delta y_B(t') + \frac{1}{2}F_x^{yy}(\mathbf{r}_0)\Delta y_B^2(t') \\ &+ \frac{1}{6}F_x^{xxx}(\mathbf{r}_0)\Delta x_B^3(t') + \cdots + \frac{1}{6}F_x^{yyy}(\mathbf{r}_0)\Delta y_B^3(t') \\ &+ \frac{1}{24}F_x^{xxxx}(\mathbf{r}_0)\Delta x_B^4(t') + \cdots + \frac{1}{24}F_x^{yyyy}(\mathbf{r}_0)\Delta y_B^4(t')\Big]\,\mathrm{d}t',\end{aligned} \tag{1.46}$$

where $\Delta x_B(t') \equiv (x_B(t') - x_0)$ and $\Delta y_B(t') \equiv (y_B(t') - y_0)$. To obtain all the necessary terms up to fourth order in time this procedure has to be repeated with a second order perturbation $h_x^{(2)}(t)$, and the resulting MSD in the x direction is the following

$$\mathrm{MSD}_x(t) = \left\langle \overline{\left\langle \Big(x_a(t) + x_b(t)) + x_c(t) + h_x^{(1)} + h_x^{(2)}(t)\Big)^2 \right\rangle} \right\rangle_r . \tag{1.47}$$

We are certain that this is enough to calculate the exact short-time MSD up to fourth order in time because the lowest time order contribution to the MSD of the perturbations $h^{(n)}$ grows with n, and the lowest non-zero contribution of $h^{(3)}$ is of order $> t^4$. Once the Eq.(1.47) expression is explicitly calculated and summed to $\mathrm{MSD}_y(t)$, we obtain the exact short-time MSD up to order t^4 (**P1**):

$$\begin{aligned}\mathrm{MSD}(t) = 4Dt + \left[v_0^2 + \frac{1}{\gamma^2}\widehat{F_i^2}\right]t^2 - \left[\frac{1}{3}v_0^2 D_R + \frac{D}{\gamma^2}\widehat{F_i^{j2}}\right]t^3 \\ + \frac{1}{24}\left[2v_0^2 D_R^2 + 10\frac{D^2}{\gamma^2}\widehat{F_i^{jk2}} - 5\frac{v_0^2}{\gamma^2}\widehat{F_i^{j2}}\right. \\ + \frac{1}{\gamma^4}\Big(14\widehat{F_i^2 F_i^{j2}} + 8\widehat{F_i^3 F_i^{ii}} + 14F_x\widehat{F_y F_x^y}F_i^i \\ \left. +14F_y\widehat{F_x F_y^x}F_i^i - 5\widehat{F_i^2 F_x^{y2}} - 5\widehat{F_i^2 F_y^{x2}}\Big)\right]t^4 + \mathcal{O}\left(t^5\right), \end{aligned} \tag{1.48}$$

where the i, j and k indexes each imply a sum over the directions x and y.

1.2.3 The intermediate scattering function

We discussed in Section 1.1.4 about how one can describe a stochastic process using partial differential Fokker-Planck equations and the probability distribution function $P(\mathbf{r}, t)$. In such cases, the calculation of the MD and MSD is direct, as they are respectively the first and second moments of $\mathbf{r} - \mathbf{r}_0$ with respect to P: $\mathrm{MD} = \langle \mathbf{r} - \mathbf{r}_0 \rangle$ and $\mathrm{MSD} = \langle (\mathbf{r} - \mathbf{r}_0)^2 \rangle$, where $\langle \cdot \rangle$ is defined as $\int \mathbf{dr}(\cdot)P(\mathbf{r}, t)$. Sometimes finding the real space solution of the equations $P(\mathbf{r}, t)$ and performing these averages directly can prove challenging, so it helps to move into Fourier space and use the properties of the *intermediate scattering function*, or ISF, defined as

$$\mathcal{F}(\mathbf{k}, t) \equiv \tilde{P}(\mathbf{k}, t)\tilde{P}(-\mathbf{k}, 0), \tag{1.49}$$

where $\tilde{P}$ is the Fourier transform of P and $\mathbf{k}$ is the wave number conjugate to $\mathbf{r}$. The ISF can then be related to the different moments of the density by differentiation, for example for an isotropic 3D system we have that [110]:

$$\left\langle (\mathbf{r} - \mathbf{r}_0)^{2n} \right\rangle = (-1)^{2n}\frac{(2n+1)!}{n!}\frac{\partial^n}{\partial(\mathbf{k}^2)^n}\mathcal{F}(|\mathbf{k}|, t)\bigg|_{\mathbf{k}^2=0}, \tag{1.50}$$

while in one dimension, such as in publication **P4**:

$$\langle (x - x_0)^n \rangle = \mathrm{i}^n \frac{\partial^n}{\partial k^n}\mathcal{F}(k, t)\bigg|_{k=0}. \tag{1.51}$$

1.3 Janus particles and thermophoresis

When possible, real-life experiments are always warranted when studying a subject, as they provide challenges and insights that analytic modeling and simulations do not. Since publication **P5** (Fig.1.7a) features an experimental realization of a system of active particles in a disordered landscape, this section is dedicated to this specific experimental setup, the underlying physical mechanism and its modeling.

1.3.1 The setup

There are three main components to the setup: a laser which provides energy to the system, a mixture of water and 2,6-lutidine at a temperature just below its demixing threshold, where the particles move, and finally the active particles themselves. The active particles are made out of silica and are half-coated in a thin layer of carbon. This type of asymmetrically coated particle, or *Janus particle*, is a staple in active matter systems [35, 111], as this asimmetry can be exploited to engineer simple self-propulsion mechanisms. In our case, the mechanism employed is called *thermophoresis* [112]: when light is shined upon the particles, the carbon half, being opaque, absorbs a larger part of it, increasing its own temperature. This generates a temperature gradient in the medium surrounding the particle, which leads to its localized demixing (see Fig.1.7b). Finally, the flows generated in the medium by the presence of the demixed fluid around the coating push the particle, either in the direction of the coating or opposite to it it based on whether the laser intensity is respectively smaller or larger than a certain threshold I_r [97, 113]. Since the intensity of light impacts the active speed of the particles, a modulation in the light field can be directly seen as a motility field [114]. The presence of an uneven light field leads to a further effect: a torque which rotates particles either away from or towards more intensely illuminated areas, on the base again of whether the laser intensity is respectively smaller or larger than I_r. This effect is called negative/positive phototaxis respectively. Now, in order to create a disordered light field for the particles to move through, the technique explained in Sec.1.1.2 is used: the coherent laser light is beamed through a disordered filter, which generates by diffraction a speckle field on the other side.

1.3.2 Modeling

The experiment is modeled as a bidimensional system of dry interacting active Brownian particles with an active speed that depends on their position, leading to

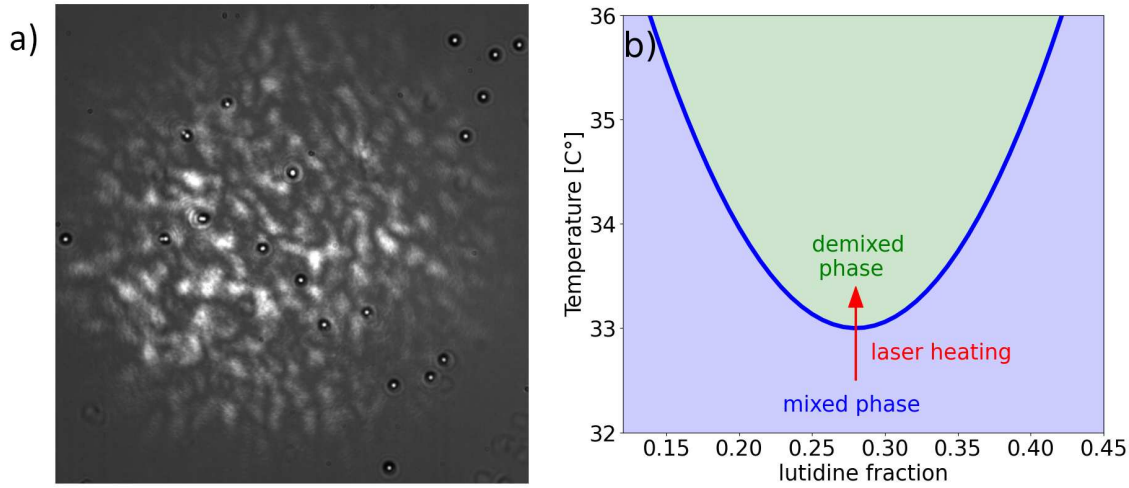

Figure 1.7: a) Janus particles in a speckle light field (photo provided by Gianni Jacucci). b) Sketch of the phase diagram of a water-lutidine mixture. At rest, the temperature of the system is just below the phase transition line, so that the heating induced by shining a laser on the Janus particles causes a localized demixing.

the following equations for the positions $\mathbf{r}$ and orientations ϕ of each particle i:

$$\begin{aligned}\gamma'\dot{\mathbf{r}}_i(t) &= \gamma' v_0(\mathbf{r}_i)\mathbf{n}(\phi_i) - \sum_{j\neq i} \nabla U_{LJ}\left(|\mathbf{r}_i - \mathbf{r}_j|\right) + \mathbf{f}(t),\\ \beta'\dot{\phi}_i(t) &= \beta'\omega(\phi_i, \mathbf{r}_i) + f_i^r(t),\end{aligned} \tag{1.52}$$

where ω is the torque and γ' and β' are modified versions of respectively the translational and rotational diffusion constants γ and β defined in Eqs.(1.6), corrected to take into consideration the interface effects of the substrate surface. In the case of particles directly touching the surface, these correction factors amount to $\gamma' = \frac{16}{9}\gamma$ and $\beta' = \frac{8}{7}\beta$ [115]. The Lennard-Jones potential U_{LJ} describes an interaction which is repulsive at very short distances and attractive otherwise:

$$U_{LJ}(|\mathbf{r}_i - \mathbf{r}_j|) = 4\epsilon\left[\left(\frac{d}{|\mathbf{r}_i - \mathbf{r}_j|}\right)^{12} - \left(\frac{d}{|\mathbf{r}_i - \mathbf{r}_j|}\right)^{6}\right], \tag{1.53}$$

where d is the diameter of the particles and ϵ is the maximum depth of the potential, which also defines the energy scale of the system. Eqs.(1.52) are very similar to the equations for the basic ABP model, Eq.(1.4), with the main differences being the presence of a motility field $v_0(\mathbf{r}_i)$ and the torque term $\omega(\phi_i, \mathbf{r}_i)$:

$$\omega(\phi_i, \mathbf{r}_i) = \frac{c}{d} v_0(\mathbf{r}_i)\left[\nabla v_0(\mathbf{r}_i) \times \mathbf{n}(\phi_i)\right] \cdot \hat{e}_z. \tag{1.54}$$

This torque models a positive or negative phototaxis for respectively a negative or positive value of c. These equations can be integrated numerically, for example with an Euler-Maruyama scheme, while the motility field can be generated by taking the Fourier transform of white noise, as discussed in Sec.1.1.2. Typical snapshots of the simulations can be seen in Fig.1.8.

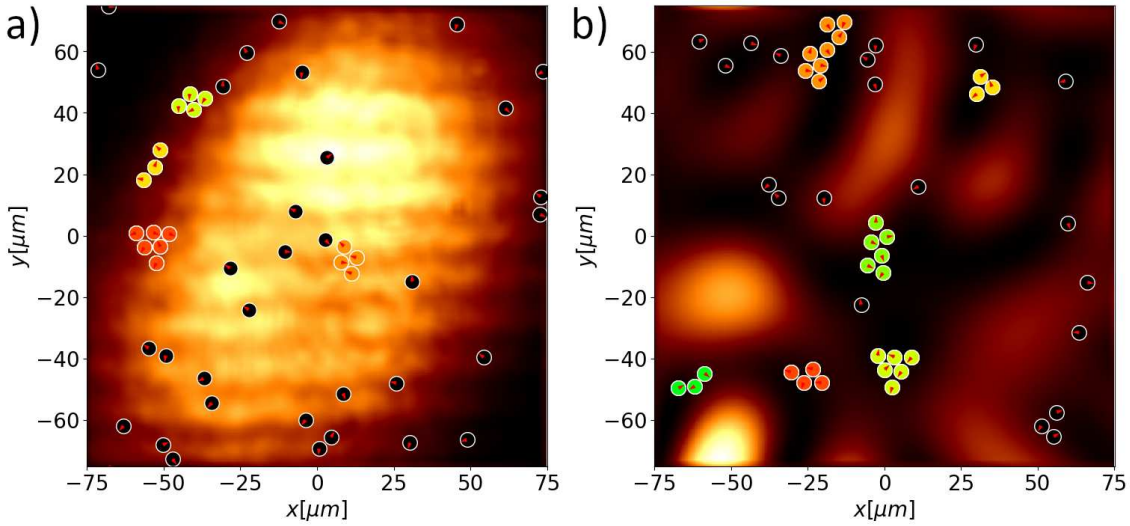

Figure 1.8: Simulation snapshots for a Gaussian-like a) and a speckle b) motility field. Different clusters are colored in different colors, while particles not part of any cluster are left in black. The red arrows show the orientation of the particles.

Chapter 2

Active entangled polymers

Polymers are systems of interconnected repeating units, called monomers. Such structures are ubiquitous in nature: the clothes we wear, as well as any plastic object or even the basic macromolecules in our body, like proteins, DNA and carbohydrates can all be considered polymeric systems [116]. On a macroscopic scale, polymers can also be used to model ropes, chains and living beings like snakes or worms [117], which, being active, are particularly relevant for this project. Indeed, in this chapter we evaluate the interplay between activity and particle deformability by considering complex active polymers, which monomers are active particles themselves. In order for the reader to appreciate the results of publication **P6**, we discuss some relevant polymer models: the *Rouse model* in Sec.2.1, which sets the basics for the study of free polymers, the *tube model* in Sec.2.2, necessary to understand highly entangled polymer systems, and in Sec.2.3 the model used in **P6** to describe active polymers.

2.1 Free polymers: the Rouse model

As publication **P6** is mostly concerned with the rheology of polymer solutions, this section and the next are mainly focused on their mechanical response. Instead of doing rigorous calculations, we will rely more on useful approximations, scalings and related interpretations, similarly to what is done in Ref. [118]. For now, we consider a very simplified model, where we have a very diluted solution of polymers made of chains of N beads connected via harmonic springs with elastic coefficient $k \equiv \frac{3k_BT}{2b^2}$. This value of k ensures, in the presence of thermal white noise independent between monomers $\mathbf{f}_i$, Eq.(1.2), that the beads keep on average a distance b between neighbors: $\langle(\mathbf{r}_{i+1} - \mathbf{r}_i)^2\rangle = b^2$. The system is overdamped and the monomer positions $\mathbf{r}_i$ follow the equations:

$$\begin{aligned}
\gamma\dot{\mathbf{r}}_1 &= -k(\mathbf{r}_1 - \mathbf{r}_2) + \mathbf{f}_1, \\
\gamma\dot{\mathbf{r}}_i &= -k(2\mathbf{r}_i - \mathbf{r}_{i-1} - \mathbf{r}_{i+1}) + \mathbf{f}_i, \quad 1 < i < N \\
\gamma\dot{\mathbf{r}}_N &= -k(\mathbf{r}_N - \mathbf{r}_{N-1})) + \mathbf{f}_N.
\end{aligned} \tag{2.1}$$

A simple result that can be extracted from this set of equations is the behavior of the center of mass of the polymer $\mathbf{r}_{CM} \equiv \frac{1}{N}\sum_i \mathbf{r}_i$:

$$\begin{aligned} \dot{\mathbf{r}}_{CM} &\equiv \sum_{i=1}^{N} \frac{\dot{\mathbf{r}}_i}{N} = \sum_{i=1}^{N} \frac{\mathbf{f}_i}{N\gamma} \\ \Rightarrow N\gamma\dot{\mathbf{r}}_{CM} &= \mathbf{f}_{CM}, \end{aligned} \tag{2.2}$$

where, since the $\mathbf{f}_i$ are independent identical Gaussian-distributed variables, $\mathbf{f}_{CM}$ is also white noise, with variance $\langle f_{CM,\alpha}(t) f_{CM,\beta}(t')\rangle = 2k_BTN\gamma\delta_{\alpha,\beta}\delta(t-t')$. Essentially, the center of mass of the polymer moves exactly as a free Brownian particle with friction $N\gamma$ and diffusion coefficient $D_N = \frac{k_BT}{N\gamma}$. With this, we can calculate the typical time τ_R necessary for the polymer to diffuse of a distance of the order of its size:

$$\tau_R \sim \frac{\langle R_{ee}^2\rangle}{D_N} = \frac{N\gamma\langle R_{ee}^2\rangle}{k_BT}, \tag{2.3}$$

where $\langle R_{ee}\rangle \equiv \langle|\mathbf{r}_N - \mathbf{r}_1|\rangle$ is the average end-to-end distance of the polymer, containing information on its configuration. In fact, if $\langle R_{ee}\rangle = Nb$, the polymer is completely stretched, and the smaller $\langle R_{ee}\rangle$ is, the more coiled is the polymer. The τ_R timescale, or *Rouse time*, is made relevant by the fact that at time τ_R all the monomers have on average interacted with each other (either directly or through other monomers), and the polymer has hence relaxed. This means that the motion of the monomers has become coherent and they all diffuse with the center of mass. Since the beads do not repel each other, it is possible to draw a direct comparison between a polymer of this kind, called *ideal chain*, and a random walk. Specifically, the MSD of a random walk and the $\langle R_{ee}\rangle$ of an ideal chain have the same *scaling behavior*, with respect to time for the MSD and to the number of monomers for the $\langle R_{ee}\rangle$: $\langle R_{ee}^2\rangle = b^2N$. The more realistic scaling of a *real chain* [119, 120], where we have repulsive interactions between different monomers, is not discussed here, as it is not necessary to understand the entangled case. If we consider the ideal chain scaling and also our monomers to be spheres of diameter b, we can use Eq.(1.6) and write

$$\tau_R \sim \frac{N^2b^3\eta_m}{k_BT}, \tag{2.4}$$

where η_m is the viscosity of the medium. Another relevant time scale is the typical time it takes for monomers diffuse of a distance equal to the bond length, corresponding to the typical interaction time τ_0. Similarly to how τ_R was extracted, we have

$$\tau_0 \sim \frac{b^3\eta_m}{k_BT}. \tag{2.5}$$

We can use these two timescales as qualitative limits in time of the mechanical response of our polymer. In fact, for times smaller than τ_0, the configuration of

the polymer does not change, leading to an elastic response, while for times larger than τ_R the polymer moves diffusively and responds to stress as a Newtonian fluid would. This complicated time-dependent response of the system indicates that we are dealing with *viscoelasticity*, a concept that requires a short introduction.

2.1.1 Viscoelasticity and the stress relaxation modulus

Let us consider a thin flat solid with thickness h. In order to study the linear mechanical response of such a system, a force F is applied to one face of the material tangential to the surface, while the other side remains fixed. This causes a deformation of magnitude Δx in the material, and allows us to measure the *shear strain* of the material $\zeta = \Delta x/h$ and the *shear stress* $\sigma = F/A$, where A is the cross section of the material. For perfectly elastic solids, the stress is proportional to the strain, and their ratio is defined as the *shear modulus* $G = \sigma/\zeta$.

If, instead of a solid, we decide to study the response of a fluid, this approach no longer works, because the application of a fixed amount of shear strain to the system does not originate any stress. What we can do instead, is to increase the strain over time (e.g. move one of the plates constricting the system at constant speed): in fact, in liquids the stress is a function of the *shear rate* $\dot{\zeta} = \frac{\mathrm{d}\zeta}{\mathrm{d}t}$. For Newtonian liquids, shear stress and rate are proportional, and their ratio is the viscosity of the material $\eta = \sigma/\dot{\zeta}$.

Now, viscoelastic materials, such as polymers and in general soft materials, live somewhere in the middle between solids and liquids. Polymers specifically, as we have seen, show an elastic solid-like response at short times, a viscous liquid-like response at long times and some different behavior at intermediate times, when they are in the process of relaxing. Since the response of the system is now time-dependent, the stress becomes a function of time too [118]:

$$\sigma(t) = \int_{-\infty}^{t} G(t-t')\dot{\zeta}(t')\mathrm{d}t', \tag{2.6}$$

where $G(t) = \sigma(t)/\zeta(t)$ is now referred to as *stress relaxation modulus*. We can further define a time-dependent viscosity $\eta(t) = \sigma(t)/\dot{\zeta}(t)$, and if we consider a constant shear rate $\dot{\zeta}$, we have:

$$\eta(t) = \frac{\sigma(t)}{\dot{\zeta}} \int_{-\infty}^{t} G(t-t')\dot{\zeta}\mathrm{d}t' = \int_{0}^{t} G(t'')\mathrm{d}t''. \tag{2.7}$$

Some other relevant quantities that we can extract from $G(t)$ are the *relaxation time* of the system τ_d, that is the time at which the system has completely relaxed and $G(t)$ falls exponentially, and the long-time viscosity $\eta = \lim_{t\to\infty} \eta(t)$. Given the richness of information contained in $G(t)$, this quantity is used extensively in the study of polymer relaxation dynamics.

2.1.2 The Rouse viscoelastic response

In order to study how polymers relax in the viscoelastic regime, it is important to note that polymer chains are self-similar, i.e. sections of the chain behave similarly to the full polymer. When relaxing, each of these sections constitutes a *relaxation mode*, with typical relaxation time τ_p for a section of length N/p and $1 \leq p \leq N$. When a polymer section relaxes, all the monomers within that section start moving coherently. We focus first on the whole-polymer relaxation mode ($p = 1$): we already know that at time τ_R the whole polymer relaxes (hence $\tau_1 = \tau_R$), so its response will be purely diffusive for times larger than τ_R. The stress relaxation modulus after this time can be then approximated with a *Maxwell element* [121], a combination of an elastic element and a viscous one, giving the following formula for $G(t)$:

$$G(t \geq \tau_M) = G_M \mathrm{e}^{-t/\tau_M}, \tag{2.8}$$

where τ_M is the relaxation time, in this case equal to τ_R, and $G_M \equiv G(\tau_R)$ is connected to the elasticity of the material. In polymer networks, elasticity is related to the thermal energy within each polymer (also called *entropic elasticity* [118,122]), so $G(\tau_R)$ is proportional to the chain number density Φ/Nb^3 (where Φ is the average number of monomers in a volume b^3) times the thermal energy k_BT:

$$G(\tau_R) \sim k_BT\frac{\Phi}{Nb^3}. \tag{2.9}$$

The $G(t)$ for $t \geq \tau_R$ is then

$$G(t \geq \tau_R) \sim k_BT\frac{\Phi}{Nb^3}\mathrm{e}^{-t/\tau_R}. \tag{2.10}$$

We can use the results for $p = 1$ to calculate the values of τ_p and $G(\tau_p)$ for all other p. Knowing that the full-chain relaxation time is N^2 times larger than the relaxation time of a single monomer, $\tau_R \sim \tau_0 N^2$, we can extrapolate an approximation of τ_p:

$$\tau_p \sim \tau_0 \left(\frac{N}{p}\right)^2, \qquad 1 \leq p \leq N. \tag{2.11}$$

In order to find $G(\tau_p)$ we count all unrelaxed modes at time τ_p, p per chain, as each will give its entropic contribution by the equipartiton theorem:

$$G(\tau_p) \sim k_BT\frac{\Phi}{Nb^3}p. \tag{2.12}$$

Using Eq.(2.11) we can then substitute p:

$$G(\tau_p) \sim k_BT\frac{\Phi}{b^3}\sqrt{\frac{\tau_0}{\tau_p}}, \tag{2.13}$$

Time scale	Description	$\propto$ MSD	$G(t)$
$t < \tau_0$	Beads are independent	Dt	G_0
$\tau_0 \leq t < \tau_R$	Rouse relaxation	$D\sqrt{t\tau_0}$	$G_0\sqrt{\frac{\tau_0}{t}}$
$t \geq \tau_R$	Relaxation of the whole polymer	$\frac{D}{N}t$	$\frac{G_0}{N}e^{-t/\tau_R}$

Table 2.1: Behavior of the mean squared displacement MSD and the stress relaxation modulus $G(t)$ of a Rouse polymer at different time scales.

which in the continuum limit of τ_p becomes

$$G(\tau_0 \leq t < \tau_R) \sim k_B T \frac{\Phi}{b^3}\sqrt{\frac{\tau_0}{t}}, \tag{2.14}$$

where $\sqrt{\frac{t}{\tau_0}} \equiv n(t)$ is the size of polymer sections relaxed at time t. Finally, we can combine the intermediate (Eq.2.14) and long time (Eq.2.10) behaviors of $G(t)$ in the following equation:

$$G(\tau_0 \leq t) \sim k_B T \frac{\Phi}{b^3}\sqrt{\frac{\tau_0}{t}}\mathrm{e}^{-t/\tau_R}, \tag{2.15}$$

while before τ_0 the response is simply elastic:

$$G(t < \tau_0) \sim k_B T \Phi / b^3 \equiv G_0. \tag{2.16}$$

Now that we have $G(t)$ we can also calculate the polymer viscosity η:

$$\eta = \int_0^\infty G(t)\mathrm{d}t \sim \frac{k_B T}{b^3}\Phi\sqrt{\tau_0\tau_R} \sim \frac{k_B T}{b^3}\Phi\tau_0 N \sim \eta_m \Phi N. \tag{2.17}$$

Finally, knowing the length of polymer strands that have relaxed at a certain time $n(t)$ allows us to find an estimate for the MSD of monomers at intermediate times. Using self-similarity and the diffusion coefficient for the center of mass of the full polymer $D_N = \frac{k_B T}{N\gamma}$, we have

$$D(\tau_0 \leq t < \tau_R) \sim \frac{k_B T}{n(t)\gamma} \sim \frac{k_B T}{\gamma}\sqrt{\frac{\tau_0}{t}}, \tag{2.18}$$

which indicates that the polymer behaves subdiffusively at intermediate regimes:

$$\mathrm{MSD}(\tau_0 \leq t < \tau_R) \sim D(t)t \sim \frac{k_B T}{\gamma}\sqrt{\tau_0 t}. \tag{2.19}$$

The results for the $G(t)$ and MSD are summarized in Table (2.1).

2.2 Entangled polymers: the tube model

When we consider monomer-monomer repulsion (e.g. in the form of volume exclusion), the physics and behavior of a solution of polymers changes radically as a function of the polymer concentration. Broadly, three different regimes can be observed: dilute solutions, where polymers are essentially independent with respect to each other, semi-dilute solutions where polymers start interacting, and finally polymer melts, where we reach such a high concentration that almost all of the space is occupied by polymers. This last situation is especially interesting, as it heavily features entanglement, a phenomenon typical of polymeric systems [123]. Interestingly, entangled systems are easier to describe than semi-dilute systems, as the spatial concentration of polymers is approximately constant throughout the whole sample, leading to a scaling behavior of the end-to-end distance that, despite the repulsive interactions, is still that of an ideal chain $\langle R_{ee}^2 \rangle \sim b^2 N$ [124] and allowing for theoretical models such as the tube model by Doi and Edwards [108]. In this model, each polymer can only move within its own *primitive tube*, which is a representation of the topological constraints, or *entanglement points*, provided by the other polymers (Fig.2.1a). The axis of this tube is called *primitive path*, its contour length is denoted by L_{pp} and the radius of the primitive tube is defined as a. As the polymer relaxes, it undergoes two main regimes: at first short sections of the polymer relax freely within the tube, then, hindered by the presence of the neighbors, further relaxation can only proceed by slowly moving the whole polymer along the primitive tube, a process called *reptation*.

2.2.1 Free Rouse relaxation

Since the polymer is allowed to move freely within the tube, short strands of it can explore space with the usual random walk behavior $\langle |\mathbf{r}_i - \mathbf{r}_{i+n}|^2 \rangle = b^2 n$. We define the entanglement number N_e as the maximum strand size which can move freely within the tube: $b^2 N_e \sim a^2 \Rightarrow N_e \sim a^2/b^2$. Consequently, the average primitive path contour length is $\langle L_{pp} \rangle \sim aN/N_e \sim bN/\sqrt{N_e}$, behaving itself too as a random walk with step size a. Between time τ_0 and the *entanglement time* $\tau_e \sim \tau_0 N_e^2$ the polymer relaxes by Rouse relaxation (Sec.2.1), with the typical MSD and viscoelastic behaviors:

$$\mathrm{MSD}(\tau_0 \leq t < \tau_e) \sim \frac{k_B T}{\gamma}\sqrt{t\tau_0}, \qquad G(\tau_0 \leq t < \tau_e) \sim \frac{k_B T}{b^3}\sqrt{\frac{\tau_0}{t}}, \tag{2.20}$$

where, given the high concentration, $\Phi = 1$.

At the end of this time window the stress relaxation modulus reaches the value

$$G(\tau_e) \equiv G_e \sim \frac{k_B T}{b^3 N_e}. \tag{2.21}$$

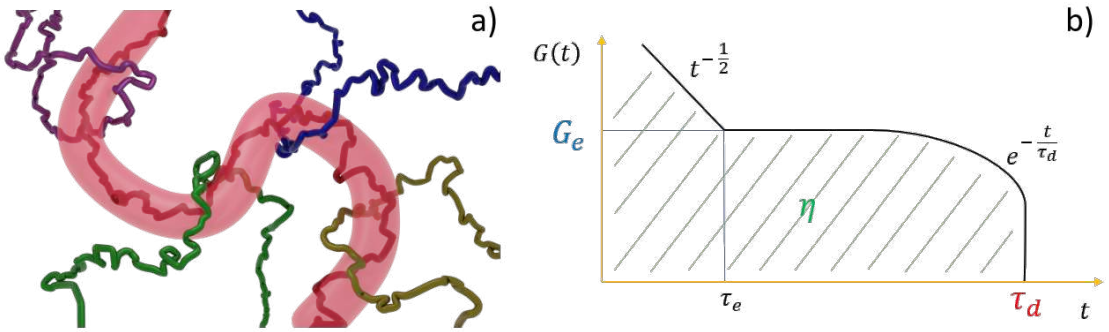

Figure 2.1: a) Sketch of the tube model: the main red polymer is effectively confined by its neighbors within a primitive tube of radius a and length L_{pp}. b) Typical behavior of the stress relaxation modulus $G(t)$ as a function of time for an entangled polymer. First we have Rouse relaxation until the entanglement time τ_e, then a plateau G_e until the relaxation time τ_d and finally an exponential decay. The area under this function constitutes the value of the long-time viscosity η.

2.2.2 Reptation

Mechanical response

At this phase of the relaxation, polymer sections of size larger than N_e can only relax along the primitive tube, almost stopping the $G(t)$ from decaying further, and forming a plateau at G_e. This stage lasts until the decorrelation time τ_d, which is given by the time necessary to the center of mass of the polymer to exit the initial primitive tube by diffusively exploring an area $\langle L_{pp}^2 \rangle$:

$$\tau_d \sim \frac{\langle L_{pp}^2 \rangle}{D_N} \sim b^2 \frac{N^2}{N_e} \frac{\gamma N}{k_B T} \sim \frac{\eta_m b^3 N^3}{k_B T N_e}. \tag{2.22}$$

Between τ_e and τ_d the $G(t)$ is almost constant, with the only decay given by the amount of polymer that has already exited the tube (Fig.2.1b). The plateau in the $G(t)$ makes the mechanical response of the solution at these timescales very similar to that of an elastic solid with shear modulus G_e. When time τ_d is reached, the polymer can finally relax and the $G(t)$ decays exponentially as $G_e \mathrm{e}^{-t/\tau_d}$, with a corresponding long-time viscous response. Since reptation takes a very long time, scaling with N^3, the plateau dominates the mechanical response of the solution and allows us to use the approximation $G(t) \simeq G_e \mathrm{e}^{-t/\tau_d}$ to calculate the long-time viscosity of the system:

$$\eta \sim \int_0^\infty G_e \mathrm{e}^{-t/\tau_d} \mathrm{d}t = G_e \tau_d \sim \frac{\eta_m N^3}{N_e^2}. \tag{2.23}$$

This result is vastly larger than what we found for the unentangled polymer: viscosity now scales with the cube of the polymer size instead of linearly.

MSD

The main feature of reptation is that polymers can only effectively move forward or backward in their primitive tube, in a sort of one-dimensional motion. It is then helpful to define a new variable s_i, that describes the 1D position of a monomer along the tube. The MSD of s_i is then subdiffusive before τ_R and diffusive after, essentially performing Rouse motion in 1D. Considering that the primitive path itself behaves as a random walk with step length a, we can write for the total MSD of a monomer:

$$\langle(\mathbf{r}_i(t) - \mathbf{r}_i(t'))^2\rangle \sim a^2\sqrt{\langle(s_i(t) - s_i(t'))^2\rangle}, \tag{2.24}$$

where

$$\langle(s_i(t) - s_i(t'))^2\rangle \sim \begin{cases} D\sqrt{(t-t')\tau_0} & \tau_e \leq t' \leq t < \tau_R, \\ \frac{D}{N}(t-t') & \tau_R \leq t' \leq t < \tau_d. \end{cases} \tag{2.25}$$

This means that during reptation, the monomer MSD undergoes two regimes: before τ_R it scales with $t^{1/4}$, and afterwards with $t^{1/2}$.

After the end of reptation, the polymer will simply move diffusively. The long-time diffusion coefficient for a polymer in an entangled solution D_l can be calculated from the relaxation time τ_d (Eq.2.22):

$$D_l \sim \frac{\langle R_{ee}^2\rangle}{\tau_d} \sim \frac{k_B T N_e}{\gamma N^2}, \tag{2.26}$$

where the scaling behavior of an ideal chain was used. We notice that the long time diffusion coefficient of an entangled polymer is a factor $\sim N$ smaller than that of a free polymer.

To summarize, the time evolution of the tube model can be reduced to five main regimes, separated by four time scales (Table 2.2). The first time scale, τ_0, indicates the average time it takes for a bead to interact with the closest one. Before τ_0 the beads are independent with respect to each other, and motion is dominated by the Brownian term. After τ_0 the beads start interacting, but still do not feel the constraints given by the other polymers, resulting in simple Rouse relaxation. The reptation behavior begins on average after the *entanglement time* $\tau_e = \tau_0 N_e^2$, where $N_e \sim (a/b)^2$ is the maximum average number of beads that can move freely without interacting with the primitive tube. After this time the polymer is unable to relax in all directions anymore, but only forward or backward in the tube, hence the name reptation. The next step is reached when the polymer reaches its natural Rouse relaxation time $\tau_R \sim \tau_0 N^2$ and starts moving as a whole along the primitive tube. Finally, the last regime takes place when the polymer escapes the initial primitive tube at $\tau_d \sim \tau_e(N/N_e)^3$.

Time scale	Description	$\propto$ MSD	$G(t)$
$t < \tau_0$	Beads are independent	Dt	G_0
$\tau_0 \leq t < \tau_e$	Rouse relaxation	$D\sqrt{t\tau_0}$	$G_0\sqrt{\frac{\tau_0}{t}}$
$\tau_e \leq t < \tau_R$	Rouse relaxation along tube (1D)	$a^2\sqrt{D}\sqrt[4]{t\tau_0}$	$\frac{G_0}{N_e}$
$\tau_R \leq t < \tau_d$	Polymer reptation along tube	$a^2\sqrt{D/Nt}$	$\frac{G_0}{N_e}$
$t \geq \tau_d$	Relaxation of the whole polymer	$D_l t$	$\frac{G_0}{N_e}e^{-t/\tau_d}$

Table 2.2: Behavior of the mean squared displacement MSD and the stress relaxation modulus $G(t)$ of an entangled polymer at different time scales.

2.3 Modeling and analysing active polymers

Activity can be implemented in many different ways in polymer systems [117, 125, 126]. For example, it is possible to have motor particles pushing the polymers around, similar to kinesin and microtubules [127, 128], polymers made up of active Janus particles [129], or filaments where each section is pushed tangentially forward, similar for example to how worms move [130–132]. Since in publication **P6** we simulated active entangled polymers tangentially moved, we provide here a short introduction on how to model and analyze this specific system.

2.3.1 Active entangled polymers - modeling

We define the polymers as chains of N beads each in a 3-dimensional space, with maximum bond distance $b_0 = 1.5d$ between consecutive beads moving, where d is the diameter of the monomers. The polymers are assumed to be completely flexible, where the beads are connected via finite-extensible non-linear elastic (FENE) springs with potential U_s [133]:

$$U_s(r) = \begin{cases} -\frac{Kb_0^2}{2}\ln\left[1 - \left(\frac{r}{b_0}\right)^2\right], & r \leq b_0, \\ \infty, & r > b_0, \end{cases} \tag{2.27}$$

where $K = 30\epsilon/d^2$ is the stiffness of the spring and ϵ is the energy scale of the system. They repel each other with a WCA potential U_r

$$U_r(r) = \begin{cases} 4\epsilon\left[\left(\frac{d}{r}\right)^{12} - \left(\frac{d}{r}\right)^{6}\right] + \epsilon, & r \leq r_c, \\ 0, & r > r_c, \end{cases} \tag{2.28}$$

where $r_c \equiv \sqrt[6]{2}d$. The angular interactions for each monomer are taken into account within the bending potential U_a:

$$U_{a,i} = \kappa \sum_{j=i-1}^{i+1} (1 - \mathbf{t}_j \cdot \mathbf{t}_{j+1}), \tag{2.29}$$

where $\mathbf{t}_i \equiv \frac{\mathbf{r}_{i+1}-\mathbf{r}_i}{|\mathbf{r}_{i+1}-\mathbf{r}_i|}$ is the vector tangential to the polymer between beads i and $i+1$, and κ is the bending energy. Finally, the active force $\mathbf{F}_a$ is implemented tangentially with respect to the polymer [134]:

$$\mathbf{F}_{a,i} = F_a(\mathbf{t}_{i-1} + \mathbf{t}_i), \tag{2.30}$$

where the active force strength F_a is constant. Our system is overdamped, leading to the following equation of motion for each bead:

$$\gamma\dot{\mathbf{r}} = -\boldsymbol{\nabla}(U_s + U_r + U_a) + \mathbf{F}_a + \mathbf{f}(t), \tag{2.31}$$

where γ is the translational friction coefficient and $\mathbf{f}$ is white noise, see Eq.(1.2). To be in the entangled regime we consider long chains with $N > 200$ and a volume fraction $\rho = 0.85$.

System equilibration

In publication **P6**, the system starts in passive equilibrium and activity is turned on at time $t = 0$. In order to reach the equilibrium regime for the system it is necessary for it to relax. As we have seen in Sec.2.2, though, the time necessary for an entangled polymer to exit its primitive tube, and hence relax, τ_d, grows with the cube of the polymer length $\propto L^3$ and can be very large. To avoid running extremely long thermalization simulations, there are methods that perform operations which would not be allowed during a normal simulation, but that considerably speed the process up. One example is the double-bridging hybrid (DBH) bond-swapping algorithm combined with core softening described by Dietz et al. in Ref. [135]. The standard DBH algorithm [136] works by swapping bonds and angles with *Monte Carlo* (MC) moves [137] during a molecular dynamics simulation. The MC moves work in the following way: bonds of neighboring monomers in different polymers are swapped, essentially exchanging strands between the polymers, with a probability P given by the *Metropolis criterion* [138]:

$$P = \min\left(1, \exp\left(-\frac{U_e - U_s}{k_B T}\right)\right), \tag{2.32}$$

where U_e and U_s are the potential energies of the system respectively after and before the MC step. The possibility to swap entire strands of polymers, which

is not allowed in normal molecular dynamics simulations, reduces the relaxation time considerably, going from $\propto L^3$ to a much more manageable $\propto L$. While this method works well for flexible polymers, in the case of semiflexible polymers the MC moves must overcome very large energy barriers $U_e - U_s$, which hinder the speed of the DBH algorithm. This problem is fixed by starting with softer cores and progressively increasing the hardness of the monomers, until the normal DBH algorithm can be employed.

2.3.2 Active entangled polymers - analysis

Correlation functions

Measuring a few correlation functions can yield a lot of information. The stress relaxation modulus, $G(t)$, allows us to study the rheology and mechanical response of the system [139]:

$$G(t) = \frac{V}{k_B T} \sum_{\alpha \neq \beta} \langle \sigma_{\alpha\beta}(t) \sigma_{\alpha\beta}(0) \rangle \,, \tag{2.33}$$

where V is the volume of the system and $\sigma_{\alpha\beta}$ is the α, β component of the stress tensor:

$$\sigma_{\alpha\beta} = \frac{1}{V} \left\langle \sum_{ij} F_{ij,\alpha} r_{ij,\beta} \right\rangle , \tag{2.34}$$

where $\mathbf{F}_{ij}$ and $\mathbf{r}_{ij}$ are the force and distance between monomer i and j respectively, and we sum over all monomer pairs. From $G(t)$ we can extract the elastic plateau G_e, the viscosity η and the relation time τ_d (see Sec.2.1.1).

The MSD yields information on the dynamics of the system. It can be averaged on the motion of each monomer, or just on the centers of mass of the polymers:

$$\mathrm{MSD}_{CM}(t) = \langle (\mathbf{r}_{CM}(t) - \mathbf{r}_{CM}(0))^2 \rangle, \tag{2.35}$$

where in the case of monomers of equal mass, the center of mass $\mathbf{r}_{CM}(t) \equiv \sum_{i=1}^{N} \mathbf{r}_i(t)/N$. Finally, the end-to-end distance squared $\langle R_{ee}^2 \rangle = \langle (\mathbf{r}_N - \mathbf{r}_1)^2 \rangle$ is an indicator of polymer configuration and measuring $\langle R_{ee} \rangle^2$ as a function of the polymer length N reveals if we are dealing with ideal or real chains.

Topological quantities

The mechanism that distinguishes entangled polymer solutions is the impossibility for polymer chains to cross each other. When two polymer chains interact, instead of just colliding, they form topological structures known as entanglement points (Fig.2.2), making topology fundamental in order to gain a deeper understanding of such systems. In particular, the quantity N_e, that is the average number of

monomer between entanglement points, is very relevant, as in the passive case it is inversely proportional to the height of the stress correlation plateau G_e [140]. The key for the measure of topological quantities is the primitive path model (see Sec.2.2): once we individuate the primitive path for each polymer, we can extract N_e, as well as other important quantities, such as the number of entanglements per polymer Z and the primitive path length L_{pp}. We cover here two different ways of extracting the aforementioned primitive path: the primitive path analysis theorized by Everaers et al. [140, 141] and the Z1+ method developed by M. Kröger [142].

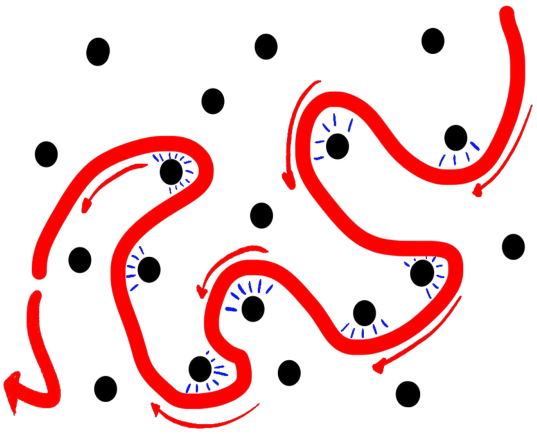

Figure 2.2: Sketch of the 2D cross-section of the tube model in the case of active polymers. We have an active polymer (in red) that reptates along its primitive path, while its neighboring polymers form topological obstacles, known as entanglement points (in black). The stresses generated by the interactions between the polymer and the entanglement points (in blue) originate the short-term elastic response typical of entangled polymer networks.

Primitive Path Analysis (PPA) This method individuates primitive paths by first fixing the positions of the polymer extremes, then disabling all excluding volume interactions within the same chain and finally reducing the temperature of the system almost to zero. This means that monomers in the same chain will relax only with the FENE attracting interaction while still not being able to cross other chains, which effectively straightens the polymers while keeping their entanglement points intact. An example of final configuration is shown in Fig.2.3 a). Once the energy of the system is minimized in this way, the average primitive path length $\langle L_{pp} \rangle$ is calculated by measuring the average contour length of the resulting polymers. In order to estimate the entanglement length from the primitive path analysis $\mathcal{N}_e^{PPA}$

we use the end-to-end scaling behaviour of entangled polymer chains R_{ee} [133]:

$$\langle R_{ee}(N)\rangle = l_K^{pp} L_{pp} = l_K^{pp}(N) l_b^{pp}, \tag{2.36}$$

where l_K^{pp} is the *Kuhn* (i.e. persistence) length of the primitive path and l_b^{pp} is the average bond length, defined as

$$l_b^{pp} = \frac{\sum_{j=1}^{N} |\mathbf{r}_{j+1} - \mathbf{r}_j|}{N}. \tag{2.37}$$

The entanglement length estimator will then be

$$\mathcal{N}_e^{PPA} = \frac{l_K^{pp}}{l_b^{pp}}. \tag{2.38}$$

Since $\mathcal{N}_e^{PPA}$ is just an estimator of the entanglement length N_e, it converges to N_e only in the infinite polymer length limit $N \to \infty$.

Z1+ Differently from the PPA method just described, the Z1+ program finds the primitive paths with a more geometric approach: it iteratively simplifies the original polymer configuration based on the position of entanglement points, eventually revealing the basic topological structure of the primitive paths. We start by taking for each polymer (or path) all sets of three consecutive nodes one after the other, where in the first iteration the nodes are defined by the position of the monomers. We then check the area of the triangle formed by the three nodes for eventual obstacles, defined by paths that intersect this area. Nodes are then added or removed to the path in order to minimize the aforementioned areas, while not allowing the sides of such areas to cross any obstacle. When, after multiple iterations, these areas cannot be further reduced, the nodes of the resulting paths will represent the topological entanglement points of the system. The average number of entanglement points $\langle Z\rangle$ is then the mean of the number of nodes per path, while $\langle L_{pp}\rangle$ is the average length of the paths. As an estimator for N_e, in publication **P6** we chose the modified single chain coil estimator defined by R. Hoy et al. [143] as

$$\mathcal{N}_e^{Z}(N) = (N-1)\left(\frac{\langle L_{pp}^2\rangle}{\langle R_{ee}^2\rangle}\right)^{-1}. \tag{2.39}$$

An example of primitive paths calculated with Z1+ can be found in Fig.2.3b)

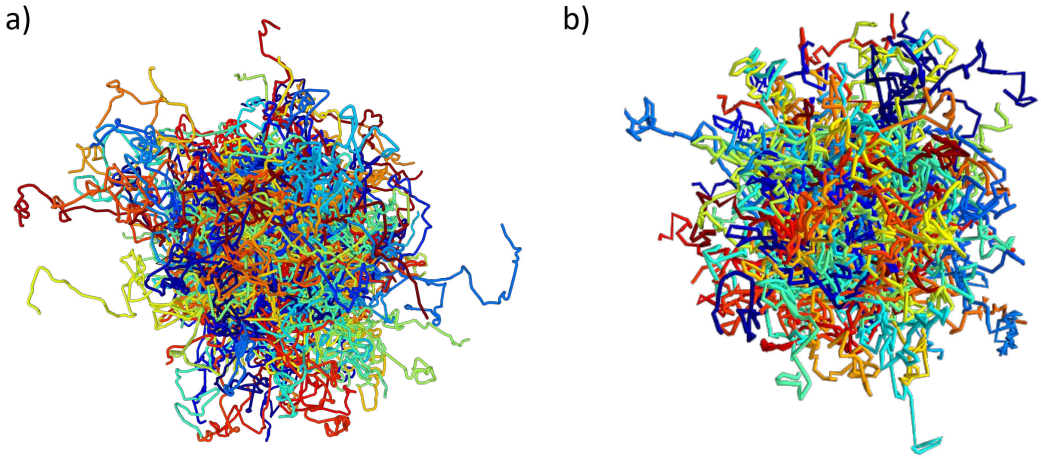

Figure 2.3: Figure a) shows the final configuration after primitive path analysis (PPA) for a typical simulation snapshot, in this case for a passive system with polymer size $N = 725$. Figure b) instead shows the primitive paths calculated with Z1+ for a passive system with polymer size $N = 1450$. Since Z1+ is a purely geometric method, the primitive paths generated in this way feature sharp angles that PPA-generated paths do not.

Chapter 3

Scientific publications

In the following, Publications **P1**–**P6** that form the basis of this dissertation are reproduced. For each publication, I present a summary of my contributions and when necessary a notice on copyright and licensing.

P1 Active Brownian and inertial particles in disordered environments: Short-time expansion of the mean-square displacement

Reproduced from

D. Breoni, M. Schmiedeberg and H. Löwen, *Active Brownian and inertial particles in disordered environments: Short-time expansion of the mean-square displacement*,
Physical Review E **102**, 062604 (2020),
with the permission of *AIP Publishing.*

Digital Object Identifier (DOI): `https://doi.org/10.1103/PhysRevE.102.062604`

Statement of contribution

HL directed the project. I performed analytic calculations and numerical simulations. MS performed the original calculations for a passive particle that were used as a starting point for this manuscript. All authors discussed the results and wrote the manuscript.

Copyright and license notice

PHYSICAL REVIEW E **102**, 062604 (2020)

Active Brownian and inertial particles in disordered environments: Short-time expansion of the mean-square displacement

Davide Breoni [1], Michael Schmiedeberg [2], and Hartmut Löwen [1]

[1] *Institut für Theoretische Physik II: Weiche Materie, Heinrich Heine-Universität Düsseldorf, 40225 Düsseldorf, Germany*

[2] *Institut für Theoretische Physik 1, Friedrich-Alexander-Universität Erlangen-Nürnberg, 91058 Erlangen, Germany*

(Received 21 October 2020; accepted 17 November 2020; published 7 December 2020)

We consider an active Brownian particle moving in a disordered two-dimensional energy or motility landscape. The averaged mean-square displacement (MSD) of the particle is calculated analytically within a systematic short-time expansion. As a result, for overdamped particles, both an external random force field and disorder in the self-propulsion speed induce ballistic behavior adding to the ballistic regime of an active particle with sharp self-propulsion speed. Spatial correlations in the force and motility landscape contribute only to the cubic and higher-order powers in time for the MSD. Finally, for inertial particles two superballistic regimes are found where the scaling exponent of the MSD with time is $\alpha = 3$ and $\alpha = 4$. We confirm our theoretical predictions by computer simulations. Moreover, they are verifiable in experiments on self-propelled colloids in random environments.

DOI: 10.1103/PhysRevE.102.062604

I. INTRODUCTION

The motion of active colloidal particles in complex environments is a vivid topic of recent physics research [1–3]. In particular, if self-propelled particles are moving in a heterogeneous or random medium, then there is a plethora of new effects created by disorder. Examples include trapping and clogging of particles [4–6], destruction of flocks [7], the control of crowds [8,9], and subdiffusive long-time dynamics [4,10–12]. The random environment can be established by a porous medium [13,14], by fixed obstacle particles [15–20], or by optical fields (such as a speckle field [21–27]) which can create both random external potentials [28–34] or a motility landscape [35,36].

While the control of particle motion in a random environment is crucial for many applications such as steered drug delivery and minimal invasive surgery, also the fundamental physics needs to be understood within statistical mechanics. In particular, analytical solutions for simple model systems are important here to unravel the underlying principles. A particular successful model for self-propelled particles is that of active Brownian motion [37–39] designed for colloidal microswimmers. Basically, the particle performs overdamped motion under the action of an internal effective drive directed along its orientation which is experiencing Brownian fluctuations establishing a persistent random walk of the particle. In this model, the mean-square displacement (MSD) of the particle exhibits a crossover from ballistic behavior governed by directed self-propulsion to final long-time diffusion with a diffusion coefficient that scales with the square of the self-propulsion velocity. The motion of self-propelled particles in various random environments has been studied by using computer simulations of active Brownian particles or related models [4,40–56]. Also some experiments for active particle in disordered landscapes have been performed on colloids [7,8,16,57] and bacteria [58]. However, analytical results are sparse, even for a single active particle. In one spatial dimension, exact results have been obtained for a run-and-tumble particle [11]. In higher dimensions, analytical results are available for discrete lattice models [10] and for a highly entangled slender self-propelled rod [59,60].

Here we present analytical results for the off-lattice model of active Brownian motion in two dimensions by exploring the short-time behavior of the mean-square displacement. The self-propelled particle is experiencing a space-dependent landscape of quenched disorder [61,62] of an external force or the internal motility field. We calculate the averaged MSD of the particle for arbitrary disorder strength in a systematic short-time expansion. As a result, for overdamped particles, randomness in the external force field and the particle motility both contribute to the initial ballistic regime. Spatial correlations in the force and motility landscape contribute only to the cubic and higher-order powers in time for the MSD. Finally, for inertial particles which are initially almost at rest three subsequent regimes can occur where the scaling exponent of the MSD with time crosses over from an initial $\alpha = 2$ to a transient $\alpha = 3$ and a final $\alpha = 4$. The latter superballistic regimes are traced back to the initial acceleration. We remark that similar superballistic exponents have been found for an active Brownian particle in linear shear flow [38] and for animal motion [63] but the physical origin is different in these cases. Our predictions are confirmed by computer simulations and are in principle verifiable in experiments on self-propelled colloids in random environments.

As an aside, we also present results for a passive particle in an random force landscape. Note that we consider the short-time behavior that is also briefly mentioned in [28–32,64,65] though in these works usually the focus is on the long-time

behavior [28–32,65] or the mean first passage time [64] of such systems.

The paper is organized as follows: In the next section we discuss the model of a single Brownian particle interacting with an external random landscape, in the subsequent one we move on to the case of a random motility field and in both cases we consider both an overdamped and an underdamped particle. Finally, in Sec. IV we conclude with a summary of our results and possible continuations of our work.

II. ACTIVE PARTICLE IN A DISORDERED POTENTIAL ENERGY LANDSCAPE

A. Overdamped active Brownian motion

We start by considering a single active Brownian particle moving in the two-dimensional plane. The dynamics is assumed to be overdamped as relevant for micron-sized swimmers and self-propelled colloids at low Reynolds number. The position of the particle center is described by its trajectory $\vec{r}(t) = (x(t), y(t))$ and its orientation is given by a unit vector $\hat{u}(t) = (\cos\phi(t), \sin\phi(t))$, where ϕ is the angle of the orientation vector with the x axis and t is the time. The equations of motion of an overdamped active Brownian particle for the translation and rotation degrees of freedom are given by

$$\gamma\dot{\vec{r}}(t) = \gamma v_0\hat{u}(t) + \vec{f}(t) + \vec{F}(\vec{r}(t)), \tag{1}$$

$$\gamma_R\dot{\phi}(t) = f_R(t), \tag{2}$$

where γ and γ_R are, respectively, the translational and rotational friction coefficients and v_0 is the self-propulsion velocity which is directed along the orientation vector $\hat{u}(t)$. The terms $\vec{f}(t)$ and $f_R(t)$ represent Gaussian white noise forces and torques originating from the solvent kicks with

$$\langle\vec{f}(t)\rangle = 0, \tag{3}$$

$$\langle f_i(t)f_j(t')\rangle = 2D\gamma^2\delta(t-t')\delta_{ij}, \tag{4}$$

$$\langle f_R(t)\rangle = 0, \tag{5}$$

$$\langle f_R(t)f_R(t')\rangle = 2D_R\gamma_R^2\delta(t-t'). \tag{6}$$

Here $\langle\cdot\rangle$ is the thermal noise average, D is the translational free diffusion constant, and D_R is the rotational one.

Importantly, the particle is exposed starting at $t = 0$ to an external force field $\vec{F}(\vec{r})$ representing the static quenched disorder. We assume that the external force is conservative, i.e., that it can be derived as a gradient from a random potential energy $V(\vec{r})$ such that

$$\vec{F}(\vec{r}) = -\vec{\nabla}V(\vec{r}) \tag{7}$$

holds. For the scalar potential energy we choose a general decomposition into two-dimensional Fourier modes and assume that the amplitudes in front of these modes are randomly Gaussian distributed and uncorrelated. In detail, the random potential $V(\vec{r})$ is expanded as

$$V(\vec{r}) = -\sum_{i,j=0}^{\infty}\left[\epsilon_{ij}^{(1)}\cos(k_ix + k_jy) + \epsilon_{ij}^{(2)}\sin(k_ix + k_jy)\right], \tag{8}$$

where $k_n = \frac{2\pi}{L}n$, L denoting a large periodicity length. The amplitudes $\epsilon_{ij}^{(\alpha)}$ are Gaussian random numbers which fulfill

$$\overline{\epsilon_{ij}^{(\alpha)}} = 0 \quad\text{and}\quad \overline{\epsilon_{ij}^{(\alpha)}\epsilon_{mn}^{(\beta)}} = \overline{\epsilon_{ij}^{(\alpha)2}}\delta_{im}\delta_{jn}\delta^{\alpha\beta}, \tag{9}$$

where $\overline{(\cdot)}$ denotes the disorder average. We further assume the potential to be isotropic, meaning that the $\epsilon_{i,j}$ are only functions of $i^2 + j^2$.

Now we compute the MSD $\Delta(t)$ of the particle which is initially at time $t = 0$ at position $\vec{r}_0$ with orientational angle ϕ_0. In this paper, we consider a disorder-averaged MSD, in detail it is a *triple* average over (i) the thermal noise $\langle\cdot\rangle$, (ii) the disorder $\overline{(\cdot)}$, and (iii) the initial conditions $\langle\langle\cdot\rangle\rangle$. As we switch on the potential at $t = 0$, due to translational invariance and self-propulsion isotropy, the latter are assumed to be homogeneously distributed in space and in the orientational angle. Consequently,

$$\Delta(t) := \langle\langle\ \overline{\langle(\vec{r}(t) - \vec{r}_0)^2\rangle}\ \rangle\rangle. \tag{10}$$

In order to simplify the notation, the average over both disorder and initial conditions for the various components and derivatives of the forces will be abbreviated by the symbol $\widehat{(\cdot)}$, for example, $\langle\langle\overline{F_x^2(\vec{r}_0)}\rangle\rangle \equiv \widehat{F_x^2}$.

In Appendix we detail the analytical systematic short-time expansion in terms of powers of time t for the MSD. To fourth order, the final result reads as

$$\begin{aligned}\Delta(t) = 4Dt &+ \left[v_0^2 + \frac{1}{\gamma^2}\widehat{F_i^2}\right]t^2 - \left[\frac{1}{3}v_0^2D_R + \frac{D}{\gamma^2}\widehat{F_i^{j2}}\right]t^3 \\ &+ \frac{1}{24}\Bigg[2v_0^2D_R^2 + 10\frac{D^2}{\gamma^2}\widehat{F_i^{jk2}} - 5\frac{v_0^2}{\gamma^2}\widehat{F_i^{j2}} \\ &+ \frac{1}{\gamma^4}\Big(14\widehat{F_i^2F_i^{i2}} + 8\widehat{F_i^3F_i^{ii}} + 14\widehat{F_xF_yF_x^yF_i^i} \\ &+ 14\widehat{F_yF_xF_y^xF_i^i} - 5\widehat{F_i^2F_x^{y2}} - 5\widehat{F_i^2F_y^{x2}}\Big)\Bigg]t^4 + \mathcal{O}(t^5).\end{aligned} \tag{11}$$

Here our convention in the notation is that the presence of any index i, j, or k implies an additional sum over the directions x and y. For example, in this compact notation, we have $\widehat{F_i^2} \equiv \sum_{i=x,y}\widehat{F_i^2}$. Subscripts in F indicate the Cartesian component of the force, while superscripts denote a spatial derivative. For example, $\widehat{F_i^{j2}} = \sum_{i=x,y}\sum_{j=x,y}\widehat{(\frac{\partial F_i}{\partial j})^2}$.

In order to assess the presence of scaling regimes for the MSD, it is necessary to know if the prefactors of t^α are negative or positive and hence what the sign of the various force products is. In Eq. (11), it can be shown that all products are positive with the exception of $\widehat{F_i^3F_i^{ii}}$. In the special case of a single mode potential, that we define as a potential where only $\epsilon_{11} \neq 0$, one can simplify this negative product with all the ones with $1/\gamma^4$ prefactor and obtain the shorter and positive expression $6\widehat{F_i^2F_j^{k2}}$ (see Appendix). In the more general case positivity is not ensured.

Let us now discuss the basic result contained in Eq. (11). First, in the absence of any external forces, we recover the

analytical expression for a free active particle [37] where

$$\Delta(t) = 4Dt + 2\frac{v_0^2}{D_R^2}(D_R t + e^{-D_R t} - 1)$$
$$= 4Dt + v_0^2 t^2 - \frac{1}{3}v_0^2 D_R t^3 + \frac{1}{12}v_0^2 D_R^2 t^4 + \mathcal{O}(t^5) \quad (12)$$

expanded up to order $\mathcal{O}(t^5)$. Conversely, for finite forces but in the limit of no activity, $v_0 = 0$, we get results for a passive particle in a random potential energy landscape [65].

In general, for both $v_0 \neq 0$ and $\vec{F} \neq 0$, as far as the influence of disorder is concerned, the first leading correction in the MSD is in the ballistic t^2 term. The physical interpretation of this term is rooted in the fact that in a disordered energy landscape on average the particle actually feels a nonvanishing force such that it is drifting. The resulting ballistic contribution is on top of the activity itself which also contributes to the transient ballistic regime. We define now the crossover time $t^c_{1\to 2}$ as the ratio A_1/A_2 between the two regimes scaling with $A_1 t$ and $A_2 t^2$. This quantity indicates the time when the ballistic regime becomes prominent over the diffusive one. In this case $t^c_{1\to 2}$ depends on the self-propulsion velocity and the strength of the potential, and more specifically it shrinks as those grow:

$$t^c_{1\to 2} = \frac{4D}{\widehat{F_i^2}/\gamma^2 + v_0^2}, \quad (13)$$

meaning that an active particle subject to a random force field begins earlier to move ballistically. Spatial correlations in the random potential energy landscape are contributing to the t^3 term in lowest order and affect the higher powers in time as well. Clearly, from the result (11), the prefactor in front of the t^3 term is negative such that there is no regime where a pure t^3 scaling in the MSD can be observed.

Finally, one could deduce from Eq. (11) that there is a special limit of parameters where the dominant regime is an acceleration where $\Delta(t) \propto t^4$. In order to see this, one can set v_0 and D to be small, while considering large wave vectors k and amplitudes ϵ in the potential decomposition Eq. (8) such that any combination of $\epsilon^2 k^4$ is much larger than one. However, this is not a scaling regime, as the term $\mathcal{O}(t^6)$ dominates on $\mathcal{O}(t^4)$ in the same limit.

We compared the result (11) to standard Brownian dynamics computer simulations. In our simulations, we first generated a random energy landscape, and then the particle was exposed to the selected landscape with an initial random position and orientation. Then we integrated the equations of motion with a Euler finite difference scheme involving a finite time step of typically $\Delta t = 10^{-6}/D_R$. In order to simplify calculations for the simulations, we always used single mode potentials. The MSD was then appropriately averaged over many starting configurations, the number of which was always larger than 10^4. This amount was large enough to yield statistical errors always below 1% of the averaged values of the MSD. We believe these samples are hence large enough to ensure ergodicity for the initial conditions.

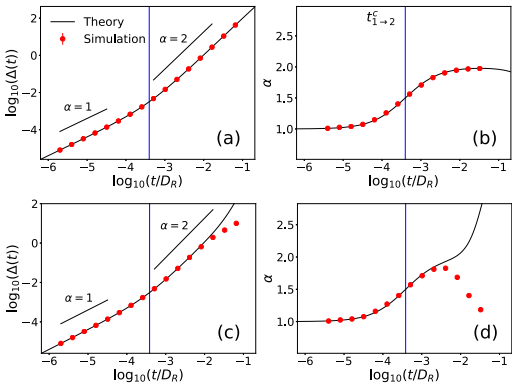

FIG. 1. Mean-square displacement [(a) and (c)], scaling exponent α [(b) and (d)], and crossing time $t^c_{1\to 2}$ (marked by a blue line) for an overdamped active particle in a random single mode potential. In (a) and (b) we used the parameters $v_0 = 100\sqrt{DD_R}$, $\epsilon = 100D\gamma$, and $L = 100\sqrt{D/D_R}$. As described by the theory, the initial diffusive behavior is soon replaced by the ballistic behavior. In (c) and (d) the parameters $v_0 = 50\sqrt{DD_R}$, $\epsilon = 100D\gamma$, and $L = 10\sqrt{D/D_R}$ also show first the diffusive and then the ballistic regimes, but for larger times the short-time expansion approximation breaks down earlier, as the average $\epsilon^2 k^4$ is larger.

Figure 1 shows examples for the scaling behavior of both the MSD and its scaling exponent

$$\alpha(t) := \frac{d(\log(\Delta(t)))}{d(\log(t))} \quad (14)$$

as functions of time in a double logarithmic plot. As can be deduced from Figs. 1(a) and 1(b), the initial diffusive regime where $\Delta(t) \propto t$ and the subsequent ballistic regime $\Delta(t) \propto t^2$ are clearly visible and reproduced by our short-time expansion. As expected, for large times there are increasing deviations between theory and simulation as the theory is a short-time expansion, and this is especially noticeable for large values of $\epsilon^2 k^4$, as for example is shown in Figs. 1(c) and 1(d).

B. Underdamped active Langevin motion

For macroscopic self-propelled particles or particles in a gaseous medium, inertial effects are getting relevant and overdamped active Brownian motion is generalized toward underdamped active Langevin motion [39,66]. The equations of motion for an inertial active particle in a random potential energy landscape are then generalized to

$$m\ddot{\vec{r}}(t) + \gamma\dot{\vec{r}}(t) = \gamma v_0 \hat{u}(t) + \vec{F}(\vec{r}(t)) + \vec{f}(t), \quad (15)$$

$$\gamma_R \dot{\phi}(t) = f_R(t), \quad (16)$$

where m is the particle mass. For simplicity, as in many previous studies for inertia [18,67–69], we have neglected rotational inertia here which could be included by using a finite moment of inertia [39,66].

Now the initial condition average $\langle\langle\cdot\rangle\rangle$ has to be performed not only over particle positions and orientations but also over the initial particle velocity $\vec{r}(0)$. The resulting triple-averaged short-time expansion of the mean-square displacement is now:

$$\Delta(t) = \sigma_v^2 t^2 + \frac{\gamma}{m}\left[\frac{4}{3}\frac{\gamma}{m}D - \sigma_v^2\right]t^3 + \frac{1}{m^2}\left[\frac{7}{12}\gamma^2\sigma_v^2 + \frac{1}{4}\widehat{F_i^2} + \frac{1}{4}\gamma^2 v_0^2 - \frac{\gamma^3}{m}D\right]t^4 + \mathcal{O}(t^5), \tag{17}$$

where $\sigma_v^2 = \langle\langle \dot{x}^2(0) + \dot{y}^2(0)\rangle\rangle$ is the variance of the initial speed of the particle. This result bears different dynamical scaling regimes. First, for short times the MSD starts ballistically with t^2 due to the initial velocities. Of course, this regime is absent if the particle is initially at rest when $\sigma_v^2 = 0$. Remarkably, for $\sigma_v^2 \ll D\gamma/m$ the leading behavior is governed by the term t^3, *cubic* in time, as the prefactor is positive. Please note that for an initially thermalized particle with a Maxwellian velocity distribution, the prefactor is negative, implying the absence of this cubic regime. Finally, the presence of an external disordered force field now contributes to the t^4 term as does the self-propulsion. This is plausible, as if on average a constant (external or internal self-propulsion) force is present, then the particle is constantly accelerated which leads to the t^4 scaling. Consequently, for $\sigma_v^2 \ll D\gamma/m \ll \widehat{F_i^2}/\gamma^2 + v_0^2$ there are *three* subsequent scaling regimes: from initially ballistic, over to the cubic regime, and finally to the constant acceleration regime.

The typical crossover time between the t^2 and t^3 scalings and the one between t^3 and t^4 are referred to as $t^c_{2\to3}$ and $t^c_{3\to4}$. Their values are as follows:

$$t^c_{2\to3} = \frac{m}{\gamma}\frac{\sigma_v^2}{\frac{4}{3}\frac{\gamma}{m}D - \sigma_v^2}, \tag{18}$$

$$t^c_{3\to4} = m\gamma\frac{\frac{4}{3}\frac{\gamma}{m}D - \sigma_v^2}{\frac{7}{12}\gamma^2\sigma_v^2 + \frac{1}{4}\widehat{F_i^2} + \frac{1}{4}\gamma^2 v_0^2 - \frac{\gamma^3}{m}D}, \tag{19}$$

where we assume that both prefactors of t^3 and t^4 in Eq. (17) are positive.

Using Langevin dynamics computer simulations, we have compared the theoretical short-time expansion with simulation data in Fig. 2. We used for the time evolution of the system a symmetrical stochastic splitting method that separates the stochastic and deterministic parts of the differential equations [70,71], with a typical time step of $\Delta t = 10^{-10}/D_R$. As for the overdamped case, we used a single mode potential field and we averaged the MSD over more than 10^4 configurations of the initial conditions and the potential.

A double-logarithmic plot indeed reveals three distinctive regimes where the MSD scales as t^α with $\alpha = 2, 3, 4$ and there is good agreement between theory and simulation if the times are not too large. It is important to note that the cubic regime can only be seen for initially cool systems which are exposed to thermal fluctuations. These can be experimentally prepared for example for granular hoppers [66] which are initially at rest and then brought into motion by instantaneously changing the vibration amplitude and frequency.

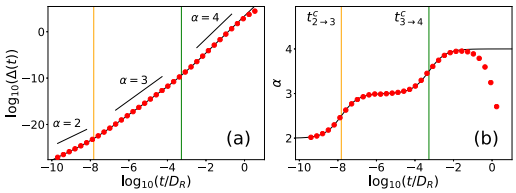

FIG. 2. Mean-square displacement (a) for an underdamped active particle in a random single mode potential, with scaling exponent α (b) and crossing times $t^c_{2\to3}$, $t^c_{3\to4}$. The parameters used are $v_0 = 100\sqrt{DD_R}$, $\epsilon = 100D\gamma$, $L = 100\sqrt{D/D_R}$, and $\sigma_v = 0.0002\sqrt{DD_R}$, and the unit for mass is the mass of the particle m. The three different scalings t^2, t^3, and t^4 are in this case clearly distinguishable from each other.

Hence though the t^3 regime is not visible for a thermalized system it shows up for relaxational dynamics even for passive particles.

III. ACTIVE PARTICLE IN A DISORDERED MOTILITY LANDSCAPE

A. No aligning torque, overdamped

We now consider a self-propelling velocity that fluctuates [72] as a function of the position of the particle. We denote hence the fluctuating part of the self-propelling velocity with $\delta v(\vec{r})$, while the constant part will still be named v_0, leading to a total propulsion velocity $[v_0 + \delta v(\vec{r})]\hat{u}(\phi)$ or motility field. As in the case of the random potential, the random motility field is decomposed into two-dimensional Fourier modes, with Gaussian uncorrelated amplitudes:

$$\delta v(\vec{r}) = \sum_{i,j=0}^{\infty}\left[\zeta_{ij}^{(1)}\cos(k_i x + k_j y) + \zeta_{ij}^{(2)}\sin(k_i x + k_j y)\right], \tag{20}$$

where the $\zeta_{ij}^{(\alpha)}$ prefactors have the same statistical properties as the $\epsilon_{ij}^{(\alpha)}$ prefactors in (9).

The main differences between the motility and potential fields are that the first one does not appear as a gradient in the equations of motion and that it is coupled to $\hat{u}(\phi)$.

In absence of an aligning torque and inertia the system fulfills the equations:

$$\gamma\dot{\vec{r}}(t) = \gamma(v_0 + \delta v(\vec{r}))\hat{u}(\phi) + \vec{f}(t), \tag{21}$$

$$\gamma_R\dot{\phi}(t) = f_R(t), \tag{22}$$

leading to the following short-time mean-square displacement:

$$\Delta(t) = 4Dt + \left(v_0^2 + \widehat{\delta v^2}\right)t^2 - \tfrac{1}{3}\left[2D\widehat{\delta v^{i2}} + D_R\left(v_0^2 + \widehat{\delta v^2}\right)\right]t^3 + \tfrac{1}{24}\left[6D^2\widehat{\delta v^{ij2}} + 8DD_R\widehat{\delta v^{i2}} + 2D_R^2\left(v_0^2 + \widehat{\delta v^2}\right) + 7\widehat{\delta v^2\delta v^{i2}} + 4\widehat{\delta v^3\delta v^{ii}} - 5v_0^2\widehat{\delta v^{i2}}\right]t^4 + \mathcal{O}(t^5), \tag{23}$$

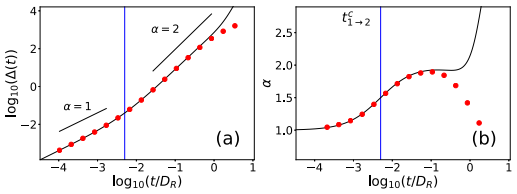

FIG. 3. Mean-square displacement (a), scaling exponent α (b), and crossing time $t^c_{1\to 2}$ for an underdamped active particle in a random single mode motility field. The parameters $v_0 = 20\sqrt{DD_R}$ and $\zeta = 20\sqrt{DD_R}$, $L = 100\sqrt{D/D_R}$ feature the initial diffusive behavior and the ballistic behavior.

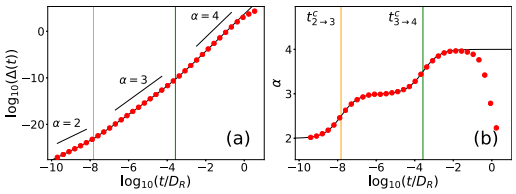

FIG. 4. Mean-square displacement (a) for an underdamped active particle in a random single mode motility field, with scaling exponent α (b) and crossing times $t^c_{2\to 3}$, $t^c_{3\to 4}$. The parameters used are $v_0 = 100\sqrt{DD_R}$, $\zeta = 100\sqrt{DD_R}$, $L = 100\sqrt{D/D_R}$, and $\sigma_v = 0.0002\sqrt{DD_R}$, and the unit of mass is the mass of the particle m. The three different scalings t^2, t^3, and t^4 are clearly distinguishable.

where we use the same notation as described for Eq. (11): The symbol $\widehat{(\cdot)}$ indicates an average over disorder and initial conditions, while the superscripts of δv indicate sums over derivatives. We also remark that the product $\widehat{\delta v^3 \delta v^{ii}}$ is negative, while all the others are positive.

From the results in Eq. (23) we can extract similar considerations as those we discussed in Sec. II A for Eq. (11). In the limit of a vanishing motility field $\delta v(\vec{r}) = 0$, the mean-square displacement of an active particle with constant speed [see Eq. (12)] is recovered. For a finite total self-propulsion velocity the first correction to the linear MSD is a t^2 term which is always positive, leading to a ballistic regime. The typical crossover time related to this transition $t^c_{1\to 2}$ is now

$$t^c_{1\to 2} = \frac{4D}{\widehat{\delta v^2} + v_0^2}. \tag{24}$$

Similarly to Eq. (11), the space configuration of the field appears for the first time in the $\mathcal{O}(t^3)$ term of the equation as a negative term that does not constitute a regime. The $\mathcal{O}(t^4)$ prefactor is positive for a large motility field and a small v_0, but as the higher-order terms always overshadow this, the particle never shows a pure accelerating behavior.

All these results have been confirmed by simulations similar to those described in Sec. II A. In Fig. 3 we can see an example of such a simulation, where the plots of the MSD and its scaling exponent α behave in accord to our theory for short times, with first a diffusive regime and then a ballistic one.

B. No aligning torque, underdamped

The underdamped equations of motion for a massive particle subject to a random motility field and no aligning torque are as follows:

$$m\ddot{\vec{r}}(t) + \gamma\dot{\vec{r}}(t) = \gamma(v_0 + \delta v(\vec{r}))\hat{u}(\phi) + \vec{f}(t), \tag{25}$$

$$\gamma_R\dot{\phi}(t) = f_R(t), \tag{26}$$

we ignore the effects of angular inertia, for the same reason explained in Sec. II B.

The resulting MSD, averaged over disorder, initial conditions, and thermal noise is as follows:

$$\Delta(t) = \sigma_v^2 t^2 + \frac{\gamma}{m}\left[\frac{4}{3}\frac{\gamma}{m}D - \sigma_v^2\right]t^3 + \frac{\gamma^2}{m^2}\left[\frac{7}{12}\sigma_v^2 + \frac{1}{4}\left(v_0^2 + \widehat{\delta v^2}\right) - \frac{\gamma}{m}D\right]t^4 + \mathcal{O}(t^5). \tag{27}$$

The three consecutive scaling regimes that characterized Eq. (17): t^2, t^3, and t^4, can be also found in Eq. (27) by requiring now $\sigma_v^2 \ll D\gamma/m \ll \widehat{\delta v^2} + v_0^2$. The crossing time $t_{3\to 4}$ changes accordingly, while $t_{2\to 3}$ remains the same that we calculated in the potential case [see Eq. (18)]:

$$t^c_{2\to 3} = \frac{m}{\gamma}\frac{\sigma_v^2}{\frac{4}{3}\frac{\gamma}{m}D - \sigma_v^2}, \tag{28}$$

$$t^c_{3\to 4} = \frac{m}{\gamma}\frac{\frac{4}{3}\frac{\gamma}{m}D - \sigma_v^2}{\frac{7}{12}\sigma_v^2 + \frac{1}{4}\left(v_0^2 + \widehat{\delta v^2}\right) - \frac{\gamma}{m}D}, \tag{29}$$

where we assume that both the prefactors of t^3 and t^4 in Eq. (27) are positive.

These results were compared to the numerical MSD calculated with the help of Langevin dynamics simulations. In Fig. 4 we present the typical results that can be obtained when the limit $\sigma_v^2 \ll D\gamma/m \ll \widehat{\delta v^2} + v_0^2$ applies, and hence three different regimes appear.

C. Aligning torque

In this subsection we discuss the special case of the presence of an aligning torque $\tau(\vec{r}, \phi)$ that redirects the self-propulsion of the particle toward either the maxima or the minima of the motility field. An aligning torque is important for colloidal realizations of active systems [35,73–75]. Since one common way of realizing a motility field is by the use of light fields, we refer to the self-propulsion toward the maxima of the field as *positive phototaxis* and the one toward the minima as *negative phototaxis*.

Here we only focus on the underdamped case, characterized by the following equations:

$$\gamma\dot{\vec{r}}(t) = \gamma(v_0 + \delta v(\vec{r}))\hat{u}(\phi) + \vec{f}(t), \tag{30}$$

$$\gamma_R\dot{\phi}(t) = \gamma_R\tau(\vec{r}, \phi) + f_R(t), \tag{31}$$

where $\tau(\vec{r},\phi) \equiv q[v_0 + \delta v(\vec{r})][\vec{\nabla}\delta v(\vec{r}) \times \vec{u}(\phi)] \cdot \vec{e}_z$. The sign of the prefactor q determines whether the phototaxis is positive ($q < 0$) or negative ($q > 0$).

The averaged MSD up to $\mathcal{O}(t^4)$ is as follows:

$$\Delta(t) = 4Dt + \left(v_0^2 + \widehat{\delta v^2}\right)t^2 - \tfrac{1}{3}\big[2D(1 + qv_0)\widehat{\delta v^{i2}} + D_R\left(v_0^2 + \widehat{\delta v^2}\right)\big]t^3 + \mathcal{O}(t^4). \tag{32}$$

In the special case of no translational diffusion ($D = 0$) the next order of the MSD is as follows:

$$\Delta(t) = \cdots + \tfrac{1}{24}\big[2D_R^2\left(v_0^2 + \widehat{\delta v^2}\right) + 7\widehat{\delta v^2 \delta v^{i2}} - 5v_0^2\widehat{\delta v^{i2}} + 4\widehat{\delta v^3 \delta v^{ii}} - 4q\left(v_0^3\widehat{\delta v^{i2}} + 3v_0\widehat{\delta v^2 \delta v^{i2}}\right) + 3q^2\left(v_0^4\widehat{\delta v^{i2}} + 6v_0^2\widehat{\delta v^2 \delta v^{i2}}\widehat{\delta v^4 \delta v^{i2}}\right)\big]t^4 + \mathcal{O}(t^5). \tag{33}$$

Analyzing Eqs. (32) and (33) we first notice that in the limit of $q = 0$ we recover the previous case with no aligning torque. When q is nonzero, it appears for the first time as prefactor of t^3 if $D > 0$ and as prefactor of t^4 otherwise. What is peculiar about q is that for different experimental setups its sign can change, and when it is negative, all the prefactors where it appears become positive. One can intuitively understand the reason for this by considering that a positive phototaxis means that the particle redirects itself toward the motility field maxima, and hence will show an MSD which is larger than in the negative phototaxis case. Even when q is negative and large though, this does not constitute a regime of either order t^3 or t^4, as the higher-order terms in time feature higher powers of q that overshadow the lower orders.

IV. CONCLUSIONS AND OUTLOOK

In conclusion we have systematically computed the quenched disorder average of the mean-square displacement for an active particle in a random potential or motility landscape. The amplitude of the ballistic regime is affected by the strength of disorder but spatial derivatives in the landscapes only contribute to the next cubic term in time. For an inertial particle two new superballistic scaling regimes are found where the MSD scales as t^3 or as t^4.

Our method can be applied to other more complex situations [76]. First, the generalization to an anisotropic potential is straightforward, even though tedious. Second, the landscapes can be time dependent as for real speckle patterns [26], moving activity waves [75,77], and propagating ratchets [36,78,79] The same analysis can be performed for time-dependent disorder. Moreover, the same analysis can in principle be done for other models of active particles, including the simpler active Ornstein Uhlenbeck particle [80] or more sophisticated pusher or puller descriptions for the self-propagation. A refreshing or resetting of the landscapes can be considered as well [81,82]. Finally, the model can be extended to a viscoelastic solvent [83–86] with a random viscoelasticity where memory effects become important.

ACKNOWLEDGMENTS

We thank S. U. Egelhaaf and C. Zunke for helpful discussions. The work of D.B. was supported within the EU MSCA-ITN ActiveMatter (Proposal No. 812780). H.L. acknowledges funds from the German Research Foundation (DFG) within SPP 2265 within Project No. LO 418/25-1.

APPENDIX: EXAMPLE OF MEAN-SQUARE DISPLACEMENT CALCULATION

In this Appendix we present an example for how we calculated the analytical results in this paper. Specifically, we will show the procedure used for the case of an overdamped particle in a random potential [see Eq. (11)].

1. Model system

The equation of motion for the time-dependent position $x(t)$ of the particle is given by Eqs. (1) and (2). Taylor expanding $\vec{F}(\vec{r}(t))$ around the starting position $\vec{r}(0) \equiv \vec{r}_0$ yields

$$\vec{F}(\vec{r}(t)) = \sum_{n_x=0}^{\infty}\sum_{n_y=0}^{\infty} \frac{[x(t) - x_0]^{n_x}[y(t) - y_0]^{n_y}}{n_x! n_y!} \times \left(\frac{\partial^{n_x+n_y}\vec{F}}{\partial x^{n_x}\partial y^{n_y}}\right)(\vec{r}_0). \tag{A1}$$

We truncate this expression in the following way:

$$\vec{F}(\vec{r}(t)) \simeq \begin{pmatrix} F_x(\vec{r}_0) + F_x^x(\vec{r}_0)[x(t) - x_0] \\ F_y(\vec{r}_0) + F_y^y(\vec{r}_0)[y(t) - y_0] \end{pmatrix}, \tag{A2}$$

where a subscript in F denotes a component of the force and a superscript indicates a partial derivative.

In this way we approximate our system to an active particle subject to two Brownian oscillators in the x and y directions independent of each other. The additional force terms of higher order will be treated in perturbation theory. The goal is to calculate the mean-square displacement $\Delta(t) := \langle\langle\overline{(\vec{r}(t) - \vec{r}_0)^2}\rangle\rangle$ for short times up to fourth order in time but for arbitrary strength of the random forces.

2. Active Brownian oscillator

We will focus on the equation in the x component, as the one in y can be treated in an analogous way. First we consider the formal solution of the active Brownian oscillator

$$\gamma\dot{x}_B = f_x(t) + \gamma v_0 \cos(\phi(t)) + F_x(\vec{r}_0) + F_x^x(\vec{r}_0)[x_B(t) - x_0], \tag{A3}$$

which is

$$\begin{aligned} x_B(t) &= x_0 + \frac{F_x(x_0)}{F_x'(x_0)}\left[e^{\frac{1}{\gamma}F_x'(x_0)t} - 1\right] \\ &\quad + \frac{1}{\gamma}\int_0^t e^{\frac{1}{\gamma}F_x'(x_0)(t-t')} f_x(t')dt' \\ &\quad + v_0\int_0^t e^{\frac{1}{\gamma}F_x'(x_0)(t-t')}\cos(\phi(t'))dt' \\ &=: x_0 + x_a(t) + x_b(t) + x_c(t), \end{aligned} \tag{A4}$$

where

$$\phi(t) = \frac{1}{\gamma_R}\int_0^t f_R(t')dt. \tag{A5}$$

The mean-square displacement in the x direction is

$$\begin{aligned}\Delta_{xB}(t) &= \langle\langle\overline{[x_a(t)+x_b(t)+x_c(t)]^2}\rangle\rangle \\ &= 2Dt + \left(\frac{\widehat{F_x^2}}{\gamma^2}+\frac{v_0^2}{2}\right)t^2 + \frac{1}{6}\left(8D\frac{\widehat{F_x^{x2}}}{\gamma^2} - D_R v_0^2\right)t^3 \\ &\quad + \frac{1}{24}\left(14\frac{\widehat{F_x^2 F_x^{x2}}}{\gamma^4} + 7\frac{\widehat{F_x^{x2}}}{\gamma^2}v_0^2 + D_R^2 v_0^2\right)t^4 + \mathcal{O}(t^5).\end{aligned} \tag{A6}$$

Note that we omitted all averages over odd powers of the force or its derivatives, as they are all accompanied by odd functions in space that go to zero when averaging over the initial conditions.

3. Perturbation approach

Now we will treat the time perturbation, considering terms up to fourth order in time. In order to do this, we will have to consider all the terms in Eq. (A3) for which $n_x + n_y \leqslant 4$.

We want to determine the solution

$$x(t) = x_B(t) + h_x^{(1)}(t) \tag{A7}$$

that fulfills the following differential equation:

$$\begin{aligned}&\gamma\dot{x}_B(t) + \gamma\dot{h}_1(t) \\ &\quad = f_x(t) + \gamma v_0\cos(\phi(t)) \\ &\qquad + \sum_{n_x=0}^{4}\sum_{n_y=0}^{4}\frac{\left[x_B(t)+h_x^{(1)}-x_0\right]^{n_x}\left[y_B(t)+h_y^{(1)}-y_0\right]^{n_y}}{n_x!n_y!} \\ &\qquad \times\left(\frac{\partial^{n_x+n_y}F_x}{\partial x^{n_x}\partial y^{n_y}}\right)(\vec{r}_0).\end{aligned} \tag{A8}$$

If we consider a small perturbation $h_x^{(1)}(t)$, then we obtain:

$$\begin{aligned}\gamma h_x^{(1)}(t) \simeq \int_0^t \Big\{&F_x^y(\vec{r}_0)[y_B(t')-y_0] + \frac{F_x^{xx}(\vec{r}_0)}{2}[x_B(t')-x_0]^2 \\ &+ F_x^{xy}(\vec{r}_0)[x_B(t')-x_0][y_B(t')-y_0] \\ &+ \frac{F_x^{yy}(\vec{r}_0)}{2}[y_B(t')-y_0]^2 \\ &+ \frac{F_x^{xxx}(\vec{r}_0)}{6}[x_B(t')-x_0]^3 + \ldots\Big\}dt',\end{aligned} \tag{A9}$$

where we first used the differential equation of the unperturbed Brownian oscillator and then assumed that $h_x^{(1)}(t)$ is small. The fifth-order derivatives of the force have been omitted because they would not lead to any terms of forth or smaller order in t.

Similarly, we calculate the second-order perturbation $h_x^{(2)}(t)$, while higher-order perturbations are not necessary.

The mean-square displacement within the first- and second-order perturbation theory is

$$\Delta_x(t) = \overline{\left\langle\left\langle\left[x_a(t)+x_b(t)+h_x^{(1)}+h_x^{(2)}(t)\right]^2\right\rangle\right\rangle}, \tag{A10}$$

and the only thing left is to explicitly calculate this expression and sum it to the respective one for the y direction.

4. Simplification of averages

Given the potential described in Eq. (8), one is able to simplify the various expressions for the averages of the forces and their derivatives. For example we have:

$$\widehat{F_x^2} = \frac{1}{2}\sum_{i,j,\alpha}\overline{\epsilon_{ij}^{(\alpha)2}}k_i^2, \tag{A11}$$

$$\widehat{F_x^{x2}} = \frac{1}{2}\sum_{i,j,\alpha}\overline{\epsilon_{ij}^{(\alpha)2}}k_i^4, \tag{A12}$$

$$\widehat{F_x F_x^{xx}} = -\frac{1}{2}\sum_{i,j,\alpha}\overline{\epsilon_{ij}^{(\alpha)2}}k_i^4 = -\widehat{F_x^{x2}}, \tag{A13}$$

$$\widehat{F_x^2 F_x^{y2}} = \frac{3}{8}\sum_{i,j,\alpha}\overline{\epsilon_{ij}^{(\alpha)4}}k_i^4 k_j^2 + \frac{1}{4}\sum_{\substack{i\neq m\wedge j\neq n\\ \alpha,\beta}}\overline{\epsilon_{ij}^{(\alpha)2}}\,\overline{\epsilon_{mn}^{(\beta)2}}k_i^2 k_m^2 k_n^2, \tag{A14}$$

$$\widehat{F_x^2 F_y F_x^{xy}} = -\widehat{F_x^2 F_x^{y2}}, \tag{A15}$$

etc.

Using these relations we can write the whole expression for the MSD using only terms that we know to be positive. One has to be careful though, especially with the products containing four terms, as for example in Eq. (A16). These kind of products contain both a common mode average and a cross mode one [for example, respectively the first and second sum in Eq. (A16)]. It can happen that two different products contain the same (or opposite) common mode average but a different cross mode one. For example:

$$\widehat{F_x^2 F_x^{x2}} = \frac{3}{8}\sum_{i,j,\alpha}\overline{\epsilon_{ij}^{(\alpha)4}}k_i^6 + \frac{1}{4}\sum_{\substack{i\neq m\wedge j\neq n\\ \alpha,\beta}}\overline{\epsilon_{ij}^{(\alpha)2}}\,\overline{\epsilon_{mn}^{(\beta)2}}k_i^4 k_m^2, \tag{A16}$$

$$\widehat{F_x^3 F_x^{xx}} = -\frac{3}{8}\sum_{i,j,\alpha}\overline{\epsilon_{ij}^{(\alpha)4}}k_i^6 - \frac{3}{4}\sum_{\substack{i\neq m\wedge j\neq n\\ \alpha,\beta}}\overline{\epsilon_{ij}^{(\alpha)2}}\,\overline{\epsilon_{mn}^{(\beta)2}}k_i^4 k_m^2. \tag{A17}$$

In this case the absolute value of the cross mode of (A19) is three times larger than that of (A18), while the common mode is the same. In other cases, these cross modes can even disappear:

$$\widehat{F_x^2 F_x^{y2}} = \frac{3}{8}\sum_{i,j,\alpha}\overline{\epsilon_{ij}^{(\alpha)4}}k_i^4 k_j^2 + \frac{1}{4}\sum_{\substack{i\neq m\wedge j\neq n\\ \alpha,\beta}}\overline{\epsilon_{ij}^{(\alpha)2}}\,\overline{\epsilon_{mn}^{(\beta)2}}k_i^2 k_m^2 k_n^2, \tag{A18}$$

$$\widehat{F_x F_y F_x^x F_x^y} = \frac{3}{8}\sum_{i,j,\alpha}\overline{\epsilon_{ij}^{(\alpha)4}}k_i^4 k_j^2. \tag{A19}$$

In the special case of a single mode potential the following expression of Eq. (11):

$$\begin{aligned}&14\widehat{F_i^2 F_i^{i2}} + 8\widehat{F_i^3 F_i^{ii}} + 14\widehat{F_x F_y F_x^y F_i^i} \\ &\quad + 14\widehat{F_y F_x F_y^x F_i^i} - 5\widehat{F_i^2 F_x^{y2}} - 5\widehat{F_i^2 F_y^{x2}}\end{aligned} \tag{A20}$$

simplifies to $6\widehat{F_i^2 F_j^{k2}}$.

[1] C. Bechinger, R. Di Leonardo, H. Löwen, C. Reichhardt, G. Volpe, and G. Volpe, Rev. Mod. Phys. **88**, 045006 (2016).

[2] C. Reichhardt and C. J. O. Reichhardt, Rep. Prog. Phys. **80**, 026501 (2017).

[3] G. Gompper, R. G. Winkler, T. Speck, A. Solon, C. Nardini, F. Peruani, H. Löwen, R. Golestanian, U. B. Kaupp, L. Alvarez, T. Kiorboe, E. Lauga, W. C. K. Poon, A. DeSimone, S. Muinos-Landin, A. Fischer, N. A. Soeker, F. Cichos, R. Kapral, P. Gaspard, M. Ripoll, F. Sagues, A. Doostmohammadi, J. M. Yeomans, I. S. Aranson, C. Bechinger, H. Stark, C. K. Hemelrijk, F. J. Nedelec, T. Sarkar, T. Aryaksama, M. Lacroix, G. Duclos, V. Yashunsky, P. Silberzan, M. Arroyo, and S. Kale, J. Phys.: Condens. Matter **32**, 193001 (2020).

[4] O. Chepizhko and F. Peruani, Phys. Rev. Lett. **111**, 160604 (2013).

[5] C. Reichhardt and C. J. O. Reichhardt, Phys. Rev. E **97**, 052613 (2018).

[6] C. J. O. Reichhardt and C. Reichhardt, New J. Phys. **20**, 025002 (2018).

[7] A. Morin, N. Desreumaux, J.-B. Caussin, and D. Bartolo, Nat. Phys. **13**, 63 (2017).

[8] E. Pinçe, S. K. P. Velu, A. Callegari, P. Elahi, S. Gigan, G. Volpe, and G. Volpe, Nat. Commun. **7**, 10907 (2016).

[9] S. Koyama, D. Inoue, A. Okada, and H. Yoshida, Artif. Life Robotics **25**, 529 (2020).

[10] T. Bertrand, Y. Zhao, O. Bénichou, J. Tailleur, and R. Voituriez, Phys. Rev. Lett. **120**, 198103 (2018).

[11] Y. Ben Dor, E. Woillez, Y. Kafri, M. Kardar, and A. P. Solon, Phys. Rev. E **100**, 052610 (2019).

[12] A. Morin, D. Lopes Cardozo, V. Chikkadi, and D. Bartolo, Phys. Rev. E **96**, 042611 (2017).

[13] P. Grančič and F. Štěpánek, Phys. Rev. E **84**, 021925 (2011).

[14] E. Blagodatskaya and Y. Kuzyakov, Soil Biol. Biochem. **67**, 192 (2013).

[15] D. Takagi, J. Palacci, A. B. Braunschweig, M. J. Shelley, and J. Zhang, Soft Matter **10**, 1784 (2014).

[16] C. Lozano, J. R. Gomez-Solano, and C. Bechinger, Nat. Mater. **18**, 1118 (2019).

[17] C. Jin, J. Vachier, S. Bandyopadhyay, T. Macharashvili, and C. C. Maass, Phys. Rev. E **100**, 040601(R) (2019).

[18] Z. Mokhtari, T. Aspelmeier, and A. Zippelius, Europhys. Lett. **120**, 14001 (2017).

[19] R. Alonso-Matilla, B. Chakrabarti, and D. Saintillan, Phys. Rev. Fluids **4**, 043101 (2019).

[20] M. Brun-Cosme-Bruny, A. Förtsch, W. Zimmermann, E. Bertin, P. Peyla, and S. Rafaï, Phys. Rev. Fluids **5**, 093302 (2020).

[21] G. Volpe, G. Volpe, and S. Gigan, Sci. Rep. **4**, 3936 (2014).

[22] G. Volpe, L. Kurz, A. Callegari, G. Volpe, and S. Gigan, Opt. Express **22**, 18159 (2014).

[23] J. Bewerunge and S. U. Egelhaaf, Phys. Rev. A **93**, 013806 (2016).

[24] A. S. Nunes, S. K. P. Velu, I. Kasianiuk, D. Kasyanyuk, A. Callegari, G. Volpe, M. M. T. da Gama, G. Volpe, and N. A. M. Araújo, Soft Matter **16**, 4267 (2020).

[25] G. Pesce, G. Volpe, O. M. Maragó, P. H. Jones, S. Gigan, A. Sasso, and G. Volpe, J. Opt. Soc. Am. B **32**, B84 (2015).

[26] M. Paoluzzi, R. Di Leonardo, and L. Angelani, J. Phys.: Condens. Matter **26**, 375101 (2014).

[27] S. Bianchi, R. Pruner, G. Vizsnyiczai, C. Maggi, and R. Di Leonardo, Sci. Rep. **6**, 27681 (2016).

[28] J. Bewerunge, A. Sengupta, R. F. Capellmann, F. Platten, S. Sengupta, and S. U. Egelhaaf, J. Chem. Phys. **145**, 044905 (2016).

[29] J. Bewerunge, I. Ladadwa, F. Platten, C. Zunke, A. Heuer, and S. U. Egelhaaf, Phys. Chem. Chem. Phys. **18**, 18887 (2016).

[30] R. D. L. Hanes, M. Schmiedeberg, and S. U. Egelhaaf, Phys. Rev. E **88**, 062133 (2013).

[31] F. Evers, R. D. L. Hanes, C. Zunke, R. F. Capellmann, J. Bewerunge, C. Dalle-Ferrier, M. C. Jenkins, I. Ladadwa, A. Heuer, R. Castañeda-Priego, and S. U. Egelhaaf, Eur. Phys. J.: Spec. Top. **222**, 2995 (2013).

[32] R. D. L. Hanes, C. Dalle-Ferrier, M. Schmiedeberg, M. C. Jenkins, and S. U. Egelhaaf, Soft Matter **8**, 2714 (2012).

[33] R. L. Stoop and P. Tierno, Commun. Phys. **1**, 1 (2018).

[34] S. Chaki and R. Chakrabarti, Soft Matter **16**, 7103 (2020).

[35] C. Lozano, B. ten Hagen, H. Löwen, and C. Bechinger, Nat. Commun. **7**, 12828 (2016).

[36] C. Lozano, B. Liebchen, B. ten Hagen, C. Bechinger, and H. Löwen, Soft Matter **15**, 5185 (2019).

[37] J. R. Howse, R. A. L. Jones, A. J. Ryan, T. Gough, R. Vafabakhsh, and R. Golestanian, Phys. Rev. Lett. **99**, 048102 (2007).

[38] B. ten Hagen, R. Wittkowski, and H. Löwen, Phys. Rev. E **84**, 031105 (2011).

[39] H. Löwen, J. Chem. Phys. **152**, 040901 (2020).

[40] O. Chepizhko and F. Peruani, Eur. Phys. J.: Spec. Top. **224**, 1287 (2015).

[41] O. Chepizhko, E. G. Altmann, and F. Peruani, Phys. Rev. Lett. **110**, 238101 (2013).

[42] W. Schirmacher, B. Fuchs, F. Höfling, and T. Franosch, Phys. Rev. Lett. **115**, 240602 (2015).

[43] O. Chepizhko and T. Franosch, Soft Matter **15**, 452 (2019).

[44] O. Chepizhko and T. Franosch, New J. Phys. **22**, 073022 (2020).

[45] C. Reichhardt and C. J. Olson Reichhardt, Phys. Rev. E **90**, 012701 (2014).

[46] C. Reichhardt and C. J. O. Reichhardt, Soft Matter **10**, 2932 (2014).

[47] N. Kumar, S. Ramaswamy, and A. K. Sood, Phys. Rev. Lett. **106**, 118001 (2011).

[48] N. Kumar, H. Soni, S. Ramaswamy, and A. K. Sood, Nat. Commun. **5**, 4688 (2014).

[49] R. Das, M. Kumar, and S. Mishra, Phys. Rev. E **98**, 060602(R) (2018).

[50] D. A. Quint and A. Gopinathan, Phys. Biol. **12**, 046008 (2015).

[51] M. S. Simon, J. M. Sancho, and K. Lindenberg, Eur. Phys. J. B **89**, 1 (2016).

[52] W.-j. Zhu, X.-q. Huang, and B.-q. Ai, Chin. Phys. B **27**, 080504 (2018).

[53] B.-q. Ai, F.-h. Meng, Y.-l. He, and X.-m. Zhang, Soft Matter **15**, 3443 (2019).

[54] C. Sándor, A. Libál, C. Reichhardt, and C. J. Olson Reichhardt, Phys. Rev. E **95**, 032606 (2017).

[55] M. Zeitz, K. Wolff, and H. Stark, Eur. Phys. J. E **40**, 23 (2017).

[56] T. Jakuszeit, O. A. Croze, and S. Bell, Phys. Rev. E **99**, 012610 (2019).

[57] G. Volpe, I. Buttinoni, D. Vogt, H.-J. Kümmerer, and C. Bechinger, Soft Matter **7**, 8810 (2011).

[58] T. Bhattacharjee and S. S. Datta, Soft Matter **15**, 9920 (2019).

[59] S. Mandal, C. Kurzthaler, T. Franosch, and H. Löwen, Phys. Rev. Lett. **125**, 138002 (2020).

[60] P. Romanczuk, M. Bär, W. Ebeling, B. Lindner, and L. Schimansky-Geier, Eur. Phys. J.: Spec. Top. **202**, 1 (2012).

[61] J.-P. Bouchaud and A. Georges, Phys. Rep. **195**, 127 (1990).

[62] Y. Duan, B. Mahault, Y.-q. Ma, X.-q. Shi, and H. Chaté, arXiv:2010.02356 [cond-mat].

[63] P. F. C. Tilles, S. V. Petrovskii, and P. L. Natti, Sci. Rep. **7**, 14364 (2017).

[64] M. Wilkinson, M. Pradas, and G. Kling, arXiv:2008.07854 [cond-mat].

[65] C. Zunke, Driven and obstructed colloids in random energy landscapes, Ph.D. thesis, Heinrich-Heine-Universität, Düsseldorf, 2017.

[66] C. Scholz, S. Jahanshahi, A. Ldov, and H. Löwen, Nat. Commun. **9**, 5156 (2018).

[67] M. Enculescu and H. Stark, Phys. Rev. Lett. **107**, 058301 (2011).

[68] S. C. Takatori and J. F. Brady, Phys. Rev. Fluids **2**, 094305 (2017).

[69] S. Das, G. Gompper, and R. G. Winkler, Sci. Rep. **9**, 6608 (2019).

[70] G. Bussi and M. Parrinello, Phys. Rev. E **75**, 056707 (2007).

[71] D. A. Sivak, J. D. Chodera, and G. E. Crooks, Phys. Rev. X **3**, 011007 (2013).

[72] V. Zaburdaev, M. Schmiedeberg, and H. Stark, Phys. Rev. E **78**, 011119 (2008).

[73] S. Jahanshahi, C. Lozano, B. Liebchen, H. Löwen, and C. Bechinger, Commun. Phys. **3**, 1 (2020).

[74] S. Jahanshahi, C. Lozano, B. ten Hagen, C. Bechinger, and H. Löwen, J. Chem. Phys. **150**, 114902 (2019).

[75] A. Geiseler, P. Hänggi, and F. Marchesoni, Sci. Rep. **7**, 41884 (2017).

[76] E. Woillez, Y. Kafri, and N. S. Gov, Phys. Rev. Lett. **124**, 118002 (2020).

[77] H. Merlitz, H. D. Vuijk, J. Brader, A. Sharma, and J.-U. Sommer, J. Chem. Phys. **148**, 194116 (2018).

[78] A. Zampetaki, P. Schmelcher, H. Löwen, and B. Liebchen, New J. Phys. **21**, 013023 (2019).

[79] N. Koumakis, A. T. Brown, J. Arlt, S. E. Griffiths, V. A. Martinez, and W. C. K. Poon, Soft Matter **15**, 7026 (2019).

[80] D. Martin, J. O'Byrne, M. E. Cates, É. Fodor, C. Nardini, J. Tailleur, and F. van Wijland, arXiv:2008.12972 [cond-mat].

[81] T. Mano, J.-B. Delfau, J. Iwasawa, and M. Sano, Proc. Natl. Acad. Sci. U.S.A. **114**, E2580 (2017).

[82] A. Scacchi and A. Sharma, Mol. Phys. **116**, 460 (2018).

[83] J. R. Gomez-Solano, A. Blokhuis, and C. Bechinger, Phys. Rev. Lett. **116**, 138301 (2016).

[84] J. Berner, B. Müller, J. R. Gomez-Solano, M. Krüger, and C. Bechinger, Nat. Commun. **9**, 999 (2018).

[85] K. Qi, E. Westphal, G. Gompper, and R. G. Winkler, Phys. Rev. Lett. **124**, 068001 (2020).

[86] L. Theeyancheri, S. Chaki, N. Samanta, R. Goswami, R. Chelakkot, and R. Chakrabarti, Soft Matter **16**, 8482 (2020).

P2 Active noise-driven particles under space-dependent friction in one dimension

Reproduced from

D. Breoni, H. Löwen, and R.Blossey, *Active noise-driven particles under space-dependent friction in one dimension*, Physical Review E **103**, 052602 (2021), with the permission of *AIP Publishing.*

Digital Object Identifier (DOI): `https://doi.org/10.1103/PhysRevE.103.052602`

Statement of contribution

HL and RB directed the project. I performed analytic calculations and numerical simulations. RB contributed analytical results for the probability density functions. All authors discussed the results and wrote the manuscript.

Copyright and license notice

PHYSICAL REVIEW E **103**, 052602 (2021)

Active noise-driven particles under space-dependent friction in one dimension

D. Breoni [1], H. Löwen [1], and R. Blossey [2]
[1]*Institut für Theoretische Physik II: Weiche Materie, Heinrich Heine-Universität Düsseldorf, Universitätsstraße 1, 40225 Düsseldorf, Germany*
[2]*University of Lille, UGSF CNRS UMR8576, 59000 Lille, France*

(Received 19 February 2021; accepted 14 April 2021; published 4 May 2021)

We study a Langevin equation describing the stochastic motion of a particle in one dimension with coordinate x, which is simultaneously exposed to a space-dependent friction coefficient $\gamma(x)$, a confining potential $U(x)$ and nonequilibrium (i.e., active) noise. Specifically, we consider frictions $\gamma(x) = \gamma_0 + \gamma_1|x|^p$ and potentials $U(x) \propto |x|^n$ with exponents $p = 1, 2$ and $n = 0, 1, 2$. We provide analytical and numerical results for the particle dynamics for short times and the stationary probability density functions (PDFs) for long times. The short-time behavior displays diffusive and ballistic regimes while the stationary PDFs display unique characteristic features depending on the exponent values (p, n). The PDFs interpolate between Laplacian, Gaussian, and bimodal distributions, whereby a change between these different behaviors can be achieved by a tuning of the friction strengths ratio γ_0/γ_1. Our model is relevant for molecular motors moving on a one-dimensional track and can also be realized for confined self-propelled colloidal particles.

DOI: 10.1103/PhysRevE.103.052602

I. INTRODUCTION

Particles moving under the influence of a stochastic driving force in one dimension [1] are a fruitful laboratory for the exploration of the statistical mechanics of active systems, since they allow, in suitably chosen cases, for an analytic treatment. Following the initial works on one-dimensional active particles [2,3], the problem is currently receiving increased attention, since the results can be of relevance for various soft matter and biological systems in a larger sense [4–8]. One-dimensional models for active particles, in spite of their inherent simplicity, are indeed of relevance even for the description of collective effects [9–12].

A standard type of model under scrutiny is the persistent Brownian motion, the persistence being forced by activity. Maybe the simplest model for an active particle in one dimension is a discrete *run-and-tumble process* where the direction of self-propulsion discretely flips, i.e., the driving is assured by a random directional velocity, see, e.g., Refs. [10,13–19].

It is defined by the Langevin equation

$$\dot{x}(t) = v_0\sigma(t), \tag{1}$$

where the stochastic term $\eta(t) = v_0\sigma(t)$ is a telegraphic noise with values $\pm v_0$, with the sign flipped at a given tumbling rate. In particular, this model has been explored for a single particle in the presence of external potentials [20–22] and random disorder [10,16].

On a second level of complexity, one can consider a Brownian particle self-propelled along its orientation such that only the projection on the x axis is contributing to the actual particle propulsion but the orientation diffuses on the unit circle or unit spheres [23]. These models of *active Brownian particles* were extensively discussed in the literature [7] and can be realized by self-propelled Janus colloids in channel-like confinement [24–26]. For low activity, the fluctuation-dissipation theorem which couples the strength of the Brownian noise and the friction via the bath temperature should be fulfilled. Hence, in the limit of vanishing activity, the stationary probability density function (PDF) is a Boltzmann distribution. Also simpler variants of these models where the drive just enters via colored noise, often called active Ornstein-Uhlenbeck particles, have been explored in one dimension [27–32].

A third complementary approach starts from Langevin equations coupling an active white noise term to a spatially dependent diffusion coefficient [33], or friction [34,35]. The basic idea here is the gradient in the friction induces a drift velocity which drives the particle at constant noise. In near-equilibrium situations, a spatial dependence of the friction enforces a spatial dependence of the noise strength according to the fluctuation-dissipation theorem which guarantees a relaxation of the PDF to the stationary Boltzmann distribution. Here we deliberately abandon the validity of the fluctuation-dissipation theorem and therefore postulate a *nonequilibrium noise* in the presence of a friction gradient to define a nonequilibrium model with inherent activity. We refer to this kind of noise as "active" noise in the sequel. The equilibrium limit of a stationary Boltzmann distribution is reached if the friction gradient vanishes. Though these kind of nonequilibrium noise models were proposed more than a decade ago [34,35] and bear interesting descriptions for the biologically motivated case of molecular motors moving on a one-dimensional track [36–41] such as the action of chromatin remodeling motors on nucleosomes [42], they have not yet been studied systematically.

Here we propose a class of one-dimensional models with active noise in different friction gradients and external

confining potentials which we solve analytically. Our motivation to do so is threefold: first, any exactly soluble model in nonequilibrium is of fundamental importance for a basic understanding of particle transport. Second, we obtain qualitatively different PDFs which can be categorized within these active noise models. Third, our results are relevant for applications in the biological context and for artificial colloidal particles.

The model we discuss is based on a Langevin equation of a particle with nonequilibrium noise and space-dependent friction in one dimension with a spatial coordinate x. The particle is exposed to a space-dependent friction coefficient $\gamma(x) = \gamma_0 + \gamma_1|x|^p$ and an external potential $U(x) \propto |x|^n$ with exponents $p = 1, 2$ and $n = 0, 1, 2$. For short times, we provide analytical results for the mean displacement and the mean-squared displacement. Depending on the parameters, we find a crossover from an initial diffusive to a ballistic regime for $p = 1, 2$ and $n \neq 0$ as typical for any model of a single free active particle. For long times and $n > 0$, we obtain the stationary PDFs from the corresponding Fokker-Planck equation. The PDFs are non-Boltzmannian and display a rich variety of behaviors: from Gaussian-like to Laplace-like distributions, and variants of bimodal-Gaussian-like distributions. A change between these different behaviors can be achieved by a tuning of the ratio of the friction parameters γ_0/γ_1. To test the robustness of our results, we evaluate the effect of additional thermal noise [34,35].

As already mentioned, our proposed model is relevant for molecular motors moving on a one-dimensional track and can also be realized for confined self-propelled colloidal particles. In fact, colloids can be exposed to almost any arbitrary external potential by using optical fields [43–45] and almost any kind of noise can externally be programed by external fields [46,47]. A space-dependent friction can be imposed be a viscosity gradient in the suspending medium on the particle scale, a situation typically encountered for viscotaxis [48–51].

II. A PARTICLE UNDER NONEQUILIBRIUM NOISE: THE MODEL

Following Ref. [35], the model Langevin equation of a single active particle on a one-dimensional trajectory $x(t)$, we use in this work is given by the expression

$$\gamma(x)\dot{x}(t) = -U'(x) + \sqrt{A}\xi(t), \tag{2}$$

in which $U(x)$ is the confining potential, and $\xi(t)$ a Gaussian random noise with

$$\langle \xi(t)\rangle = 0, \quad \langle \xi(t)\xi(t')\rangle = \delta(t - t'), \tag{3}$$

and $A > 0$ characterizes the noise strength. The brackets $\langle ...\rangle$ denote a noise average. The Langevin equation (2) can be rewritten in the standard multiplicative noise form as

$$\dot{x}(t) = -\frac{U'(x)}{\gamma(x)} + \frac{\sqrt{A}}{\gamma(x)}\xi(t), \tag{4}$$

which we will interpret in the Stratonovich sense.

The factor $\gamma(x)$ in Eqs. (2) and (4) is a space–dependent friction force. It has been introduced in models for molecular motors in [34] and been modeled by an expression $\gamma(x) = 1 + \delta\tanh(x\beta)$ with parameters δ, β $(0 < \delta < 1)$, a function saturating at both large positive and negative values of the argument displaying a linear crossover zone. Aiming at analytic results, in this work we use an algebraic expression

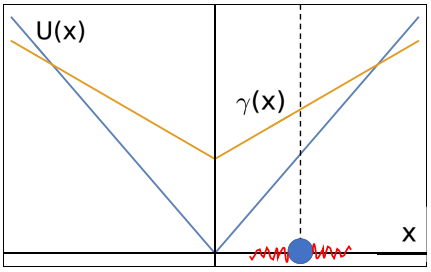

FIG. 1. Sketch of the confining potential $U(x) = \kappa|x|$, a linear friction gradient $\gamma(x) = \gamma_0 + \gamma_1|x|$ in arbitrary units.The particle, shown by a blue dot on the x axis, is activated by noise (indicated in red), under the influence of the potential and the friction gradient.

$$\gamma(x) = \gamma_0 + \gamma_1|x|^p \tag{5}$$

for the friction term with two parameters $\gamma_0 > 0$ and $\gamma_1 \geqslant 0$ and an integer exponent $p \geqslant 0$, which, although unbounded, will allow us to uncover interesting properties of the stationary probability density functions. These arise when we consider the particle in low-order polynomial confining potentials which we take to be of the general form

$$U(x) = \frac{\kappa}{n}|x|^n \tag{6}$$

with $\kappa \geqslant 0$ and another integer exponent $n \geqslant 0$ An illustration of the situation we address is given for the case $p = n = 1$ corresponding to a wedgelike potential $U(x) = \kappa|x|$ with a friction term $\gamma(x) = \gamma_0 + \gamma_1|x|$, see Fig. 1.

III. SHORT-TIME BEHAVIOR

We start our discussion by determining the short-time behavior of the active-noise driven particle and compute the short-time mean displacement (MD) and the mean-square displacement (MSD) for the Langevin equation (2), as done previously [52]. Specifically, we address the cases of a freely moving particle, $U'(x) = 0$ (i.e., $n = 0$) and a particle moving in the potential $U(x) = (\kappa/n)|x|^n$ for $n = 1, 2$, which, respectively, correspond to a particle on a (double) ramp (or, under gravity) and in a harmonic oscillator potential.

A. Constant friction gradient

Free particle. First we consider the case of $p = 1$, i.e., a constant friction gradient acting on a free particle. Due to the spatial dependence of the friction term, the choice of initial position $x_0 = x(t = 0)$ is important. In the immediate vicinity of the origin, the initial motion will be that of a free Brownian particle since $\gamma_0 \gg \gamma_1|x_0|$. In order to see an effect of the x dependence of the friction term, we place the particle initially far away from the origin with $|x_0| \gg 0$ to prevent the particle to traverse from the positive sector $x_0 > 0$ to the negative sector $x_0 < 0$ or vice versa, so that we ignore the nonanalyticity of

$\gamma(x)$ at the origin. We can then consider the case $x_0 > 0$, drop the modulus and use separation of the variables in Eq. (2) to find

$$\gamma_0(x(t)-x_0)+\frac{\gamma_1}{2}\left(x(t)^2-x_0^2\right)=\sqrt{A}\int_0^t dt'\xi(t') \tag{7}$$

resulting in

$$x(t)=\gamma_1^{-1}\left(-\gamma_0+\sqrt{\gamma_0^2+c(t)}\right) \tag{8}$$

with

$$c(t)\equiv 2\gamma_1\left(\frac{\gamma_1}{2}x_0^2+\gamma_0 x_0+\sqrt{A}\int_0^t dt'\xi(t')\right). \tag{9}$$

The resulting MD $\langle x(t)-x_0\rangle$ can then be obtained by an expansion of the square root as

$$\langle x(t)-x_0\rangle=\frac{1}{\gamma_0+\gamma_1 x_0}\overline{\xi}(t)+\sum_{m=2}^{\infty}(-1)^{m-1}\times\frac{(2m-3)!}{2^{m-2}m!(m-2)!}\frac{\gamma_1^{m-1}\overline{\xi}^m(t)}{(\gamma_0+\gamma_1 x_0)^{2m-1}}, \tag{10}$$

where

$$\overline{\xi^m}(t)\equiv\left\langle\left(\sqrt{A}\int_0^t dt'\xi(t')\right)^m\right\rangle=\begin{cases}\frac{m!}{2^{m/2}(m/2)!}(At)^{m/2} & m \text{ even}\\ 0 & m \text{ odd},\end{cases} \tag{11}$$

such that the final expression for the MD, after reintroducing the left side of the plane by symmetry, is

$$\langle x(t)-x_0\rangle=-\mathrm{sgn}(x_0)\sum_{m=1}^{\infty}\frac{(4m-3)!}{2^{3m-2}m!(2m-2)!}\frac{\gamma_1^{2m-1}}{\gamma(x_0)^{4m-1}}(At)^m. \tag{12}$$

The details of how we obtained Eq. (10) can be found in the Appendix.

Let us now discuss this result for the MD in more detail: first of all, if the friction gradient vanishes (i.e., in the case $\gamma_1=0$), there is no drift at all as ensured by left-right symmetry. Second, for positive friction gradients γ_1 the leading term for short times in the MD is linear in time and in the friction gradient $-\mathrm{sgn}(x_0)\gamma_1 At/2\gamma(x_0)+\mathcal{O}(t^2)$ resulting in a drift velocity of $-\mathrm{sgn}(x_0)\gamma_1 A/2\gamma(x_0)$. Interestingly the particle drift is along the negative gradient of the friction implying that the particle migrates on average to the place where the friction is small. This is plausible since at positions with smaller friction there are stronger fluctuations which promote the particle to the position of even lower friction on average. A similar qualitative argument was put forward for colloids moving under hydrodynamic interactions (see Ref. [53], p. 54), which represent another case of multiplicative noise, see also Ref. [54]. Third, in a more mathematical sense, the series in Eq. (13) is an asymptotic series which strictly speaking does not converge for $m\to\infty$ but nevertheless gives a good approximation to the MD to any finite order in time. This asymptotic expansion even holds if the cusp in the friction at $x=0$ were to be included as any corrections do not contribute to the short-time expansion in powers of time.

Similarly, one can calculate the MSD, which we define as

$$\Delta(t)=\langle(x(t)-x_0)^2\rangle. \tag{13}$$

One obtains a simple relation to the MD as follows:

$$\Delta(t)=-\mathrm{sgn}(x_0)\frac{2\gamma(x_0)}{\gamma_1}\langle x(t)-x_0\rangle. \tag{14}$$

Taking the asymptotic series as an approximation for finite times, we can now discuss for both the MD and the MSD the *crossing times* $t_{m\to m+1}$, defined as the ratios A_m/A_{m+1} between two consecutive regimes scaling with $A_m t^m$ and $A_{m+1}t^{m+1}$. These crossing times define the moments at which the $(m+1)^{th}$ terms of the time series start to dominate over the previous ones [52]. In this case, the crossing times of both the MD and MSD are given by

$$t_{m\to m+1}=\frac{4(m+1)(2m-1)}{(4m+1)(4m-1)(4m-2)}\frac{\gamma(x_0)^4}{A\gamma_1^2}. \tag{15}$$

The sequence of crossing times is monotonously decreasing, i.e., crossing times between larger regimes always occur before those of smaller ones. This in turn means that the only real regime for the free particle is the first one, linear in time. The same reasoning applies to the MSD, as it is proportional to the MD.

Generally, we characterize these regimes with time-dependent *scaling exponents*

$$\beta(t)\equiv\frac{d(\log_{10}(\langle x(t)-x_0\rangle))}{d(\log_{10}(t))} \tag{16}$$

and

$$\alpha(t)\equiv\frac{d(\log_{10}(\Delta(t)))}{d(\log_{10}(t))}. \tag{17}$$

If these exponents are constant over a certain regime of time they indicate that the MD (or the MSD) are a power-law in time proportional to t^β (or t^α).

Finally, we define a typical *passage time* for the particle to reach the origin and cross the cusp in the friction at $x=0$. Beyond such a passage time our theory should not be applicable any longer, as we ignored the presence of the cusp in the friction. We decided to run the simulations for longer than this time in order to show how the theory breaks down. Such a typical passage time t_1^c is set by requiring

$$\langle x(t_1^c)\rangle\equiv 0, \tag{18}$$

which means that on average the particle has reached the origin. Of course this is only an estimate. The definition of a passage time can be improved by requiring that the particle is one standard deviation away from the origin on average

$$\langle x(t_2^c)\rangle+\sqrt{\Delta(t_2^c)}\equiv 0 \tag{19}$$

for $x_0>0$. This defines a second typical passage time t_2^c which is in general smaller than t_1^c. Taken together, the two passage times t_1^c and t_2^c provide a rough estimate for the validity of our theory.

Explicit data for the MD and MSD are shown in Figs. 2(a) and 2(c), with the associated exponents $\beta(t)$ and $\alpha(t)$ given in Figs. 2(b) and 2(d). The typical passage times t_1^c (in purple) and t_2^c (in orange) are also indicated by vertical lines. In the

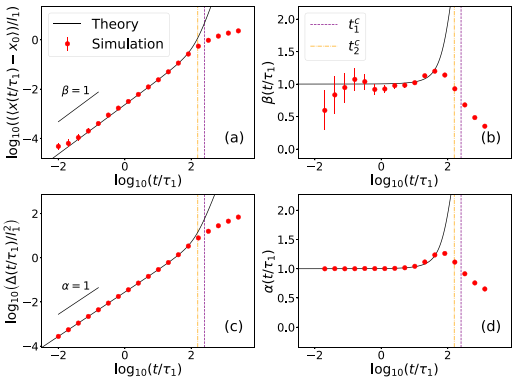

FIG. 2. Constant friction gradient and free particle $(p, n) = (1, 0)$. (a) mean displacement; (b) associated scaling exponent $\beta(t)$; (c) mean-squared displacement $\Delta(t)$; (d) associated scaling exponent $\alpha(t)$. The length unit is $l_1 \equiv \gamma_0/\gamma_1$, while the time unit is $\tau_1 \equiv l_1^2/A$. The initial position is $x_0 = 5l_1$. Simulation data are shown with error bars as red symbols. The theory is the solid line. The typical passage times t_1^c and t_2^c are indicated by purple and orange vertical lines.

figure we compare our analytic results (taken by summing up the series up to a finite order of 5) with the full numerical solution of the Langevin equation, Eq. (4), in Stratonovich interpretation; details of the numerical method are discussed in the Appendix.

First of all in the time regime $t < t_2^c$ the asymptotic theory is in good agreement with the simulation data. Both theory and simulations are dominated by the linear time dependence in the MD and MSD as indicated by the slope of the MD and MSD and likewise by the scaling exponents $\beta(t)$ and $\alpha(t)$ which are both close to unity. In both theory and simulation the scaling exponents $\beta(t)$ and $\alpha(t)$ first show a trend to increase to transient values larger than unity, i.e., towards superdiffusive behavior. Beyond t_2^c this trend weakens in the simulations such that both exponents fall significantly below unity. This is due to the fact that the particle has arrived at the position of minimal friction at the origin and therefore decelerates. However, in the theory there is an artificial monotonic increase in the slope due to the fact that there is even unphysical negative frictions for position smaller than γ_0/γ_1 (for the case $x_0 > 0$).

Linear confining potential. Now we consider the case $n = 1$ where $U(x) = \kappa|x|$, for $p = 1$. As before, we assume $x_0 \gg 0$ and drop the modulus in the potential. The force is then constant $U'(x) = -\kappa$ and the equation of motion can be solved by separation of variables as in the free case $n = 0$. The result for the MD is

$$\langle x(t) - x_0\rangle = -\mathrm{sgn}(x_0)\left[\frac{\kappa t}{\gamma(x_0)} + \sum_{m=2}^{\infty}\frac{(2m-3)!}{2^{m-2}(m-2)!} \times \frac{\gamma_1^{m-1}}{\gamma(x_0)^{2m-1}}\sum_{k=0}^{\lfloor m/2\rfloor}\frac{A^k\kappa^{m-2k}}{(m-2k)!2^k k!}t^{m-k}\right], \quad (20)$$

where the Gauss bracket $\lfloor\cdot\rfloor$ indicates the closest integer from below and the case $x_0 < 0$ is reintroduced via left-right symmetry. For short times, the MD is given by

$$\langle x(t) - x_0\rangle = -\mathrm{sgn}(x_0)\left[\left(\frac{\kappa}{\gamma(x_0)} + \frac{\gamma_1 A}{2\gamma(x_0)^3}\right)t + \left(\frac{\gamma_1\kappa^2}{2\gamma(x_0)^3} + \frac{3\gamma_1^2\kappa A}{2\gamma(x_0)^5} + \frac{15\gamma_1^2A^2}{8\gamma(x_0)^7}\right)t^2\right] + \mathcal{O}(t^3) \quad (21)$$

with an initial effective drift velocity

$$-\mathrm{sgn}(x_0)\left(\frac{\kappa}{\gamma(x_0)} + \frac{\gamma_1 A}{2\gamma(x_0)^3}\right), \quad (22)$$

which is a superposition of two effects arising from: (i) the direct force $-\mathrm{sgn}(x_0)\kappa$ already present in the equilibrium noise case (where $\gamma_1 = 0$), and (ii) the linear friction gradient. As in the free particle case ($n = 0$), the MD and the MSD fulfill a linear relationship given by

$$\Delta(t) = -\frac{2\gamma(x_0)}{\gamma_1}\left[\frac{\kappa t}{\gamma(x_0)} + \mathrm{sgn}(x_0)\langle x(t) - x_0\rangle\right], \quad (23)$$

such that the short-time expansion for the MSD is given by

$$\Delta(t) = \frac{A}{\gamma(x_0)^2}t + \left(\frac{\kappa^2}{\gamma(x_0)^2} + \frac{3\gamma_1\kappa A}{\gamma(x_0)^4} + \frac{15\gamma_1A^2}{4\gamma(x_0)^6}\right)t^2 + \mathcal{O}(t^3). \quad (24)$$

Clearly, for $\kappa = 0$, the free case is recovered.

We see from the MSD that we have first a diffusive and later a ballistic regime while for the MD the dominating term is the drift, as the particle feels the effects of the constant force. In fact, the crossing time between these two regimes in the MSD is

$$t_{1\to 2} = \frac{4A\gamma(x_0)^4}{4\kappa^2\gamma(x_0)^4 + 12\gamma_1\gamma(x_0)^2\kappa A + 15\gamma_1^2A^2} \quad (25)$$

and can be made arbitrarily small by formally varying the parameters A and κ, meaning that one can, in principle, have two wide regimes of initial diffusive and subsequent ballistic dynamics. Two regimes with a crossover time $t_{1\to 2}$ already exist for equilibrium noise $\gamma_1 = 0$ but the effect is persistent and tunable via nonequilibrium noise as documented by Eq. (25).

Results for the MD and the MSD as well as the scaling exponents and passage times t_1^c and t_2^c are shown in Fig. 3, obtained by both theory and simulation. The crossover between the initial diffusive and subsequent ballistic behavior in the MSD is clearly visible, in particular in $\alpha(t)$, which shows a plateau around $\alpha(t) = 2$ for intermediate times. The simulation data even reveal a transient subsequent superballistic behavior, which then falls off once the particle arrives at the origin, where it decelerates due to the opposed friction gradient. Again, for times smaller than the passage duration, theory and simulation are in very good agreement. Finally, the reason why the agreement of theory and numerics in Fig. 3(b) is much better than that of Fig. 2(b) is that the drift is now dominated by the deterministic potential, while in the case of the free particle it was completely noise driven.

Harmonic potential. Finally, for the harmonic oscillator: $U(x) = \frac{1}{2}\kappa x^2$, or $n = 2$, separation of variables is no longer possible and we therefore resort to a short-time expansion gained by perturbation theory (see Ref. [52]). In doing so,

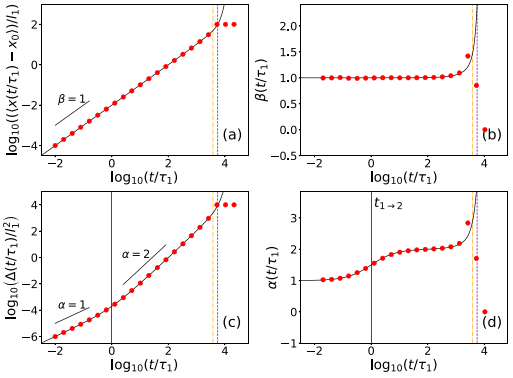

FIG. 3. Same as Fig. 2, but now for $n = 1$. (a) mean displacement; (b) scaling exponent $\beta(t)$; (c) mean-squared displacement $\Delta(t)$; (d) scaling exponent $\alpha(t)$. In (c) and (d) the crossing time $t_{1\to2}$ is indicated by a vertical green line. Parameter values are: $\kappa = \gamma_0 l_1/\tau_1, x_0 = 100 l_1$.

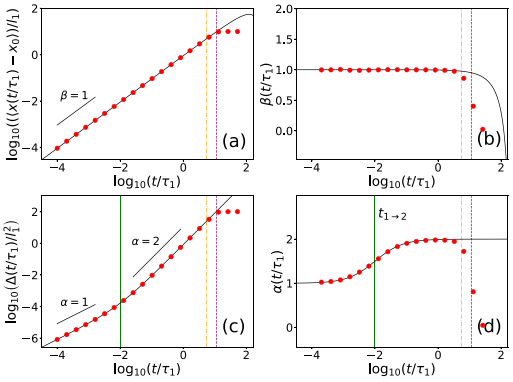

FIG. 4. Same as Fig. 2, but now for $n = 2$: (a) mean displacement $\langle x(t) - x_0\rangle$ and (b) scaling exponent $\beta(t)$; (c) mean-squared displacement $\Delta(t)$, and (d) scaling exponent $\beta(t)$. The parameters are $\kappa = \gamma_0/\tau_1$ and $x_0 = 10 l_1$.

first we take the solution of the $(p, n) = (1, 1)$ system, with a constant force of $-\kappa x_0$, and next we consider a harmonic oscillator potential centered in x_0 as a perturbation. Following this procedure, the short-time expansions of the MD and MSD are

$$\langle x(t) - x_0\rangle = -\mathrm{sgn}(x_0)\left(\left[\frac{\kappa|x_0|}{\gamma(x_0)} + \frac{\gamma_1 A}{2\gamma(x_0)^3}\right]t + \left[-\frac{|x_0|\kappa^2}{2\gamma(x_0)^2} + \frac{\gamma_1\kappa^2 x_0^2}{2\gamma(x_0)^3} - \frac{3}{4}\frac{\kappa A\gamma_1}{\gamma(x_0)^4} + \frac{3}{2}\frac{|x_0|\kappa\gamma_1^2 A}{\gamma(x_0)^5} + \frac{15}{8}\frac{\gamma_1^3 A^2}{\gamma(x_0)^7}\right]t^2\right) + \mathcal{O}(t^3) \tag{26}$$

and

$$\Delta(t) = \frac{A}{\gamma(x_0)^2}t + \left[\frac{x_0^2\kappa^2}{\gamma(x_0)^2} - \frac{\kappa A}{\gamma(x_0)^3} + 3\frac{\gamma_1\kappa|x_0|A}{\gamma(x_0)^4} + \frac{15}{4}\frac{\gamma_1^2 A^2}{\gamma(x_0)^6}\right]t^2 + \mathcal{O}(t^3). \tag{27}$$

In this case, the MD only shows a linear behavior, while the MSD displays two different regimes, diffusive and ballistic, separated by the crossing time

$$t_{1\to2} = \frac{4\gamma(x_0)^4 A}{4\gamma(x_0)^4 x_0^2\kappa^2 - 4\gamma(x_0)^3\kappa A + 12\gamma_1\gamma(x_0)^2\kappa x_0 A + 15\gamma_1^2 A^2}. \tag{28}$$

Figure 4 shows the comparison of the perturbation theory with the full numerical simulations revealing very good agreement for times smaller than a typical passage time. Clearly, for larger times, the particles becomes confined by the harmonic potential around the origin as signaled by a plateau arising in the MD and MSD for times larger than the typical passage time. Correspondingly, both scaling exponents $\beta(t)$ and $\alpha(t)$ drop to zero.

B. Linear friction gradient

We now turn to a linear friction gradient, $p = 2$, where there is no nonanalyticity in the spatial dependence of the friction at the origin. Then Eq. (2) becomes

$$(\gamma_0 + \gamma_1 x^2)\dot{x}(t) = -U'(x) + \sqrt{A}\xi(t). \tag{29}$$

Bearing in mind that the free case is a simple special case of the $n = 1$ one (for $\kappa = 0$), we directly show the results for $n = 0, 1$ for any $\kappa \geqslant 0$. The MD is

$$\langle x(t) - x_0\rangle = \sum_{m=1}^{\infty} a_m\langle\zeta^m(t)\rangle = \sum_{m=1}^{\infty} a_m \sum_{k=0}^{\lfloor m/2\rfloor} \frac{m! A^k(-\mathrm{sgn}(x_0)\kappa)^{m-2k}}{(m-2k)!2^k k!} t^{m-k}, \tag{30}$$

where the factors a_m are straightforwardly obtained by Taylor expanding the expression $(x(t) - x_0)$, calculated using separation of variables, in powers of

$$\zeta(t) = -\mathrm{sgn}(x_0)\kappa t + \sqrt{A}\int_0^t dt'\xi(t'). \tag{31}$$

Here $a_1 = \gamma(x_0)^{-1}$, but the expressions for the coefficients a_m for $m \geqslant 2$ are quite involved so that we refrain from showing them explicitly. In a similar way, the MSD is

$$\Delta(t) = \sum_{m=2}^{\infty} b_m\langle\zeta^m(t)\rangle = \sum_{m=2}^{\infty} b_m \sum_{k=0}^{\lfloor m/2\rfloor} \frac{m! A^k(-\mathrm{sgn}(x_0)\kappa)^{m-2k}}{(m-2k)!2^k k!} t^{m-k}, \tag{32}$$

where $b_2 = \gamma(x_0)^{-2}$ and the coefficients b_m for $m \geqslant 3$ are again quite involved. The behavior of both the MD and the MSD are very similar to the ones for the $p = 1$ case, with a simple diffusive behavior if $\kappa = 0$ and both a diffusive and ballistic behavior otherwise. A comparison between theory

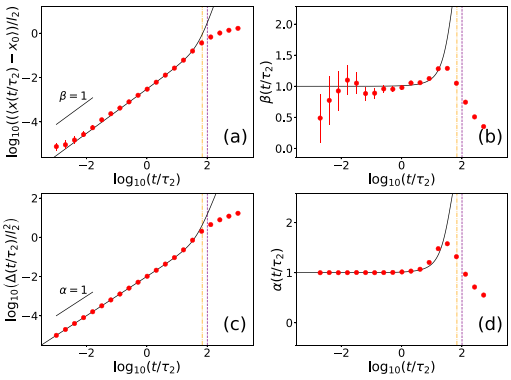

FIG. 5. Linear friction gradient $p = 2$ for a free particle ($n = 0$): (a) mean displacement $\langle x(t) - x_0 \rangle$ and (b) scaling exponent $\beta(t)$; (c) mean-squared displacement $\Delta(t)$, (d) scaling exponent $\alpha(t)$. The length units used is $l_2 = \sqrt{\gamma_0/\gamma_1}$ and the time unit is $\tau_2 = l_2^2/A$. The chosen initial position is $x_0 = 3l_2$.

and simulations is shown in Fig. 5 for the free case and in Fig. 6 for $n = 1$.

For the case $n = 2$ we used perturbation theory to calculate up to the first order in time for the MD and up to the second order in time for the MSD:

$$\langle x(t) - x_0 \rangle = \left(-\frac{\kappa x_0}{\gamma(x_0)} + a_2 A \right) t + \mathcal{O}(t^2), \tag{33}$$

$$\Delta(t) = \frac{At}{\gamma(x_0)^2} + \left[\frac{\kappa^2 x_0^2}{\gamma(x_0)^2} - \frac{\kappa A}{\gamma(x_0)^3} - 3b_3 A \kappa x_0 + 3b_4 A^2 \right] t^2 + \mathcal{O}(t^3), \tag{34}$$

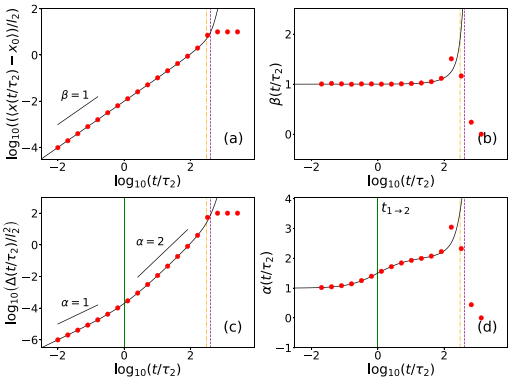

FIG. 6. Same as Fig. 5, but now for $n = 1$: (a) mean displacement $\langle x(t) - x_0 \rangle$ and (b) scaling exponent $\beta(t)$; (c) mean-squared displacement $\Delta(t)$, (d) scaling exponent $\alpha(t)$ and indicated crossing time $t_{1\to 2}$. Parameter values: $\kappa = \gamma_0 l_2/\tau_2$, $x_0 = 10l_2$.

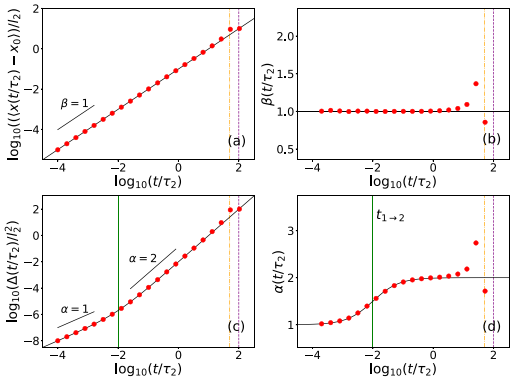

FIG. 7. Same as Fig. 5, but now for $n = 2$: (a) mean displacement $\langle x(t) - x_0 \rangle$ and (b) scaling exponent $\beta(t)$; (c) mean-squared displacement $\Delta(t)$, (d) scaling exponent $\alpha(t)$ and indicated crossing time $t_{1\to 2}$. Parameter values: $\kappa = \gamma_0/\tau_2$, $x_0 = 10l_2$.

where the a_i and b_i are the coefficients already used in Eqs. (30) and (32). We see again a linear behavior for the MD while the MSD goes from diffusive to ballistic. In Fig. 7 we compare these results with numerical simulations.

IV. LONG-TIME BEHAVIOR

We now consider the stationary long-time behavior. In order to keep a normalized probability distribution function, we confine the system in a potential ($n = 1, 2$). The stochastic process then admits a stationary PDF on the infinite line in the x coordinate which can be computed from the Fokker-Planck equation corresponding to the process Eq. (2). We rewrite, analogous to Eq. (4),

$$\dot{x}(t) = a(x) + b(x)\xi(t) \tag{35}$$

with

$$a(x) \equiv -\frac{U'(x)}{\gamma(x)}, \quad b(x) \equiv \frac{\sqrt{A}}{\gamma(x)}. \tag{36}$$

The Fokker-Planck equation for this case has been derived in Refs. [35,55] and reads as

$$\partial_t p(x,t) = -\partial_x [a(x)p(x,t)] + \tfrac{1}{2}\partial_x [b(x)[\partial_x [b(x)p(x,t)]]], \tag{37}$$

admitting a stationary solution at zero flux which is given by

$$p(x) = \frac{N}{b(x)} \exp\left[\int^x dy \, \frac{2a(y)}{b^2(y)} \right], \tag{38}$$

where N is a normalization factor. The integrand in the exponential of Eq. (38), denoted by $I(y)$, can be expressed in terms of the confining potential and the friction term as

$$I(y) = -\frac{2}{A} U'(y)\gamma(y), \tag{39}$$

which shows that it is given by polynomial expressions for the cases we address now.

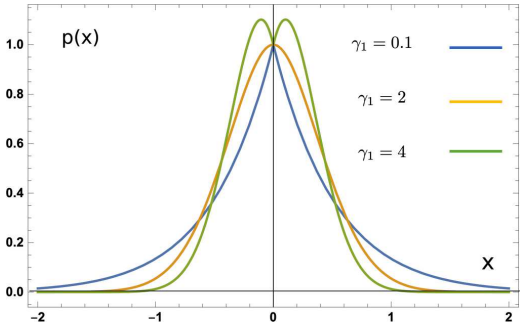

FIG. 8. Normalized PDF $p(x)$ for $\gamma(x) = \gamma_0 + \gamma_1|x|$ and $U(x) = \kappa|x|$, hence $(p, n) = (1, 1)$. Shown are curves for three sets of values of $\gamma_0 = 1$ with all other parameters set to numerical values of one. $\gamma_1 = 0.1$ blue curve, Laplace distribution; $\gamma_1 = 3$; yellow curve, Gaussian distribution. With $\gamma_1 = 4$ one obtains a bimodal "mirrored" Gaussian curve.

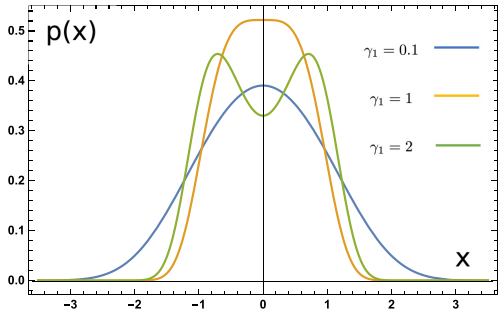

FIG. 9. Case $(p, n) = (2, 2)$. Normalized PDF $p(x)$ for $U(x) = \kappa x^2/2$ for three sets of values of γ_1 with all other parameters set to 1. $\gamma_1 = 0.1$: Gauss-like distribution; $\gamma_1 = 1$: flat-top distribution; $\gamma_1 = 2$; bimodal Gaussian-like distribution.

Taking $\gamma(x) = \gamma_0 + \gamma_1|x|^p$ and $U(x) = (\kappa/n)|x|^n$, which covers both our cases of interest for $p = 1, 2$, $n = 1, 2$, one obtains from Eq. (38)

$$p(x) = \frac{N}{\sqrt{A}}(\gamma_0 + \gamma_1|x|^p) \times \exp\left[-\frac{2\kappa}{A}\left(\frac{\gamma_0}{n}|x|^n + \frac{\gamma_1}{n+p}|x|^{n+p}\right)\right]. \quad (40)$$

We can now discuss the different cases as a function of the exponent pairs (p, n). For the lowest-order case $(p, n) = (1, 1)$ one has the superposition of the exponentials of a Laplace- and a Gaussian distribution, as shown in Fig. 8. The resulting PDF therefore interpolates between a Laplace-like distribution in the limit $\gamma_0 \gg \gamma_1$ and a Gaussian-like distribution up to $\gamma_1 = 2\gamma_0^2 a$, where the coefficient $a \equiv \kappa/A$ takes care of the different physical dimensions of γ_0 and γ_1; we set $a \equiv 1$. For still larger values of $\gamma_1 \gg \gamma_0$, the monomodal Gaussian distribution splits in what we call a bimodal "mirrored" Gaussian distribution. This name reflects the observation that the resulting distribution looks like a Gaussian placed close to a mirror, with the parts of the image behind the mirror cut out. It is important to note that for the presence of these different distribution forms the friction-dependent prefactor is important; at $x = 0$ it is a constant, but within a range of x-values around zero it reweights the distribution away from that constant, before for large values of x the exponential contribution becomes dominant.

The PDF in the case $(p, n) = (2, 1)$ shows the same behavior, which can be read off from the exponents. The leading Laplacian terms is unaltered since $n = 1$, while the subsequent term now acquires a cubic nonlinearity. In the case $(p, n) = (1, 2)$ the leading order term is now a Gaussian term, which therefore dominates at small values of γ_1. As in the previous cases, for increasing values of γ_1, the distribution immediately turns into a mirrored Gaussian-distribution, i.e., the maximum of the distribution splits into two maxima.

Finally, $(p, n) = (2, 2)$ the polynomial in the exponent is even and of fourth order, with Gaussian behavior dominating at low values of γ_1. Going from small to large γ_1, one now crosses over from a Gaussian-like to a bimodal Gaussian-like-distribution, which now is smooth at $x = 0$ due to the absence of modulus terms. This form is shown in Fig. 9. All behaviors found are summarized in Table I.

We end by considering the robustness of our results with respect to thermal fluctuations. Following Baule *et al.* [35], we consider the Langevin equation

$$\gamma(x)\dot{x}(t) = -U'(x) + \sqrt{2\gamma(x)k_BT}\eta(t) + \sqrt{A}\xi(t), \quad (41)$$

where $\eta(t)$ is a Gaussian white noise. The thermal and active processes $\eta(t)$ and $\xi(t)$ being uncorrelated, they can be

TABLE I. Graphic summary of the PDFs for the cases (p, n) for $p = 1, 2$, $n = 1, 2$, varying only the friction strengths γ_0 and γ_1. For $\gamma_1 = 0$, the distributions are either Laplacian (L) or Gaussian (G); left-most points. Increasing γ_1 leads to mirrored Gaussian behavior (MG), passing via Gaussian behavior at $\gamma_1 = 2\gamma_0^2 a$, $a = (\kappa/A) \equiv 1$. This applies to both $(p, n) = (1, 1)$ and $(p, n) = (2, 2)$. For $(p, n) = (1, 2)$, starting from a Gaussian at $\gamma_1 = 0$, the PDF changes into a mirrored Gaussian shape for finite positive γ_1. Finally, for $(p, n) = (2, 2)$, Gaussian behavior changes into bimodal Gaussian behavior (BG), passing via a flat-top behavior (FT) at $\gamma_1 = \gamma_0^2 a$, with again $a = 1$.

(p, n)	
	0 $\rightarrow \gamma_1$
$(1, 1)$	L G MG
$(2, 1)$	$\gamma_1 = 2\gamma_0^2$
$(1, 2)$	G MG
$(2, 2)$	G FT BG
	$\gamma_1 = \gamma_0^2$

superimposed to $\xi_T(t) = \eta(t) + \xi(t)$, leading to

$$\dot{x}(t) = a_T(x) + b_T(x)\xi_T(t), \tag{42}$$

with

$$a_T(x) = -\frac{1}{\gamma(x)}\left(U'(x) + \frac{k_BT}{2}\frac{\gamma'(x)}{\gamma(x)}\right) \tag{43}$$

and

$$b_T^2(x) = \frac{1}{\gamma(x)}\left(2k_BT + \frac{A}{\gamma(x)}\right). \tag{44}$$

The integrand $I(y)$ in the exponential of the PDF reads as

$$I(y) = -2\left[\frac{U'(y)\gamma(y) + k_BT\gamma'(x)}{A + 2k_BT\gamma(x)}\right], \tag{45}$$

which can be compared with Eq. (39) in the purely active case. As a robustness check it suffices to examine the behavior of the integrand $I(y)$ near the origin for small values of y and for $y \to \pm\infty$, for our four cases (p, n), $n = 1, 2$, $p = 1, 2$. For the behavior near the origin one finds that the dominator behaves in a similar fashion as $I(y)$ of Eq. (39), generating a polynomial with identical powers, since the temperature-dependent term either contributes a $\mathrm{sgn}(x)$ for $p = 1$ or a linear term for $p = 2$. The qualitative behavior of the PDFs remains thus unaltered. For large arguments, one sees that generally $I(y)$ behaves as

$$I(y) \propto -\frac{U'(y)}{k_BT}, \tag{46}$$

such that the tails of the distributions are determined by thermal fluctuations and decay exponentially, i.e., Laplace-like for $n = 1$ or Gaussian-like for $n = 2$; the active noise and the friction term then only play a role in the prefactor of the PDF.

V. DISCUSSION AND CONCLUSIONS

In this work we have studied the stochastic dynamics of an active-noise driven particle under the influence of a space-dependent friction and confinement. In order to elucidate the effect of the space dependence of the friction term, we start the dynamics for large initial values, so that the friction term dominates the dynamics. For the case of a free particle, a particle running down a ramp and a harmonic potential we have determined the mean displacement and mean-squared displacement and the corresponding scaling exponents $\beta(t)$ and $\alpha(t)$ in a short-time expansion. The mean displacements generally show diffusive behaviors, while a crossover to a ballistic regime is observed for the mean-squared displacement, except for the free particle case.

Further, we have determined the effect of the friction term in the presence of a confining potential $U(x) \propto |x|^n$ for $n = 1, 2$ for long times. We have analytically computed the stationary probability density functions from the Fokker-Planck equation. These solutions can be classified according to the exponent pairs (p, n) and the relative magnitude of the friction coefficients γ_0 and γ_1. One observes that the friction law and the confinement potential conspire to generate a set of generic behaviors: Laplace-like and Gaussian-like distributions for $n = 1$ and $n = 2$, respectively, if the spatially dependent friction term is small ($\gamma_1 \ll \gamma_0$); this behavior crosses over for $\gamma_1 = \gamma_0^2$ to Gaussian behavior for both $p = 1, 2$. In the case of $n = 2$, Laplace-like behavior is absent. For all cases of (p, n) with $n = 1, 2p = 1, 2$, one observes that for $\gamma_1 \gg \gamma_0$, the stationary PDF displays a mirrored or bimodal Gaussian-like behavior. Therefore, generally for all combinations of (p, n), at sufficiently strong space-dependent friction, the PDF becomes a bimodal distribution with a symmetrically increased weight off-center of the potential minimum.

To conclude, our study extends current studies on active particles in one dimension by the inclusion of a space-dependent friction and therefore links the problem to earlier studies of molecular motors on linear tracks. Investigations of the stationary probability density functions for the run-and-tumble process have already generated an extended catalog of distributions, see, e.g., Refs. [15], in which also bimodal-type PDFs appear (see their Fig. 7), or Ref. [56]. Placed in this context, the present study reveals a basic classification method in which such complex distributions are categorized for the case of a space-dependent friction. Our model system allows us to extract the mechanism of shape change of the PDFs in a particularly clear manner.

Our theory can be extended to active noise driven motion in two spatial dimensions. A special two-dimensional example is given by a radially symmetric situation, where the friction γ solely depends on the radial distance $r = \sqrt{x^2 + y^2}$. This case can be solved with similar methods as proposed in this paper. Another possible extension of our model could treat full viscosity landscapes [57–60]. Moreover inertial effects can be included in the particle dynamics [61–64]. Finally, collective effects for many active-noise driven particles such as motility-induced phase separation should be explored [65,66].

ACKNOWLEDGMENTS

D.B. is supported by the EU MSCA-ITN ActiveMatter (Proposal No. 812780). R.B. is grateful to H.L. for the invitation to a stay at the Heinrich-Heine University in Düsseldorf where this work was performed.

APPENDIX: ANALYTICAL AND NUMERICAL CALCULATIONS

1. Calculation of the mean displacement in the $(p, n) = (1, 0)$ case

In this Appendix we show how we obtained Eq. (10) starting from Eq. (8). First, we notice that Eq. (8) can be written as

$$x(t) = -\frac{\gamma_0}{\gamma_1} + \frac{\gamma_0 + x_0\gamma_1}{\gamma_1}\sqrt{1 + \frac{2\gamma_1\sqrt{A}}{(\gamma_0 + x_0\gamma_1)^2}\int_0^t dt'\xi(t')}. \tag{A1}$$

Given $x(t)$, we can write the equation for the MD:

$$\langle x(t) - x_0\rangle \tag{A2}$$

$$= \frac{\gamma_0 + x_0\gamma_1}{\gamma_1}\left(\left\langle\sqrt{1 + \frac{2\gamma_1\sqrt{A}}{(\gamma_0 + x_0\gamma_1)^2}\int_0^t dt'\xi(t')}\right\rangle - 1\right). \tag{A3}$$

To calculate the average in this expression, we have to Taylor expand the square root, using the following formula:

$$\sqrt{1+a} = 1 + \frac{a}{2} + \sum_{m=2}^{\infty} (-1)^{m-1} \frac{(2m-3)!}{2^{2m-2} m!(m-2)!} a^m, \quad \text{(A4)}$$

where we substitute

$$a \equiv \frac{2\gamma_1 \sqrt{A}}{(\gamma_0 + x_0\gamma_1)^2} \left\langle \int_0^t dt' \xi(t') \right\rangle. \quad \text{(A5)}$$

Equation (10) follows directly.

2. Numerical treatment of the Langevin equation

The stochastic equation

$$\dot{x}(t) = a(x) + b(x)\xi(t) \quad \text{(A6)}$$

is of the standard form

$$dx_t = a(x_t)dt + b(x_t)dW_t, \quad \text{(A7)}$$

where W_t represents a Wiener process. In order to solve this equation numerically in the Stratonovich paradigm, we implement a predictor-corrector scheme. In such a scheme, one first performs a full time step evolution of the position of the particle $x(t_i)$ using the same time coefficients $a(x(t_i))$ and $b(x(t_i))$. This predicted position x_p is used to calculate $a(x_p)$ and $b(x_p)$ and proceed to finally calculate the position at time step t_{i+1} using the averages of the coefficients calculated for $x(t_i)$ and x_p. To implement the Stratonovich paradigm, using this kind of average only for the stochastic part [and hence the $b(x)$] is necessary, but we preferred to apply this procedure as well to the deterministic part in order to improve stability of the result. The method we decided to use for the time evolution is thus a Milstein scheme, of order $\mathcal{O}(\Delta t)$ [67]. The Milstein evolution of Eq. (A7) can be written as

$$x(t_{i+1}) = x(t_i) + a(x(t_i))\Delta t + b(x(t_i))\Delta W(t_i) + \frac{1}{2} b(x(t_i)) \frac{db(x(t_i))}{dx} ((\Delta W(t_i))^2 - \Delta t), \quad \text{(A8)}$$

where $\Delta W(t_i) = W(t_{i+1}) - W(t_i)$ is a normal-distributed random variable.

It should be noted that the Milstein scheme uses the derivative of the function $b(x)$, which for our model is discontinuous at $x = 0$ for the case $p = 1$. This can be treated by adopting an algorithm developed in Ref. [68], employing colored noise from the Ornstein-Uhlenbeck process.

[1] J. P. Bouchaud, A. Comtet, A. Georges, and P. Le Doussal, Ann. Phys. **201**, 285 (1990).
[2] J. Tailleur and M. E. Cates, Phys. Rev. Lett. **100**, 218103 (2008).
[3] B. Lindner and E. M. Nicola, Eur. Phys. J.: Spec. Top. **157**, 43 (2008).
[4] J. Toner, Y. Tu, and S. Ramaswamy, Ann. Phys. Special Issue, **318**, 170 (2005).
[5] S. Ramaswamy, Annu. Rev. Condens. Matter Phys. **1**, 323 (2010).
[6] M. E. Cates and J. Tailleur, Annu. Rev. Condens. Matter Phys. **6**, 219 (2015).
[7] C. Bechinger, R. Di Leonardo, H. Löwen, C. Reichhardt, G. Volpe, and G. Volpe, Rev. Mod. Phys. **88**, 045006 (2016).
[8] J. Elgeti, R. G. Winkler, and G. Gompper, Rep. Prog. Phys. **78**, 056601 (2015).
[9] P. Romanczuk and U. Erdmann, Eur. Phys. J.: Spec. Top. **187**, 127 (2010).
[10] Y. Ben Dor, E. Woillez, Y. Kafri, M. Kardar, and A. P. Solon, Phys. Rev. E **100**, 052610 (2019).
[11] P. Illien, C. de Blois, Y. Liu, M. N. van der Linden, and O. Dauchot, Phys. Rev. E **101**, 040602(R) (2020).
[12] E. F. Teixeira, H. C. M. Fernandes, and L. G. Brunnet, arXiv:2102.03439 [cond-mat.soft].
[13] T. Demaerel and C. Maes, Phys. Rev. E **97**, 032604 (2018).
[14] K. Malakar, V. Jemseena, A. Kundu, K. V. Kumar, S. Sabhapandit, S. N. Majumdar, S. Redner, and A. Dhar, J. Stat. Mech.: Theory Exp. (2018) 043215.
[15] A. Dhar, A. Kundu, S. N. Majumdar, S. Sabhapandit, and G. Schehr, Phys. Rev. E **99**, 032132 (2019).
[16] P. Le Doussal, S. N. Majumdar, and G. Schehr, Europhys. Lett. **130**, 40002 (2020).
[17] K. Białas, J. Łuczka, P. Hänggi, and J. Spiechowicz, Phys. Rev. E **102**, 042121 (2020).
[18] D. S. Dean, S. N. Majumdar, and H. Schawe, Phys. Rev. E **103**, 012130 (2021).
[19] F. Mori, P. Le Doussal, S. N. Majumdar, and G. Schehr, Phys. Rev. E **102**, 042133 (2020).
[20] L. Angelani, J. Phys. A **50**, 325601 (2017).
[21] N. Razin, R. Voituriez, J. Elgeti, and N. S. Gov, Phys. Rev. E **96**, 032606 (2017).
[22] N. Razin, Phys. Rev. E **102**, 030103(R) (2020).
[23] B. ten Hagen, S. van Teeffelen, and H. Löwen, J. Phys.: Condens. Matter **23**, 194119 (2011).
[24] Q.-H. Wei, C. Bechinger, and P. Leiderer, Science **287**, 625 (2000).
[25] C. Lutz, M. Kollmann, and C. Bechinger, Phys. Rev. Lett. **93**, 026001 (2004).
[26] S. Herrera-Velarde, A. Zamudio-Ojeda, and R. Castañeda-Priego, J. Chem. Phys. **133**, 114902 (2010).
[27] G. Szamel, Phys. Rev. E **90**, 012111 (2014).
[28] R. Wittmann, C. Maggi, A. Sharma, A. Scacchi, J. M. Brader, and U. M. B. Marconi, J. Stat. Mech.: Theory Exp. (2017) 113207.
[29] S. Das, G. Gompper, and R. G. Winkler, New J. Phys. **20**, 015001 (2018).
[30] L. Caprini and U. Marini Bettolo Marconi, Soft Matter **14**, 9044 (2018).
[31] L. Caprini, U. M. B. Marconi, and A. Vulpiani, J. Stat. Mech.: Theory Exp. (2018) 033203.
[32] F. J. Sevilla, R. F. Rodríguez, and J. R. Gomez-Solano, Phys. Rev. E **100**, 032123 (2019).
[33] A. G. Cherstvy, A. V. Chechkin, and R. Metzler, New J. Phys. **15**, 083039 (2013).
[34] K. V. Kumar, S. Ramaswamy, and M. Rao, Phys. Rev. E **77**, 020102(R) (2008).

[35] A. Baule, K. V. Kumar, and S. Ramaswamy, J. Stat. Mech.: Theory Exp. (2008) P11008.

[36] A. Mogilner, M. Mangel, and R. J. Baskin, Phys. Lett. A **237**, 297 (1998).

[37] H. C. Fogedby, R. Metzler, and A. Svane, Phys. Rev. E **70**, 021905 (2004).

[38] A. B. Kolomeisky and H. Phillips, J. Phys.: Condens. Matter **17**, S3887 (2005).

[39] Y. A. Makhnovskii, V. M. Rozenbaum, D.-Y. Yang, S. H. Lin, and T. Y. Tsong, European Phys. J. B **52**, 501 (2006).

[40] V. M. Rozenbaum, Y. A. Makhnovskii, D.-Y. Yang, S.-Y. Sheu, and S. H. Lin, J. Phys. Chem. B **114**, 1959 (2010).

[41] Y. A. Makhnovskii, V. M. Rozenbaum, S.-Y. Sheu, D.-Y. Yang, L. I. Trakhtenberg, and S. H. Lin, J. Chem. Phys. **140**, 214108 (2014).

[42] R. Blossey and H. Schiessel, J. Phys. A **52**, 085601 (2019).

[43] F. Evers, R. D. L. Hanes, C. Zunke, R. F. Capellmann, J. Bewerunge, C. Dalle-Ferrier, M. C. Jenkins, I. Ladadwa, A. Heuer, R. Castañeda-Priego, and S. U. Egelhaaf, Eur. Phys. J.: Spec. Top. **222**, 2995 (2013).

[44] C. Lozano, B. ten Hagen, H. Löwen, and C. Bechinger, Nat. Commun. **7**, 12828 (2016).

[45] S. Jahanshahi, C. Lozano, B. Liebchen, H. Löwen, and C. Bechinger, Commun. Phys. **3**, 1 (2020).

[46] M. A. Fernandez-Rodriguez, F. Grillo, L. Alvarez, M. Rathlef, I. Buttinoni, G. Volpe, and L. Isa, Nat. Commun. **11**, 4223 (2020).

[47] A. R. Sprenger, M. A. Fernandez-Rodriguez, L. Alvarez, L. Isa, R. Wittkowski, and H. Löwen, Langmuir **36**, 7066 (2020).

[48] B. Liebchen, P. Monderkamp, B. ten Hagen, and H. Löwen, Phys. Rev. Lett. **120**, 208002 (2018).

[49] M. R. Stehnach, N. Waisbord, D. M. Walkama, and J. S. Guasto, bioRxiv (2020), doi: https://doi.org/10.1101/2020.11.05.369801.

[50] P. U. Shirke, H. Goswami, V. Kumar, D. Shah, S. Das, J. Bellare, K. V. Venkatesh, J. R. Seth, and A. Majumder, bioRxiv, 804492 (2019), doi:https://doi.org/10.1101/804492.

[51] C. E. Lopez, J. Gonzalez-Gutierrez, F. Solorio-Ordaz, E. Lauga, and R. Zenit, arXiv:2012.04788 [physics].

[52] D. Breoni, M. Schmiedeberg, and H. Löwen, Phys. Rev. E **102**, 062604 (2020).

[53] M. Doi and S. Edwards, *The Theory of Polymer Dynamics* (Clarendon Press, New York, 1986).

[54] A. W. C. Lau and T. C. Lubensky, Phys. Rev. E **76**, 011123 (2007).

[55] D. Ryter, Z. Phys. B: Condens. Matter **41**, 39 (1981).

[56] F. J. Sevilla, A. V. Arzola, and E. P. Cital, Phys. Rev. E **99**, 012145 (2019).

[57] S. Coppola and V. Kantsler, Sci. Rep. **11**, 399 (2021).

[58] C. Datt and G. J. Elfring, Phys. Rev. Lett. **123**, 158006 (2019).

[59] R. Dandekar and A. M. Ardekani, J. Fluid Mech. **895**, R2 (2020).

[60] B. Liebchen and H. Löwen, Europhys. Lett. **127**, 34003 (2019).

[61] C. Scholz, S. Jahanshahi, A. Ldov, and H. Löwen, Nat. Commun. **9**, 5156 (2018).

[62] H. Löwen, J. Chem. Phys. **152**, 040901 (2020).

[63] A. R. Sprenger, S. Jahanshahi, A. V. Ivlev, and H. Löwen, Phys. Rev. E **103**, 042601 (2021).

[64] L. Caprini and U. Marini Bettolo Marconi, J. Chem. Phys. **154**, 024902 (2021).

[65] D. Marenduzzo, Eur. Phys. J.: Spec. Top. **225**, 2065 (2016).

[66] Z. Ma, M. Yang, and R. Ni, Adv. Theory Simulat. **3**, 2000021 (2020).

[67] G. N. Mil'shtejn, Theory Probability Appl. **19**, 557 (1975).

[68] R. Perez-Carrasco and J. M. Sancho, Phys. Rev. E **81**, 032104 (2010).

P3 Brownian particles driven by spatially periodic noise

Reproduced from

D. Breoni, R.Blossey, and H. Löwen, *Brownian particles driven by spatially periodic noise*, The European Physical Journal E **45**, 18 (2022),

Digital Object Identifier (DOI): https://doi.org/10.1140/epje/s10189-022-00176-4

Statement of contribution

HL and RB directed the project. I performed analytic calculations and numerical simulations. RB contributed analytical results for the current near critical tilt. All authors discussed the results and wrote the manuscript.

Copyright and license notice

Eur. Phys. J. E (2022) 45:18
https://doi.org/10.1140/epje/s10189-022-00176-4

THE EUROPEAN PHYSICAL JOURNAL E

Regular Article - Soft Matter

Brownian particles driven by spatially periodic noise

Davide Breoni[1,a], Ralf Blossey[2], and Hartmut Löwen[1]

[1] Institut für Theoretische Physik II: Weiche Materie, Heinrich, Heine-Universität Düsseldorf, Universitätsstraße 1, 40225 Düsseldorf, Germany
[2] University of Lille, UGSF CNRS UMR8576, 59000 Lille, France

Received 19 November 2021 / Accepted 18 February 2022 / Published online 1 March 2022

Abstract We discuss the dynamics of a Brownian particle under the influence of a spatially periodic noise strength in one dimension using analytical theory and computer simulations. In the absence of a deterministic force, the Langevin equation can be integrated formally exactly. We determine the short- and long-time behaviour of the mean displacement (MD) and mean-squared displacement (MSD). In particular, we find a very slow dynamics for the mean displacement, scaling as $t^{-1/2}$ with time t. Placed under an additional external periodic force near the critical tilt value we compute the stationary current obtained from the corresponding Fokker–Planck equation and identify an essential singularity if the minimum of the noise strength is zero. Finally, in order to further elucidate the effect of the random periodic driving on the diffusion process, we introduce a phase factor in the spatial noise with respect to the external periodic force and identify the value of the phase shift for which the random force exerts its strongest effect on the long-time drift velocity and diffusion coefficient

1 Introduction

Dating back to the important paper by Einstein in the *annus mirabilis* 1905 [1], the dynamics of Brownian particles has been in the focus of statistical physics for more than 100 years now [2]. The constant interest in Brownian particles is basically inspired by two facts: First, their stochastic description requires fundamental principles such as the Langevin or Smoluchowski picture such that they serve as paradigmatic models which can be made systematically more complex. Second, there is a variety of excellent realizations of Brownian particles including mesoscopic colloidal particles in suspension [3], random walkers in the macroscopic world (such as [4]) and in the microscopic biological context [5], and even elements of the stock exchange market [6]. This facilitates a direct comparison of the stochastic averages between the stochastic modelling and real experimental data.

In its simplest one-dimensional form, the most basic model Langevin equation for a particle trajectory $x(t)$ as a function of time t is $\dot{x}(t) = \sqrt{D}\eta(t)$ in which $\eta(t)$ is white noise with zero mean and variance $\langle \eta(t)\eta(t')\rangle = \delta(t-t')$ and $D > 0$ is the diffusion constant. Here, $\langle ...\rangle$ denotes a noise average. With the initial position $x(t=0) = x_0$, the mean displacement vanishes due to symmetry, $\langle x(t) - x_0\rangle = 0$, and the mean-squared displacement is purely diffusive, $\langle (x(t)-x_0)^2\rangle = 2Dt$. Clearly, this basic equation can be extended towards more complicated situations including an additional static external force, time-dependent external forcing, higher spatial dimensions, and many interacting particles, see [7–10] for some reviews.

One particularly interesting way to extend the equation is to generalize it to a situation of multiplicative noise, where the noise strength is a positive function $D(x,t)$. While the case where D is only an explicit function of time t is well studied, for example in the context of Brownian ratchets [11–15] and heat engines [16–20], in this work we focus on the case where we have a *spatially dependent noise strength* [21–24] modelled by a positive function $D(x)$, i.e. a space-dependent diffusion coefficient, such that the most basic model for such processes is given by the Langevin equation

$$\dot{x}(t) = \sqrt{D(x(t))}\eta(t). \tag{1}$$

The special case of multiplicative noise where $\dot{x}(t) = -\kappa x(t)\eta(t)$ with positive κ [25], which is somehow related to this model, documents already that the spatial dependence of the noise gives rise to fundamentally new mathematical concepts also known as the Itô-Stratonovich problem [26]. The mathematical difficulties associated with the formal treatment of Eq. (1) are subject to intense discussion, see, e.g., the recent work by Leibovich and Barkai for the specific choice of $D(x)$ as a power-law [27] and numerous other studies [24,28–40].

In this paper, we consider a variant of this model in the context of the discussion of particle motion in tilted potentials. There is a large literature on this topic, see [41–54]. Following the original suggestion by

[a] e-mail: breoni@hhu.de (corresponding author)

Büttiker [21] and Landauer [22] the spatially-varying thermal noise source can be combined with a ratchet potential, as, e.g., recently discussed by [55]. Our model considers overdamped Brownian particles subject to an oscillating tilted potential and a space-dependent periodic noise amplitude with the same wave vector k as the force; furthermore, we will ultimately also allow a shifted phase ϕ in the random force. In its general form, the model is given by the Langevin equation

$$\gamma\dot{x}(t) = -\nabla V(x) + \sqrt{2\gamma k_B T(x)}\eta(t), \tag{2}$$

where $V(x) := -F_0\,(x + \epsilon\sin(kx)/k)$ is the potential, $T(x) := T_0\,(1 + \nu\cos(kx + \phi))^2$ is the space-dependent noise strength, γ is the friction coefficient, F_0 is the tilting force, T_0 is a reference temperature, $\eta(t)$ is a white noise, as introduced before, and ϵ and ν are dimensionless parameters. The critical tilt in this model arises when $\epsilon = 1$. In order keep the noise strength differentiable everywhere and its phase in a fixed frame we consider $0 \leq \nu \leq 1$. The period of both the force and the noise will be $L = 2\pi/k$. We remark that the case $\nu = 1$ plays a special role insofar as there are special positions at which the noise is zero. In absence of forces, the particle will therefore never cross these positions but stay confined within a periodicity length L.

Our goal in this paper is to describe the particle dynamics as functions of ϵ, ν and ϕ, either in the vicinity of the critical tilt, or in the absence of the deterministic force, $F_0 = 0$, i.e. in the purely spatial random noise case. Among our main results are the very slow dynamics in the relaxation of the mean displacement (MD) and mean-squared displacement (MSD) for long times in the $F_0 = 0$ case and an essential singularity in the stationary current for $F_0 \neq 0$ and $\epsilon \simeq \nu \simeq 1$. In the case of the full model, we build upon the results of [21] by also considering extreme temperature oscillations where the noise strength vanishes ($\nu = 1$) and adding an external driving force, while we expand on [41] by finding a theoretical approximation for both the long-time drift v_L and diffusion constant D_L and the phase value ϕ for which we have the largest increase of v_L and D_L for $\epsilon \neq 1$ and $\nu \neq 0$. Our results have been obtained both with numerical and analytical methods.

The paper is organized as follows: in the beginning we focus on the free case, for which we study the short- and long-time behaviour of MD and MSD, then we proceed with the full model, including the tilted potential, for which we study the stationary distribution and the dependence of long time diffusion and drift on ϕ and ν. Finally, we summarize the results obtained and discuss possible experimental realizations of the model.

2 Free particle case

In the case of a vanishing external force ($F_0 = 0$), the Langevin equation (2) now reads as

$$\gamma\dot{x}(t) = \sqrt{2\gamma k_B T(x)}\eta(t), \tag{3}$$

where we set $\phi = 0$ without loss of generality. We decided to approach this problem using the Stratonovich interpretation. For a given representation of the noise, this equation can be solved by direct integration in the particular case of *periodic boundary conditions* (PBC) in which we identify $x(t) \pm L$ with $x(t)$. The PBC correspond to a ring-like geometry of the one-dimensional system.

$$x(t) = \frac{2}{k}\arctan\left[\sqrt{\frac{1+\nu}{1-\nu}}\tan\left(k\sqrt{\frac{k_B T_0(1-\nu^2)}{2\gamma}}\right.\right.$$
$$\left.\left.\times\int_0^t \eta(t')dt' + \arctan\left(\sqrt{\frac{1+\nu}{1-\nu}}\tan\left(\frac{kx_0}{2}\right)\right)\right)\right] \tag{4}$$

and the limit of this solution for $\nu \to 1$ is

$$x(t) = \frac{2}{k}\arctan\left[k\sqrt{\frac{2k_B T_0}{\gamma}}\int_0^t \eta(t')dt' + \tan\left(\frac{kx_0}{2}\right)\right]. \tag{5}$$

We remark here that in the case with *no boundaries*, i.e. when we let the particle diffuse through the whole x-axis, the analysis is harder and we were not able to find an analytical expression except for the special case $\nu = 1$. In this limit PBC and the no boundaries case are identical as the particle can never trespass the points where the noise is zero.

Equations (4) and (5) can be used to express noise-averages of any power of displacement. For an arbitrary moment $M_n(t) := \langle (x(t) - x_0)^n \rangle$ we obtain

$$M_n(t) = \int_{-\infty}^{\infty}\left\{\frac{2}{k}\arctan\left[\sqrt{\frac{1+\nu}{1-\nu}}\tan\left(k\sqrt{\frac{k_B T_0(1-\nu^2)}{2\gamma}}\right.\right.\right.$$
$$\left.\left.\left.+\arctan\left(\sqrt{\frac{1+\nu}{1-\nu}}\tan\left(\frac{kx_0}{2}\right)\right)\right)\right] - x_0\right\}^n$$
$$\times\frac{\mathrm{e}^{-\frac{W^2}{2t}}}{\sqrt{2\pi t}}dW \tag{6}$$

for $\nu \neq 1$ and

$$M_n(t) = \int_{-\infty}^{\infty}\left\{\frac{2}{k}\arctan\left[k\sqrt{\frac{2k_B T_0}{\gamma}}W + \tan\left(\frac{kx_0}{2}\right)\right]\right.$$
$$\left.-x_0\right\}^n\frac{\mathrm{e}^{-\frac{W^2}{2t}}}{\sqrt{2\pi t}}dW \tag{7}$$

for $\nu = 1$. Since we are going to focus on the mean displacement $\langle x(t) - x_0 \rangle$ and the mean-squared displacement $\langle (x(t) - x_0)^2 \rangle$, we write the expressions for these two moments ($n = 1, 2$) explicitly:

$$\langle x(t)-x_0\rangle = \int_{-\infty}^{\infty} \frac{2}{k}\arctan\left[\sqrt{\frac{1+\nu}{1-\nu}}\tan\left(k\sqrt{\frac{k_BT_0(1-\nu^2)}{2\gamma}}W + \arctan\left(\sqrt{\frac{1+\nu}{1-\nu}}\tan\left(\frac{kx_0}{2}\right)\right)\right)\right] \times \frac{e^{-\frac{W^2}{2t}}}{\sqrt{2\pi t}}dW - x_0 \quad (8)$$

and

$$\langle (x(t)-x_0)^2\rangle = \int_{-\infty}^{\infty}\left\{\frac{2}{k}\arctan\left[\sqrt{\frac{1+\nu}{1-\nu}}\tan\left(k\sqrt{\frac{k_BT_0(1-\nu^2)}{2\gamma}}W + \arctan\left(\sqrt{\frac{1+\nu}{1-\nu}}\tan\left(\frac{kx_0}{2}\right)\right)\right)\right] - x_0\right\}^2 \frac{e^{-\frac{W^2}{2t}}}{\sqrt{2\pi t}}dW \quad (9)$$

for $\nu \neq 1$ and

$$\langle x(t)-x_0\rangle = \int_{-\infty}^{\infty}\frac{2}{k}\arctan\left[k\sqrt{\frac{2k_BT_0}{\gamma}}W + \tan\left(\frac{kx_0}{2}\right)\right]\frac{e^{-\frac{W^2}{2t}}}{\sqrt{2\pi t}}dW - x_0 \quad (10)$$

and

$$\langle (x(t)-x_0)^2\rangle = \int_{-\infty}^{\infty}\left\{\frac{2}{k}\arctan\left[k\sqrt{\frac{2k_BT_0}{\gamma}}W + \tan\left(\frac{kx_0}{2}\right)\right] - x_0\right\}^2 \frac{e^{-\frac{W^2}{2t}}}{\sqrt{2\pi t}}dW \quad (11)$$

for $\nu = 1$.

2.1 Short-time behavior

We can use equations (8-11) to extract the short-time behavior of the MD and MSD. Expanding the integrand in powers of t using a Taylor series and integrating the terms separately we obtain for the MD:

$$\langle x(t)-x_0\rangle = -\frac{kk_BT_0t}{\gamma}\sin(kx_0)\nu \times\left[(1+\nu)\cos^2\left(\frac{k}{2}x_0\right) + (1-\nu)\sin^2\left(\frac{k}{2}x_0\right)\right] + \mathcal{O}\left(t^2\right) \quad (12)$$

and for the MSD

$$\langle (x(t)-x_0)^2\rangle = \frac{2k_BT_0t}{\gamma}\left[(1+\nu)\cos^2\left(\frac{k}{2}x_0\right) + (1-\nu)\sin^2\left(\frac{k}{2}x_0\right)\right]^2 + \mathcal{O}\left(t^2\right). \quad (13)$$

In the special limit $\nu = 1$ we also add the second-order correction as:

$$\langle x(t)-x_0\rangle = -\frac{2kk_BT_0t}{\gamma}\cos^2\left(\frac{k}{2}x_0\right)\sin(kx_0) \times\left[1-\frac{6k^2k_BT_0t}{\gamma}\cos^2\left(\frac{k}{2}x_0\right)\cos(kx_0)\right] + \mathcal{O}\left(t^3\right) \quad (14)$$

and

$$\langle (x(t)-x_0)^2\rangle = \frac{8k_BT_0t}{\gamma}\cos^4\left(\frac{k}{2}x_0\right) \times\left[1+\frac{k^2k_BT_0t}{\gamma}\cos^2\left(\frac{k}{2}x_0\right) \times(7-11\cos(kx_0))\right] + \mathcal{O}\left(t^3\right). \quad (15)$$

Clearly, the first-order correction of (14) and (15) coincides with equations (12) and (13) in the limit $\nu \to 1$. Moreover for $\nu = 0$ we recover the white noise case solved by Einstein [1].

We now define an *effective potential of the mean displacement* such that a particle subject to this potential and constant white noise will experience the same average drift as a particle in a space-dependent noise landscape. In other words, following the spirit of the mapping proposed by Büttiker [21], the effective force resulting from this potential can be viewed as a substitute source for the drift when only white noise is considered. Hence, we define this force $F_M(x)$ up to a friction coefficient prefactor γ as the first coefficient of the short-time expansion of the MD

$$\langle x(t)-x_0\rangle = a_1(x_0,\nu)t + \mathcal{O}\left(t^2\right) \quad (16)$$

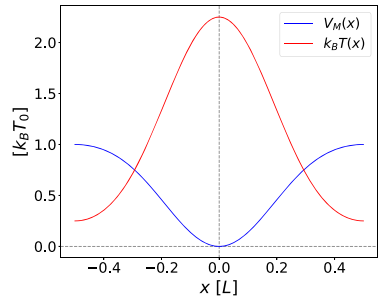

Fig. 1 Effective potential of the mean displacement V_M, obtained from the short-time drift of the mean displacement, and space-dependent noise $T(x)$ for $\nu = 0.5$ and $\phi = 0$ as functions of space x. While the averaged MD tends to the minima of V_M, where the noise strength $T(x)$ is largest, individual trajectories spend most of their time around the maxima of V_M

as follows

$$\begin{aligned} F_M(x) &:= a_1(x,\nu)\gamma \\ &= -kk_BT_0\sin(kx)\nu\left[(1+\nu)\cos^2\left(\frac{k}{2}x\right)\right. \\ &\quad \left.+(1-\nu)\sin^2\left(\frac{k}{2}x\right)\right]. \end{aligned} \tag{17}$$

The effective potential of the mean displacement is then defined by $V_M(x) = -\int_0^x F_M(x')\mathrm{d}x'$ yielding

$$\begin{aligned} V_M(x) &= k_BT_0\nu \\ &\quad \times\left[(1-\nu)\sin^4\left(\frac{k}{2}x\right) - (1+\nu)\cos^4\left(\frac{k}{2}x\right)\right. \\ &\quad \left.+1+\nu\right]. \end{aligned} \tag{18}$$

This potential is shown in Fig. 1. Even though this potential is defined just by the short-time expansion of the MD, it is still significant for any finite time, as the particle is overdamped and feels at every time a short-time drift depending only on its position. As a result, the MD of a particle subject to this potential and white noise can be perfectly mapped to the MD of a free particle with space-dependent noise.

While the average mean displacement behaves according to V_M, moving over time towards the regions where V_M is smaller and the noise strength is larger, we want to stress that individual trajectories will not accumulate in the minima of V_M but will instead freely move over all the domain, spending most of their time in the maxima of V_M instead. This is because when particles reach such low-noise regions they take a longer time escaping, as their fluctuations there are severely reduced.

2.2 Dynamics for finite and long times

Now we explore the behavior of the MD and MSD for finite and long times. First we present an asymptotic analysis for the special case $\nu = 1$. Then we use a numerical solution of the integrals in (8) and (9) as well as computer simulations of the original Langevin equation to obtain data for finite times and arbitrary ν.

2.2.1 Asymptotic analysis for $\nu = 1$ for long times

Here we present an asymptotic analysis for the MD and MSD by starting from Eq. (10) and using the asymptotic approximation

$$\arctan(\theta) \simeq \frac{\pi}{2}\mathrm{sign}(\theta) - \arctan\left(\frac{1}{\theta}\right), \tag{19}$$

for large θ. We now expand $\arctan\left(\frac{1}{\theta}\right)$ using Euler's formula [56]

$$\arctan\left(\frac{1}{\theta}\right) = \frac{\theta}{\theta^2+1} + \mathcal{O}\left(\frac{1}{\theta^3}\right) \tag{20}$$

and insert this expansion in Eq. (10) to obtain

$$\begin{aligned} \langle x(t)-x_0\rangle = \int_{-\infty}^{\infty}\frac{2}{k}\left[\frac{\pi}{2}\mathrm{sign}\left(k\sqrt{\frac{2k_BT_0t}{\gamma}}W\right.\right. \\ \left.+\tan\left(\frac{kx_0}{2}\right)\right) \\ \left.-\frac{k\sqrt{\frac{2k_BT_0t}{\gamma}}W+\tan\left(\frac{kx_0}{2}\right)}{1+\left(k\sqrt{\frac{2k_BT_0t}{\gamma}}W+\tan\left(\frac{kx_0}{2}\right)\right)^2}\right] \\ \frac{\mathrm{e}^{-\frac{W^2}{2t}}}{\sqrt{2\pi t}}dW \\ -x_0+\mathcal{O}\left(t^{-3/2}\right), \end{aligned} \tag{21}$$

which yields

$$\begin{aligned} \langle x(t)-x_0\rangle = \sqrt{\frac{\pi\gamma}{k_BT_0t}}\frac{1}{k^2}\tan\left(\frac{kx_0}{2}\right) \\ \left(1-\frac{1}{2k}\sqrt{\frac{\gamma}{k_BT_0t}}\right)-x_0 \\ +\mathcal{O}\left(t^{-3/2}\right). \end{aligned} \tag{22}$$

As a result, the leading asymptotic behavior of $\langle x(t)\rangle$ is determined by the first term involving a scaling behavior of the MD in $1/\sqrt{t}$. This is remarkably slow compared to typical behavior of a Brownian particle in a harmonic potential or of active Brownian motion where the MD reaches its asymptotic value exponentially in time [57–59] thus constituting an example of

a very slow relaxation as induced by space-dependent noise.

Likewise an asymptotic analysis for $\nu = 1$ yields for the long-time limit of the MSD

$$\lim_{t\to\infty} \left(\langle (x(t) - x_0)^2 \rangle\right) = x_0^2 + \frac{\pi^2}{k^2} \tag{23}$$

which represents the degree of smearing of the particle distribution for long times. We want to remark that the MSD calculated from a distribution with periodic boundary conditions does not describe the effective diffusion coefficient D_L in periodic systems with no boundaries, in contrast to the MD which can actually be calculated from the distribution with periodic boundary conditions even for open systems.

2.2.2 Computer simulations

We performed direct Brownian dynamics computer simulations of the original Langevin equations with a finite time step Δt to obtain numerically results for the MD and MSD at any times. In order to properly simulate a system with space-dependent noise, we used the order $\mathcal{O}(\Delta t)$ Milstein scheme [60] with a time step of $\Delta t = 10^{-3}\tau$, where $\tau := \frac{\gamma L^2}{k_B T_0}$ is a typical Brownian time scale of the system. For each simulation set we fixed the initial position x_0 within the first period $[-L/2, L/2]$ and averaged typically over 200 trajectories of length $\simeq 500\tau$.

2.2.3 MD and MSD for finite times

Data for the mean displacement and the mean position as a function of time are obtained by a numerical evaluation of the integral in Eq. (10) and by computer simulation. For $\nu = 1$ results are presented in Fig. 2 together with the corresponding short-time and long-time asymptotics (14) and (22). The displacement starts linear in time t and saturates for long times. The mean position approaches zero slowly as a power law in time proportional to $t^{-1/2}$. For large times the statistical error in the simulation data is significant but nevertheless these data are compatible with the scaling prediction of the theory.

In order to understand the very slow behavior of the MD we note that while the MD tends to zero, i.e. to the point with largest noise, this is just an effect of averaging over particles spending most of their time at the points with the smallest noise on both sides of the x-axis: $x \simeq -L/2$ and $x \simeq L/2$. This particular mechanism explains why the MD approaches its final value so slowly, as the particles have to hop from one side to the other to symmetrize their distribution. In Fig. 3a this is clearly documented in the time evolution of the particle distribution function $p(x,t)$, which gives the probability to find a particle after a time t at position x provided it started at time $t = 0$ at position x_0. The system evolves from a single-peaked distribution around x_0 to a double-peaked distribution in $\pm L/2$. Near the two points $x = \pm L/2$ of zero noise the peaks are getting sharper as $t \to \infty$ approaching to δ-peaks such that $\lim_{t\to\infty} p(x,t) = (\delta(x - L/2) + \delta(x + L/2))/2$. The intuitive reason for this is that once a particle adsorbs at the points $x = \pm L/2$ of zero noise it will never return to the region where the noise is finite.

This peculiar behavior is clearly delineated from the relaxation in a symmetric double-well potential with white noise of strength T_0. In order to reveal this, we have performed simulations for a Brownian particle in the double-well potential with two equal minima

$$U(x) := A(x^4 - Bx^2). \tag{24}$$

We set $A := 48k_BT_0/L^4$ and $B := L^2/2$ in order to have the two wells in $\pm L/2$ such that the energy barrier between the two minima is $3k_BT_0$. Our simulation for this white-noise reference case show that both the MD and the MSD decay exponentially in time t rather than with $1/\sqrt{t}$, and hence much faster than for our case of space-dependent noise. We also defined a particle hopping rate Γ_h between the two peaks of the distribution as

$$\Gamma_h(t) := \frac{N_h(t)}{t/2}, \tag{25}$$

where $N_h(t)$ is the number of times a particle hops from one peak to the other in the time interval $[t/2, t]$. Note that the relevant time window in which hopping is considered is chosen to be proportional in time in order to improve the statistics. We have a *hop* whenever the particle trespasses the $x = L/4$ or $x = -L/4$ thresholds and previously was, respectively, in the left or right peak.

In fact, as we show in Fig. 3b, for the double-well potential, the hopping rate $\Gamma_h(t)$ converges to a constant for long times. This rate is maintaining the equilibrium state with a symmetrized occupation around the two minima. The rate saturates for $t \to \infty$ to a value very close to the inverse of the mean first passage time (see for example [61]) in the double-well potential t_e [62], which in our case is given by:

$$\begin{aligned} t_e &\simeq \frac{2\pi}{\sqrt{\nabla^2 U(L/2)|\nabla^2 U(0)|}} \exp\left(\frac{U(0) - U(L/2)}{k_B T_0}\right) \\ &\simeq 1.859\tau. \end{aligned} \tag{26}$$

Conversely, for our case of space-dependent noise, the hopping rate keeps decreasing as a function of time again with an inverse power law $t^{-1/2}$. This reflects the fact that the peaks of the space-dependent noise distribution keep growing indefinitely as the particles get in average closer to the points of zero noise.

Now in Fig. 4 we explore the MD for the case $\nu \neq 1$ where the particle crosses the position of minimal noise. Here the boundary conditions do matter and we distinguish between no boundaries (Fig. 4a) with infinitely many oscillations and periodic boundary conditions of a ring-like geometry (Fig. 4b). While the short-time

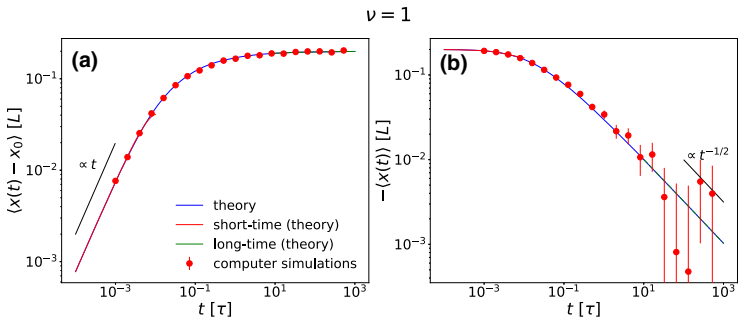

Fig. 2 Absolute values of the mean displacement $\langle x(t) - x_0 \rangle$ (**a**) and the mean position with a minus sign to ensure positivity $-\langle x(t) \rangle$ (**b**) for $\nu = 1$ and $x_0 = -0.2L$ as a function of time t. The numerical evaluation of the integral in Eq. (10) (theory) and its asymptotic short- and long-time expansions (14) and (21) are shown together with simulation data. The MD increases linear in time t for short times, while the decay to its limit scales in a very slow way with $\mathcal{O}\left(t^{-1/2}\right)$

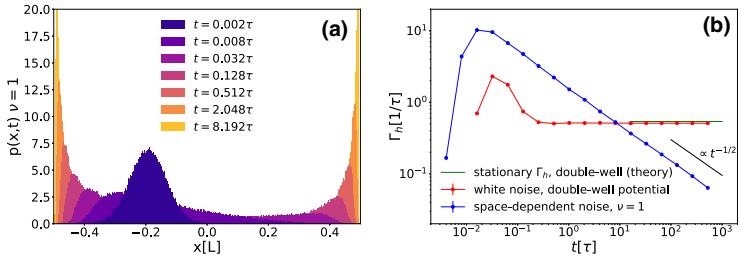

Fig. 3 **a** Probability density function $p(x, t)$ for the particle position at different times t, with $\nu = 1$ and $x_0 = -0.2L$. Here, we averaged over 10,000 different trajectories of length 10τ. **b** Hopping rate Γ_h between the two peaks in the particle distribution as a function of time t for a space-dependent noise with points of vanishing noise ($\nu = 1$), and for a double-well potential with white noise. Here, we have chosen $x_0 = -0.2L$. We also show the stationary state theoretical value of Γ_h for the double well potential, defined as the inverse of the mean first passage time t_e, derived in Eq. (26)

behavior is linear in time for both kind of boundary conditions, the MD saturates for long times to a finite value depending on ν and x_0 for the no boundaries case. This finite value is $-x_0$ for periodic boundary conditions since in this case the mean position will always end at zero due to symmetry. The asymptotic approach to zero is exponential in time as in the case of the double-well potential with noise as the particle stays mobile even when approaching the position where the noise is minimal. This is in marked contrast to the limit of $\nu = 1$ where the particle gets immobilized at the boundaries.

Now we turn to the MSD, first for the special case $\nu = 1$ shown in Fig. 5a where boundary conditions do not matter. The MSD starts linear in time and then saturates to its long-time limit $C := x_0^2 + (\pi/k)^2$. Its asymptotic approach to this saturation value is revealed by plotting the MSD shifted by C which decays to zero for large times, see Fig. 5b. Similar to the MD for $\nu = 1$, we find that the asymptotic behavior is compatible with a $1/\sqrt{t}$ scaling.

In Fig. 6 we show the MSD for $\nu \neq 1$ for both types of boundary conditions. In absence of boundary conditions (see Fig. 6a) the long-time behavior is linear in time $\approx 2D_L t$ involving a long-time diffusion coefficient D_L. Clearly the latter depends on ν but not on the initial position x_0. This dependence is depicted in the inset of Fig. 6a. We found the empirical expression $D_L(\nu) = D_0(1 - \nu^2)$ with $D_0 = k_B T_0/\gamma$ to be a very good fit to the data. This can be regarded as a parabolic fit which fulfills the inflection symmetry in ν and the constraint $D_L(\nu = 1) = 0$. The same behavior was recently found in a similar system [63].

Finally, to better clarify the behaviors of the MD and MSD for $\nu = 1$, we plot the dynamical exponents (Fig. 7) that define the scaling regimes for the MD (β, β') and MSD (α, α') close to their short-time and long-time limits, respectively:

Eur. Phys. J. E (2022) 45:18

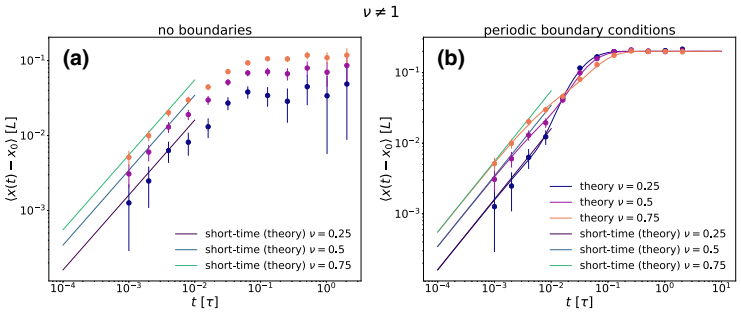

Fig. 4 Mean displacement $\langle x(t) - x_0 \rangle$ (a,b) as a function of time t for three values of $\nu = 0.25, 0.5, 0.75$ and $x_0 = -0.2L$ for no boundaries (**a**) and for periodic boundary conditions (**b**)

Fig. 5 Absolute values of the mean-squared displacement (MSD) $\langle (x(t) - x_0)^2 \rangle$ (**a**) and shifted MSD$-C$, where C is the long time limit of the MSD (**b**) as a function of time t for $\nu = 1$ and $x_0 = -0.2L$. The numerical evaluation of the integral in Eq. (11) and its asymptotic short- and long-time expansions are shown together with simulation data

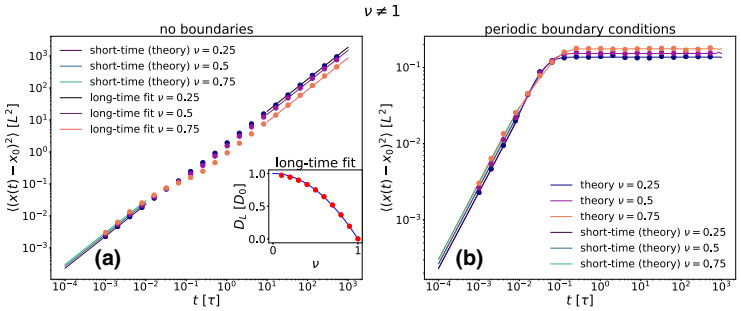

Fig. 6 **a** Mean-squared displacement (MSD) $\langle (x(t) - x_0)^2 \rangle$ as a function of time t for $\nu \neq 1$ and $x_0 = -0.2L$ both for no boundaries (**a**) and for periodic boundary conditions (**b**). The inset shows the long-time diffusion constant D_L as a function of ν for the no boundaries case

$$
\begin{aligned}
\beta &:= \frac{d(\log_{10} |\langle x(t) - x_0 \rangle|)}{d(\log_{10}(t))}, \\
\beta' &:= \frac{d(\log_{10} |\langle x(t) \rangle|)}{d(\log_{10}(t))}, \\
\alpha &:= \frac{d(\log_{10} \langle (x(t) - x_0)^2 \rangle)}{d(\log_{10}(t))}, \\
\alpha' &:= \frac{d(\log_{10} |\langle (x(t) - x_0)^2 \rangle - C|)}{d(\log_{10}(t))}.
\end{aligned}
\tag{27}
$$

Both the MD and MSD for short times are linear, while for long times the scaling of the MD converges clearly to -0.5, that corresponds to $1/\sqrt{t}$. Within the time window explored the MSD has not yet saturated to an ultimate dynamical exponent for long times. The asymptotics shown is compatible with a final scaling exponent of $-1/2$ although the approach to this final exponent is much slower for the MSD than for the MD where the saturation is clearly visible.

We remark that an algebraic asymptotic approach in the MSD was also found for equilibrium Brownian dynamics of repulsive interacting particles. Here the time-derivative of the time-dependent diffusion coefficient MSD$/t$ scales as $t^{-d/2}$ in d spatial dimensions [64–67] but the physical origins of the algebraic scaling laws are different.

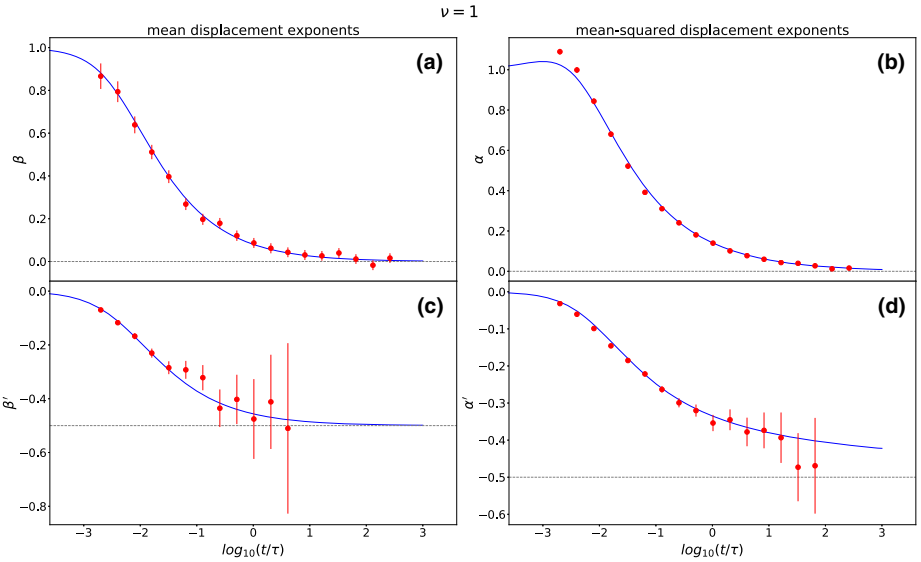

Fig. 7 Dynamical exponents of the MD (**a**, **c**) and MSD (**b**, **d**) close to 0 (**a**, **b**) and their final limit (**c**, **d**) for $\nu = 1$ and $x_0 = -0.2L$ in theory and simulation as functions of time t. As we have already seen in Fig. 2 for the MD and Fig. 4 for the MSD, both quantities grow initially linearly in time and decay to their final limit with $1/\sqrt{t}$ for the MD and slower than $1/\sqrt{t}$ for the MSD

3 Tilted potential

In this section, we leave the situation in which the Brownian particle is a free particle only driven by spatially-dependent noise. We now consider the full model, including the deterministic tilted potential. We first look at the situation near the critical value of the amplitude $\epsilon = 1$, where the tilted potential develops a plateau. The situation addressed in shown in Fig. 8.

3.1 The stationary current

Being weakly confined to a region of the deterministic potential in which the dynamics can be considered 'slow', a quasi-stationary distribution can be defined [49]. The Fokker–Planck equation corresponding to the Langevin equation, Eq. (1) in Stratonovich interpretation reads as

$$\partial_t p(x,t) = -\partial_x a(x) p(x,t) + \frac{1}{2}\partial_x [b(x)\partial_x [b(x)p(x,t)]] \tag{28}$$

with $a(x)$ the force and $b(x)$ the noise amplitude,

$$a(x) := F_0(1 + \epsilon\cos(kx)),\ \ b(x) := \sqrt{2\gamma k_B T(x)}\,. \tag{29}$$

Following the discussion in [49], the dynamics near the critical tilt value for $\epsilon \geq 1$ is characterized by a stationary current given by the one-time integrated FP-equation

$$-J_s = -a(x)p_s(x) + \frac{1}{2}b(x)\partial_x[b(x)p_s(x)]\,. \tag{30}$$

Defining $(b(x)/2)p_s(x) = \widehat{p}_s(x)$ we can rewrite the last expression as

$$-\frac{J_s}{b(x)} = -R(x)\widehat{p}_s(x) + \partial_x\widehat{p}_s(x) \tag{31}$$

with

$$R(x) = \frac{2a(x)}{b^2(x)}\,. \tag{32}$$

The equation can be solved with the Ansatz $\widehat{p}_s(x) = u(x)\cdot v(x)$ which reduces the problem to two readily integrable first-order ordinary differential equations for $u(x)$ and $v(x)$. One obtains the final expression

$$p_s(x) = \frac{2J_s}{b(x)}\int_x^\infty dy \frac{1}{b(y)} \exp\left(-\int_x^y \mathrm{d}z R(z)\right), \tag{33}$$

in which the current J_s can be obtained from the normalization integral $\int_{-\infty}^{\infty}\mathrm{d}x p_s(x) = 1$. In the following we take for simplicity (setting all other constants to one)

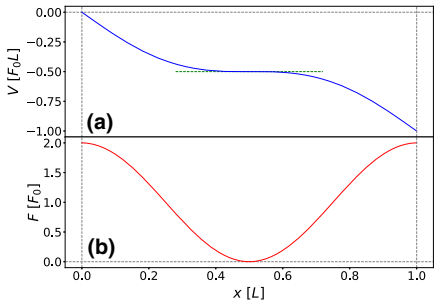

Fig. 8 Potential (**a**) and corresponding force (**b**) near the 'flat' regime $\epsilon = 1$ as a function of the spatial coordinate x

$$R(z) = \frac{1 + \epsilon\cos(z)}{(1 + \nu\cos(z))^2}\,. \tag{34}$$

Setting $b(z) := \exp(-F(z)) = \exp(-\ln(1 + \nu\cos(z))$, and expanding both $b(z)$ and $R(z)$ in Taylor series around the center of the flat region near $z = L/2$, the stationary current J_s is given by

$$J_s = \frac{1}{2}\left[\int_{-\infty}^{\infty} \mathrm{d}x \exp\left(-\widehat{F}(x)\right) \times \int_0^{\infty} dy \exp\left(-\widehat{F}(y)\right) \exp\left(-\int_x^y \mathrm{d}z\widehat{R}(z)\right)\right]^{-1} \tag{35}$$

in which the symbol $\widehat{\ldots}$ indicates the Taylor-expanded functions,

$$\widehat{F}(x) = \ln(1-\nu) + \frac{1}{2}\left(\frac{1}{1-\nu}\right)(x - L/2)^2 \tag{36}$$

and

$$\widehat{R}(z) = 2\frac{1-\epsilon}{(1-\nu)^2} + \frac{\epsilon(\nu+1) - 2\nu}{(1-\nu)^3}(z - L/2)^2\,. \tag{37}$$

The integration of $\widehat{R}(z)$ yields a cubic polynomial, but due to cancellations the resulting expression in the exponential is Gaussian in x and cubic in y. The Gaussian integral in y can be calculated exactly, while the remaining expression in y needs to be evaluated numerically for each value of ϵ and ν.

The most interesting behavior of the stationary current is found in the limit $\nu \to 1$, $\epsilon \approx 1$. The fact that the coefficients in Eqs.(36),(37) are singular in $1/(1-\nu)$ leads to a singular behavior of J_s in the form

$$J_s \propto (1-\nu)^m \exp\left[-\frac{I(\epsilon,\nu)}{(1-\nu)^n}\right]\,, \tag{38}$$

with $n = 3$, since the dominant singularity in $\widehat{R}(z)$ is $\propto (1-\nu)^{-3}$, see Eq. (37). The amplitude is $I(\epsilon,\nu) = (\epsilon(\nu+1) - 2\nu)/4$ and the rational factors combine to $m = 0$. The stationary current thus goes to zero with an essential singularity in $(1-\nu)$.

3.2 Phase difference between noise and potential

For a tilted potential, we now explore the effect of a nonzero phase $\phi \neq 0$ on the long-time behavior of the particle for different values of ν by using computer simulation.

As shown in [41], the long-time drift velocity and diffusion coefficients (v_L and D_L respectively) can be analytically calculated for the case $\nu = 0$, where we set $V(x)$ as potential.

Here the question is how the mismatch of the periodic noise and external forcing affects the long-time behavior of the particle. Intuitively one would expect that overcoming an energetic barrier is best if the maximum of the noise occurs where the external force is opposing most. Then the noise would help to bring the particle over the energetic barrier. The position where the force is opposing most is clearly given for $x = L/2 + nL$, where n is an integer. Then it is expected that mobility gets a maximum if the phase shift is $\phi = \pi$. This is indeed what we confirm by simulation. We chose $k_BT_0 = 0.01F_0L$ and $\epsilon = 1.3$. The potential barrier ΔE is given by

$$\Delta E(\epsilon) = \frac{F_0 L}{\pi}\left(\sqrt{\epsilon^2 - 1} - \mathrm{arcsec}(\epsilon)\right)\,, \tag{39}$$

yielding $\Delta E \simeq 0.04F_0L > 0.01F_0L$ for $\epsilon = 1.3$.

Given these parameters, we simulated the system for different values of ϕ and ν and results are summarized in Fig. 9. Since to the best of our knowledge there is no easy generalization of the results in [41] for a space-dependent temperature, we have compared the simulation data with a mapping on the analytical results for $v_L^{(0)}$ and $D_L^{(0)}$ [41] which were obtained for a spatially constant temperature. Since the crucial position to hop over the barrier is at $x = L/2 + nL$ where the opposing force is maximal, this represents the kinetic bottleneck for the dynamical process. Therefore it is tempting to compare our simulation results with the analytical ones where this local noise strength $T(x = L/2)$ is inserted as a homogeneous temperature. We remark that this temperature $T(x = L/2)$ depends both on the oscillation strength ν and the phase shift ϕ of T with respect to the potential. This mapping theory should work best if the particle spends most of its time close to the point $x = L/2$. In fact, Fig. 9 reveals that this simple mapping theory describes the simulation data well even for large ν. As a function of the phase mismatch ϕ, both D_L and v_L are enhanced when ϕ is between about $\frac{3}{5}\pi$ and $\frac{7}{5}\pi$. Clearly around the value $\phi = \pi$ we find the maximal enhancement of both v_L and D_L. In the complementary case, the noise strength $T(x)$ has its minimum closer to the crucial region where the opposing force is maximal, and as a result the drift velocity and diffusion are severely reduced. For $\nu = 1$ they are even brought

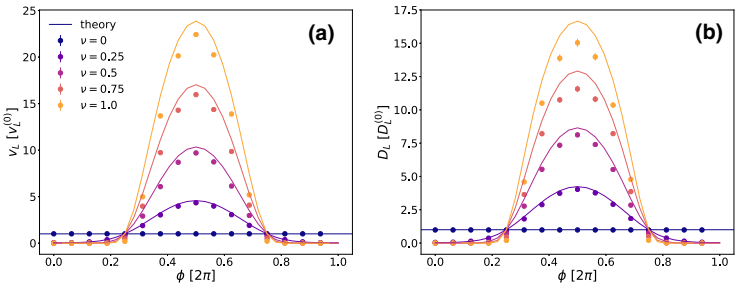

Fig. 9 Long time drift (**a**) and diffusion (**b**) for $\epsilon = 1.3$ as functions of ν and ϕ, simulations results and theory. For ϕ between about $\frac{3}{5}\pi$ and $\frac{7}{5}\pi$ both D_L and v_L are enhanced, having a maximum in $\phi = \pi$, while otherwise they are reduced

exactly to zero when $|\phi| < \text{arcsec}(\epsilon)$, since the particle is stuck and there is no systematic external force to drift over the positions of vanishing noise.

4 Conclusions and outlook

In conclusion we have presented a detailed study of a model for a Brownian particle moving in a one-dimensional environment with a space-periodic noise and under an external potential with a tilt near its critical value. In the free case we calculated the exact solution of the associated Langevin equation, and further explicitly obtained short- and long-time approximations of the MD and MSD. These results allow us to characterize the slow decay of these quantities at long times. Interesting relaxation dynamics occurs around points of vanishing noise which establish centers of growing peaks in the particle distribution, as particles slow down significantly in the neighborhoods of these points. Introducing the tilted periodic potential we first determined the stationary current for the quasi-stationary state, which for $\epsilon \geq 1$ displays an essential singularity for the maximal strength of the noise oscillations, ν. Finally, we determined numerically the effects of a space-periodic noise on the long-time diffusion and drift as functions of the phase difference between noise and potential ϕ and the strength of the noise oscillations ν, finding the largest enhancements to take place for a phase of $\phi = \pi$ and the maximal possible noise oscillations for $\nu = 1$.

Our one-dimensional model with both periodic boundary conditions or no boundaries can be realized by a colloidal particle confined in a ring or a linear channel respectively by, e.g. optical forces [48,68–70]. The space-dependent noise can be added by various means. First, one can change locally the solvent temperature. This realization has a limited applicability, since the state of the solvent can be changed drastically upon such a temperature variation. However, there are more general and more important realizations for our model. First of all, the viscosity or the friction coefficient can directly be changed without changing the ambient temperature. The solvent viscosity, for instance, can be tuned over orders of magnitude by imposed patterned substrates interacting with the solvent or even by varying the size of the colloids without changing the solvent phase [71]. Second, space-dependent noise can stem from active internal fluctuations [72,73] different from thermal fluctuations and can be embodied into an effective noise strength that can largely be tuned by activity [74–78]. Optical gradients can be used to steer activity as a function of the position, as realized and discussed in [63,79–81]. Another possibility is to tune the noise amplitude of *skyrmions*, which have a similar equation of motion [82]. Last but not least, the noise can be mimicked in valuable model systems by applying randomized kicks of an external field to the particle. For example, the noise strength can largely be tuned externally without changing the solvent at all by tuning the rotational diffusion constant of the colloids [83,84]. In fact, the effective diffusion constant of an active particle depends on its rotational diffusion constant, and in the limit of short persistence lengths one can indirectly tune the translational diffusion by tuning the rotational one.

Acknowledgements We thank L. Caprini for confirming the long-time behavior of the MSD described in Fig. 6a in an analogous system and T. Voigtmann for the interesting discussions. DB is supported by the EU MSCA-ITN ActiveMatter, (proposal No. 812780). RB is grateful to HL for the invitation to a stay at the Heinrich-Heine University in Düsseldorf where this work was performed. HL was supported by the DFG project LO 418/25-1 of the SPP 2265.

Funding Information Open Access funding enabled and organized by Projekt DEAL.

Author contribution statement

HL and RB directed the project. DB performed analytic calculations and numerical simulations. RB contributed analytical results. All authors discussed the results and wrote the manuscript.

References

1. A. Einstein, Ann. Phys. **322**, 549–560 (1905)
2. E. Frey, K. Kroy, Ann. Phys. **14**, 20–50 (2005)
3. J.P. Hansen, J. Zinn-Justin, D. Levesque, in *Liquids, Freezing and Glass Transition: Les Houches Session 51., 3-28 Juillet 1989*, ed. by P.N. Pusey. Colloidal Suspensions (North Holland, 1991)
4. H. Xiong, L. Yao, H. Tan, W. Wang, Disc. Dyn. Nat. Soc. **2012**, e405907 (2012)
5. E.A. Codling, M.J. Plank, S. Benhamou, J. R. Soc. Interf. **5**, 813–834 (2008)
6. R. Tsekov, Chin. Phys. Lett. **30**, 088901 (2013)
7. W. Hess, R. Klein, Adv. Phys. **32**, 173–283 (1983)
8. G. Nägele, Phys. Rep. **272**, 215–372 (1996)
9. J.K.G. Dhont, *An Introduction to Dynamics of Colloids* (Elsevier Science, Amsterdam, 1996)
10. P. Hänggi, F. Marchesoni, Rev. Mod. Phys. **81**, 387–442 (2009)
11. J. Rousselet, L. Salome, A. Ajdari, J. Prost, Nature **370**, 446–447 (1994)
12. J. Kula, T. Czernik, J. Łuczka, Phys. Rev. Lett. **80**, 1377–1380 (1998)
13. A.v. Oudenaarden, S.G. Boxer, *Science* (1999)
14. S.H. Wu, N. Huang, E. Jaquay, M.L. Povinelli, Nano Lett. **16**, 5261–5266 (2016)
15. P. Reimann, Phys. Rep. **361**, 57–265 (2002)
16. P. Cedraschi, M. Büttiker, Phys. Rev. B **63**, 165312 (2001)
17. E.R. Kay, D.A. Leigh, F. Zerbetto, Angew. Chem. Int. Ed. **46**, 72–191 (2007)
18. U. Seifert, Rep. Prog. Phys. **75**, 126001 (2012)
19. I.A. Martínez, Roldán, L. Dinis, D. Petrov, J.M.R. Parrondo, R.A. Rica, Nat. Phys. **12**, 67–70 (2016)
20. I.A. Martínez, d Roldán, L. Dinis, R.A. Rica, Soft Matter **13**, 22–36 (2017)
21. M. Büttiker, Zeitschrift für Physik B Conden. Matter **68**, 161–167 (1987)
22. R. Landauer, J. Stat. Phys. **53**, 233–248 (1988)
23. N.G. van Kampen, J. Math. Phys. **29**, 1220–1224 (1988)
24. P. Malgaretti, I. Pagonabarraga, J.M. Rubi, J. Chem. Phys. **138**, 194906 (2013)
25. G. Volpe, J. Wehr, Rep. Prog. Phys. **79**, 053901 (2016)
26. R. Mannella, P.V.E. McClintock, Fluct. Noise Lett. **11**, 1240010 (2012)
27. N. Leibovich, E. Barkai, Phys. Rev. E **99**, 042138 (2019)
28. P. Lançon, G. Batrouni, L. Lobry, N. Ostrowsky, EPL (Europhysics Letters) **54**, 28 (2001)
29. J. Pešek, P. Baerts, B. Smeets, C. Maes, H. Ramon, Soft Matter **12**, 3360–3387 (2016)
30. O. Farago, N. Grønbech-Jensen, J. Chem. Phys. **144**, 084102 (2016)
31. A.J. Bray, Phys. Rev. E **62**, 103–112 (2000)
32. S. Pieprzyk, D.M. Heyes, A.C. Brańka, Biomicrofluidics **10**, 054118 (2016)
33. A.M. Berezhkovskii, D.E. Makarov, J. Chem. Phys. **147**, 201102 (2017)
34. B. Kaulakys, M. Alaburda, J. Stat. Mech: Theory Exp. **2009**, P02051 (2009)
35. E. Aghion, D.A. Kessler, E. Barkai, Chaos. Solit. Fract. **138**, 109690 (2020)
36. M.A.F. dos Santos, V. Dornelas, E.H. Colombo, C. Anteneodo, Phys. Rev. E **102**, 042139 (2020)
37. Y. Xu, X. Liu, Y. Li, R. Metzler, Phys. Rev. E **102**, 062106 (2020)
38. S. Ray, J. Chem. Phys. **153**, 234904 (2020)
39. Y. Li, R. Mei, Y. Xu, J. Kurths, J. Duan, R. Metzler, New J. Phys. **22**, 053016 (2020)
40. D. Breoni, H. Löwen, R. Blossey, Phys. Rev. E **103**, 052602 (2021)
41. P. Reimann, C. Van den Broeck, H. Linke, P. Hänggi, J.M. Rubi, A. Pérez-Madrid, Phys. Rev. Lett. **87**, 010602 (2001)
42. P. Reimann, C. van den Broeck, H. Linke, P. Hänggi, J.M. Rubi, A. Pérez-Madrid, Phys. Rev. E **65**, 031104 (2002)
43. K. Sasaki, S. Amari, J. Phys. Soc. Jpn. **74**, 2226–2232 (2005)
44. P. Reimann, R. Eichhorn, Phys. Rev. Lett. **101**, 180601 (2008)
45. M. Evstigneev, O. Zvyagolskaya, S. Bleil, R. Eichhorn, C. Bechinger, P. Reimann, Phys. Rev. E **77**, 041107 (2008)
46. M. Evstigneev, S. von Gehlen, P. Reimann, Phys. Rev. E **79**, 011116 (2009)
47. L. Cheng, N.K. Yip, Physica D **297**, 1–32 (2015)
48. M.P.N. Juniper, A.V. Straube, R. Besseling, D.G.A.L. Aarts, R.P.A. Dullens, Nat. Commun. **6**, 7187 (2015)
49. T. Guérin, D.S. Dean, Phys. Rev. E **95**, 012109 (2017)
50. Z.W. Bai, W. Zhang, Chem. Phys. **500**, 62–66 (2018)
51. K. Białas, J. Spiechowicz, Chaos Interdisc. J. Nonlinear Sci. **31**, 123107 (2021)
52. D.G. Zarlenga, H.A. Larrondo, C.M. Arizmendi, F. Family, Phys. Rev. E **75**, 051101 (2007)
53. D.G. Zarlenga, H.A. Larrondo, C.M. Arizmendi, F. Family, Phys. Rev. E **80**, 011127 (2009)
54. D.G. Zarlenga, G.L. Frontini, F. Family, C.M. Arizmendi, Physica A **523**, 172–179 (2019)
55. K.I. Mazzitello, J.L. Iguain, Y. Jiang, F. Family, C.M. Arizmendi, J. Phys: Conf. Ser. **1290**, 012022 (2019)
56. H. Chien-Lih, Math. Gaz. **89**, 469–470 (2005)
57. J.R. Howse, R.A.L. Jones, A.J. Ryan, T. Gough, R. Vafabakhsh, R. Golestanian, Phys. Rev. Lett. **99**, 048102 (2007)
58. B. ten Hagen, S. van Teeffelen, H. Löwen, J. Phys.: Condens. Matter **23**, 194119 (2011)
59. A.R. Sprenger, S. Jahanshahi, A.V. Ivlev, H. Löwen, Phys. Rev. E **103**, 042601 (2021)
60. G.N. Mil'shtejn, Theory Prob. Appl. **19**, 557–562 (1975)
61. P. Malgaretti, A.M. Puertas, I. Pagonabarraga, J. Colloid Interf. Sci. **608**, 2694–2702 (2022)
62. L. Caprini, F. Cecconi, U. Marini Bettolo Marconi, J. Chem. Phys. **155**, 234902 (2021)
63. L. Caprini, U.M.B. Marconi, R. Wittmann, H. Löwen, *Soft Matter* (2022)

64. B. Cichocki, B.U. Felderhof, Phys. Rev. A **44**, 6551–6558 (1991)
65. B.J. Ackerson, L. Fleishman, J. Chem. Phys. **76**, 2675–2679 (1982)
66. H. Löwen, J. Phys.: Condens. Matter **4**, 10105–10116 (1992)
67. M. Kollmann, Phys. Rev. Lett. **90**, 180602 (2003)
68. C. Lutz, M. Kollmann, C. Bechinger, Phys. Rev. Lett. **93**, 026001 (2004)
69. C. Lutz, M. Kollmann, P. Leiderer, C. Bechinger, J. Phys.: Condens. Matter **16**, S4075–S4083 (2004)
70. M.P.N. Juniper, U. Zimmermann, A.V. Straube, R. Besseling, D.G.A.L. Aarts, H. Löwen, R.P.A. Dullens, New J. Phys. **19**, 013010 (2017)
71. I. Berndt, J.S. Pedersen, W. Richtering, J. Am. Chem. Soc. **127**, 9372–9373 (2005)
72. G. Frangipane, D. Dell'Arciprete, S. Petracchini, C. Maggi, F. Saglimbeni, S. Bianchi, G. Vizsnyiczai, M.L. Bernardini, R. Di Leonardo, eLife **7**, e36608 (2018)
73. J. Arlt, V.A. Martinez, A. Dawson, T. Pilizota, W.C.K. Poon, Nat. Commun. **9**, 768 (2018)
74. G. Szamel, Phys. Rev. E **90**, 012111 (2014)
75. R. Wittmann, C. Maggi, A. Sharma, A. Scacchi, J.M. Brader, U.M.B. Marconi, J. Stat. Mech: Theory Exp. **2017**, 113207 (2017)
76. L. Caprini, U.M.B. Marconi, Soft Matter **14**, 9044–9054 (2018)
77. L. Dabelow, S. Bo, R. Eichhorn, Phys. Rev. X **9**, 021009 (2019)
78. L. Caprini, U.M.B. Marconi, A. Puglisi, A. Vulpiani, J. Stat. Mech. Theory Exp. **2019**, 053203 (2019)
79. C. Lozano, B. ten Hagen, H. Löwen, C. Bechinger, Nat. Commun. **7**, 12828 (2016)
80. C. Lozano, B. Liebchen, B. ten Hagen, C. Bechinger, H. Löwen, Soft Matter **15**, 5185–5192 (2019)
81. N.A. Söker, S. Auschra, V. Holubec, K. Kroy, F. Cichos, Phys. Rev. Lett. **126**, 228001 (2021)
82. B.L. Brown, U.C. Täuber, M. Pleimling, Phys. Rev. B **97**, 020405 (2018)
83. M.A. Fernandez-Rodriguez, F. Grillo, L. Alvarez, M. Rathlef, I. Buttinoni, G. Volpe, L. Isa, Nat. Commun. **11**, 4223 (2020)
84. A.R. Sprenger, M.A. Fernandez-Rodriguez, L. Alvarez, L. Isa, R. Wittkowski, H. Löwen, Langmuir **36**, 7066–7073 (2020)

P4 A one-dimensional three-state run-and-tumble model with a 'cell cycle'

Reproduced from

D. Breoni, F.J.Schwarzendahl, R.Blossey, and H. Löwen, *A one-dimensional three-state run-and-tumble model with a 'cell cycle'*, The European Physical Journal E **45**, 83 (2022),

Digital Object Identifier (DOI): `https://doi.org/10.1140/epje/s10189-022-00238-7`

Statement of contribution

HL and RB directed the project. I performed analytic calculations and numerical simulations. FS contributed with helpful discussion on the topic. All authors discussed the results and wrote the manuscript.

Copyright and license notice

Eur. Phys. J. E (2022) 45:83
https://doi.org/10.1140/epje/s10189-022-00238-7

THE EUROPEAN PHYSICAL JOURNAL E

Regular Article - Living Systems

A one-dimensional three-state run-and-tumble model with a 'cell cycle'

Davide Breoni[1,a], Fabian Jan Schwarzendahl[1], Ralf Blossey[2], and Hartmut Löwen[1]

[1] Institut für Theoretische Physik II: Weiche Materie, Heinrich-Heine-Universität Düsseldorf, Universitätsstraße 1, 40225 Düsseldorf, Germany
[2] Unité de Glycobiologie Structurale et Fonctionnelle (UGSF), CNRS UMR8576, University of Lille, 59000 Lille, France

Received 13 June 2022 / Accepted 10 October 2022 / Published online 19 October 2022

Abstract We study a one-dimensional three-state run-and-tumble model motivated by the bacterium *Caulobacter crescentus* which displays a cell cycle between two non-proliferating mobile phases and a proliferating sedentary phase. Our model implements kinetic transitions between the two mobile and one sedentary states described in terms of their number densities, where mobility is allowed with different running speeds in forward and backward direction. We start by analyzing the stationary states of the system and compute the mean and squared-displacements for the distribution of all cells, as well as for the number density of settled cells. The latter displays a surprising super-ballistic scaling $\sim t^3$ at early times. Including repulsive and attractive interactions between the mobile cell populations and the settled cells, we explore the stability of the system and employ numerical methods to study structure formation in the fully nonlinear system. We find traveling waves of bacteria, whose occurrence is quantified in a non-equilibrium state diagram.

1 Introduction

Understanding the motion of bacteria has been a classic problem of biophysics [1,2]. Bacteria are propelled by their flagellae, whose motor generates a torque which translates into forward or backward motion of the bacteria. The problem has also found interest within the soft matter community, as bacteria are but one example of a much larger class of systems, commonly denoted as microswimmers [3]. The run-and-tumble (RT) model of an active particle system is originally motivated by specific features of bacterial motion: this motion only persists for a finite time, the 'run'-time, after which the bacterium stalls, the 'tumble'-period, before continuing its motion typically in a different direction, see e.g. [4]. The properties of the basic RT model have been confronted with experiments, e.g. in [5,6]. The RT model also relates to other stochastic processes, e.g. the exclusion process [7] or even to the dynamics of quantum particles [8].

RT models in one dimension are a special case within this model class. Here, the bacterium can only switch between left- and right motion in a stochastic manner. One-dimensional RT-models have proven to be an extremely rich field for analytic calculations; exemplary papers dealing with diverse aspects are: confinement [9]; space-dependent transition rates and general drift velocity distributions [10–14]; hard-core particles with spin [15]; inhomogeneous media [16]; attractive/repulsive interactions [17,18]; phase transitions [19]; entropy production [20]. Field-theoretic methods have been applied to RT models recently as well [21,22].

In some sense, the (one-dimensional) RT model can be thought of playing in active systems a role analogous to Ising models in equilibrium statistical mechanics. In the very recent past, several works have appeared carrying this analogy further, since they consider the number of 'states' in which the bacterium can find itself to go beyond the dichotomy of left- and right-moving states. Models with three and even more states have been discussed—in our Ising-model analogy, this amounts to looking at active analogues of 'Potts'-type models [23–25].

The present paper inserts itself in this line of research by considering a three-state RT model with the states: left-moving, right-moving and sedentary. Our model is motivated by the behavior of the bacterium *Caulobacter crescentus* (*CC*), a model organism in microbiology since it has a complex lifestyle [26,27]. *CC* has a bacterial analogue of a cell cycle usually found in eukaryotes; in order to undergo cell division, the bacterium has to switch from its mobile swarmer state to a spatially localized stalked state. Only from the latter state the proliferation of new cells is possible. Our model, capturing this biological feature, is however not limited

[a] e-mail: breoni@hhu.de (corresponding author)

to *CC* or bacteria alone. E.g., the green algae *Chlamydomonas reinhartii* has a similar cell cycle [28] with sedentary and swimming states and also performs a run-and-tumble motion [4]. The capacity of cell division in our RT model inks it to the problem of the growth of bacterial colonies. Recently, the authors of [29] developed a growth-expansion model which generates traveling waves in bacterial chemotaxis, in accord with experimental observations. We show that traveling waves also arise in our much simpler 1d run-and-tumble model.

The paper is organized as follows. In Sect. 2, we introduce our RT-model as a toy model, inspired by the cell cycle of *CC*. In Sect. 3, we first focus on the case of free cells for which we derive the conditions for stability of the system when spatial dependencies are neglected. In Sect. 4 we consider the spatial dependence built into the model and study the mean displacement (MD) and mean squared displacement (MSD) for a single cell in the process of duplicating, both showing a surprising t^3 regime for short times. Allowing the cells to interact via both attraction and repulsion mechanisms, this antagonistic effect is found to lead to structure formation: we numerically find traveling wave solutions of the system density and quantify their occurrence in a non-equilibrium state diagram. Finally we discuss how the model performs with parameter values specific of *CC*. Section 5 concludes the paper with a discussion of the results of our model and a brief outlook on further work.

2 The model

Inspired by the reproductive behavior of *Caulobacter crescentus* we consider a one-dimensional toy model representing bacteria that can actively move rightward, leftward or settle down, and that when settled double in number. We note that *CC* performs a run-reverse-flick motion [30], where the bacterium first performs a forward motion, then reverses its direction of motion and in a third step makes a turn mediated by a buckling instability in its flagellum [31]. Since our setup is one dimensional, the run-reverse-flick motion is equivalent to a run and tumble motion.

The 'cell cycle' of our three-state RT model motivated by *CC* is summarized in Fig. 1. We allow for three populations with the number densities $\rho_+(x,t)$, $\rho_-(x,t)$ and $\rho_0(x,t)$, functions of space x and time t, respectively corresponding to right and left movers, and to the sedentary population. The 'cell cycle' step is given by the rate of settling down, λ_s, which can occur from either moving state, and the cell doubling with rate λ_d with which a sedentary bacterium gives rise to a pair of right- and left-moving cells. The exchange of direction, i.e. the RT step, is denoted by λ_e. Finally, μ is the death rate, which we consider for motile cells only. In a proliferating system, this rate prevents exponential growth.

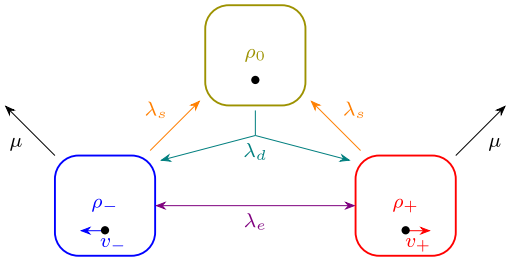

Fig. 1 Graphical representation of the transition rates among different species. These transitions are motivated by the cell cycle of *Caulobacter crescentus*, that either moves actively or settles down to reproduce. Our model contains three different species: the cells moving to the right ρ_+, those moving to the left ρ_- and the settled ones ρ_0. The moving cells can either settle via the rate λ_s, move in the opposite direction with λ_e or die with μ. Settled cells duplicate via λ_d, and generate both a left- and a right-moving cell

This idealized *CC*-'cell cycle' is implemented in terms of evolution equations for the cell number densities. In the case where there is no death or proliferation, the number densities can also be interpreted as probability densities and the evolution equations correspond to Fokker–Planck equations.

As the bacteria are micron-sized swimmers, we assume a low Reynolds number and overdamped dynamics. To describe this behavior mathematically, we first group the three densities into the vector of densities $\boldsymbol{\rho} = (\rho_+, \rho_0, \rho_-)$. The dynamics of the system will then be described by the differential equation

$$\partial_t \boldsymbol{\rho} = \mathcal{D}\partial_x^2 \boldsymbol{\rho} + \partial_x[(\partial_x \mathcal{U}) \cdot \boldsymbol{\rho}] - \mathcal{V} \cdot \partial_x \boldsymbol{\rho} + \mathcal{M}\boldsymbol{\rho} \quad (1)$$

which generalizes the standard expression of growth-expansion equations of logistic growth, usually formulated for a single density [29]. In Eq. (1), the first term is a diffusion term where the matrix $\mathcal{D}$ has the form

$$\mathcal{D} = \begin{pmatrix} D & 0 & 0 \\ 0 & 0 & 0 \\ 0 & 0 & D \end{pmatrix} \quad (2)$$

since the sedentary particles do not diffuse. The second term on the right-hand side is a nonlinear diffusion coefficient containing an interaction matrix $\mathcal{U}$ of the form

$$\mathcal{U} = \begin{pmatrix} -\kappa\rho_0 & 0 & 0 \\ 0 & \kappa_0\rho_0 & 0 \\ 0 & 0 & -\kappa\rho_0 \end{pmatrix}. \quad (3)$$

The matrix entries describe attractive interactions (negative sign) of the moving cells to regions in which particles have settled and repulsive interactions among settled cells (positive sign) in order to mimic biofilm behaviour. The third term on the right-hand side of Eq. (1) describes the active motion of the particles in

the right and left directions along the line. Hence

$$\mathcal{V} = \begin{pmatrix} v_+ & 0 & 0 \\ 0 & 0 & 0 \\ 0 & 0 & -v_- \end{pmatrix} . \tag{4}$$

Finally, we have for the cell cycle or population dynamics part, following the transitions shown in Fig. 1, the matrix $\mathcal{M}$ given by

$$\mathcal{M} = \begin{pmatrix} -(\lambda_s + \lambda_e + \mu) & \lambda_d & \lambda_e \\ \lambda_s & -\lambda_d & \lambda_s \\ \lambda_e & \lambda_d & -(\lambda_s + \lambda_e + \mu) \end{pmatrix} . \tag{5}$$

Given that our run-and-tumble model allows for proliferation and death of cells, it is important to recognize that the population dynamics of Eq. (1) is the linear limit of the more general nonlinear decay-growth equation

$$\begin{aligned} \partial_t \boldsymbol{\rho} = \mathcal{D}\partial_x^2 \boldsymbol{\rho} + \partial_x[(\partial_x \mathcal{U}) \cdot \boldsymbol{\rho}] - \mathcal{V} \cdot \partial_x \boldsymbol{\rho} \\ + \mathcal{M}_D \boldsymbol{\rho} + \mathcal{M}_{OD} \boldsymbol{\mathcal{R}}(\boldsymbol{\rho}). \end{aligned} \tag{6}$$

In Eq. (6), $\mathcal{M}_D$ and $\mathcal{M}_{OD}$ are the diagonal and off-diagonal parts of the matrix $\mathcal{M}$, i.e., one has $\mathcal{M} = \mathcal{M}_D + \mathcal{M}_{OD}$. The diagonal part describes the cell number decay, while the off-diagonal part describes the growth of the cell population. In order to limit growth, the non-diagonal term is generally nonlinear and saturating at the carrying capacity, as is common in growth-expansion models, see, e.g. [29]. The vector $\mathcal{R}$ is thus given by

$$\boldsymbol{\mathcal{R}} = \begin{pmatrix} \rho_+(1 - \frac{\rho_+}{\rho_{+,c}}) \\ \rho_0(1 - \frac{\rho_0}{\rho_{0,c}}) \\ \rho_-(1 - \frac{\rho_-}{\rho_{-,c}}) \end{pmatrix} .$$

where the carrying capacity is given by the vector

$$\boldsymbol{\rho}_c(x) \equiv (\rho_{+,c}(x), \rho_{0,c}x), \rho_{-,c}(x)) \ . \tag{7}$$

The linear limit of Eq. (6) is reached for $|\boldsymbol{\rho}| \ll |\boldsymbol{\rho}_c|$. It is important to notice that since $\mathcal{R}$ is only applied to one part of the $\mathcal{M}$ matrix, the stationary values reached by the population in the linear limit will not necessarily be those given by $\boldsymbol{\rho}_c$. The main benefit of the nonlinear model is that it prevents the number of cells from exploding independently of the parameters. In this manuscript we will mainly focus on the linear case, while explicitly referring to the full nonlinear growth equation if needed.

3 Free cells

We start by setting the cell interaction parameters $\kappa = \kappa_0 = 0$, and hence consider free cells.

3.1 Population dynamics

In this section we further set $D = 0$ as well as the velocities $v_+ = v_- = 0$, thus we first study free cells undergoing the pure population dynamics given by

$$\partial_t \boldsymbol{\rho}(x,t) = \mathcal{M}\boldsymbol{\rho}(x,t) . \tag{8}$$

This linear system of equations can be solved analytically via matrix calculations, leading to

$$\boldsymbol{\rho}(x,t) = \mathrm{e}^{\mathcal{M}t}\boldsymbol{\rho}(x,0) = \mathcal{P}\mathrm{e}^{\mathcal{E}t}\mathcal{P}^{-1}\boldsymbol{\rho}(x,0). \tag{9}$$

$\mathcal{P}$ is the eigenvector matrix of $\mathcal{M}$ and $\mathcal{E}$ is the diagonal matrix containing the eigenvalues of $\mathcal{M}$, that are

$$\begin{aligned} \mathcal{E}_1 &= -(\mu + 2\lambda_e + \lambda_s) \\ \mathcal{E}_2 &= -(\mu + \lambda_d + \lambda_s + \Lambda)/2 \\ \mathcal{E}_3 &= -(\mu + \lambda_d + \lambda_s - \Lambda)/2, \end{aligned} \tag{10}$$

where $\Lambda = \sqrt{(\mu + \lambda_d + \lambda_s)^2 + 4\lambda_d(\lambda_s - \mu)}$. We notice that the first two eigenvalues are always negative and therefore stable, while the sign of the third depends on $\lambda_s - \mu$, which can become unstable. This instability facilitates an exponential growth of the colony. In fact, for small values of $\lambda_d(\lambda_s - \mu)$ with respect to $\mu + \lambda_d + \lambda_s$ the unstable eigenvalue becomes

$$\mathcal{E}_3 \simeq \frac{\lambda_d(\lambda_s - \mu)}{\mu + \lambda_d + \lambda_s}. \tag{11}$$

The exponential growth or collapse of the system is therefore decided by the difference of λ_s and μ, or in different terms, the separating line between the two behaviors is $\lambda_s = \mu$. It is also worth pointing out that in the case of instant doubling, that is the limit of $\lambda_d \to \infty$, $\mathcal{E}_3$ simply reduces to $\lambda_s - \mu$, as can be seen in Fig. 2. Physically this is expected, as in this model cells can double only when settled and can die only when moving, meaning that the growth or decay of the system size depends exclusively on whether a moving cell is faster in settling or dying.

In the case of $\lambda_s = \mu$, it is possible to calculate the stationary value of $\boldsymbol{\rho}(x, t \to \infty)$ as a function of the initial conditions $\boldsymbol{\rho}(x, 0)$:

$$\begin{aligned} \rho_+(x, t \to \infty) &= \frac{\lambda_d}{2(2\mu + \lambda_d)} R(x,0) \\ \rho_0(x, t \to \infty) &= \frac{\mu}{2\mu + \lambda_d} R(x,0) \\ \rho_-(x, t \to \infty) &= \frac{\lambda_d}{2(2\mu + \lambda_d)} R(x,0), \end{aligned} \tag{12}$$

where $R(x,0) = 2\rho_0(x,0) + \rho_-(x,0) + \rho_+(x,0)$. Since the exchange rate between right ρ_+ and left ρ_- moving cells is symmetric, the amounts of left and right moving cells are the same in the stationary state ($\rho_+ = \rho_-$, see also Fig. 3). Furthermore, if $\lambda_d = 2\mu = 2\lambda_s$ all the

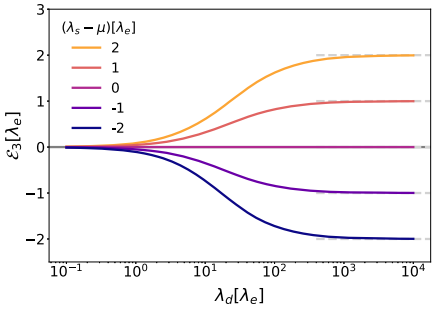

Fig. 2 Unstable eigenvalue $\mathcal{E}_3$ (solid lines) as a function of doubling rate λ_d for different values of λ_s (color code) and $\mu = 10\lambda_e$. The sign of $\mathcal{E}_3$ is the same of $\lambda_s - \mu$, and its value also stabilizes at $\lambda_s - \mu$ for very large values of λ_d (dashed lines)

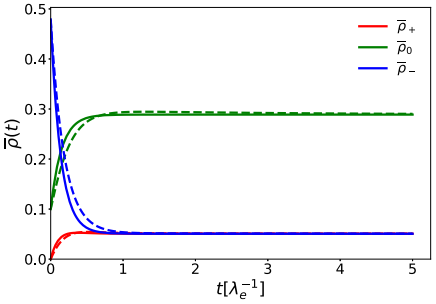

Fig. 3 Space averages of right- $\overline{\rho}_+$, left-moving $\overline{\rho}_-$ and sedentary $\overline{\rho}_0$ cells as functions of time, both for the linear model (solid lines) with $\lambda_s = \mu$ and for the nonlinear model (dashed lines) with $\lambda_s = 3\mu$. For both models λ_d is set to be equal to λ_e, while $\mu = \lambda_e$ in the nonlinear model and $\mu = 2.848\lambda_e$ in the linear one. As initial conditions we chose the constant values $\boldsymbol{\rho}(x, 0) = (0, .1, 0.479)$ for both models. For the nonlinear model we further set the carrying capacity $\boldsymbol{\rho}_c(x) = (1, 1, 1)$

three populations equilibrate to the same value, independently of the initial conditions. In the case of $\lambda_s > \mu$ it is always possible in the frame of the nonlinear growth model to find values of $\boldsymbol{\rho}_c$ for which the populations stabilize around the values given by Eq. (12). Figure 3 shows the linear and nonlinear model equations with different parameters and with the same stationary values.

3.2 Density dynamics

We now set the running speeds $v_\pm$ and the diffusion constant D to finite values, in order to study the evolution of spatial quantities of the system, such as the mean displacement MD $= \langle x - x_0 \rangle$, the mean-squared displacement MSD $= \langle (x - x_0)^2 \rangle$ and all the higher order moments, where x_0 is the average position of the system at $t = 0$. Here, the average $\langle(\cdot)\rangle$ is defined as $\int_{-\infty}^{\infty}(\cdot)P(x,t)\mathrm{d}x$, where the total probability $P(x,t)$ is

$$P(x,t) \equiv \frac{1}{N(t)}(\rho_+(x,t) + \rho_0(x,t) + \rho_-(x,t)), \quad (13)$$

$N(t) \equiv N_0(t) + N_+(t) + N_-(t)$ is the total number of cells, $N_\alpha(t) = \int_{-\infty}^{\infty}\rho_\alpha(x,t)\mathrm{d}x$ is the number of cells in phase α and α can be $(+,-,0)$.

In order to compute averages, we first solve the system by using a Fourier transform (FT):

$$\dot{\tilde{\boldsymbol{\rho}}}(k,t) = \left(-k^2\mathcal{D} - \mathrm{i}k\mathcal{V} + \mathcal{M}\right)\tilde{\boldsymbol{\rho}}(k,t), \quad (14)$$

where $\tilde{\boldsymbol{\rho}}(k,t) = FT(\boldsymbol{\rho}(x,t))$ is the Fourier transform of $\boldsymbol{\rho}(x,t)$ and k is the wave number conjugate to x. Similarly to the constant density case, the solution in Fourier space will be given by

$$\tilde{\boldsymbol{\rho}}(k,t) = \exp\left[(-k^2\mathcal{D} - \mathrm{i}k\mathcal{V} + \mathcal{M})t\right]\tilde{\boldsymbol{\rho}}(k,0). \quad (15)$$

One can use the solution of this equation to extract the intermediate scattering function (ISF)

$$\mathcal{F}(k,t) \equiv \tilde{P}(k,t)\tilde{P}(-k,0)N(t). \quad (16)$$

The ISF can be related to the different moments of the density [32] by differentiation:

$$\langle (x(t) - x_0)^n \rangle = \frac{\mathrm{i}^n}{N(t)}\frac{\partial^n}{\partial k^n}\mathcal{F}(k,t)\Big|_{k=0}, \quad (17)$$

valid in one dimension (see "Appendix").

We can also define an average for each cell population and the relative ISF:

$$\langle(\cdot)\rangle_\alpha \equiv \int_{-\infty}^{\infty}(\cdot)\frac{\rho_\alpha(x,t)}{N_\alpha(t)}\mathrm{d}x, \quad (18)$$

$$\mathcal{F}_\alpha(k,t) \equiv \frac{\tilde{\rho}_\alpha(k,t)\tilde{\rho}_\alpha(-k,0)}{N_\alpha(0)}. \quad (19)$$

The expression corresponding to Eq. (17) is then given by

$$\langle (x(t) - x_0)^n \rangle_\alpha = \frac{\mathrm{i}^n}{N_\alpha(t)}\frac{\partial^n}{\partial k^n}\mathcal{F}_\alpha(k,t)\Big|_{k=0}. \quad (20)$$

First we will discuss the behavior of the whole distribution $P(x,t)$. For simplicity, we will consider the initial condition $\boldsymbol{\rho}(x,0) = (0, \delta(x), 0)$ which is physically relevant, as it describes a cell initially settled in $x = 0$ in the process of reproducing. We do not focus on the case of an initially mobile cell, as the short-time behaviours of both the MD and MSD turn out to be simply linear and the long-time behaviours are identical to that of the initially settled cell case. We further remark that our analysis does not assume the condition $\mu = \lambda_s$ for a stable population in the linear growth model.

3.2.1 Full distribution

When $v_+ \neq v_-$, the MD is non-zero and we observe two different regimes: for short times it grows as t^2, while for long times it is proportional to t, as shown in Fig. 4a. The short-time expansion of the MD in fact yields

$$\begin{aligned}\langle x(t) - x_0 \rangle = \lambda_d v_d t^2 \\ -\frac{1}{3}\lambda_d v_d (2\mu + 4\lambda_d + \lambda_s) t^3 \\ +\mathcal{O}\left(t^4\right),\end{aligned} \tag{21}$$

where $v_d = (v_+ - v_-)/2$. The expression shows that both the transition rates and the running speeds have a role in determining this initial scaling regime. This can be interpreted as a composition of the doubling mechanism and the system acceleration given by cells suddenly starting to move. We can further define the typical crossover time $t_c^{(1)}$ as the ratio between absolute values of the coefficients of the t^2 and t^3 scalings, as this is the time at which the t^2 order contribution becomes smaller than the following ones [33,34]. This is a good estimate of the average time at which the dynamics is not dominated by the initial doubling anymore:

$$t_c^{(1)} = \frac{3}{2\mu + 4\lambda_d + \lambda_s}. \tag{22}$$

The long-time expansion of the MD yields

$$\langle x(t) - x_0 \rangle = \frac{4 v_d \lambda_d \lambda_s}{\Lambda(\mu - \lambda_d + \lambda_s + \Lambda)} t + \mathcal{O}\left(t^0\right), \tag{23}$$

where Λ is the same of Eq. (10).

As far as the MSD is concerned, in Fig. 4b we still see a t^2 regime for short times, while the long-time behavior depends on the difference between v_- and v_+. In the case they are the same, we will only see a diffusive long-time regime while otherwise this diffusive regime transitions into a ballistic one. The smaller the difference between the running speeds, the longer is the time to reach the ballistic regime. We further calculate the short-time expansion of the MSD:

$$\begin{aligned}\langle (x(t) - x_0)^2 \rangle = 2D\lambda_d t^2 \\ -\frac{2}{3}\lambda_d \left(D(2\mu + 4\lambda_d + \lambda_s) - v_a^2\right) t^3 \\ +\mathcal{O}\left(t^4\right),\end{aligned} \tag{24}$$

where $v_a = \sqrt{(v_+^2 + v_-^2)/2}$. Again, we define a crossing time $t_c^{(2)}$ for the MSD as the ratio between the absolute values of the coefficients of the t^2 and t^3 scalings:

$$t_c^{(2)} = \frac{3D}{|D(2\mu + 4\lambda_d + \lambda_s) - v_a^2|}. \tag{25}$$

If we change the population rates we observe that the growth or decay in the number of cells does not influence qualitatively the scalings we just described for both the MD and MSD. The formula for the long-time expansion of the MSD and the relative crossing time $t_l^{(2)}$ between the long-time regimes $\propto t$ and $\propto t^2$ are quite involved, so we refrain from showing them here. Finally, we study directly the full intermediate scattering function $\mathcal{F}(k,t)$ as it carries more information than the MSD and MD. In Fig. 5a, that is in the case of equal velocities, we can see that the real part of $\mathcal{F}(k,t)$ that generates the MSD among all other even moments, decays rapidly for small length scales (i.e. large k) while it has three distinct regimes for large length scales. At first the function decays or grows, following the growth in the number of cells, then at time $t_c^{(2)}$ it plateaus for a time that grows larger as k gets smaller, and finally decays completely. The plateau, starting after the transition of the cell to its moving stage at time $t_c^{(2)}$, is generated by the active cells going back to the settled stage and not moving anymore, while the final decay represents the long-time diffusive behavior that we have already seen in the MSD. In Fig. 5b we see how unequal velocities change the intermediate scattering function by introducing an oscillating behavior at long times. This is a signature of ballistic motion and of a non-vanishing imaginary part of $\mathcal{F}(k,t)$ that generates the odd moments like the MD.

3.2.2 Distribution of settled cells

The main feature of the MD and MSD of the settled cells is that they both show an initial t^3 regime, as shown in Fig. 6. The short time expansion of the MD is given by

$$\begin{aligned}\langle x(t) - x_0 \rangle_0 = \frac{1}{3}\lambda_s \lambda_d v_d t^3 \\ -\frac{1}{6}\lambda_s \lambda_d v_d (\mu - \lambda_d + \lambda_s) t^4 \\ +\mathcal{O}\left(t^5\right),\end{aligned} \tag{26}$$

with the crossing time between the t^3 and t^4 regimes $t_{c,0}^{(1)}$ being:

$$t_{c,0}^{(1)} = \frac{2}{|\mu - \lambda_d + \lambda_s|}. \tag{27}$$

The MSD shows the initial t^3 regime as well:

$$\begin{aligned}\langle (x(t) - x_0)^2 \rangle_0 = \frac{2}{3} D \lambda_s \lambda_d t^3 \\ -\frac{1}{6}\lambda_s \lambda_d \left(2D(\mu - \lambda_d + \lambda_s) - v_a^2\right) t^4 \\ +\mathcal{O}\left(t^5\right).\end{aligned} \tag{28}$$

with the crossing time $t_{c,0}^{(2)}$:

$$t_{c,0}^{(2)} = \frac{4D}{|2D(\mu - \lambda_d + \lambda_s) - v_a^2|}. \tag{29}$$

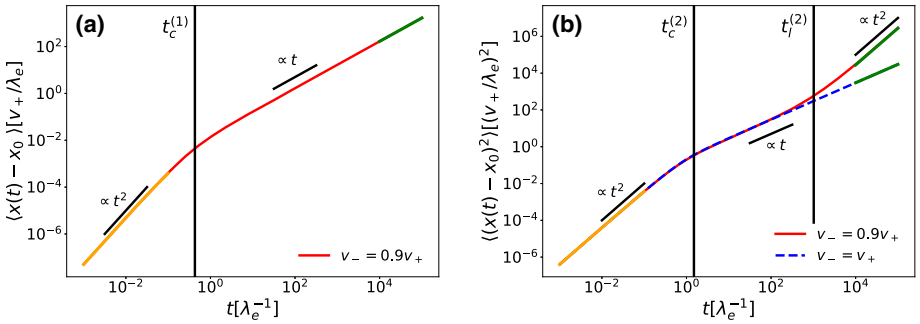

Fig. 4 **a** Mean displacement (MD), **b** mean-squared displacement (MSD), respective crossing times $t_c^{(1)}$, $t_c^{(2)}$ and short- and long-time approximations for the initial conditions $\boldsymbol{\rho}(x,0) = (0, \delta(x), 0)\lambda_e/v_+$, all rates equal to λ_e and $D = 0.2v_+^2/\lambda_e$. In (**b**) the solid red line shows unequal swim velocities ($v_- = 0.9v_+$) and the dashed blue line equal swim speeds ($v_- = v_+$). The orange lines represent the short-time approximations, while the green lines are the long-time approximations

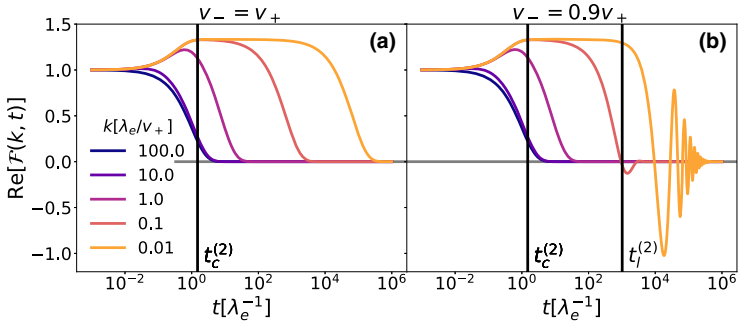

Fig. 5 Real part of the intermediate scattering function $\mathcal{F}(k,t)$ for **a** equal swimming speeds and **b** unequal swimming speeds ($v_- = 0.9v_+$) for the initial conditions $\boldsymbol{\rho}(x,0) = (0, \delta(x), 0))\lambda_e/v_+$, all rates equal to λ_e and $D = 0.2v_+^2/\lambda_e$. The black lines represent the MSD short crossing time $t_c^{(2)}$ and, in the case of different speeds, long crossing time $t_l^{(2)}$

The reason why we observe the t^3-behaviour for short times is the fact that the settled population can only change by doubling, moving and then settling, with each one of these processes being at least of order t. We also notice that for $D = 0$ the MSD grows initially with t^4, as in this case the short time MSD for moving cells grows with t^2 and not t.
The long-time asymptotes for both MD and MSD of the settled particles are identical to those of the whole population.

4 Interacting cells

4.1 Attraction to settled regions

We now discuss the case of interacting cells. Our model contains an effective attractive force that pushes the moving cells towards the regions where the density of settled cells is larger. This force is meant to represent how bacteria tend to assemble in resource-rich regions to reproduce or how they accumulate in order to form biofilms [35,36]; therefore the parameter $\kappa > 0$ in Eq. (1). The interaction terms $\kappa\partial_x(\partial_x(\rho_0)\rho_\pm)$ render the equation nonlinear such that it is not analytically solvable. Instead we first perform a linear stability analysis around the homogeneous stationary solution to the linear system $\hat{\boldsymbol{\rho}}$ computed in Eq. (12) (see also Fig. 3) by adding a small perturbation $\delta\boldsymbol{\rho}(x,t)$ and neglecting the nonlinear terms in the perturbation $(\delta\boldsymbol{\rho}(x,t))^2$. We then arrive at the following system of equations for the perturbation:

$$\begin{aligned}
\partial_t\delta\rho_+ &= -v_+\partial_x\delta\rho_+ - \kappa\partial_x^2(\delta\rho_0)\hat{\rho}_+ + D\partial_x^2\delta\rho_+ \\
&\quad - (\lambda_s + \lambda_e + \mu)\delta\rho_+ + \lambda_e\delta\rho_- + \lambda_d\delta\rho_0 \\
\partial_t\delta\rho_0 &= -\lambda_d\delta\rho_0 + \lambda_s(\delta\rho_+ + \delta\rho_-) \\
\partial_t\delta\rho_- &= v_-\partial_x\delta\rho_- - \kappa\partial_x^2(\delta\rho_0)\hat{\rho}_- + D\partial_x^2\delta\rho_- \\
&\quad - (\lambda_s + \lambda_e + \mu)\delta\rho_- + \lambda_e\delta\rho_+ + \lambda_d\delta\rho_0,
\end{aligned} \tag{30}$$

where the stationary values for the density are symmetric, $\hat{\rho}_+ = \hat{\rho}_-$. We apply both a Fourier transform in space and a Laplace transform in time to Eq. (30) and solve the resulting characteristic equation of the system. We obtain three different solutions for the eigenvalues of the system $s_i(k)$, of which only one, $s_1(k)$, can have

Eur. Phys. J. E (2022) 45:83

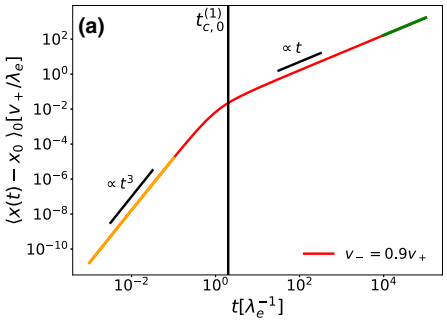

Fig. 6 **a** Mean displacement (MD), **b** mean-square-displacement (MSD), respective crossing times $t_c^{(1)}$, $t_c^{(2)}$ and short- and long-time approximations for settled cells, with initial conditions $\boldsymbol{\rho}(x,0) = (0, \delta(x), 0))\lambda_e/v_+$, all rates equal to λ_e and $D = 0.2v_+^2/\lambda_e$. In (**b**) the solid red line shows unequal swim velocities ($v_- = 0.9v_+$) and the dashed blue line equal swim speeds ($v_- = v_+$). The orange lines represent the short-time approximations, while the green lines are the long-time approximations

a positive real part. In the following we focus on $s_1(k)$, since its positive real part introduces instabilities in the system.

First of all, for $k \to 0$, the value of $s_1(k)$ is one of the eigenvalues of the system matrix where the initial densities are constant, and more specifically the one that can be positive:

$$s_1(0) = \mathcal{E}_3 \simeq \frac{\lambda_d(\lambda_s - \mu)}{\mu + \lambda_d + \lambda_s}. \tag{31}$$

This means that one of the conditions for the system to be stable is that the number of cells does not grow exponentially, which is expected.

The second limit we consider is $k \to \infty$. We have that

$$\lim_{k\to\infty} s_1(k) \to \frac{2\kappa\hat{\rho}_+\lambda_s}{D} - \lambda_d. \tag{32}$$

This second condition states that the diffusion constant contrasts directly the instabilities generated by a large settling rate and the attractive constant κ, as it disperses too large clusters of active cells, while a large doubling rate helps the stability by reducing the size of groups of settled cells. Knowing the limits of $s_1(k)$ in $k = 0$ and $k = \infty$, i.e long- and short-range perturbations respectively, we are sure that the system will be unstable if the real part of either of them is larger than zero, giving us two stability conditions for the system:

$$\begin{aligned} \mu &\geq \lambda_s, \\ \lambda_d &\geq \frac{2\kappa\hat{\rho}_+\lambda_s}{D}. \end{aligned} \tag{33}$$

For $D = 0$, $s_1(k)$ grows asymptotically like k, making the system always unstable. In Fig. 7 we show the behavior of the eigenvalue $\mathrm{Re}(s_1(k))$ for different values of D. Notice that for the set of parameters considered,

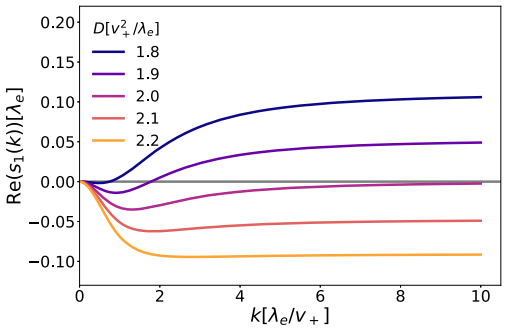

Fig. 7 Eigenvalue $s_1(k)$ as a function of wavenumber k for different values of D, where all rates are equal to λ_e, $v_- = v_+$ and $\kappa = \lambda_e^{-1}$

if $D = 2v_+^2/\lambda_e$ the stability conditions are only narrowly fulfilled, but the real part of s_1 stays negative for all the values of k. Lastly, when the cell running speeds are not isotropic, the imaginary part of s_1 can be non-zero, meaning that there can be stable periodicity in the system.

While the real part of the other two solutions s_2 and s_3 is always negative, their imaginary part is non-zero for large values of k. More specifically, for large k and finite D their imaginary part is proportional to k, while the real part goes with $-Dk^2$. A finite imaginary part indicates oscillations in the system, although the negative real part means that these oscillations are only transient. Signatures of these oscillations can also be seen in our numerical solutions (see the next Section).

4.2 Repulsion among settled cells

We now include a self-repulsive potential for the cells that do not move, given by $\kappa_0 > 0$ in the matrix $\mathcal{U}$ in

Eq. 1. This repulsion models the need for settled bacteria to not overcrowd any particular region and deplete its resources while reproducing. What is particularly interesting about having both an attractive and a repulsive part in the potential is that the interplay of these two opposing effects can lead to structures forming in the system, as we will show now. If we repeat the analysis described in the last subsection including $\kappa_0 > 0$, we find that the limits of $s_1(k)$ are

$$\begin{aligned} s_1(0) &= \mathcal{E}_3 \\ s_1(k \to \infty) &= -\kappa_0 \hat{\rho}_0 k^2 + \mathcal{O}(k). \end{aligned} \tag{34}$$

The main difference with Eqs. (31), (32) is that s_1 will always be negative for a sufficiently large value of k. This means that if we choose parameters for which s_1 can be positive, its largest root k_r will indicate the smallest allowed instability of the system, with size $l = 2\pi/k_r$. We consequently expect instabilities to form for systems of size L larger than l. As an example of this we numerically calculated the values of k_r for different values of the running speeds v_+ and v_-, quantifying their occurrence using two non-dimensional parameters, the maximum speed v_m and the reduced difference speed v_r defined by

$$v_\mathrm{m} \equiv \frac{\max(v_+, v_-)}{\sqrt{D\lambda_e}} \qquad v_\mathrm{r} \equiv \frac{v_+ - v_-}{v_+ + v_-}. \tag{35}$$

We chose specifically to vary the running speeds as they can easily tune the asymmetry of the system, leading to interesting instabilities. In Fig. 8 we can see k_r as a function of v_r and v_m, written in units of $k_0 = 2\pi/L$. We expect the system to develop instabilities for values of $k_r > k_0$, so we fitted the separatrix $k_r = k_0$ to a second-order polynomial, $v_\mathrm{m}^f(v_\mathrm{r})$:

$$v_\mathrm{m}^f = 2.76 \pm 0.01 + (2.73 \pm 0.03) v_\mathrm{r} - (1.14 \pm 0.04) v_\mathrm{r}^2. \tag{36}$$

This particular fit was determined using the linear growth model for the parameter values indicated in the caption to Fig. 8.

In order to study the emergence of such instabilities in detail, we further implemented a numerical solver for both Eqs. (1) and (6), using an explicit fourth-order Runge–Kutta algorithm [37] for the time integration and a finite difference scheme in space. We performed calculations both with the linear and the nonlinear growth model, setting respectively $\lambda_s = \mu$ and $\lambda_s \geq \mu$. We use a finite box of length L with periodic boundary conditions. Setting the time step to $\Delta t = 10^{-4}\lambda_e^{-1}$ we calculated $\sim 10^6$ steps to ensure that the system settles into a steady state. Our calculations are initialized using the steady-state solutions of the linear system (Eqs. (12)), to which we add small fluctuations given by Gaussian noise. We find that our system develops wave-like structures, which are static for $v_+ = v_-$ and become traveling waves when $v_+ \neq v_-$ - see Fig. 9 for the linear

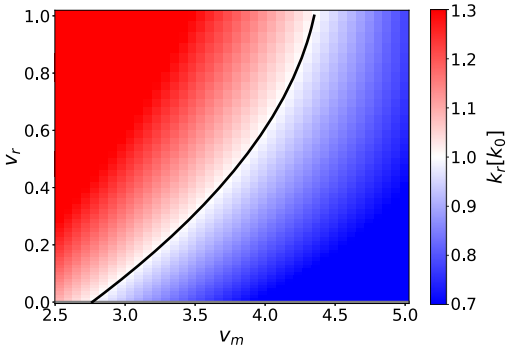

Fig. 8 Largest root of $s_1(k)$, k_r, as function of v_r and v_m. As parameters we chose $\lambda_s = \lambda_d = \mu = 0.1\lambda_e$, $\kappa = 0.2\lambda_e^{-1}$, $\kappa_0 = 0.05\lambda_e^{-1}$ and $D = 0.001L^2\lambda_e$. In blue we see the parameters for which the system is not large enough to enable instabilities, while in black we have the second order polynomial that fits the $k_r = k_0$ curve

growth case and Fig. 11 for the nonlinear case. Testing different initial conditions, e.g. choosing $\rho_0(x)$ as a narrow Gaussian peak that approximates an initially settled single cell, we also observed that these wave-like structures always form, even if the specific shape of the wave can be affected. In our analysis we preferred to use the steady-state solution of Eqs. (12) as initial condition, as it makes comparison with the theoretical results of Fig. 8 more straightforward. Intuitively, the attractive term κ leads to the formation of peaks, induced by the instability in Eq. (33). These peaks are then stabilized by the repulsive term κ_0. The asymmetry of the running speeds makes the peaks move.

Migrating bands of bacteria have indeed been observed experimentally [38–43] and have also been modeled theoretically [29,44,45], always considering only one species of cells. A particularly surprising feature of our model is that in this final stationary state all three distributions evolve in the same direction at the same speed, independently of the intrinsic running speed of the cells.

We replicated the diagram of Fig. 8 with numerical integration of the model equation, and the resulting non-equilibrium state diagram is shown in Fig. 10. We find a clear transition from a stable system (shown in blue), where all species are constant in space, to the appearance of wave-like structures (shown in red to yellow). The gradient visualizes the change in stationary speed of the waves v_s, defined as the speed of the waves in the stationary state divided by $\sqrt{D\lambda_e}$, and is hence non-dimensional. This quantity is almost vanishing near the transition, and grows the further away we move from it. The formation of these waves is typical of systems with a large difference between v_+ and v_- or rather small absolute speeds. We fitted the separatrix to a second order polynomial $v_\mathrm{m}^f(v_\mathrm{r})$ and obtained

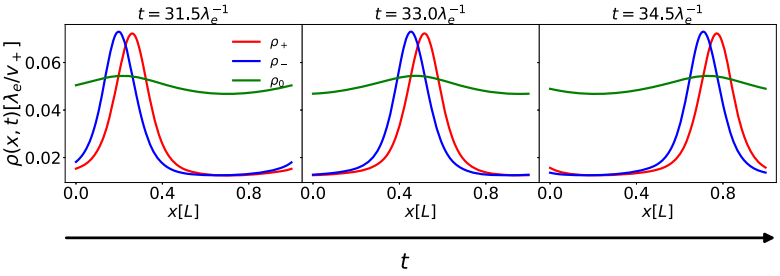

Fig. 9 Density of left ρ_-, right ρ_+ and sedentary ρ_0 cells as functions of space at different times (increasing from (**a**) to (**c**)). We set here $\lambda_s = \lambda_d = \mu = .1\lambda_e$, $\kappa = .2\lambda_e^{-1}$, $\kappa_0 = .05\lambda_e^{-1}$, $v_+ = 2v_- = .1L\lambda_e$ and $D = 0.001L^2\lambda_e$

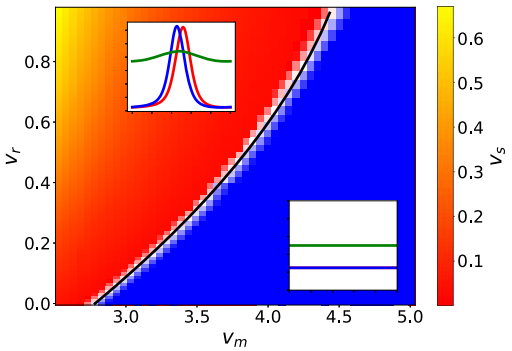

Fig. 10 State diagram of the system as a function of v_r and v_m. As parameters we chose $\lambda_s = \lambda_d = \mu = 0.1\lambda_e$, $\kappa = 0.2\lambda_e^{-1}$, $\kappa_0 = 0.05\lambda_e^{-1}$ and $D = 0.001L^2\lambda_e$. In blue we see the parameters for which the system is stably constant, while in red to yellow we see the parameters for which the system generates traveling wave structures. Examples of both long-time behaviors are shown in their respective area. The gradient shows the stationary velocity of the waves v_s, while in black we have the second order polynomial that fits the transition curve v_m^f

$$v_\mathrm{m}^f = 2.78 \pm 0.01 + (2.56 \pm 0.03)v_\mathrm{r} - (0.88 \pm 0.03)v_\mathrm{r}^2. \tag{37}$$

We find that our numerical calculations and theory are in very good qualitative agreement.

4.3 Application to Caulobacter crescentus

Table 1 gives an idea of the experimentally measured values for *CC* which have been extracted from recent papers on its swimming behaviour [46–49]. It is noteworthy to comment on the running speeds v_+, v_-. While the torque generated by the flagellar motor differs significantly during forward and backward motion, the resulting velocities are not dramatically different (and, in fact, experimentally hard to measure) [49]. We have performed calculations with the parameters of Table 1 for different values of κ and κ_0 which are undetermined from experiments. Since for *Caulobacter* $\mu < \lambda_s$, we have included the saturating nonlinearity for the growth in the model. The results show that the waves still form provided the ratio κ/κ_0 is large enough (Fig. 11).

Table 1 Values of the parameters for *Caulobacter crescentus* taken from [46–49]

Run-and-tumbling rate (s^{-1})	λ_e	10^{-1}
Settling rate (s^{-1})	λ_s	10^{-5}
Doubling rate (s^{-1})	λ_d	10^{-4}
Decay rate (s^{-1})	μ	10^{-6}
Running speed right (m/s)	v_+	4×10^{-5}
Running speed left (m/s)	v_-	3.5×10^{-5}
Diffusion coefficient (m^2/s)	D	2×10^{-9}

5 Conclusions and outlook

In this work we proposed and studied a 1D 3-state model motivated by the cell cycle progression of the bacterium *Caulobacter crescentus*, including both its run and tumble motion and its reproductive behavior. We first analyzed the free cell space-independent case and calculate the parameter regimes for which the number of cells grows or declines. Adding the spatial dependence we subsequently determined dynamical quantities of the system such as the mean displacement, the mean-squared displacement and the intermediate scattering function. We found a surprising super-ballistic behavior of the MSD at short times with a t^3 scaling which stems from the interplay of cells doubling and cells starting to swim.

Subsequently, we included attractive and repulsive interactions between cells into our model, representing their tendency to swim towards regions in which cells are settled and to avoid overcrowding. We determined the stability conditions and, using numerical methods, we studied the fully nonlinear system in which we identify traveling waves of cells. Their occurrence is quantified in a non-equilibrium state diagram.

Our model lends itself to further extensions in several ways. E.g., one could account for complex nutrient landscapes and for a more detailed description of the cell cycle, which is well-studied from various aspects [27]; another possible system for application are *Chlamydomonas reinhartii* cells [28]. The cell cycle can be

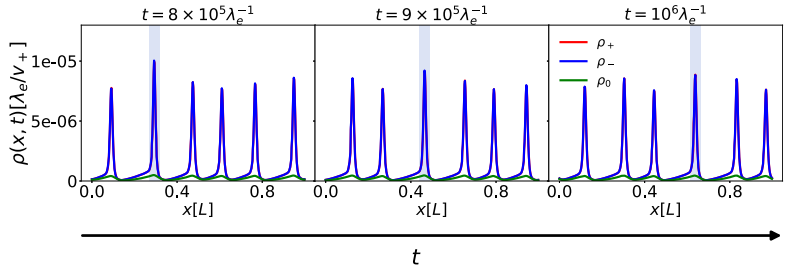

Fig. 11 Nonlinear growth model, density of left ρ_-, right ρ_+ and sedentary ρ_0 cells as functions of space at different times (increasing from (**a**) to (**c**)). Because of the large value of λ_e compared to the other rate parameters, the right-moving and left-moving populations have almost the same shape, making the red line disappear under the blue line. The shaded areas indicate the largest peak, and how it moves in time towards the right. We chose as parameters the values typical of *CC* shown in Table 1. For the interaction potentials, for which no experimental estimates can be made at present, we chose $\kappa = \kappa_0 = 10\lambda_e^{-1}$, while for the carrying capacity of the system we set $\boldsymbol{\rho}_c(x,t) = (0.04, 0.04, 0.04)\lambda_e/v_+$

included in cell-resolved simulations such as performed recently in [50,51]. Another direction could be a two-dimensional field description that includes the nematic ordering of cells such as in [52]. In a higher-dimensional model it would also be interesting to see what the effect of different swimming strategies such as run and tumble, run-reverse or run-reverse-flick [30] is. Finally, an exploration of the fully nonlinear model—nonlinear diffusive interactions as well as nonlinear growth—including a full higher-dimensional tumbling behaviour for a multi-species system would be an interesting problem in the context of biofilm growth.

Acknowledgements DB is supported by the EU MSCA-ITN ActiveMatter, (proposal No. 812780). RB is grateful to HL for the invitation to a stay at the Heinrich-Heine-University in Düsseldorf where this work was performed. HL was supported by the DFG Project LO 418/25-1 of the SPP 2265. The authors thank the referees for the constructive criticism of their work.

Funding Open Access funding enabled and organized by Projekt DEAL.

Author contribution statement

HL and RB directed the project. DB performed analytic calculations and numerical simulations. All authors discussed the results and wrote the manuscript.

Data availability The datasets generated during and/or analysed during the current study are available from the corresponding author on reasonable request.

Appendix

Relation between intermediate scattering function and momenta of the density in 1D

We show here the calculation that justifies Eq. (17) in one dimension in the case where the initial conditions for the cell density are $\boldsymbol{\rho}(x, t=0) = (0, N(0)\delta(x), 0)$. First, we write the definition for the moments $\langle (x(t) - x_0)^n \rangle = \langle x^n(t) \rangle$:

$$\langle x^n(t) \rangle = \int_{-\infty}^{\infty} \mathrm{d}x\, x^n P(x,t), \tag{38}$$

where $P(x,t)$ is the probability density of the position. We then apply a Fourier transform and its inverse in the integral

$$\langle x^n(t) \rangle = \frac{1}{2\pi} \int_{-\infty}^{\infty} \mathrm{d}x \int_{-\infty}^{\infty} \mathrm{d}k\, \mathrm{e}^{ikx} \left(\mathrm{i}^n \frac{\partial^n \tilde{P}(k,t)}{\partial k^n} \right), \tag{39}$$

where $\tilde{P}(k,t)$ is the Fourier Transform of $P(x,t)$. Finally, we exchange the order of integration to get

$$\begin{aligned} \langle x^n(t) \rangle &= \frac{1}{2\pi} \int_{-\infty}^{\infty} \mathrm{d}k\, 2\pi\delta(k) \left(\mathrm{i}^n \frac{\partial^n \tilde{P}(k,t)}{\partial k^n} \right) \\ &= \mathrm{i}^n \frac{\partial^n \tilde{P}(k,t)}{\partial k^n} \bigg|_{k=0}. \end{aligned} \tag{40}$$

Knowing that for the initial conditions that we have chosen $\tilde{\boldsymbol{\rho}}(-k,0) = (0, N(0), 0)$, we have

$$\mathcal{F}(k,t) \equiv \tilde{P}(k,t)\tilde{P}(-k,0)N(t) = \tilde{P}(k,t)N(t), \quad (41)$$

and hence

$$\langle x^n(t)\rangle = \mathrm{i}^n \frac{\partial^n \tilde{P}(k,t)}{\partial k^n}\bigg|_{k=0} = \frac{\mathrm{i}^n}{N(t)} \frac{\partial^n \mathcal{F}(k,t)}{\partial k^n}\bigg|_{k=0}. \quad (42)$$

References

1. H.C. Berg (ed.) *E. coli in Motion Biological and Medical Physics, Biomedical Engineering* (Springer, New York, 2004). ISBN 978-0-387-00888-2 978-0-387-21638-6
2. H. C. Berg, *Random Walks in Biology: New and Expanded Edition* (Princeton University Press, 2018). ISBN 978-1-4008-2002-3
3. J. Elgeti, R.G. Winkler, G. Gompper, Rep. Prog. Phys. **78**, 056601 (2015)
4. M. Polin, I. Tuval, K. Drescher, J.P. Gollub, R.E. Goldstein, Science **325**, 487–490 (2009)
5. F. Detcheverry, Phys. Rev. E **96**, 012415 (2017)
6. G. Fier, D. Hansmann, R.C. Buceta, Soft Matter **14**, 3945–3954 (2018)
7. T. Bertrand, P. Illien, O. Bénichou, R. Voituriez, New J. Phys. **20**, 113045 (2018)
8. C. Maes, K. Meerts, W. Struyve, Physica A Stat. Mech. Appl. 127323 (2022)
9. L. Angelani, J. Phys. A Math. Theor. **50**, 325601 (2017)
10. L. Angelani, R. Garra, Phys. Rev. E **100**, 052147 (2019)
11. A. Dhar, A. Kundu, S.N. Majumdar, S. Sabhapandit, G. Schehr, Phys. Rev. E **99**, 032132 (2019)
12. P. Singh, A. Kundu, Phys. Rev. E **103**, 042119 (2021)
13. C. Monthus, J. Stat. Mech. Theory Exp. **2021**, 083212 (2021)
14. D. Frydel, J. Stat. Mech. Theory Exp. **2021**, 083220 (2021)
15. R. Dandekar, S. Chakraborti, R. Rajesh, Phys. Rev. E **102**, 062111 (2020)
16. P. Singh, S. Sabhapandit, A. Kundu, J. Stat. Mech. Theory Exp. **2020**, 083207 (2020)
17. P. Le Doussal, S.N. Majumdar, G. Schehr, Phys. Rev. E **104**, 044103 (2021)
18. C.M. Barriuso Gutiérrez, C. Vanhille-Campos, F. Alarcón, I. Pagonabarraga, R. Brito, C. Valeriani, Soft Matter **17**, 10479–10491 (2021)
19. F. Mori, G. Gradenigo, S.N. Majumdar, J. Stat. Mech. Theory Exp. **2021**, 103208 (2021)
20. D. Frydel, Phys. Rev. E **105**, 034113 (2022)
21. R. Garcia-Millan, G. Pruessner, J. Stat. Mech. Theory Exp. **2021**, 063203 (2021)
22. Z. Zhang, G. Pruessner, J. Phys. A Math. Theor. **55**, 045204 (2022)
23. U. Basu, S.N. Majumdar, A. Rosso, S. Sabhapandit, G. Schehr, J. Phys. A Math. Theor. **53**, 09LT01 (2020)
24. P. Grange, X. Yao, J. Phys. A Math. Theor. **54**, 325007 (2021)
25. D. Frydel, Phys. Fluids **34**, 027111 (2022)
26. C.W. Shebelut, J.M. Guberman, S. van Teeffelen, A.A. Yakhnina, Z. Gitai, Proc. Natl. Acad. Sci. **107**, 14194–14198 (2010)
27. E. Biondi (ed.) *Cell Cycle Regulation and Development in Alphaproteobacteria* (Springer, Cham, 2022). ISBN 978-3-030-90620-7 978-3-030-90621-4
28. E. Harris, D. Stern, G. Witman, *The Chlamydomonas Sourcebook*, vol. 1 (2009)
29. A.V. Narla, J. Cremer, T. Hwa, Proc. Natl. Acad. Sci. **118**, e2105138118 (2021)
30. M. Grognot, K.M. Taute, Curr. Opin. Microbiol. **61**, 73–81 (2021)
31. K. Son, J.S. Guasto, R. Stocker, Nat. Phys. **9**, 494–498 (2013)
32. C. Kurzthaler, S. Leitmann, T. Franosch, Sci. Rep. **6**, 36702 (2016)
33. D. Breoni, M. Schmiedeberg, H. Löwen, Phys. Rev. E **102**, 062604 (2020)
34. D. Breoni, H. Löwen, R. Blossey, Phys. Rev. E **103**, 052602 (2021)
35. L. Hall-Stoodley, J.W. Costerton, P. Stoodley, Nat. Rev. Microbiol. **2**, 95–108 (2004)
36. M.G. Mazza, J. Phys. D Appl. Phys. **49**, 203001 (2016)
37. W.H. Press, S.A. Teukolsky, W.T. Vetterling, B.P. Flannery, *Numerical Recipes 3rd Edition: The Art of Scientific Computing* (Cambridge University Press, 2007). ISBN 978-0-521-88068-8
38. J. Adler, Science (New York, N.Y.) **153**, 708–716 (1966)
39. J. Adler, J. Bacteriol. **92**, 121–129 (1966)
40. J. Adler, Science **166**, 1588–1597 (1969)
41. J.E. Berleman, T. Chumley, P. Cheung, J.R. Kirby, J. Bacteriol. **188**, 5888–5895 (2006)
42. L. Stricker, I. Guido, T. Breithaupt, M.G. Mazza, J. Vollmer, J. R. Soc. Interface **17**, 20200559 (2020)
43. S. Liu, S. Shankar, M.C. Marchetti, Y. Wu, Nature **590**, 80–84 (2021)
44. J. Cremer, T. Honda, Y. Tang, J. Wong-Ng, M. Vergassola, T. Hwa, Nature **575**, 658–663 (2019)
45. L. Caprini, C. Maggi, U. Marini Bettolo Marconi, J. Chem. Phys. **154**, 244901 (2021)
46. G. Li, J.X. Tang, Biophys. J . **91**, 2726–2734 (2006)
47. Y. Lin, S. Crosson, N.F. Scherer, Mol. Syst. Biol. **6**, 445 (2010)
48. B. Liu, M. Gulino, M. Morse, J.X. Tang, T.R. Powers, K.S. Breuer, Proc. Natl. Acad. Sci. **111**, 11252–11256 (2014)
49. P.P. Lele, T. Roland, A. Shrivastava, Y. Chen, H.C. Berg, Nat. Phys. **12**, 175–178 (2016)
50. Z. You, D.J. Pearce, A. Sengupta, L. Giomi, Phys. Rev. X **8**, 031065 (2018)
51. F. J. Schwarzendahl, D. A. Beller. (2022) arXiv:2205.05185 [cond-mat, q-bio]
52. D. Dell'Arciprete, M.L. Blow, A.T. Brown, F.D.C. Farrell, J.S. Lintuvuori, A.F. McVey, D. Marenduzzo, W.C.K. Poon, Nat. Commun. **9**, 4190 (2018)

P5 Patchy landscapes promote stability of small groups

Reproduced from

G. Jacucci D. Breoni, S. Heijnen J. Palomo P. Jones H. Löwen G. Volpe S. Gigan *Patchy landscapes promote stability of small groups*, arXiv:2310.01620 [cond-mat.soft] (2023),

Digital Object Identifier (DOI): `https://doi.org/10.48550/arXiv.2310.01620`

Statement of contribution

Author contributions are defined based on the CRediT (Contributor Roles Taxonomy) and listed alphabetically. Conceptualization: SG, GJ, HL, GV. Data curation: DB, GJ. Formal analysis: DB, GJ. Resources: SG, SH, PJ, HL, JP, GV. Writing: GJ wrote the manuscript with the help of all authors. Funding acquisition: SG, GJ, HL, GV.

Patchy landscapes promote stability of small groups

Gianni Jacucci[a,*], Davide Breoni[b], Sandrine Heijnen[c], José Palomo[d], Philip Jones[e], Hartmut Löwen[b], Giorgio Volpe[c], and Sylvain Gigan[a]

[a]Laboratoire Kastler Brossel, Sorbonne Université, Ecole Normale Supérieure-Paris Sciences et Lettres (PSL) Research University, Centre National de la Recherche Scientifique (CNRS) UMR 8552, Collège de France, 24 rue Lhomond, 75005 Paris, France
[b]Institut für Theoretische Physik II—Weiche Materie, Heinrich-Heine-Universität Düsseldorf, Universitätsstraße 1, D-40225 Düsseldorf, Germany
[c]Department of Chemistry, University College London, 20 Gordon Street, London WC1H 0AJ, United Kingdom
[d]Laboratoire de Physique de l'Ecole Normale Supérieure, ENS, Université PSL, CNRS, Sorbonne Université, Université Paris Cité, F-75005 Paris, France
[e]Department of Physics & Astronomy, University College London, Gower Street, London WC1E 6BT, United Kingdom
[*]To whom correspondence should be addressed. E-mail: giovanni.iacucci@lkb.ens.fr

ABSTRACT

Group formation and coordination are fundamental characteristics of living systems, essential for performing tasks and ensuring survival. Interactions between individuals play a key role in group formation, and the impact of resource distributions is a vibrant area of research. Using active particles in a tuneable optical environment as a model system, we demonstrate that heterogeneous energy source distributions result in smaller, more stable groups with reduced individual exchange between clusters compared to homogeneous conditions. Reduced group sizes can be beneficial to optimise resources in heterogeneous environments and to control information flow within populations. Devoid of biological complications, our system provides insights into the importance of patchy landscapes in ecological dynamics and holds implications for refining swarm intelligence algorithms and enhancing crowd control techniques.

Introduction

Group living is widespread across different levels of biological organisation[1] and confers many advantages to individuals, such as increased survival from predators[2–4], enhanced foraging efficiency[5–7], or improved communication and decision making[8–10]. The formation, maintenance, and disbanding of groups depend not only on the interactions among individuals but also on the characteristics of the surrounding environment, such as spatial or temporal heterogeneity[11]. For instance, while large group sizes are advantageous for foraging in homogeneous environments, the presence of a patchy landscape of resources compels individuals to adopt smaller group formations as an adaptive strategy to ensure sufficient resources for all members[12–15]. However, the challenge of simultaneously monitoring multiple individuals in natural ecosystems poses limits to our understanding of the dynamics of such groups, particularly regarding their durability and time stability[16,17].

Recently, active colloids have emerged as a useful tool for studying collective behaviour in living systems[18,19]. These artificial systems, unlike natural ones[20–23], have the advantage of evolving on short timescales. Moreover, they are tuneable, and their small sizes make data acquisition more convenient. Previous studies have investigated the role of individual interactions in group formation, such as those due to attraction[24–26], repulsion[27], alignment[28,29], reorientation[30,31], or vision[32,33] and communication[34,35]. The role of physical features in the environment has also been explored, such as the presence of obstacles[36–41] or of a disordered potential[42]. However, the impact that a heterogeneous distribution of energy sources has on collective phenomena is not clear yet. Indeed, while work exists that studied the impact of linear gradients in the energy source[43–45], natural landscapes of resources hardly follow linear gradients and the impact of patchiness on group dynamics is largely unknown.

Here, we use phototactic active colloids moving in a spatially complex distribution of resources, generated optically, to investigate the role of patchy landscapes in the dynamics of group formation and cohesion. Our results demonstrate that patchiness restricts the size of groups and increases their stability by decreasing the exchange of individuals compared to a homogeneous landscape.

Results

As phototactic active particles, we used monodispersed silica colloids (diameter $d = 4.77 \pm 0.20\,\mu\text{m}$) with a 90 nm carbon half-coating (Methods). These particles self-propel in a water-2,6-lutidine critical mixture when exposed to light. The propulsion arises from the critical mixture's local demixing, induced by the carbon heating upon light absorption.[27,43–48].

We created an energy source landscape with controllable spatial heterogeneity by shining a laser on an optical diffuser, generating a diffraction pattern of randomly distributed light

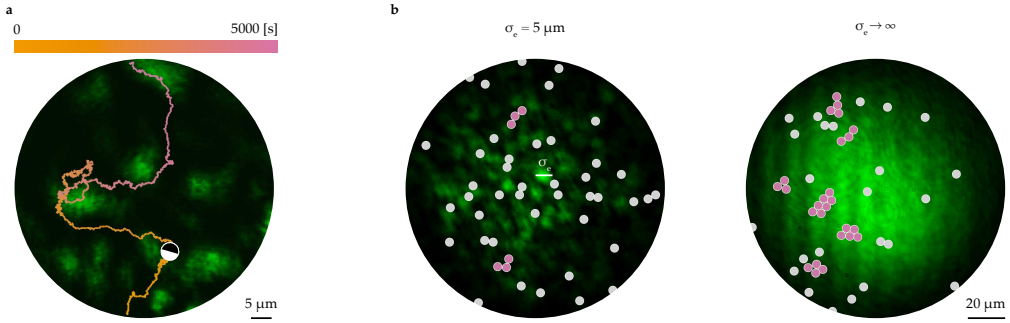

Figure 1. Active particles in complex energy landscapes. a) Trajectory of an active particle in a spatially complex distribution of energy, with high light intensities in green. The particle self-propels, avoiding the most intense illumination. The trajectory displays the particle's centre position over 45 minutes. **b)** As the particles prefer to stay in the dark areas, the group (defined as comprising more than two individuals) size appears to be determined by the spatial characteristics of the environment—σ_e, i.e. the average size of the energy patches. The particles belonging to a group are coloured in pink while the isolated particles and the particles in pairs are in grey.

patches, whose intensity follows a negative exponential probability distribution[49,50]. The energy density of the landscape and the typical size of its patches (σ_e) can be precisely controlled by optical means—Figure S1 and Methods for details. σ_e is defined as the full width at half maximum of the landscape's autocorrelation. Figure 1a shows a typical example of a particle trajectory in a complex illumination. What can be qualitatively observed is that an active particle tends to navigate in the energy landscape by spending most of its time in the low-illumination areas—in other words, it performs negative phototaxis. This property of the individual trajectories has a direct consequence on group formation, with a group being defined as a collection of more than two particles in contact. As shown in Figure 1b, in a heterogeneous energy landscape ($\sigma_e \simeq d = 5\,\mu m$), active particles tend to form smaller groups compared to the case of a homogeneous illumination ($\sigma_e \to \infty$). Under both illumination conditions, the average local energy density ($I = 0.1\,\mu W\mu m^{-2}$) was kept the same by matching the incoming power and envelope size Figure S2.

In order to explain the phenomena illustrated in Figure 1, we first need to better understand the statistics of the dynamics of the individual particles on the underlying energy landscape. Figure 2a shows quantitatively that particles perform negative phototaxis. By comparing the light intensity at locations visited by the particles along their trajectories with the overall energy landscape, we can observe that particles tend to avoid the most intense light regions. Delving deeper, Figure 2b shows that as active particles navigate the darker, low-energy channels of the light landscape, they tend to align perpendicular to the light intensity gradient. This is due to their continuous interactions with the two-dimensional gradient, channelling their trajectories between high-energy patches and causing them to move perpendicular to the gradient—i.e.

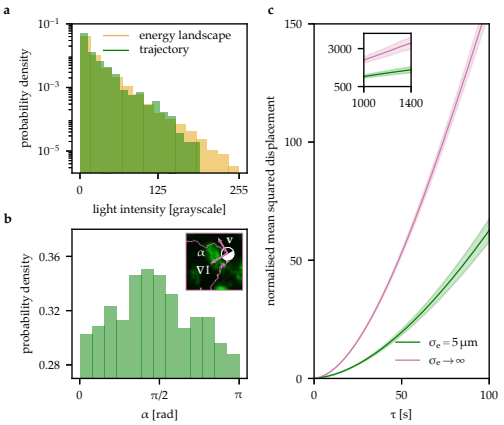

Figure 2. Statistics of single particle trajectories on the energy landscape. A complex energy landscape ($\sigma_e = 5\,\mu m$) affects the spatial occupancy and statistical features of particle trajectories. **a)** Histogram comparing the distribution of the light intensity in the locations visited by the particles with the intensity distribution of the energy landscape. **b)** Particles tend to move perpendicular to the gradient of the illumination ($\alpha = \pi/2$). α, illustrated in the inset, is the angle between the velocity of the particle ($\mathbf{v}$) and the intensity gradient (∇I). **c)** A lower mean squared displacement reflects avoidance of high-energy areas compared to a more homogeneous environment (Gaussian illumination, $\sigma_e \to \infty$). The inset shows the long-time diffusive behaviour. Shaded areas indicate standard deviations on the mean squared displacement. Data was obtained from averaging at least 20 trajectories, each lasting 45 minutes.

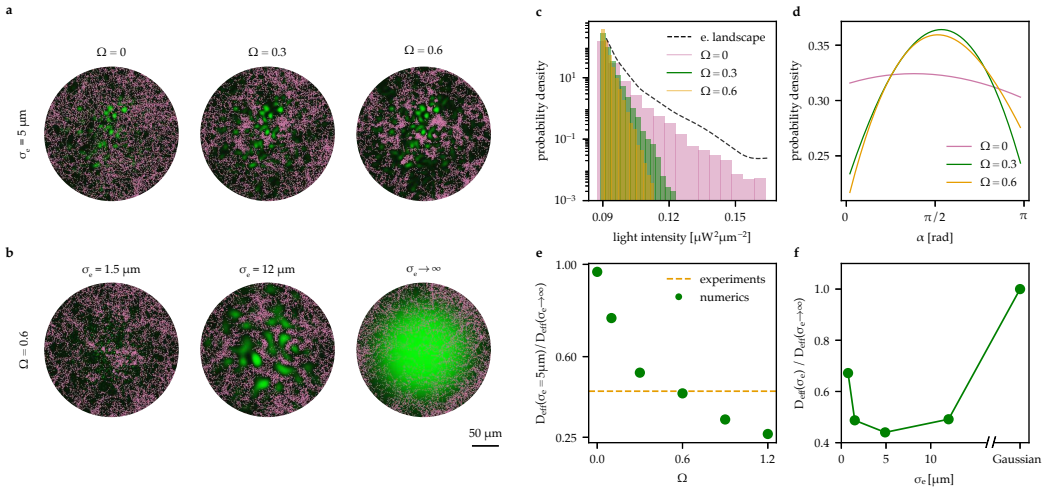

Figure 3. Modeling the dynamics of active particles in complex energy landscapes. A torque and spatial heterogeneities in the energy landscape determine the dynamics of the active particles. Simulated trajectories of individual active particles with **a)** different torque values (Ω) for a fixed $\sigma_e = 5\,\mu$m, and **b)** environment heterogeneity (σ_e), for a fixed $\Omega = 6$. **c)** In a complex environment ($\sigma_e = 5\,\mu$m), increasing the torque causes the particles to avoid high-energy areas. **d)** In the presence of a torque, particles move more perpendicular to the gradient ($\alpha = \pi/2$). **e)** The difference in the effective diffusion coefficients between complex and Gaussian illuminations observed in the experiments is most accurately described by $\Omega = 0.6$. **f)** Role of the heterogeneity of the energy landscape (σ_e) on the effective diffusion coefficient ($D_{\text{eff}}(\sigma_e)$) for a fixed value of the torque ($\Omega = 0.6$). The effective diffusion coefficient, normalised to its value for a Gaussian illumination, is minimised when the spatial variation of the landscape is comparable to the size of the particles. All simulations averaged 150 particles over 50 minutes each. The standard deviation of the data is represented in e) as shaded areas for experiments and vertical bars for numerics, comparable with the size of the scatter plot points. In f), the errors match the scatter point size.

along low-intensity areas. This is evidenced by the peak at the angle $\alpha = \pi/2$ in Figure 2b. Here, α represents the angle between the particle's instantaneous velocity and the local intensity gradient, as illustrated in the inset of Figure 2b. This result extends beyond observations in one-dimensional light gradients, where previous findings associated $\alpha = \pi$ ($\alpha = 0$) with negative (positive) phototaxis[45].

A complex energy landscape determines not only the preferential orientation of the active colloids but also their speed. Both in homogeneous energy landscapes[43,44] and in one-dimensional light gradients[45] a linear increase of the velocity with the light intensity was observed after a given activation energy. This is also reproduced in two-dimensional gradients when the illumination has a Gaussian profile ($\sigma_e \to \infty$ in Figure S3a). In this case the local value of the gradient is relatively low, making it comparable to the previously reported linear cases also in terms of orientation with respect to the gradient ($\alpha = \pi$ in Figure S4a)[43–45]. However, when the heterogeneity of the landscape is comparable to the size of the particles ($\sigma_e = 5\,\mu$m in Figure S3b) the velocity does not show a monotonic increase with the light intensity. This results from local values of the light gradient which are much stronger than in the previous cases, giving rise to a complex dependency of the speed of the particle on the energy landscape. Active particles do indeed experience a torque proportional to the light gradient, which, in turn, is proportional to the local light intensity. This torque causes them to change direction and reduce speed near high-energy patches[43–45]. The aligning torque is a consequence of breaking the axial symmetry of the velocity field around the particle[51]. The torque-induced reorientation and avoidance of high-energy zones reduce the mean squared displacement of active particles in a complex landscape when compared to a Gaussian illumination, as seen in Figure 2c. The mean squared displacement, despite the decrease, exhibits a superdiffusive transition followed by a long-time return to typical diffusion, as for typical active colloids in both scenarios[19].

To disentangle the role of the torque (the dimensionless parameter Ω, Figure 3a) exerted by the field gradient and the heterogeneity of the energy landscape (σ_e, Figure 3b) on the microscale dynamics, we employed a particle-based model that includes an aligning torque proportional to the gradient of the optical field (Methods)[43–45]. Figure 3c confirms how the presence of a torque prevents particles from accessing the high

energy regions, with a cutoff in energy that decreases as the torque increases. The emergence of this behaviour coincides also with a preferential orientation of the particles' velocity perpendicular to the gradient of the illumination, whereas at $\Omega = 0$ the velocity shows a relatively weak dependence on the gradient (Figure 3d). Our model further validates that under a two-dimensional Gaussian illumination, the preferred orientation relative to the gradient ($\alpha = \pi$ in Figure S4b) is governed by the effect of the torque. Additionally, as depicted in Figure 3e, the discrepancy in the long-term behavior of the mean squared displacement between $\sigma_e = 5\,\mu m$ and $\sigma_e \to \infty$ in Figure 2 can be attributed to the torque. In a complex illumination, an increase in torque restricts access to regions of higher energy, thereby reducing the mean squared displacement. Importantly, altering the heterogeneity of the environment (and thus the gradient value) while keeping the torque constant also results in a lower mean squared displacement, as shown in Figure 3f (represented as effective diffusion coefficient). This finding highlights the significant influence of environmental heterogeneity on particle dynamics— i.e. when σ_e is on a similar length scale to the particle size, it significantly affects its long-time diffusion coefficient. Conversely, in the asymptotic cases where energy variations occur on scales much smaller or larger than the particle, differences on long-time diffusivity are less marked.

To study the impact of the differences in individual trajectories on the collective behaviour of active systems we performed experiments with a higher concentration of particles ($\approx 4\%$, compared to $\approx 0.1\%$ in Figure 2). When the concentration of active particles increases, they are more likely to collide with each other, slowing down and forming groups. A group lasts until the propulsion direction of one of the individuals points outside the cluster and its speed is such that it can escape the group by winning over the short-range attraction among particles[26,27].

A heterogeneous energy landscape plays a key role in the formation of groups. As illustrated in Figure 4a, particles tend to aggregate, and eventually separate, in the dark regions of the optical landscape where their motility is lower. In complex energy landscapes, groups exhibit greater durability, with the average rate of aggregation and fragmentation events minimised when the spatial heterogeneity matches the individual particle scale (Figure 4b). The torque does indeed play a dual role in maintaining group stability. Firstly, it makes encounters between individuals more difficult by causing particles to linger in low energy regions for longer periods of time, which reduces the rate of aggregation. Secondly, once groups have formed, the torque orients particles toward areas of low energy, causing them to face inward the cluster and reducing the likelihood of fragmentation. The importance of the torque is further confirmed by Figure S5a, where decreasing it leads to i) an overall decrease of the rates and ii) a smaller difference in rates between homogeneous and complex energy landscapes.

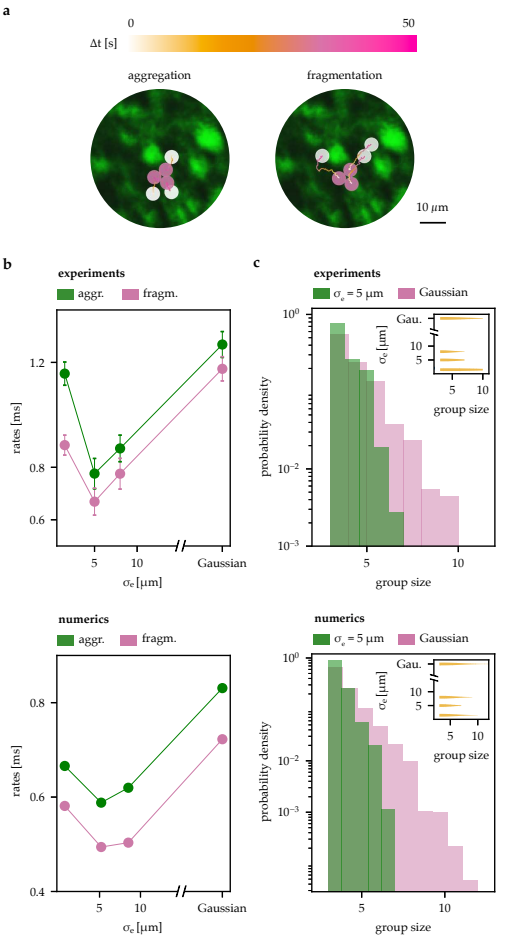

Figure 4. Group formation analysis. Comparison of group formation in energy landscapes with different spatial characteristics, i.e. different sizes of the energy patches (σ_e). **a)** Experimental trajectories showing an example of group aggregation and fragmentation in a complex landscape with $\sigma_e = 5\,\mu m$. When the patchiness of the landscape is comparable to the dimension of the particles, it reduces both the rate of individual exchange between them and the group size, **b)** and **c)**, respectively. In both panels of **c)**, the insets show the distribution of sizes for different spatial heterogeneities. In b), the error bars represent the standard deviation of the data.

The patchiness of the landscape also has a significant impact on group size, as demonstrated in Figure 4c. As individuals display avoidance behaviour towards high energy regions,

groups tend to grow until they fill the space confined between adjacent high-energy patches. The data presented in Figure 4c support this qualitative relationship, revealing that complex energy landscapes with heterogeneity comparable to the particle size lead to a reduction in the group dimension. The interplay between the dimension of energy patches and the group size is strongly influenced by the torque exerted by the gradient of resources. Decreasing the torque provides colloids with more freedom to move, enabling larger groups to form, as depicted in Figure S5a.

Notably, the differences in group dynamics depicted in Figure 4 cannot be solely attributed to a lower average motility of active particles in complex landscapes. Even when the mean squared displacement in a homogeneous energy landscape is reduced to match that in patchy ones (as shown in Figure S5b), disparities persist in both group dimension and stability. This further demonstrates that the spatial complexity of the energy landscape plays a critical role in shaping group dynamics.

Discussion

In summary, our study investigated how heterogeneous energy landscapes affect group formation using active particles in optical fields as a model system. We found that by manipulating the spatial complexity of the landscape, we can control the size of groups and the exchange of individuals between them. Our findings offer important biological perspectives. While smaller groups optimise resource allocation in patchy environments, their increased stability and reduced individual exchange might compromise genetic diversity. Yet, such limited interchange could also curtail the spread of diseases and parasites among groups and the transmission of antibiotic resistance in bacteria[52]. As our experimental approach provides a versatile and precise method to modulate the spatial dynamics of the energy landscape using light—with a natural extension to explore its temporal properties—it could be instrumental in studying search strategies in the presence of limited resources. Its applicability could span various contexts, ranging from animals engaged in foraging or migration to guiding robots through complex search-and-rescue missions.

Methods

Materials

Glass capillaries were purchased from CM Scientific (5005-050 and 5001-050 for single particle and cluster experiments, respectively). The lutidine was purchased and used as received: 2,6-lutidine ($\geq$ 99%, Sigma-Aldrich). Deionised (DI) water ($\geq 18\,\mathrm{M\Omega\cdot cm}$) was collected from a Milli-Q purification system. Aqueous colloidal dispersions (5% w/v) of silica (SiO_2) colloids, used for sample preparation, were purchased from Microparticles GmbH. Additionally, carbon rods measuring 300 mm in length and 6.15 mm in diameter were procured from Agar Scientific and subsequently cut to a length of 50 mm and tapered for the coating of Janus particles through sputtering.

Particles fabrication

Janus particles were synthesised from SiO_2 colloids with a diameter of $d = 4.77 \pm 0.20\,\mu\mathrm{m}$. Initially, a monolayer of colloids was deposited on a clean glass slide by evaporating a 40 µL droplet containing a 2.5% w/v dispersion of the colloids in DI water. Subsequently, an automatic carbon coater (AGB7367A, Agar Scientific) was employed to coat the particles with a 90 nm thick layer of carbon. The thickness of the carbon layer was confirmed through atomic force microscopy (AFM) measurements. After coating, sonication was performed to dislodge the half-coated particles in DI water from the glass slide, facilitating their use for sample preparation. To reduce the interaction between particles, and the sticking of the particles to the substrate, the Janus colloids were functionalised with bovine serum albumin (BSA, Sigma Aldrich). This was done by replacing the water solvent of the colloidal suspension with a 1%w/v water solution of BSA. Prior to utilisation, the colloidal dispersions underwent centrifugation at 1000 relative centrifugal force (RCF) for 3 minutes, resulting in the formation of a pellet. The supernatant was subsequently discarded and replaced with a solution containing 28.6% w/v of water and 2,6-lutidine. This purification procedure was repeated three times to ensure the removal of any remaining BSA water solution from the original dispersion.

Sample preparation

In single-particle experiments (Figure 1 and Figure 2), a suspension of Janus particles was confined in a rectangular capillary with a width of 700 µm, a length of 50 mm, and a thickness of 50 µm. The capillary was then sealed by applying a UV-curable glue to avoid evaporation and drifts. In the multiple-particles systems (Figure 4), we reduced the sample's thickness by using a capillary with a width of 100 µm, a length of 50 mm, and a thickness of 10 µm to restrict the motion of the colloids to two dimensions.

Experimental setup

Figure S1 shows a schematic of the experimental setup. A laser (Oxxius 532 nm, 300 mW of maximum output power) and a diffuser (1°, Newport 10DKIT-C1) are used to illuminate the Janus particles with a random optical field, also known as speckle. The laser is directed to the sample via two mirrors (M1, M2) and a 4f-lens configuration (L1=L2, Thorlabs, LA1461-A-ML) illuminating the back aperture of a 10x objective (Nikon, N10X-PF, NA=0.3). By changing the position of the diffuser and that of the sample, it is possible to control both the dimension of the speckle grains and the size of the illumination envelope. To create a Gaussian illumination, we removed the diffuser and one lens (L1) to image the beam on the sample. The illumination envelope was fixed to be close to the acquisition area of the camera ($\approx 200 \times 200\,\mu\mathrm{m}^2$ and $\approx 100 \times 100\,\mu\mathrm{m}^2$ in the single and multiple particles experiments, respectively) and it was kept the

same for different patchiness of the landscape (Figure S2). The intensity of the laser—controlled by a half-waveplate (FOCtek, WPF212H) and a polarising beam splitter (FOCtek, BSC1204) was then adjusted to have a comparable energy density in the different optical landscapes, i.e. different values of σ_e. The active particles were imaged with a 20x objective (Nikon, N20X-PF, NA=0.5) and a tube lens (L3, Thorlabs, LA1805-A-ML) on a camera (Basler, acA5472-17um). A white LED (Thorlabs, MWWHF2), for simplicity not depicted in Figure S1, coupled to a fibre (Thorlabs, M28L01) is used for imaging. The particles' dynamics were analysed by reconstructing their trajectories from videos (typically of the duration of 50 minutes at 2 frame per second (fps)) using a homemade code based on the python package *Trackpy*[53,54]. The position of the sample was controlled in three dimensions using an *xyz*-stage (Thorlabs, RB13M/M). The *z*-coordinate was adjusted with a stepper motor (Thorlabs, ZFS25B). For all experiments, the suspension of Janus particles was kept close to the critical temperature of the water-lutidine mixture ($T_{\text{exp}} \simeq 31\,^{\circ}\text{C}$, $\Delta T \simeq 3\,^{\circ}\text{C}$) by a heater driven via a temperature controller (Thorlabs, HT19R and TC200, respectively).

Numerical model

We numerically implemented an Euler-Maruyama time integrator for the evolution of the positions $\mathbf{r}_i$ and orientations ϕ_i of each particle i in two dimensions, defined by the following equations, based on[45]:

$$\dot{\mathbf{r}}_i(t) = v(\mathbf{r}_i)\mathbf{n}_i - \frac{1}{\gamma'}\sum_{j\neq i}\nabla V\left(|\mathbf{r}_i - \mathbf{r}_j|\right) + \sqrt{2D}\xi_i(t), \quad (1)$$

$$\dot{\phi}_i(t) = \omega(\phi_i, \mathbf{r}_i) + \sqrt{2D_r}\xi_i^{\phi}(t), \quad (2)$$

where $\mathbf{n}_i = (\cos(\phi), \sin(\phi))$, ξ_i and ξ_i^{ϕ} represent Gaussian white noise. The translational and rotational diffusion coefficients D and D_r are defined as

$$D = \frac{k_B T}{\gamma'}, \quad D_r = \frac{k_B T}{\beta'}, \quad (3)$$

where $\gamma' = \frac{16}{3}\pi\eta d$ and $\beta' = \frac{8}{7}\pi\eta d^3$ are respectively the translational and rotational friction coefficient, corrected by taking into account a distance from the substrate $s = d/2$[41], and $\eta = 2.1 \times 10^{-3}\,\text{Pa s}$ is the viscosity of water-lutidine. The torque ω, which is defined as:

$$\omega(\phi_i, \mathbf{r}_i) = \frac{\Omega d}{D} v(\mathbf{r}_i)\left[\nabla v(\mathbf{r}_i) \times \mathbf{n}_i\right] \cdot \hat{e}_z, \quad (4)$$

where the adimensional prefactor Ω determines whether the torque steers the particle towards the light ($\Omega < 0$) or away from it ($\Omega > 0$). The value of Ω that best fits the experimental change in the long-time mean squared displacement is $\Omega = 0.6$ (Figure 3e). V is a 6-12 Lennard-Jones potential with cutoff distance at five colloid diameters d and depth $\varepsilon \simeq 8k_B T$. This value was chosen by fitting the experimental cluster aggregation and fragmentation rates for a Gaussian illumination. The intensity speckle field was generated by scaling the Fourier transform of a white noise map to match the specific characteristics of the optical fields observed in experiments: average intensity per unit of area and grain size. This intensity field was then translated into a motility field using the results from[45]. The gradient of the motility field acting on the particle $\nabla v(\vec{r}_i)$ was averaged over the square area where the particle is inscribed.

Cluster analysis

We defined the clusters by measuring all distances among particles and then creating bonds between all the particles with distances smaller than the cutoff radius 1.25d. Similarly to Ref.[26,41], clusters made of 2 particles (i.e. dimers) were disregarded in the analysis as they are unstable in time. We determined whether a cluster survives from one timestep to the next by confronting its particles with those of all the clusters in the next timestep. We consider any of these clusters to be the same as a previous one if it satisfies two properties: i) that more than half of its particles are shared with the old cluster (i.e. the cluster has not decreased more than half in size); ii) that at least half of the particles of the new cluster are also present in the old one, i.e. the cluster has not grown more than double in size. We calculated mainly two properties regarding clusters for each experiment: the cluster size and the monomer acquisition/loss rate. The first is simply the average number of monomers for each cluster, while the second is defined as the number of monomer acquisition/loss events (i.e. the number of times clusters receive/lose a single monomer during the experiment) normalised by the total experiment time and the average number of particles.

Data availability

All data needed to evaluate the conclusions in the paper are present in the paper and/or the Supplementary Materials.

Acknowledgements

The authors thank Dr. Raphaël Jeanneret and Dr. Jean Francois Allemand for suggesting the use of bovine serum albumin to reduce particles attraction and Alessia Gentili for insightful discussions on cluster analysis. This project has received funding from the European Union's Horizon 2020 research and innovation programme under the Marie Skłodowska-Curie grant agreement No 945298-ParisRegionFP, GJ is a fellow of the Paris Region Fellowship Programme supported by the Paris Region. The work of HL was supported by the German Research Foundation (project LO 418/29-1). DB and SH acknowledge support by the EU MSCA-ITN ActiveMatter (Proposal No. 812780).

Author Contributions

Author contributions are defined based on the CRediT (Contributor Roles Taxonomy) and listed alphabetically. Conceptualization: SG, GJ, HL, GV. Data curation: DB, GJ. Formal

analysis: DB, GJ. Resources: SG, SH, PJ, HL, JP, GV. Writing: GJ wrote the manuscript with the help of all authors. Funding acquisition: SG, GJ, HL, GV.

Conflict of interest

The authors declare that they have no competing financial interests.

References

1. Sumpter, D. J. T. *Collective animal behavior.* (Princeton University Press, Princeton, NJ, US, 2010).
2. Rosenthal, S. B., Twomey, C. R., Hartnett, A. T., Wu, H. S. & Couzin, I. D. Revealing the hidden networks of interaction in mobile animal groups allows prediction of complex behavioral contagion. *Proceedings of the National Academy of Sciences* **112**, 4690–4695 (2015).
3. Sosna, M. M. G. *et al.* Individual and collective encoding of risk in animal groups. *Proceedings of the National Academy of Sciences* **116**, 20556–20561 (2019).
4. Klamser, P. P. & Romanczuk, P. Collective predator evasion: Putting the criticality hypothesis to the test. *PLOS Computational Biology* **17**, e1008832 (2021).
5. Brown, C. R., Brown, M. B. & Shaffer, M. L. Food-sharing signals among socially foraging cliff swallows. *Animal Behaviour* **42**, 551–564 (1991).
6. Jackson, D. E. & Ratnieks, F. L. Communication in ants. *Current Biology* **16**, R570–R574 (2006).
7. Feinerman, O., Pinkoviezky, I., Gelblum, A., Fonio, E. & Gov, N. S. The physics of cooperative transport in groups of ants. *Nature Phys* **14**, 683–693 (2018).
8. Strandburg-Peshkin, A., Farine, D. R., Couzin, I. D. & Crofoot, M. C. Shared decision-making drives collective movement in wild baboons. *Science* **348**, 1358–1361 (2015).
9. Couzin, I. D. *et al.* Uninformed individuals promote democratic consensus in animal groups. *Science* **334**, 1578–1580 (2011).
10. Brush, E. R., Krakauer, D. C. & Flack, J. C. Conflicts of interest improve collective computation of adaptive social structures. *Sci. Adv.* **4**, e1603311 (2018).
11. Gordon, D. M. The Ecology of Collective Behavior. *PLoS Biol* **12**, e1001805 (2014).
12. Gueron, S. & Levin, S. A. The dynamics of group formation. *Mathematical Biosciences* **128**, 243–264 (1995).
13. Chapman, C., Chapman, L. & Wrangham, R. Ecological constraints on group size: An analysis of spider monkey and chimpanzee subgroups. *Behavioral Ecology and Sociobiology* **36**, 59–70 (1995).
14. Aureli, F. *et al.* Fission-Fusion Dynamics: New Research Frameworks. *Current Anthropology* **49**, 627–654 (2008).
15. Teichroeb, J. A. & Sicotte, P. Test of the ecological-constraints model on ursine colobus monkeys (*Colobus vellerosus*) in Ghana. *American Journal of Primatology* **71**, 49–59 (2009).
16. Hughey, L. F., Hein, A. M., Strandburg-Peshkin, A. & Jensen, F. H. Challenges and solutions for studying collective animal behaviour in the wild. *Philosophical Transactions of the Royal Society B: Biological Sciences* **373**, 20170005 (2018).
17. Tuia, D. *et al.* Perspectives in machine learning for wildlife conservation. *Nature Communications* **13**, 792 (2022).
18. Romanczuk, P., Bär, M., Ebeling, W., Lindner, B. & Schimansky-Geier, L. Active Brownian particles: From individual to collective stochastic dynamics. *Eur. Phys. J. Spec. Top.* **202**, 1–162 (2012).
19. Bechinger, C. *et al.* Active Particles in Complex and Crowded Environments. *Rev. Mod. Phys.* **88**, 045006 (2016).
20. Cavagna, A. & Giardina, I. Bird Flocks as Condensed Matter. *Annu. Rev. Condens. Matter Phys.* **5**, 183–207 (2014).
21. Santini, L., Isaac, N. J. B. & Ficetola, G. F. TetraDENSITY: A database of population density estimates in terrestrial vertebrates. *Global Ecology and Biogeography* **27**, 787–791 (2018). _eprint: https://onlinelibrary.wiley.com/doi/pdf/10.1111/geb.12756.
22. King, A. J., Fehlmann, G., Biro, D., Ward, A. J. & Fürtbauer, I. Re-wilding Collective Behaviour: An Ecological Perspective. *Trends in Ecology & Evolution* **33**, 347–357 (2018).
23. Northrup, J. M. *et al.* Conceptual and methodological advances in habitat-selection modeling: guidelines for ecology and evolution. *Ecological Applications* **32**, e02470 (2022).
24. Grégoire, G. & Chaté, H. Onset of Collective and Cohesive Motion. *Phys. Rev. Lett.* **92**, 025702 (2004). Publisher: American Physical Society.
25. Palacci, J., Sacanna, S., Steinberg, A. P., Pine, D. J. & Chaikin, P. M. Living Crystals of Light-Activated Colloidal Surfers. *Science* **339**, 936–940 (2013).
26. Ginot, F., Theurkauff, I., Detcheverry, F., Ybert, C. & Cottin-Bizonne, C. Aggregation-fragmentation and individual dynamics of active clusters. *Nat Commun* **9**, 696 (2018).
27. Buttinoni, I. *et al.* Dynamical clustering and phase separation in suspensions of self-propelled colloidal particles.

Phys. Rev. Lett. **110**, 238301 (2013). ArXiv:1305.4185 [cond-mat].

28. Vicsek, T., Czirók, A., Ben-Jacob, E., Cohen, I. & Shochet, O. Novel Type of Phase Transition in a System of Self-Driven Particles. *Phys. Rev. Lett.* **75**, 1226–1229 (1995).

29. Bricard, A., Caussin, J.-B., Desreumaux, N., Dauchot, O. & Bartolo, D. Emergence of macroscopic directed motion in populations of motile colloids. *Nature* **503**, 95–98 (2013).

30. Van Drongelen, R., Pal, A., Goodrich, C. P. & Idema, T. Collective dynamics of soft active particles. *Phys. Rev. E* **91**, 032706 (2015).

31. Zhang, J., Alert, R., Yan, J., Wingreen, N. S. & Granick, S. Active phase separation by turning towards regions of higher density. *Nat. Phys.* **17**, 961–967 (2021).

32. Durve, M., Saha, A. & Sayeed, A. Active particle condensation by non-reciprocal and time-delayed interactions. *Eur. Phys. J. E* **41**, 49 (2018).

33. Lavergne, F. A., Wendehenne, H., Bäuerle, T. & Bechinger, C. Group formation and cohesion of active particles with visual perception–dependent motility. *Science* **364**, 70–74 (2019).

34. Altemose, A. *et al.* Chemically Controlled Spatiotemporal Oscillations of Colloidal Assemblies. *Angewandte Chemie International Edition* **56**, 7817–7821 (2017).

35. Ziepke, A., Maryshev, I., Aranson, I. S. & Frey, E. Multiscale organization in communicating active matter. *Nat Commun* **13**, 6727 (2022).

36. Reichhardt, C. & Olson Reichhardt, C. J. Active matter transport and jamming on disordered landscapes. *Phys. Rev. E* **90**, 012701 (2014).

37. Morin, A., Desreumaux, N., Caussin, J.-B. & Bartolo, D. Distortion and destruction of colloidal flocks in disordered environments. *Nature Phys* **13**, 63–67 (2017).

38. Reichhardt, C. & Reichhardt, C. J. O. Clogging and depinning of ballistic active matter systems in disordered media. *Phys. Rev. E* **97**, 052613 (2018).

39. Frangipane, G. *et al.* Invariance properties of bacterial random walks in complex structures. *Nat Commun* **10**, 2442 (2019).

40. Kurzthaler, C. *et al.* A geometric criterion for the optimal spreading of active polymers in porous media. *Nat Commun* **12**, 7088 (2021).

41. Dias, C. S., Trivedi, M., Volpe, G., Araújo, N. A. M. & Volpe, G. Environmental memory boosts group formation of clueless individuals (2023). 2306.00516.

42. Pinçe, E. *et al.* Disorder-mediated crowd control in an active matter system. *Nat Commun* **7**, 10907 (2016).

43. Lozano, C., ten Hagen, B., Löwen, H. & Bechinger, C. Phototaxis of synthetic microswimmers in optical landscapes. *Nat Commun* **7**, 12828 (2016).

44. Gomez-Solano, J. R. *et al.* Tuning the motility and directionality of self-propelled colloids. *Sci Rep* **7**, 14891 (2017).

45. Jahanshahi, S., Lozano, C., Liebchen, B., Löwen, H. & Bechinger, C. Realization of a motility-trap for active particles. *Commun Phys* **3**, 127 (2020).

46. Volpe, G., Buttinoni, I., Vogt, D., Kuemmerer, H.-J. & Bechinger, C. Microswimmers in Patterned Environments. *Soft Matter* **7**, 8810 (2011).

47. Buttinoni, I., Volpe, G., Kümmel, F., Volpe, G. & Bechinger, C. Active Brownian motion tunable by light. *J. Phys.: Condens. Matter* **24**, 284129 (2012).

48. Lozano, C., Bäuerle, T. & Bechinger, C. Active Brownian Particles with Programmable Interaction Rules. In Tailleur, J., Gompper, G., Marchetti, M. C., Yeomans, J. M. & Salomon, C. (eds.) *Active Matter and Nonequilibrium Statistical Physics*, 219–229 (Oxford University PressOxford, 2022), 1 edn.

49. Volpe, G., Volpe, G. & Gigan, S. Brownian Motion in a Speckle Light Field: Tunable Anomalous Diffusion and Selective Optical Manipulation. *Sci Rep* **4**, 3936 (2014).

50. Bianchi, S., Pruner, R., Vizsnyiczai, G., Maggi, C. & Di Leonardo, R. Active dynamics of colloidal particles in time-varying laser speckle patterns. *Sci Rep* **6**, 27681 (2016).

51. Bickel, T., Zecua, G. & Würger, A. Polarization of active Janus particles. *Physical Review E* **89**, 050303 (2014).

52. Bennett, P. M. Plasmid encoded antibiotic resistance: acquisition and transfer of antibiotic resistance genes in bacteria. *British journal of pharmacology* **153**, S347–S357 (2008).

53. Crocker, J. C. & Grier, D. G. Methods of Digital Video Microscopy for Colloidal Studies. *Journal of Colloid and Interface Science* **179**, 298–310 (1996).

54. Allan, D. B., Caswell, T., Keim, N. C., van der Wel, C. M. & Verweij, R. W. soft-matter/trackpy: v0.6.1 (2023). URL https://doi.org/10.5281/zenodo.7670439.

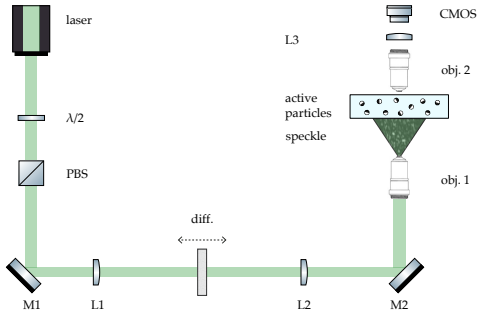

Figure S1. Experimental setup. A laser and a diffuser are used to generate a spatially complex energy landscape for active particles. The laser is directed to the sample via two mirrors (M1, M2) and a 4f-lens configuration (L1=L2) illuminating the back aperture of an objective (obj. 1). Active particles are imaged via a second objective (obj. 2), a tube lens (L3) and a camera (CMOS). The trajectories are then reconstructed using a custom software. The speckle grain size and envelope can be adjusted by changing the longitudinal position of the diffuser with respect to the sample. The laser power is controlled by a half-waveplate ($\lambda/2$) and a polarising beamsplitter (PBS).

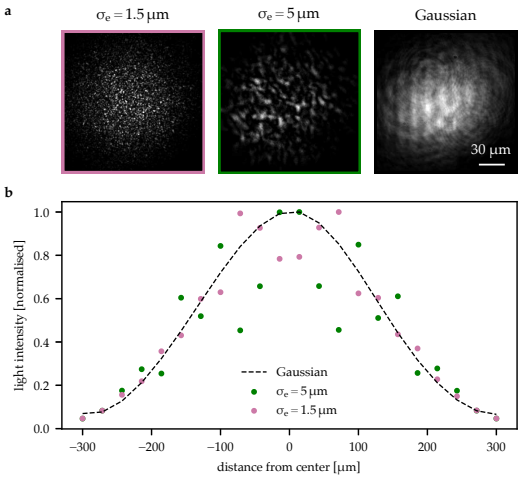

Figure S2. Illumination profile. a) Three representative illumination patterns for different speckle grain sizes (σ_e). **b)** Radially averaged intensity profile as a function of distance, based on images in a). The illumination profiles share a common envelope, indicating that the active particles experience the same energy density across different energy landscapes.

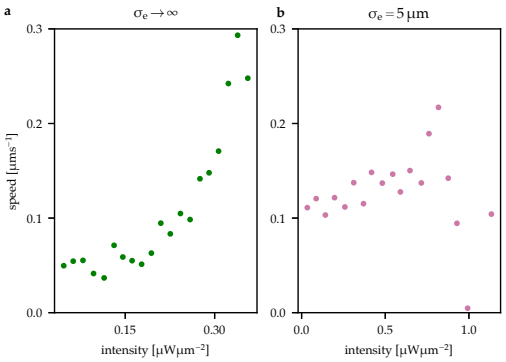

Figure S3. Velocity as a function of light intensity. a) In a Gaussian illumination ($\sigma_e \to \infty$), where the gradient is small, there is a monotonic increase in velocity with light intensity. **b)** In contrast, in a complex case ($\sigma_e = 5\,\mu m$)—where the local gradient is much larger and linearly dependent on the light intensity—the speed shows a weak dependence on the intensity. This arises as a result of the torque exerted by the gradient, causing particles to change direction and therefore reducing their speed near high-intensity regions.

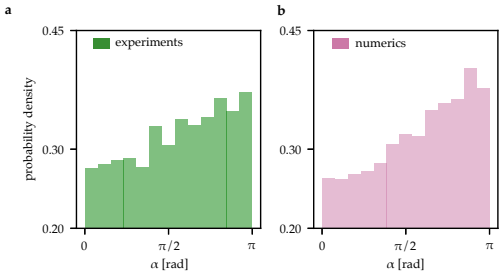

Figure S4. Orientation of an active particle in a Gaussian energy landscape. When moving in a Gaussian energy landscape ($\sigma_e \to \infty$)—i.e. in the presence of a light gradient on a scale much larger than their size—active particles tend to align preferentially antiparallel to the global gradient of the illumination ($\alpha = \pi$). **a)** experiments, **b)** numerics.

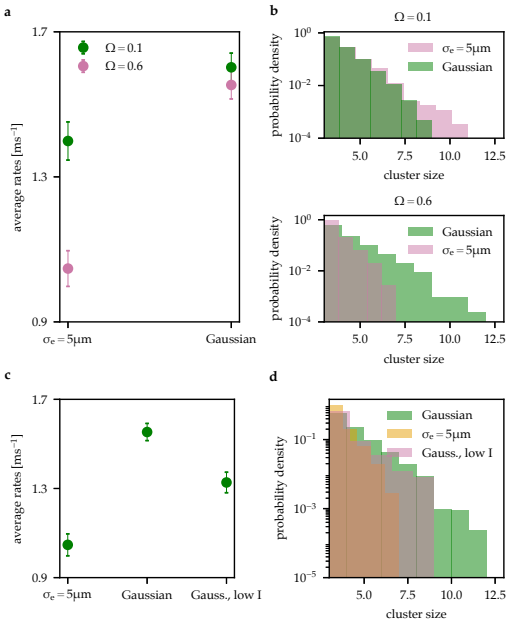

Figure S5. Effect of torque and lower motility on group formation. Numerical simulations show that a smaller torque ($\Omega = 0.1$ vs $\Omega = 0.6$) leads to a less marked difference in rates **a)** and group size **b)** between complex ($\sigma_e = 5\,\mu m$) and Gaussian motility fields (Gaussian). In order to investigate whether the difference in group dynamics was solely influenced by the lower average motility of active particles in complex illumination, simulations were conducted in a homogeneous motility field with an identical average motility to that of the inhomogeneous scenario—achieved by reducing the light intensity (Gaussian, low I). However, reducing the average motility does not bridge the gap, in terms of both rates and sizes, **c)** and **d)**, respectively, between homogeneous and complex illuminations.

P6 Giant Activity-Induced Stress Plateau in Entangled Polymer Solutions

Reproduced from

D. Breoni C. Kurzthaler B. Liebchen H. Löwen S. Mandal, *Giant Activity-Induced Stress Plateau in Entangled Polymer Solutions*, arXiv:2310.02929 [cond-mat.soft] (2023),

Digital Object Identifier (DOI): `https://doi.org/10.48550/arXiv.2310.02929`

Statement of contribution

CK, BL, HL and SM conceptualized the project. SM coded the program and together with me performed the simulations and analyzed the data. I produced the figures. CK and SM wrote the manuscript with the help of all authors.

Giant Activity-Induced Stress Plateau in Entangled Polymer Solutions

Davide Breoni,[1] Christina Kurzthaler,[2] Benno Liebchen,[3] Hartmut Löwen,[1] and Suvendu Mandal[3,*]

[1] *Institut für Theoretische Physik II: Weiche Materie, Heinrich Heine-Universität Düsseldorf, Universitätsstraße 1, 40225 Düsseldorf, Germany*

[2] *Max Planck Institute for the Physics of Complex Systems, Nöhnitzer Straße 38, 01187 Dresden, Germany*

[3] *Technische Universität Darmstadt, Karolinenplatz 5, 64289 Darmstadt, Germany*

We study the viscoelastic properties of highly entangled, flexible, self-propelled polymers using Brownian dynamics simulations. Our results show that the active motion of the polymer increases the height of the stress plateau by orders of magnitude due to the emergence of grip forces at entanglement points. Identifying the activity-induced energy of a single polymer and the ratio of polymer length to self-propulsion velocity as relevant energy and time scales, we find the stress autocorrelation functions collapse across Péclet numbers. We predict that the long-time viscosity scales with polymer length squared $\sim L^2$, in contrast to equilibrium counterparts $\sim L^3$. These insights offer prospects for designing new materials with activity-responsive mechanical properties.

Entangled polymer solutions represent fundamental building blocks of many biological materials, where they serve functions as diverse as cell mitosis [1–5] and transcription of genetic material [6–8]. Furthermore, they are important collective life forms, which provide individuals resistance to environmental stresses [9–12], and lay the foundation for numerous technological applications [12–14]. The rheological properties of these complex materials are governed by the elasticity and structure of their conformations, such as their long, slender linear [15], twisted [16], or loop conformations [17], their strong entanglement, and their specific microscopic interactions, which makes them a fascinating many-body problem in physics.

The viscoelastic properties of these strongly-interacting systems at thermodynamic equilibrium have been thoroughly studied in the realm of polymer physics. A major breakthrough has been the theoretical prediction of rheological properties of entangled linear polymer melts in terms of their stress autocorrelation function, which exhibits a prominent plateau at intermediate times, characterizing the elastic response, and relaxes exponentially at long times [18–20]. The relation between phenomenological parameters of the underlying tube model and microscopic system properties to ultimately predict the stress plateau has been established by analyzing the polymers' primitive paths [21, 22], which correspond to the axes of entangled polymer tubes [21, 22]. While it has been shown that the stress plateau of linear polymer solutions remains unaffected by external driving [23], tuning the topological properties of the polymers can lead to a qualitative change of the stress relaxation dynamics [17]. The latter display a power-law behavior for loop polymer melts and recover a stress plateau only upon adding linear polymer chains to the solution [17].

Recent work has demonstrated that microscopic interactions among the entangled constituents can be governed by active components, such as molecular motors in solution [3, 4, 6–8] or the intrinsic motility of the individuals [9–12], which drive these systems far from equilibrium and generate dynamical and structural behaviors distinct from their passive counterparts. Understanding the interplay of entanglement and activity is not only fundamental to living systems but also crucial for designing and processing new soft materials with tailored properties. In particular, incorporating active components in addition to tuning the entanglement has the potential to improve the mechanical properties of materials. Yet, theoretical studies in this direction are limited and no universal behaviors or scaling predictions have been established to guide experimental progress.

Here, we use Brownian dynamics simulations to characterize the viscoelastic properties of highly-entangled, flexible, self-propelled polymers in terms of the time-dependent stress autocorrelation function and viscosity. Our results reveal a remarkable amplification of the stress plateau, a phenomenon intricately linked to the interplay of active motion and topological uncrossability of polymers, leading to the emergence of grip forces. In particular, neighboring polymers form hairpin structures that exert forces, pulling the entangled test polymer in the direction of their self-propulsion, effectively preventing its sliding at the entanglement points. It is noteworthy that the magnitude of these grip forces depends on the self-propulsion velocity. Subsequently, we show that the stress autocorrelation functions for a broad range of polymer lengths and Péclet numbers can be collapsed onto a single master curve by identifying the relevant energy and time scales. Finally, we predict that the long-time viscosity scales with the square of the polymer length $\sim L^2$, which becomes exact for high Péclet numbers in the highly-entangled regime.

Model– We perform 3D Brownian dynamics simulations of highly-entangled polymer solutions of N self-propelled, flexible polymer chains using the bead-spring model [24]. Each chain consists of N_p monomers with diameter σ and has a length of $L = N_p\sigma$. The connectivity and repulsion of the beads are modeled using the finitely extensible nonlinear elastic potential

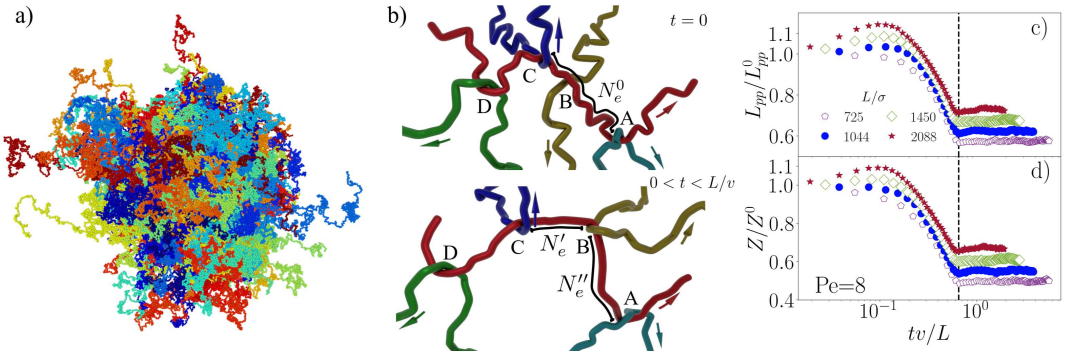

Figure 1. (a) Simulation snapshot of entangled, flexible polymers (each polymer has its own color). (b) 3D illustration depicting the primitive path of a test polymer (red line) confined within an effective tube formed by surrounding self-propelled polymers at various times t. In the equilibrium state ($t = 0$), a combination of strong entanglement points (A, C, and D) and weak entanglement point (B) coexists, with strong entanglements distinguished by the presence of hairpin structures. Due to activity, prior to reaching the steady state ($t \gtrsim L/v$), the number of strong entanglement points increases (as shown by the yellow polymer wrapping around the red polymer at point B), resulting in the elongation of the primitive path. The direction of self-propulsion is indicated by colored arrows, while the distance between successive entanglement points defines the entanglement length N_e. (c) Contour length of the primitive path L_{pp}, normalized by the equilibrium primitive path L_{pp}^0 as a function of time for different polymer lengths L and fixed Péclet number $\mathrm{Pe} = 8$. Time is rescaled by the ratio of polymer length to self-propulsion velocity L/v. (d) Number of entanglement points Z, normalized by the number of entanglement points Z^0 for $\mathrm{Pe} = 0$, as a function time.

(FENE) [24] and the Weeks-Chandler-Andersen potential (WCA) [25] with energies ϵ_{FENE} and ϵ_{WCA}, respectively. Angular interactions along chain backbones are captured using a bending potential for each monomer $U_{\mathrm{ang},i} = \kappa \sum_{j=i-1,i,i+1}(1 - \mathbf{t}_j \cdot \mathbf{t}_{j+1})$, where $\mathbf{t}_j = (\mathbf{r}_{j+1} - \mathbf{r}_j)/(|\mathbf{r}_{j+1} - \mathbf{r}_j|)$ represents the tangent vector between consecutive monomers having positions $\mathbf{r}_j$ and κ corresponds to the bending energy. The polymers are subject to Brownian motion modeled by stochastic forces $\mathbf{F}_{r,i}$, where $\langle F_{r,i}^{\alpha}(t) F_{r,j}^{\beta}(t')\rangle = 2k_BT\zeta\delta_{ij}\delta_{\alpha\beta}\delta(t' - t)$ with friction coefficient ζ and thermal energy k_BT. Their self-propulsion is modeled by an active force $\mathbf{F}_{p,i}$ acting tangentially to the polymer contour [26–28], so that (without interactions) each bead moves at a velocity of $v = |\mathbf{F}_{p,i}|/\zeta$ ($|\mathbf{F}_{p,i}|$ being constant across all monomers). Thus, the equation of motion for each monomer read

$$\zeta \frac{\mathrm{d}\mathbf{r}_i}{\mathrm{d}t} = -\nabla_i U + \mathbf{F}_{p,i} + \mathbf{F}_{r,i}. \tag{1}$$

Dimensionless parameters, derived from length and time units (σ and $\tau_0 = \sigma^2/D_0$, with $D_0 = k_BT/\zeta$ as the short-time diffusion coefficient of a monomer), include the Péclet number ($\mathrm{Pe} = v\sigma/D_0$) for assessing the significance of active motion relative to diffusion, along with coupling parameters ($\epsilon_{\mathrm{WCA}}/k_BT$, $\epsilon_{\mathrm{FENE}}/k_BT$, and κ/k_BT). Additionally, we define the dimensionless density $\rho^\star = N_{\mathrm{tot}}\sigma^3/V$, where V denotes the volume of the simulation box. We keep fixed values of $\rho^\star = 0.85$, $\epsilon_{\mathrm{WCA}}/k_BT = 1.0$, $\epsilon_{\mathrm{FENE}}/k_BT = 30$, and $\kappa/k_BT = 1.0$, while systematically varying the polymer length ($L/\sigma = 100, ...2088$), resulting in a dimensionless entanglement length $N_e \cong 41$ [29]. Equations of motion are solved numerically using a modified version of LAMMPS with a time step of $\delta t = 10^{-4}\tau_0$. Equilibration is achieved through a bond-swapping algorithm with core softening [see SI [30]], and all time measurements are referenced from this equilibration point. Notably, both active and passive highly-entangled polymer systems exhibit an ideal chain scaling relation for the end-to-end distance $R_{ee} \propto L^{1/2}$, in contrast to dilute active polymer solutions [27], indicating that activity does not affect this scaling [see SI [30]].

Activity-enhanced stress plateau– The viscoelastic properties of polymer solutions are encoded in the stress autocorrelation function

$$G(t) = \frac{V}{3k_BT} \sum_{\alpha \neq \beta} \langle \sigma_{\alpha\beta}(t)\sigma_{\alpha\beta}(0)\rangle\,, \tag{2}$$

where the sum runs over all off-diagonal components of the stress tensor $\sigma_{\alpha\beta}$ and $\langle..\rangle$ denotes an ensemble average. In equilibrium systems, for the case of short, unentangled linear polymer solutions, this yields the power-law dynamics described by the Rouse model, $G(t) \sim t^{-1/2}$ [19]. In contrast, highly-entangled polymers are forced to move along the direction of their contour, while their motion perpendicular to it is restricted to a tube-like region formed by the surrounding polymers [Fig.1(a)]. Consequently, the stress autocorrelation function exhibits a plateau G_0 at intermediate times and an

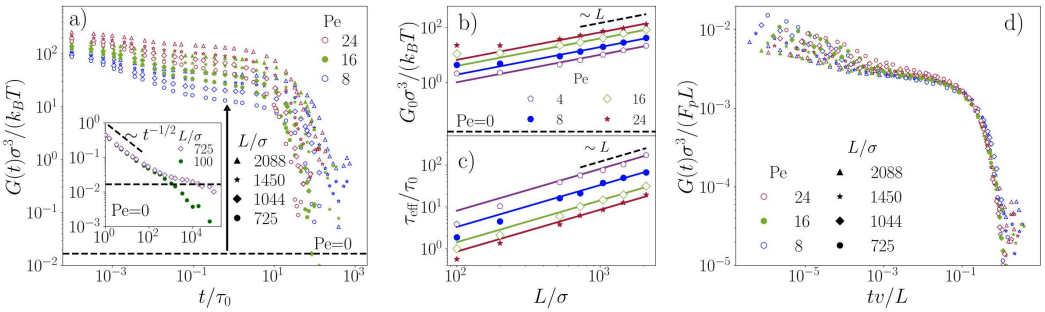

Figure 2. (a) Stress autocorrelation function $G(t)$ for different Péclet numbers and polymer lengths as a function of time. Inset: The stress autocorrelation function in equilibrium for $L = 725\sigma$ validates the well-established prediction $G_0 = 4\rho k_B T/(5N_e^0)$ (dashed line), where N_e^0 is the entanglement length between two subsequent entanglement points. Axes are labeled as in the main figure. Black arrow indicates the giant activity-induced stress plateau compared to the equilibrium state. (b) Stress plateau G_0 and (c) disengagement time $\tau_{\rm eff}$ as a function of polymer length L extracted from our simulations for a wide range of Péclet numbers. (d) Rescaled stress autocorrelation function $G(t)\sigma^3/F_pL$ as a function of the rescaled time tv/L.

exponential decay $G_0 e^{-t/\tau_{\rm eff}}$ at long times. The stress plateau G_0, a hallmark of entangled polymer chains, quantifies the elasticity of the system, while the disengagement time $\tau_{\rm eff} \sim L^3$ corresponds to the characteristic time the polymer requires to move its own length L along the tube.

To investigate the effect of activity, we compute the stress autocorrelation function $G(t)$ for self-propelled polymers of different lengths, $L = 100, ...2088\sigma$, and Péclet numbers, Pe $= 1, ...24$, see Fig. 2(a). At very short times ($t \lesssim 10^{-3}\tau_0$), the active polymer solution is slightly harder ($G(t)$ increases by a factor of 4 compared to the passive counterpart [see SI [30]]), which can be attributed to the increased fluctuations exhibited by the self-propelled polymers within their tubes.

At intermediate times, $t \sim \tau_0$, the difference between the stress autocorrelation function $G(t)$ of passive and active systems becomes significantly larger, which becomes apparent in an increase of the plateau height G_0 by three orders in magnitude [see Fig. 2(a)]. This amplification arises from grip forces exerted on the red test polymer by neighboring polymers [Fig.1(b)]. First, these neighboring polymers form hairpin structures around the test polymer, stretching its primitive path, thereby slowing down the relaxation of $G(t)$ as the test polymer traverses within an elongated tube. This effect becomes pronounced when we keep the Péclet number constant while increasing the polymer length [Fig.2(b)]. Second and more strikingly, these grip forces also act as barriers, effectively preventing the test polymer from sliding at the entanglement points. This results in a substantial increase in the plateau height as Pe increases at a fixed polymer length [Fig.2(a) and SI [30]]. Hence, both mechanisms contribute to a giant enhancement of the elastic stress plateau height, a phenomenon exclusive to self-propelled entangled systems. When the test polymer disengages from its tube, the grip forces imposed by the surrounding polymers diminish, leading to a relaxation of the stress autocorrelation function from the plateau at long times [see Fig. 2(a)].

This physical picture can be corroborated by measuring the average contour length of the primitive path, denoted as L_{pp}, and the average number Z of entanglement points. To elucidate topological entanglement dynamics, we employed the Z1+ topological analysis algorithm [29, 31–34], which systematically undergoes a sequence of geometric minimizations. The primitive path is rigorously defined as the shortest path between the two ends of a polymer chain while preserving its topological uncrossability. At intermediate times $tv/L \sim 0.1$, our simulations show that upon increasing the polymer length at a fixed Pe $= 8$, L_{pp} and Z increase by 10% compared to the passive counterpart [see Fig. 1(c-d)]. This observation suggests that the active system becomes more entangled, with the number of entanglement points rising from $Z = 105$ to 115 for $L/\sigma = 2088$. Moreover, we evaluated the entanglement length N_e using the relation $N_e = (N_p - 1)\langle R_{ee}^2\rangle/\langle L_{pp}^2\rangle$ [29, 33]. In contrast to L_{pp}, the end-to-end distance R_{ee} exhibits a gradual decrease until it eventually saturates at long times ($tv/L \gg 1$) at a fixed Pe $= 8$ [see SI [30]]. Consequently, at intermediate times ($tv/L \sim 0.1$), we observe a reduction of approximately 30% in N_e relative to the passive counterpart [see SI [30]].

It is tempting to validate the giant increase in the stress plateau G_0 via the well-established relation for equilibrium systems $G_0 = 4\rho k_B T/(5N_e)$ [35]. However, our observations reveal a 30% decrease in N_e with increasing polymer length L at a fixed Péclet number (Pe $= 8$), while the stress plateau G_0 increases by orders of mag-

nitude. By employing a dimensional argument, we show that the enhanced stress plateau can rather be related to the active energy of a single polymer F_pL, where F_p denotes the magnitude of the active force. For large Pe $\gg 1$, this energy dominates over thermal energy and thus represents the relevant energy scale of our system, leading to our prediction $G_0 \sim F_pL/\sigma^3$. To quantify this phenomenon, we show the plateau height G_0 as a function of the polymer length L for a range of Péclet numbers in Fig. 2(b). It turns out that G_0 indeed increases linearly as a function of the polymer length in the highly entangled regime ($L \gtrsim 500\sigma$). This occurs since the polymers are forced to move within elongated tubes as well as the system gets highly entangled (the number of entanglement points Z increases compared to the passive counterpart). However, for unentangled chains with $L \lesssim 100\sigma$, the stress plateau vanishes and we recover an algebraic decay $\sim t^{-1/2}$, in agreement with the Rouse model, which validates the idea that the stress plateau is a unique feature of highly entangled polymer solutions (see SI [30]).

At long times $t \gg \tau_0$, the stress autocorrelation function follows the expected exponential decay $G(t) \sim G_0 \exp(-t/\tau_{\text{eff}})$, where τ_{eff} represents the disengagement time of our active system [see Fig. 2(a)]. At these times, the transverse motion becomes nearly frozen, allowing the polymer to self-propel and diffuse freely along the tube at timescales of L/v and $\sim L^3$, respectively. The disengagement time τ_{eff} is determined by the faster of these two mechanisms and we use the interpolation formula given below as an estimate:

$$\tau_{\text{eff}}^{-1} = D_0\sigma/L^3 + v/L. \tag{3}$$

Remarkably, our computer simulations show that active entangled polymers relax much faster than their passive counterparts, resulting in a disengagement time that scales as $\tau_{\text{eff}} \sim L$ [see Fig.2(c)]. This is in contrast to the passive case, where the disengagement time scales as $\sim L^3$ for larger polymer lengths, as observed in experiments [36].

By combining the relevant time $\tau_{\text{eff}} \sim L/v$ and energy scales $G_0 \sim F_pL/\sigma^3$, the data collapse onto a single curve at intermediate and long times, as depicted in Fig.2(d). The data collapse is excellent over nearly three decades in time, confirming our predictions.

Time-dependent viscosity– Following our previous predictions ($G_0 \sim LF_p/\sigma^3$ and $\tau_{\text{eff}} \sim L/v$), the time-dependent and stationary viscosity are expected to scale as $\eta \sim G_0\tau_{\text{eff}} \sim L^2$. Only recently, it has been claimed that in the hydrodynamic limit (i.e., at long times and at large length scales) the Green-Kubo relation is valid even for suspensions of active dumbells [37]. This work inspired us to use the Green-Kubo relation, offering access to the time-dependent viscosity of our entangled system via

$$\eta(t) = \int_0^t G(t')dt', \tag{4}$$

which is shown in Fig. 3(a) over 6 decades in time. Our study suggests that at short times $t \lesssim \tau_0$, activity and entanglement play a minor role, but at intermediate times the data become significantly different. Following our previous predictions ($G_0 \sim LF_p/\sigma^3$ and $\tau_{\text{eff}} \sim L/v$), the time-dependent and stationary viscosity are expected to scale as $\eta \sim G_0\tau_{\text{eff}} \sim L^2$. Rescaling the data accordingly, we find a collapse onto a single master curve over 4 orders of magnitude in time [Fig. 3(b)].

Finally, as our data saturate at long times we can estimate the stationary viscosity of the system via $\eta_\infty \equiv \lim_{t\to\infty} \eta(t)$. First, we find that the stationary viscosity remains independent of Pe when the polymer length is fixed [see Fig. 3(a)]. Second and more strikingly, the predicted scaling $\eta_\infty \sim L^2$ is confirmed by an asymptotic data collapse in the regime of high entanglement ($L \gtrsim 500\sigma$) and high Péclet numbers (Pe $\gtrsim 8$) [Fig. 3(c)]. Hence, highly-engtangled active solutions follow a generic scaling of L^2, which is distinct from the characteristic L^3 scaling that broadly applies to equilibrium systems. Deviations become apparent for shorter polymer lengths ($L \leq 250$), where the solution becomes less entangled. This can be attributed to the fact that as we increase the Péclet number, the tube diameter ($\sim \sqrt{N_e}\sigma$) [19] also becomes larger. Therefore, it requires even longer polymers to observe a highly-entangled state.

Conclusions– Our study reveals a profound impact of activity on entangled polymer solutions, notably enhancing the stress plateau height, and predicts a scaling law for the stationary viscosity $\eta_\infty \sim L^2$, which goes beyond common knowledge and contrasts with the characteristic $\eta_\infty \sim L^3$ law for equilibrium systems.

Our findings open up new avenues for quantifying the viscoelastic properties of various experimental systems. While on the macroscale the dynamics of highly entangled *T. Tubifex* worms [14] could be studied, on the microscale activated nanotubes [38], synthetic polymer chains [39], or chromatin [8] represent potential realizations for entangled systems with unique properties. Our framework can provide insights for systems under deformation/shear, which may allow measuring the material properties of these systems in the presence of another time scale (inverse shear rate).

While significant progress has been made in understanding the viscoelastic properties of passive entangled systems under deformation [40–43], it is essential to highlight two key distinctions: First, active entangled systems exhibit a remarkable increase in the stress plateau height, whereas deformed passive entangled polymers typically experience a reduction in the stress plateau height [40, 41]. Second, active entangled systems remain force-free and do not develop a finite stress, con-

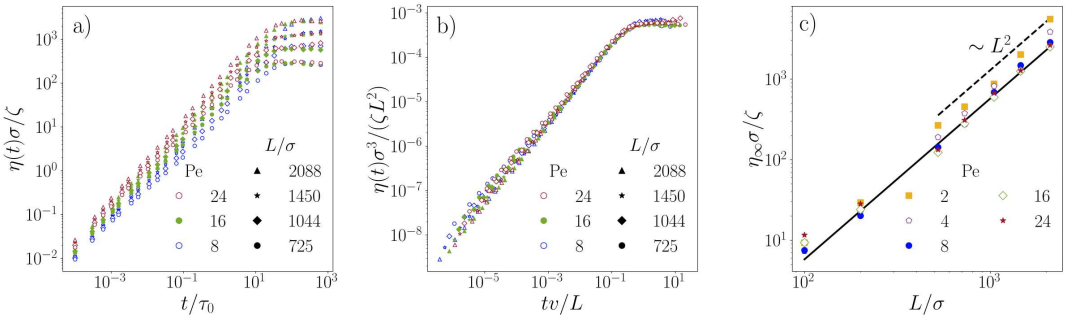

Figure 3. (a) Time-dependent viscosity for a wide range of Péclet numbers and polymer lengths. (b) A data collapse is obtained by rescaling the viscosity by $\eta(t)\sigma^3/\zeta L^2$ and the time scale by tv/L. (c) Long-time viscosity η_∞ as a function of polymer length L extracted from simulations for a wide range of Péclet numbers. The black line indicates the scaling of $\eta_\infty \sim L^2$.

trasting with the behavior of deformed passive entangled systems [44].

Moreover, our study focuses on self-propelled flexible polymers, yet many polymers found in nature are semi-flexible [45–53]. Therefore, a future challenge is to include the finite bending rigidity of polymers in our analysis and explore how the stress plateau and disengagement time vary with swimming speed. This would deepen our understanding of the behavior of biological filaments and contribute to the development of advanced materials with tailored viscoelastic properties, such as synthetic cells [54, 55].

S.M. gratefully acknowledges Robert S. Hoy and Joseph D. Dietz for valuable discussions regarding the equilibration of entangled polymer solutions, as well as Martin Kröger for sharing the topological analysis code before publishing it. The work of D.B. was supported within the EU MSCA-ITN ActiveMatter (proposal No. 812780). H.L. acknowledges funds from the German Research Foundation (DFG) project LO 418/29-1.

* suvendu.mandal@pkm.tu-darmstadt.de

[1] J. Howard, *Mechanics of Motor Proteins and the Cytoskeleton* (Springer, 2005).
[2] A. R. Bausch and K. Kroy, A bottom-up approach to cell mechanics, Nat. Phys. **2**, 231 (2006).
[3] V. Schaller, C. Weber, C. Semmrich, E. Frey, and A. R. Bausch, Polar patterns of driven filaments, Nature **467**, 73 (2010).
[4] T. Sanchez, D. T. N. Chen, S. J. DeCamp, M. Heymann, and Z. Dogic, Spontaneous motion in hierarchically assembled active matter, Nature **491**, 431 (2012).
[5] B. Alberts, *Molecular Biology of the Cell* (Garland Science, 2017).
[6] V. Levi, Q. Ruan, M. Plutz, A. S. Belmont, and E. Gratton, Chromatin dynamics in interphase cells revealed by tracking in a two-photon excitation microscope, Biophys. J. **89**, 4275 (2005).
[7] A. Zidovska, D. A. Weitz, and T. J. Mitchison, Micron-scale coherence in interphase chromatin dynamics, Proc. Natl. Acad. Sci. **110**, 15555 (2013).
[8] D. Saintillan, M. J. Shelley, and A. Zidovska, Extensile motor activity drives coherent motions in a model of interphase chromatin, Proc. Natl. Acad. Sci. **115**, 11442 (2018).
[9] A. Deblais, S. Woutersen, and D. Bonn, Rheology of entangled active polymer-like T. Tubifex Worms, Phys. Rev. Lett. **124**, 188002 (2020).
[10] A. Deblais, A. C. Maggs, D. Bonn, and S. Woutersen, Phase separation by entanglement of active polymerlike worms, Phys. Rev. Lett. **124**, 208006 (2020).
[11] Y. Ozkan-Aydin, D. I. Goldman, and M. S. Bhamla, Collective dynamics in entangled worm and robot blobs, Proc. Natl. Acad. Sci. **118**, e2010542118 (2021).
[12] V. P. Patil, H. Tuazon, E. Kaufman, T. Chakrabortty, D. Qin, J. Dunkel, and M. S. Bhamla, Ultrafast reversible self-assembly of living tangled matter, Science **380**, 392 (2023).
[13] S. Yardimci, T. Gibaud, W. Schwenger, M. R. Sartucci, P. D. Olmsted, J. S. Urbach, and Z. Dogic, Bonded straight and helical flagellar filaments form ultra-low-density glasses, Proc. Natl. Acad. Sci. **120**, e2215766120 (2023).
[14] A. Deblais, K. Prathyusha, R. Sinaasappel, H. Tuazon, I. Tiwari, V. P. Patil, and M. S. Bhamla, Worm blobs as entangled living polymers: From topological active matter to flexible soft robot collectives, Soft Matter **19**, 7057-7069 (2023).
[15] S. L. Wingstrand, N. J. Alvarez, Q. Huang, and O. Hassager, Linear and nonlinear universality in the rheology of polymer melts and solutions, Phys. Rev. Lett. **115**, 078302 (2015).
[16] J. Smrek, J. Garamella, R. Robertson-Anderson, and D. Michieletto, Topological tuning of DNA mobility in entangled solutions of supercoiled plasmids, Sci. Adv. **7**, eabf9260 (2021).

[17] M. Kapnistos, M. Lang, D. Vlassopoulos, W. Pyckhout-Hintzen, D. Richter, D. Cho, T. Chang, and M. Rubinstein, Unexpected power-law stress relaxation of entangled ring polymers, Nat. Mater. **7**, 997 (2008).
[18] M. Doi and S. F. Edwards, The theory of polymer dynamics, The Clarendon Press, Oxford University Press (1986).
[19] M. Rubinstein and R. H. Colby, Polymer physics, Oxford University Press (2003).
[20] P.-G. De Gennes, Reptation of a polymer chain in the presence of fixed obstacles, J. Chem. Phys. **55**, 572 (1971).
[21] R. Everaers, S. K. Sukumaran, G. S. Grest, C. Svaneborg, A. Sivasubramanian, and K. Kremer, Rheology and Microscopic Topology of Entangled Polymeric Liquids, Science **303**, 823 (2004).
[22] R. S. Hoy and M. Kröger, Unified analytic expressions for the entanglement length, tube diameter, and plateau modulus of polymer melts, Phys. Rev. Lett. **124**, 147801 (2020).
[23] J.-X. Hou, C. Svaneborg, R. Everaers, and G. S. Grest, Stress relaxation in entangled polymer melts, Phys. Rev. Lett. **105**, 068301 (2010).
[24] K. Kremer and G. S. Grest, Dynamics of entangled linear polymer melts: A molecular-dynamics simulation, J. Chem. Phys. **92**, 5057 (1990).
[25] J. D. Weeks, D. Chandler, and H. C. Andersen, Role of repulsive forces in determining the equilibrium structure of simple liquids, J. Chem. Phys. **54**, 5237 (1971).
[26] C. Kurzthaler, S. Mandal, T. Bhattacharjee, H. Löwen, S. S. Datta, and H. A. Stone, A geometric criterion for the optimal spreading of active polymers in porous media, Nat. Commun. **12**, 7088 (2021).
[27] V. Bianco, E. Locatelli, and P. Malgaretti, Globulelike conformation and enhanced diffusion of active polymers, Phys. Rev. Lett. **121**, 217802 (2018).
[28] K. R. Prathyusha, S. Henkes, and R. Sknepnek, Dynamically generated patterns in dense suspensions of active filaments, Phys. Rev. E **97**, 022606 (2018).
[29] M. Kröger, J. D. Dietz, R. S. Hoy, and C. Luap, The z1+ package: Shortest multiple disconnected path for the analysis of entanglements in macromolecular systems, Comput. Phys. Commun. **283**, 108567 (2023).
[30] See Supplemental Material at [URL], for details of the equilibration process, primitive path analysis, and investigation of viscoelasticity at shorter polymer lengths across various Péclet numbers.
[31] M. Kröger, Shortest multiple disconnected path for the analysis of entanglements in two-and three-dimensional polymeric systems, Comput. Phys. Commun. **168**, 209 (2005).
[32] S. Shanbhag and M. Kröger, Primitive Path Networks Generated by Annealing and Geometrical Methods: Insights into Differences, Macromolecules **40**, 2897 (2007).
[33] R. S. Hoy, K. Foteinopoulou, and M. Kröger, Topological analysis of polymeric melts: Chain-length effects and fast-converging estimators for entanglement length, Phys. Rev. E **80**, 031803 (2009).
[34] N. C. Karayiannis and M. Kröger, Combined Molecular Algorithms for the Generation, Equilibration and Topological Analysis of Entangled Polymers: Methodology and Performance, Int. J. Mol. Sci. **10**, 5054 (2009).
[35] H.-P. Hsu and K. Kremer, Static and dynamic properties of large polymer melts in equilibrium, J. Chem. Phys. **144**, 154907 (2016).
[36] M. Keshavarz, H. Engelkamp, J. Xu, E. Braeken, M. B. Otten, H. Uji-i, E. Schwartz, M. Koepf, A. Vananroye, J. Vermant, *et al.*, Nanoscale study of polymer dynamics, ACS nano **10**, 1434 (2016).
[37] M. Han, M. Fruchart, C. Scheibner, S. Vaikuntanathan, J. J. De Pablo, and V. Vitelli, Fluctuating hydrodynamics of chiral active fluids, Nat. Phys. **17**, 1260 (2021).
[38] A. Bacanu, J. F. Pelletier, Y. Jung, and N. Fakhri, Inferring scale-dependent non-equilibrium activity using carbon nanotubes, Nat. Nanotechnol. **18**, 905 (2023).
[39] T. Yang, B. Sprinkle, Y. Guo, J. Qian, D. Hua, A. Donev, D. W. Marr, and N. Wu, Reconfigurable microbots folded from simple colloidal chains, Proc. Natl. Acad. Sci. **117**, 18186 (2020).
[40] E. Van Ruymbeke and D. Vlassopoulos, *Macromolecular Rheology* (Wiley, 2022).
[41] H.-P. Hsu and K. Kremer, Clustering of entanglement points in highly strained polymer melts, Macromolecules **52**, 6756 (2019).
[42] S.-Q. Wang, S. Ravindranath, Y. Wang, and P. Boukany, New theoretical considerations in polymer rheology: Elastic breakdown of chain entanglement network, J. Chem. Phys. **127**, 10.1063/1.2753156 (2007).
[43] M. Cates, T. McLeish, and G. Marrucci, The rheology of entangled polymers at very high shear rates, EPL **21**, 451 (1993).
[44] T. C. O'Connor, A. Hopkins, and M. O. Robbins, Stress relaxation in highly oriented melts of entangled polymers, Macromolecules **52**, 8540 (2019).
[45] S. Banerjee, M. L. Gardel, and U. S. Schwarz, The actin cytoskeleton as an active adaptive material, Annu. Rev. Condens. Matter Phys. **11**, 421 (2020).
[46] R. G. Winkler and G. Gompper, The physics of active polymers and filaments, J. Chem. Phys. **153**, 040901 (2020).
[47] T. Eisenstecken, G. Gompper, and R. G. Winkler, Internal dynamics of semiflexible polymers with active noise, J. Chem. Phys. **146**, 154903 (2017).
[48] T. Eisenstecken and R. G. Winkler, Path integral description of semiflexible active Brownian polymers, J. Chem. Phys. **156**, 10.1063/5.0081020 (2022).
[49] L. Harnau, R. G. Winkler, and P. Reineker, Dynamic structure factor of semiflexible macromolecules in dilute solution, J. Chem. Phys. **104**, 6355 (1996).
[50] K. Kroy and E. Frey, Force-extension relation and plateau modulus for wormlike chains, Phys. Rev. Lett. **77**, 306 (1996).
[51] O. Hallatschek, E. Frey, and K. Kroy, Propagation and relaxation of tension in stiff polymers, Phys. Rev. Lett. **94**, 077804 (2005).
[52] P. Lang and E. Frey, Disentangling entanglements in biopolymer solutions, Nat. Commun. **9**, 1 (2018).
[53] S. Mandal, C. Kurzthaler, T. Franosch, and H. Löwen, Crowding-Enhanced Diffusion: An Exact Theory for Highly Entangled Self-Propelled Stiff Filaments, Phys. Rev. Lett. **125**, 138002 (2020).
[54] J. C. Blain and J. W. Szostak, Progress toward synthetic cells, Annu. Rev. Biochem **83**, 615 (2014).
[55] K. A. Ganzinger and P. Schwille, More from less–bottom-up reconstitution of cell biology, J. Cell Sci. **132**, jcs227488 (2019).

Supplemental Material: Giant Activity-Induced Stress Plateau in Entangled Polymer Solutions

Davide Breoni,[1] Christina Kurzthaler,[2] Benno Liebchen,[3] Hartmut Löwen,[1] and Suvendu Mandal[3,*]

[1] *Institut für Theoretische Physik II: Weiche Materie, Heinrich Heine-Universität Düsseldorf, Universitätsstraße 1, 40225 Düsseldorf, Germany*

[2] *Max Planck Institute for the Physics of Complex Systems, Nöhnitzer Straße 38, 01187 Dresden, Germany*

[3] *Technische Universität Darmstadt, Karolinenplatz 5, 64289 Darmstadt, Germany*

(Dated: September 29, 2023)

System equilibration

A well-known challenge in the field of entangled polymer physics has been the excessively long timescales required to reach equilibrium, with relaxation times scaling as the cube of the polymer length, i.e., $\sim L^3$. To circumvent the need for exceedingly lengthy simulations, we employ a highly efficient approach known as the double-bridging hybrid (DBH) bond-swapping algorithm, in conjunction with core softening techniques as outlined in Dietz et al.'s work [1]. The DBH algorithm operates by executing Monte Carlo (MC) moves to swap bonds and angles within the context of molecular dynamics simulations [Fig. 1]. Notably, this technique allows for the exchange of entire strands of polymers, a capability not available in standard molecular dynamics simulations. As a result, it substantially reduces the relaxation time, transitioning from the daunting $\sim L^3$ scaling to a much more manageable $\sim L$.

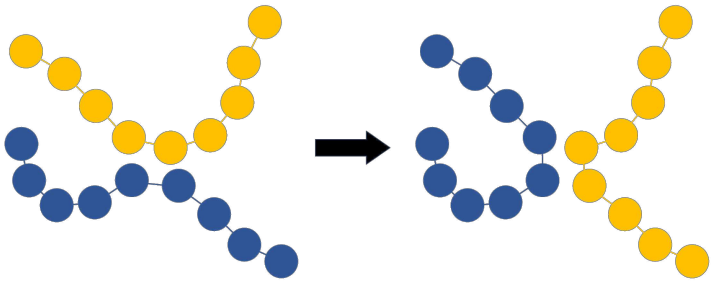

Figure 1. Representation of a double-bridging hybrid Monte Carlo move, demonstrating the exchange of bonds between separate polymer chains.

Primitive path analysis and topology

To explore the system's topology, we employ the Z1+ algorithm developed by M. Kröger [2]. The Z1+ algorithm iteratively simplifies the initial polymer configuration based on entanglement point positions, thus revealing the essential topological structure of the primitive paths [see Fig. 2(a)]. It begins by examining sets of three consecutive nodes along each polymer, initially defined by monomer positions. It evaluates the area enclosed by the triangle formed by these nodes, accounting for potential obstacles defined by intersecting paths. After multiple iterations, when further area reduction becomes unattainable, the resulting nodes represent the system's topological entanglement points. The average number of entanglement points, denoted as Z, is calculated as the mean number of nodes per path, while L_{pp} signifies the average path length. Figure 2(b) presents the final primitive path of a tracer polymer and its neighboring paths obtained using the Z1+ algorithm from a simulation configuration.

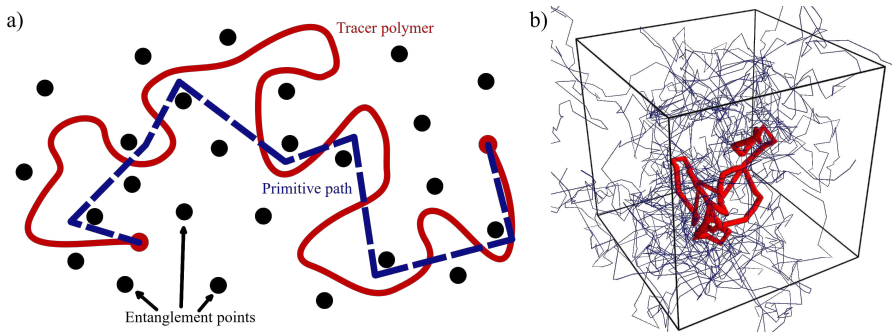

Figure 2. (a) Schematic representation illustrating the operation of the Z1+ algorithm. The primitive path (blue) relative to a tracer polymer (red) is depicted, with entanglement points (black) representing obstacles posed by other polymers. (b) Snapshot from a simulation displaying the primitive paths of a tracer polymer (red) and all of its neighboring polymers (blue). This configuration corresponds to Pe = 0 and $L = 1450\sigma$.

Polymer conformation and entanglement length

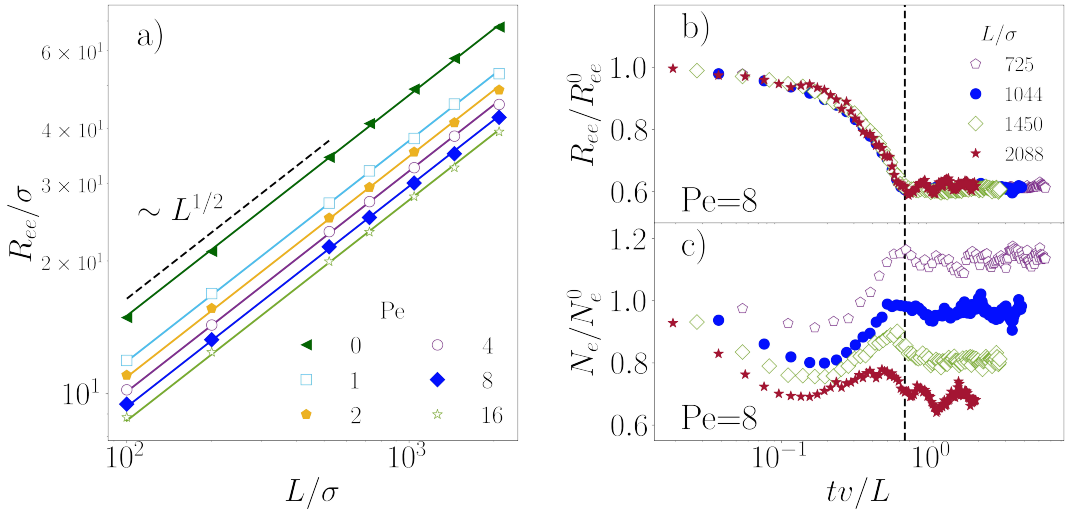

Figure 3. (a) End-to-end distance R_{ee} as a function of polymer size L/σ for various Péclet numbers Pe, exhibiting the characteristic end-to-end scaling behavior reminiscent of an ideal polymer chain, $\sim L^{1/2}$. (b) R_{ee}/R_{ee}^0 as a function of time for varied L at a fixed Pe = 8, time scaled by L/v. (c) Entanglement length N_e, normalized by the equilibrium value N_e^0 for Pe = 8, as a function of time.

Our investigation of the end-to-end distance R_{ee} of polymer chains at long times reveals a striking consistency: irrespective of the applied Péclet number (Pe), the system exhibits a common scaling law, $R_{ee} \sim L^{1/2}$, similar to ideal polymer solutions [see Fig. 3(a)]. Intriguingly, the prefactor of this scaling relation steadily decreases with increasing Pe, reminiscent of a coil-to-globule transition, observed in dilute active flexible polymer solutions [3]. However, in our complex, densely entangled networks, a true globule-like structure doesn't occur; instead, the $L^{1/2}$ scaling exponent

remains valid across all Pe values, highlighting a consistent entangled behavior in response to activity.

In Fig. 3(b), we explore the temporal evolution of the end-to-end distance for various polymer lengths L at a fixed Péclet number Pe = 8. Given that the $R_{ee} \sim L^{1/2}$ scaling remains valid across for all Péclet numbers, we anticipate the normalized R_{ee}/R_{ee}^0 to collapse at long times ($tv/L \gg 1$), as depicted in Fig. 3(b). Furthermore, we note a gradual reduction in R_{ee}, persisting until $tv/L \sim 1$. In contrast, we observe a 10% increase in the contour length of the primitive path (L_{pp}) at intermediate times ($tv/L \sim 0.1$), as illustrated in Fig. 1(c) of the main text. As a consequence, the entanglement length (N_e/N_e^0) is expected to exhibit a 30% decline at $tv/L \sim 0.1$ before ultimately reaching a saturation value at long times [see Fig. 3(c)].

Viscoelasticity at a fixed polymer length

We explore the complete time-dependent stress autocorrelation functions across a range of Péclet numbers (Pe), while keeping the polymer length fixed at $L/\sigma = 725$. In equilibrium, we find the familiar stress plateau $G_0 = 4\rho k_B T/(5N_e^0)$ [Fig. 4]. However, upon introducing activity, we observe that the short-time behavior of $G(t)$ increases by a factor of 4 compared to its equilibrium counterpart. This emphasizes the active role in shaping the early-time dynamics within the entangled tubes.

Moving on to intermediate times, $t \sim \tau_0$, the grip forces between neighboring polymers intensify, effectively acting as barriers for the individual polymer chains. Consequently, the system struggles to relax, resulting in a remarkable increase in the stress plateau. In fact, for $L/\sigma = 725$, the stress plateau height increases by more than three orders of magnitude [Fig. 4]. This striking phenomenon highlights the pivotal role played by activity-induced grip forces in shaping the viscoelastic responses

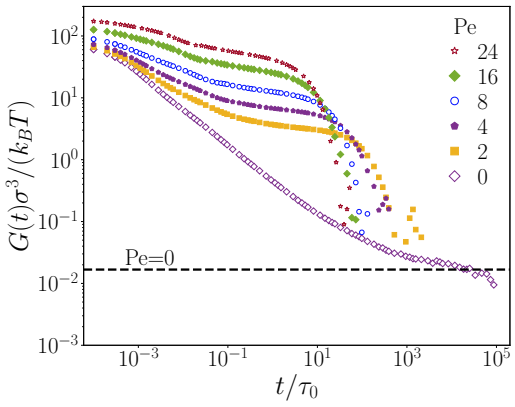

Figure 4. Stress relaxation modulus $G(t)$ as a function of t/τ_0 for $L = 725\sigma$ and varying P'eclet numbers. The dashed line represents the well-established prediction $G_0 = 4\rho k_B T/(5N_e^0)$.

Viscoelasticity of less entangled systems

To demonstrate the unique nature of the stress plateau enhancement due to activity in entangled solutions, we investigate polymer solutions with shorter polymer lengths, specifically $L = 100\sigma$. In Fig. 5, it becomes evident that the stress plateau is entirely absent from $G(t)$. Instead, the stress relaxation modulus now exhibits a distinct behavior: an initial $\sim t^{-1/2}$ decrease at short times, followed by an eventual exponential decay. This behavior aligns with the predictions of the Rouse model $G(t) \simeq k_B T\rho\,(t/\tau_0)^{-1/2}\,\mathrm{e}^{-t/\tau_R}$ (τ_R is the Rouse time) [4], which describes the relaxation dynamics of polymers in this low-entanglement-regime.

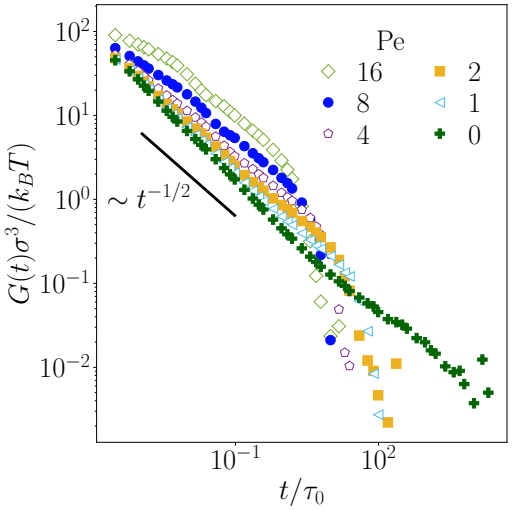

Figure 5. Stress relaxation modulus $G(t)$ as a function of t/τ_0 for $L = 100\sigma$ and varying Péclet numbers. The stress relaxation modulus exhibits an initial decay characterized by $\sim t^{-1/2}$ behavior, followed by a subsequent exponential decay, notably lacking the entangled plateau.

Movie

The movie (M1.mp4) illustrates the dynamic evolution of primitive paths involving a test polymer (in red) along with its neighboring polymers (in blue) in a simulation setting characterized by Pe = 4, $L = 1450\sigma$, and $\rho^\star = 0.85$. Notably, it reveals an increase in the primitive path, expanding from $L_{pp}/\sigma = 291.3$ to $L_{pp}/\sigma = 348.6$ at intermediate times $tv/L \sim 0.14$. Ultimately, the contour length of the primitive path L_{pp} decreases by 40% compared to its passive counterpart at long times ($tv/L \geq 1$).

* suvendu.mandal@pkm.tu-darmstadt.de

[1] J. D. Dietz and R. S. Hoy, Facile equilibration of well-entangled semiflexible bead–spring polymer melts, J. Chem. Phys. **156**, 10.1063/5.0072386 (2022).
[2] M. Kröger, J. D. Dietz, R. S. Hoy, and C. Luap, The z1+ package: Shortest multiple disconnected path for the analysis of entanglements in macromolecular systems, Comput. Phys. Commun. **283**, 108567 (2023).
[3] V. Bianco, E. Locatelli, and P. Malgaretti, Globulelike conformation and enhanced diffusion of active polymers, Phys. Rev. Lett. **121**, 217802 (2018).
[4] M. Rubinstein and R. H. Colby, Polymer physics, Oxford University Press https://doi.org/10.1002/pi.1472 (2003).

Chapter 4

Concluding remarks

This dissertation comprises multiple works on activity, complex environments and their relationship. Publication **P1** *Active Brownian and inertial particles in disordered environments: Short-time expansion of the mean-square displacement* [144] is an analytical study of the motion active Brownian particles in disordered landscapes in two dimensions. In it, the short time expansion of the mean squared displacement (MSD) of the particles is calculated exactly for both disordered motility and potential landscapes, and both in the underdamped and overdamped regime. In particular, the contribution of noise to the MSD is explored, and for underdamped system new superballistic regimes are found. The strongest achievement of this publication is the systematic method with which the exact MSD is calculated, which can be extended to a large variety of systems, from different models of active matter [145, 146] to responsive media [55, 147], to time-dependent random fields [91, 148].

In publication **P2** *Active noise-driven particles under space-dependent friction in one dimension* [149] the same method used to calculate the short-time MSD of **P1** is employed in the case of a 1D Brownian particle in an environment where potential and friction are space-dependent. As a result, we find that the space-dependent friction can lead to a ballistic regime at short times, effectively driving the particle with noise. The work also features analytical results for the stationary probability density function of the position in the presence of the aforementioned landscapes. Some possibilities for continuation of this work are the study of similar systems in 2D, the inclusion of inertia [150, 151] or collective phenomena [152, 153].

Publication **P3** *Brownian particles driven by spatially periodic noise* [154] features a study of Brownian particles moving in a 1D periodic temperature landscape, later accompanied by a tilted periodic potential. We find, as in **P2**, that the space dependent noise strength leads to a drift, which in this case turns out to be really slow, as the MD is proportional to $\sqrt{t}$. When also considering the tilted potential, we calculated the value of phase shift between potential and temperature for which the long-time diffusion and velocity are maximized. In the special case of a potential near the critical tilt (at which the potential becomes monotonically decreasing) we calculated the probability current. A system such as the one described in

this publication can be realized experimentally by setting Brownian particles in a ring-like structure [155] where a gradient in the temperature is externally induced. In order to achieve higher degrees in noise gradient, one can also vary, instead of the temperature, the viscosity [60, 156], or utilize active particles and tune their rotational diffusion [157].

Publication **P4** *A one-dimensional three-state run-and-tumble model with a 'cell cycle'* [158] proposes a 1D model for organisms with a life cycle. It draws inspiration from the bacterium *Caulobacter crescentus*, which during its lifetime switches from motile to static [159, 160], and defines three different populations, one passive and two active (backward and forward motion), with the possibility for particles to change populations with a certain rate and to interact with each other. The study calculates the MSD and MD in the non-interacting regime and finds the formation of interesting wave-like structures for certain parameters when cell-cell interactions are turned on. This model is very flexible and can be extended in multiple ways: it is possible to modify the cell cycle to describe other types of cells [161, 162], move into 2D space and include a description of the nematics of cells [163, 164] or more complex swimming behaviors [165].

In publication **P5** *Patchy landscapes promote stability of small groups* [166] we have a realization of active Brownian particles in a disordered motility field. The ABPs are Janus particles moving thanks to thermophoresis in a mixture of water and 2,6-lutidine [35, 111, 112]. The source of activity, and hence the motility field, is laser light, which can be filtered to produce a disordered speckle field [89, 90]. This work shows the effects of a disordered field on active particles, as disorder severely hampers their diffusion reduces both the size of clusters and their ability to exchange particles with each other. As a follow-up to this project, the motility fields could be dynamically tuned [167], as one of the most convenient property of light fields is that they can be easily modified: one could for example go from homogeneous to speckle field during the same experiment or change the structure of the speckle.

At last, publication **P6** *Giant Activity-Induced Stress Plateau in Entangled Polymer Solutions* [168] discusses the effects that activity has on the rheology of strongly entangled polymer solutions, finding a remarkable increase in the elasticity plateau and a reduction in both the relaxation time and the viscosity as functions of the polymer length. This work is an important step forward in the study and characterization of active and entangled polymer systems, such as chromatin [169], worms [117] or activated nanotubes [170]. It also opens up to the possibility of realizing active materials [171, 172], which viscoelastic properties could be tuned externally by varying the energy intake of the system (and hence the activity).

References

[1] L. E. Orgel, *The origin of life—a review of facts and speculations*, Trends in Biochemical Sciences **23**, 491 (1998).

[2] N. Kitadai and S. Maruyama, *Origins of building blocks of life: A review*, Geoscience Frontiers **9**, 1117 (2018).

[3] R. Swendsen, *An Introduction to Statistical Mechanics and Thermodynamics: Second Edition* (Oxford University Press, 2020).

[4] Y. Bar-yam, *Dynamics Of Complex Systems* (CRC Press, 2019).

[5] D. J. T. Sumpter, in *Collective Animal Behavior* (Princeton University Press, 2010).

[6] D. M. Gordon, *The Ecology of Collective Behavior*, PLOS Biology **12**, e1001805 (2014).

[7] S. B. Rosenthal, C. R. Twomey, A. T. Hartnett, H. S. Wu, and I. D. Couzin, *Revealing the hidden networks of interaction in mobile animal groups allows prediction of complex behavioral contagion*, Proceedings of the National Academy of Sciences **112**, 4690 (2015).

[8] B. A. Hazlett, *The Behavioral Ecology of Hermit Crabs*, Annual Review of Ecology and Systematics **12**, 1 (1981).

[9] M. C. Marchetti, J. F. Joanny, S. Ramaswamy, T. B. Liverpool, J. Prost, M. Rao, and R. A. Simha, *Hydrodynamics of soft active matter*, Reviews of Modern Physics **85**, 1143 (2013).

[10] C. Bechinger, R. Di Leonardo, H. Löwen, C. Reichhardt, G. Volpe, and G. Volpe, *Active particles in complex and crowded environments*, Reviews of Modern Physics **88**, 045006 (2016).

[11] S. Ramaswamy, *The Mechanics and Statistics of Active Matter*, Annual Review of Condensed Matter Physics **1**, 323 (2010).

[12] D. Needleman and Z. Dogic, *Active matter at the interface between materials science and cell biology*, Nature Reviews Materials **2**, 1 (2017).

[13] J. Hu, S. Zhou, Y. Sun, X. Fang, and L. Wu, *Fabrication, properties and applications of Janus particles*, Chemical Society Reviews **41**, 4356 (2012).

[14] A. Walther and A. H. E. Müller, *Janus Particles: Synthesis, Self-Assembly, Physical Properties, and Applications*, Chemical Reviews **113**, 5194 (2013).

[15] S. van Teeffelen and H. Löwen, *Dynamics of a Brownian circle swimmer*, Physical Review E **78**, 020101 (2008).

[16] M. R. Shaebani, A. Wysocki, R. G. Winkler, G. Gompper, and H. Rieger, *Computational models for active matter*, Nature Reviews Physics **2**, 181 (2020).

[17] D. Vigolo, R. Rusconi, H. A. Stone, and R. Piazza, *Thermophoresis : microfluidics characterization and separation*, Soft Matter **6**, 3489 (2010).

[18] M. Yang and M. Ripoll, *Thermoosmotic microfluidics*, Soft Matter **12**, 8564 (2016).

[19] M. Y. Sherman, E. Timkina, and A. Glagolev, *Viscosity taxis in Escherichia coli*, FEMS Microbiology Letters **13**, 137 (1982).

[20] B. Liebchen, P. Monderkamp, B. ten Hagen, and H. Löwen, *Viscotaxis: Microswimmer Navigation in Viscosity Gradients*, Physical Review Letters **120**, 208002 (2018).

[21] A. R. Sprenger, M. A. Fernandez-Rodriguez, L. Alvarez, L. Isa, R. Wittkowski, and H. Löwen, *Active Brownian Motion with Orientation-Dependent Motility: Theory and Experiments*, Langmuir **36**, 7066 (2020).

[22] A. R. Sprenger, S. Jahanshahi, A. V. Ivlev, and H. Löwen, *Time-dependent inertia of self-propelled particles: The Langevin rocket*, Physical Review E **103**, 042601 (2021).

[23] J. Kula, T. Czernik, and J. Łuczka, *Brownian Ratchets: Transport Controlled by Thermal Noise*, Physical Review Letters **80**, 1377 (1998).

[24] E. R. Kay, D. A. Leigh, and F. Zerbetto, *Synthetic Molecular Motors and Mechanical Machines*, Angewandte Chemie International Edition **46**, 72 (2007).

[25] S.-H. Wu, N. Huang, E. Jaquay, and M. L. Povinelli, *Near-Field, On-Chip Optical Brownian Ratchets*, Nano Letters **16**, 5261 (2016).

[26] N. G. van Kampen, *Itô versus Stratonovich*, Journal of Statistical Physics **24**, 175 (1981).

[27] C. Gardiner, *Stochastic Methods* (Springer Berlin Heidelberg, 2010).

[28] R. Mannella and P. V. E. McClintock, *Itô versus Stratonovich: 30 years later*, Fluctuation and Noise Letters (2012).

[29] D. Pavlov and A. Kasumyan, *Patterns and mechanisms of schooling behavior in fish: A review*, Journal of Ichthyology **40**, S163 (2000).

[30] A. Garcimartín, J. M. Pastor, L. M. Ferrer, J. J. Ramos, C. Martín-Gómez, and I. Zuriguel, *Flow and clogging of a sheep herd passing through a bottleneck*, Physical Review E **91**, 022808 (2015).

[31] A. Cavagna and I. Giardina, *Bird Flocks as Condensed Matter*, Annual Review of Condensed Matter Physics **5**, 183 (2014).

[32] R. Di Leonardo, L. Angelani, D. Dell'Arciprete, G. Ruocco, V. Iebba, S. Schippa, M. P. Conte, F. Mecarini, F. De Angelis, and E. Di Fabrizio, *Bacterial ratchet motors*, Proceedings of the National Academy of Sciences **107**, 9541 (2010).

[33] J. Arlt, V. A. Martinez, A. Dawson, T. Pilizota, and W. C. K. Poon, *Painting with light-powered bacteria*, Nature Communications **9**, 768 (2018).

[34] R. Alert and X. Trepat, *Physical Models of Collective Cell Migration*, Annual Review of Condensed Matter Physics **11**, 77 (2020).

[35] I. Buttinoni, J. Bialké, F. Kümmel, H. Löwen, C. Bechinger, and T. Speck, *Dynamical Clustering and Phase Separation in Suspensions of Self-Propelled Colloidal Particles*, Physical Review Letters **110**, 238301 (2013).

[36] J. Palacci, S. Sacanna, A. P. Steinberg, D. J. Pine, and P. M. Chaikin, *Living Crystals of Light-Activated Colloidal Surfers*, Science **339**, 936 (2013).

[37] H. Risken, in *The Fokker-Planck Equation: Methods of Solution and Applications*, edited by H. Risken (Springer, Berlin, Heidelberg, 1996).

[38] E. Fodor, C. Nardini, M. E. Cates, J. Tailleur, P. Visco, and F. van Wijland, *How Far from Equilibrium Is Active Matter?*, Physical Review Letters **117**, 038103 (2016).

[39] J. O'Byrne, Y. Kafri, J. Tailleur, and F. van Wijland, *Time irreversibility in active matter, from micro to macro*, Nature Reviews Physics **4**, 167 (2022).

[40] T. Vicsek and A. Zafeiris, *Collective motion*, Physics Reports **517**, 71 (2012).

[41] M. Ballerini, N. Cabibbo, R. Candelier, A. Cavagna, E. Cisbani, I. Giardina, V. Lecomte, A. Orlandi, G. Parisi, A. Procaccini, M. Viale, and V. Zdravkovic, *Interaction ruling animal collective behavior depends on topological rather than metric distance: Evidence from a field study*, Proceedings of the National Academy of Sciences **105**, 1232 (2008).

[42] M. G. Mazza, *The physics of biofilms—an introduction*, Journal of Physics D: Applied Physics **49**, 203001 (2016).

[43] A. Corbetta and F. Toschi, *Physics of Human Crowds*, Annual Review of Condensed Matter Physics **14**, 311 (2023).

[44] N. Kumar, H. Soni, S. Ramaswamy, and A. K. Sood, *Flocking at a distance in active granular matter*, Nature Communications **5**, 4688 (2014).

[45] T. Vicsek, A. Czirók, E. Ben-Jacob, I. Cohen, and O. Shochet, *Novel Type of Phase Transition in a System of Self-Driven Particles*, Physical Review Letters **75**, 1226 (1995).

[46] J. Toner and Y. Tu, *Long-Range Order in a Two-Dimensional Dynamical XY Model: How Birds Fly Together*, Physical Review Letters **75**, 4326 (1995).

[47] J. Toner, Y. Tu, and S. Ramaswamy, *Hydrodynamics and phases of flocks*, Annals of Physics **318**, 170 (2005).

[48] C. Maggi, U. M. B. Marconi, N. Gnan, and R. Di Leonardo, *Multidimensional stationary probability distribution for interacting active particles*, Scientific Reports **5**, 10742 (2015).

[49] L. Caprini and U. M. B. Marconi, *Active particles under confinement and effective force generation among surfaces*, Soft Matter **14**, 9044 (2018).

[50] D. Martin, J. O'Byrne, M. E. Cates, E. Fodor, C. Nardini, J. Tailleur, and F. van Wijland, *Statistical mechanics of active Ornstein-Uhlenbeck particles*, Physical Review E **103**, 032607 (2021).

[51] L. Angelani, R. Di Leonardo, and M. Paoluzzi, *First-passage time of run-and-tumble particles*, The European Physical Journal E **37**, 59 (2014).

[52] G. Gradenigo and S. N. Majumdar, *A first-order dynamical transition in the displacement distribution of a driven run-and-tumble particle*, Journal of Statistical Mechanics: Theory and Experiment **2019**, 053206 (2019).

[53] E. Blagodatskaya and Y. Kuzyakov, *Active microorganisms in soil: Critical review of estimation criteria and approaches*, Soil Biology and Biochemistry **67**, 192 (2013).

[54] M. Dogterom and G. H. Koenderink, *Actin–microtubule crosstalk in cell biology*, Nature Reviews Molecular Cell Biology **20**, 38 (2019).

[55] K. Qi, E. Westphal, G. Gompper, and R. G. Winkler, *Enhanced Rotational Motion of Spherical Squirmer in Polymer Solutions*, Physical Review Letters **124**, 068001 (2020).

[56] A. Bahat, I. Tur-Kaspa, A. Gakamsky, L. C. Giojalas, H. Breitbart, and M. Eisenbach, *Thermotaxis of mammalian sperm cells: A potential navigation mechanism in the female genital tract*, Nature Medicine **9**, 149 (2003).

[57] H.-R. Jiang, N. Yoshinaga, and M. Sano, *Active Motion of a Janus Particle by Self-Thermophoresis in a Defocused Laser Beam*, Physical Review Letters **105**, 268302 (2010).

[58] M. Yang and M. Ripoll, *A self-propelled thermophoretic microgear*, Soft Matter **10**, 1006 (2014).

[59] J. Burelbach, D. Frenkel, I. Pagonabarraga, and E. Eiser, *A unified description of colloidal thermophoresis*, The European Physical Journal E **41**, 7 (2018).

[60] C. Datt and G. J. Elfring, *Active Particles in Viscosity Gradients*, Physical Review Letters **123**, 158006 (2019).

[61] W. F. Paxton, K. C. Kistler, C. C. Olmeda, A. Sen, S. K. St. Angelo, Y. Cao, T. E. Mallouk, P. E. Lammert, and V. H. Crespi, *Catalytic Nanomotors: Autonomous Movement of Striped Nanorods*, Journal of the American Chemical Society **126**, 13424 (2004).

[62] J. K. G. Dhont, *An Introduction to Dynamics of Colloids* (Elsevier, 1996).

[63] I. S. Aranson, *Active colloids*, Physics-Uspekhi **56**, 79 (2013).

[64] R. P. Feynman, R. B. Leighton, and M. Sands, *The Feynman Lectures on Physics, Vol. I: The New Millennium Edition: Mainly Mechanics, Radiation, and Heat* (Hachette UK, 2015).

[65] H. Mori, *Transport, Collective Motion, and Brownian Motion*)*, Progress of Theoretical Physics **33**, 423 (1965).

[66] W. Coffey and Y. P. Kalmykov, *The Langevin Equation: With Applications to Stochastic Problems in Physics, Chemistry and Electrical Engineering* (World Scientific, 2012).

[67] A. Einstein, *Über die von der molekularkinetischen Theorie der Wärme geforderte Bewegung von in ruhenden Flüssigkeiten suspendierten Teilchen*, Annalen der Physik **vol. 4, t. 17**, (1905).

[68] A. Einstein, *Investigations on the Theory of the Brownian Movement* (Courier Corporation, 1956).

[69] F. M. White, *Fluid Mechanics* (McGraw-Hill Education - Europe, New York, NY, 2015).

[70] J. R. Howse, R. A. L. Jones, A. J. Ryan, T. Gough, R. Vafabakhsh, and R. Golestanian, *Self-Motile Colloidal Particles: From Directed Propulsion to Random Walk*, Physical Review Letters **99**, 048102 (2007).

[71] H. Löwen, *Inertial effects of self-propelled particles: From active Brownian to active Langevin motion*, The Journal of Chemical Physics **152**, 040901 (2020).

[72] S. Behera, D. P. Dogra, M. K. Bandyopadhyay, and P. P. Roy, *Understanding crowd flow patterns using active-Langevin model*, Pattern Recognition **119**, 108037 (2021).

[73] L. Caprini, A. Ldov, R. K. Gupta, H. Ellenberg, R. Wittmann, H. Löwen, and C. Scholz. *Emergent memory from tapping collisions in active granular matter*, (2023). arXiv:2310.19566 [cond-mat].

[74] L. Caprini and U. Marini Bettolo Marconi, *Inertial self-propelled particles*, The Journal of Chemical Physics **154**, 024902 (2021).

[75] C. Reichhardt and C. J. O. Reichhardt, *Depinning and nonequilibrium dynamic phases of particle assemblies driven over random and ordered substrates: a review*, Reports on Progress in Physics **80**, 026501 (2016).

[76] O. Chepizhko and F. Peruani, *Diffusion, Subdiffusion, and Trapping of Active Particles in Heterogeneous Media*, Physical Review Letters **111**, 160604 (2013).

[77] T. Bertrand, Y. Zhao, O. Bénichou, J. Tailleur, and R. Voituriez, *Optimized Diffusion of Run-and-Tumble Particles in Crowded Environments*, Physical Review Letters **120**, 198103 (2018).

[78] D. M. v. Roon, G. Volpe, M. M. T. d. Gama, and N. A. M. Araújo, *The role of disorder in the motion of chiral active particles in the presence of obstacles*, Soft Matter **18**, 6899 (2022).

[79] A. Morin, N. Desreumaux, J.-B. Caussin, and D. Bartolo, *Distortion and destruction of colloidal flocks in disordered environments*, Nature Physics **13**, 63 (2017).

[80] J. Toner, N. Guttenberg, and Y. Tu, *Swarming in the Dirt: Ordered Flocks with Quenched Disorder*, Physical Review Letters **121**, 248002 (2018).

[81] E. Pinçe, S. K. P. Velu, A. Callegari, P. Elahi, S. Gigan, G. Volpe, and G. Volpe, *Disorder-mediated crowd control in an active matter system*, Nature Communications **7**, 10907 (2016).

[82] S. Ro, Y. Kafri, M. Kardar, and J. Tailleur, *Disorder-Induced Long-Ranged Correlations in Scalar Active Matter*, Physical Review Letters **126**, 048003 (2021).

[83] C. Reichhardt and C. J. Olson Reichhardt, *Active matter transport and jamming on disordered landscapes*, Physical Review E **90**, 012701 (2014).

[84] D. Takagi, J. Palacci, A. B. Braunschweig, M. J. Shelley, and J. Zhang, *Hydrodynamic capture of microswimmers into sphere-bound orbits*, Soft Matter **10**, 1784 (2014).

[85] C. Sándor, A. Libál, C. Reichhardt, and C. J. Olson Reichhardt, *Dynamic phases of active matter systems with quenched disorder*, Physical Review E **95**, 032606 (2017).

[86] C. Lozano, J. R. Gomez-Solano, and C. Bechinger, *Active particles sense micromechanical properties of glasses*, Nature Materials **18**, 1118 (2019).

[87] G. Frangipane, G. Vizsnyiczai, C. Maggi, R. Savo, A. Sciortino, S. Gigan, and R. Di Leonardo, *Invariance properties of bacterial random walks in complex structures*, Nature Communications **10**, 2442 (2019).

[88] T. Bhattacharjee and S. S. Datta, *Bacterial hopping and trapping in porous media*, Nature Communications **10**, 2075 (2019).

[89] G. Volpe, L. Kurz, A. Callegari, G. Volpe, and S. Gigan, *Speckle optical tweezers: micromanipulation with random light fields*, Optics Express **22**, 18159 (2014).

[90] G. Volpe, G. Volpe, and S. Gigan, *Brownian Motion in a Speckle Light Field: Tunable Anomalous Diffusion and Selective Optical Manipulation*, Scientific Reports **4**, 3936 (2014).

[91] M. Paoluzzi, R. D. Leonardo, and L. Angelani, *Run-and-tumble particles in speckle fields*, Journal of Physics: Condensed Matter **26**, 375101 (2014).

[92] I. M. Vellekoop and A. P. Mosk, *Focusing coherent light through opaque strongly scattering media*, Optics Letters **32**, 2309 (2007).

[93] C. Zhang, Y. Xin, and X. Zhu, *Multiscale and local engineering of speckle morphology through disordered media*, Optics Letters **47**, 6029 (2022).

[94] R. D. L. Hanes, C. Dalle-Ferrier, M. Schmiedeberg, M. C. Jenkins, and S. U. Egelhaaf, *Colloids in one dimensional random energy landscapes*, Soft Matter **8**, 2714 (2012).

[95] F. Evers, R. D. L. Hanes, C. Zunke, R. F. Capellmann, J. Bewerunge, C. Dalle-Ferrier, M. C. Jenkins, I. Ladadwa, A. Heuer, R. Castañeda-Priego, and S. U. Egelhaaf, *Colloids in light fields: Particle dynamics in random and periodic energy landscapes*, The European Physical Journal Special Topics **222**, 2995 (2013).

[96] C. Lozano, B. ten Hagen, H. Löwen, and C. Bechinger, *Phototaxis of synthetic microswimmers in optical landscapes*, Nature Communications **7**, 12828 (2016).

[97] S. Jahanshahi, C. Lozano, B. Liebchen, H. Löwen, and C. Bechinger, *Realization of a motility-trap for active particles*, Communications Physics **3**, 1 (2020).

[98] J. Als-Nielsen and D. McMorrow, *Elements of Modern X-ray Physics* (John Wiley & Sons, 2011).

[99] R. Durrett and R. Durrett, *Probability: Theory and Examples* (Cambridge University Press, 2019).

[100] K. Itô, *On a formula concerning stochastic differentials*, Nagoya Mathematical Journal **3**, 55 (1951).

[101] N. Podewitz, F. Jülicher, G. Gompper, and J. Elgeti, *Interface dynamics of competing tissues*, New Journal of Physics **18**, 083020 (2016).

[102] A. Sengupta, T. Kruppa, and H. Löwen, *Chemotactic predator-prey dynamics*, Physical Review E **83**, 031914 (2011).

[103] C.-J. Chen and C. Bechinger, *Collective response of microrobotic swarms to external threats*, New Journal of Physics **24**, 033001 (2022). Publisher: IOP Publishing.

[104] J. Tailleur and M. E. Cates, *Statistical Mechanics of Interacting Run-and-Tumble Bacteria*, Physical Review Letters **100**, 218103 (2008).

[105] J. Li, S. K. Schnyder, M. S. Turner, and R. Yamamoto, *Role of the Cell Cycle in Collective Cell Dynamics*, Physical Review X **11**, 031025 (2021).

[106] P. Glendinning, *Stability, Instability and Chaos: An Introduction to the Theory of Nonlinear Differential Equations* (Cambridge University Press, 1994).

[107] B. t. Hagen, S. van Teeffelen, and H. Löwen, *Non-Gaussian behaviour of a self-propelled particle on a substrate*, Condensed Matter Physics **12**, 725 (2009).

[108] M. Doi and S. F. Edwards, *The theory of polymer dynamics*, The Clarendon Press, Oxford University Press (1986).

[109] M. Caraglio and T. Franosch, *Analytic Solution of an Active Brownian Particle in a Harmonic Well*, Physical Review Letters **129**, 158001 (2022).

[110] C. Kurzthaler, S. Leitmann, and T. Franosch, *Intermediate scattering function of an anisotropic active Brownian particle*, Scientific Reports **6**, 36702 (2016).

[111] A. Würger, *Self-Diffusiophoresis of Janus Particles in Near-Critical Mixtures*, Physical Review Letters **115**, 188304 (2015).

[112] I. Buttinoni, G. Volpe, F. Kümmel, G. Volpe, and C. Bechinger, *Active Brownian motion tunable by light*, Journal of Physics: Condensed Matter **24**, 284129 (2012).

[113] J. R. Gomez-Solano, S. Samin, C. Lozano, P. Ruedas-Batuecas, R. van Roij, and C. Bechinger, *Tuning the motility and directionality of self-propelled colloids*, Scientific Reports **7**, 14891 (2017).

[114] C. Lozano, B. Liebchen, B. t. Hagen, C. Bechinger, and H. Löwen, *Propagating density spikes in light-powered motility-ratchets*, Soft Matter **15**, 5185 (2019).

[115] C. S. Dias, M. Trivedi, G. Volpe, N. A. M. Araújo, and G. Volpe. *Environmental Memory Boosts Group Formation of Clueless Individuals*, (2023). arXiv:2306.00516 [cond-mat].

[116] J. M. G. Cowie and V. Arrighi, *Polymers: Chemistry and Physics of Modern Materials, Third Edition* (CRC Press, 2007).

[117] A. Deblais, K. R. Prathyusha, R. Sinaasappel, H. Tuazon, I. Tiwari, V. P. Patil, and M. Saad Bhamla, *Worm blobs as entangled living polymers: from topological active matter to flexible soft robot collectives*, Soft Matter **19**, 7057 (2023).

[118] M. Rubinstein and R. H. Colby, *Polymer physics*, Oxford University Press (2003).

[119] P. J. Flory, *The Configuration of Real Polymer Chains*, The Journal of Chemical Physics **17**, 303 (1949).

[120] M. Bley, U. Baul, and J. Dzubiella, *Controlling solvent quality by time: Self-avoiding sprints in nonequilibrium polymerization*, Physical Review E **104**, 034501 (2021).

[121] R. Christensen, *Theory of Viscoelasticity: An Introduction* (Elsevier, 2012).

[122] C. Ortiz and G. Hadziioannou, *Entropic Elasticity of Single Polymer Chains of Poly(methacrylic acid) Measured by Atomic Force Microscopy*, Macromolecules **32**, 780 (1999).

[123] P. de Gennes, *Entangled polymers*, Physics Today **36**, 33 (1983).

[124] Y.-H. Zang and P. J. Carreau, *A correlation between critical end-to-end distance for entanglements and molecular chain diameter of polymers*, Journal of Applied Polymer Science **42**, 1965 (1991).

[125] R. G. Winkler, J. Elgeti, and G. Gompper, *Active Polymers — Emergent Conformational and Dynamical Properties: A Brief Review*, Journal of the Physical Society of Japan **86**, 101014 (2017).

[126] R. G. Winkler and G. Gompper, *The physics of active polymers and filaments*, The Journal of Chemical Physics **153**, 040901 (2020).

[127] A. W. C. Lau, B. D. Hoffman, A. Davies, J. C. Crocker, and T. C. Lubensky, *Microrheology, Stress Fluctuations, and Active Behavior of Living Cells*, Physical Review Letters **91**, 198101 (2003).

[128] W. Lu, M. Winding, M. Lakonishok, J. Wildonger, and V. I. Gelfand, *Microtubule–microtubule sliding by kinesin-1 is essential for normal cytoplasmic streaming in Drosophila oocytes*, Proceedings of the National Academy of Sciences **113**, E4995 (2016).

[129] J. Yan, M. Han, J. Zhang, C. Xu, E. Luijten, and S. Granick, *Reconfiguring active particles by electrostatic imbalance*, Nature Materials **15**, 1095 (2016).

[130] R. E. Isele-Holder, J. Elgeti, and G. Gompper, *Self-propelled worm-like filaments: spontaneous spiral formation, structure, and dynamics*, Soft Matter **11**, 7181 (2015).

[131] A. Deblais, A. Maggs, D. Bonn, and S. Woutersen, *Phase Separation by Entanglement of Active Polymerlike Worms*, Physical Review Letters **124**, 208006 (2020).

[132] Y. Ozkan-Aydin, D. I. Goldman, and M. S. Bhamla, *Collective dynamics in entangled worm and robot blobs*, Proceedings of the National Academy of Sciences **118**, e2010542118 (2021).

[133] H.-P. Hsu and K. Kremer, *Static and dynamic properties of large polymer melts in equilibrium*, The Journal of Chemical Physics **144**, 154907 (2016).

[134] C. Kurzthaler, S. Mandal, T. Bhattacharjee, H. Löwen, S. S. Datta, and H. A. Stone, *A geometric criterion for the optimal spreading of active polymers in porous media*, Nature Communications **12**, 7088 (2021).

[135] J. D. Dietz and R. S. Hoy, *Facile equilibration of well-entangled semiflexible bead–spring polymer melts*, The Journal of Chemical Physics **156**, 014103 (2022).

[136] R. Auhl, R. Everaers, G. S. Grest, K. Kremer, and S. J. Plimpton, *Equilibration of long chain polymer melts in computer simulations*, The Journal of Chemical Physics **119**, 12718 (2003).

[137] J. Hammersley, *Monte Carlo Methods* (Springer Science & Business Media, 2013).

[138] N. Metropolis, A. W. Rosenbluth, M. N. Rosenbluth, A. H. Teller, and E. Teller, *Equation of State Calculations by Fast Computing Machines*, The Journal of Chemical Physics **21**, 1087 (1953).

[139] J.-X. Hou, C. Svaneborg, R. Everaers, and G. S. Grest, *Stress Relaxation in Entangled Polymer Melts*, Physical Review Letters **105**, 068301 (2010).

[140] R. Everaers, S. K. Sukumaran, G. S. Grest, C. Svaneborg, A. Sivasubramanian, and K. Kremer, *Rheology and Microscopic Topology of Entangled Polymeric Liquids*, Science **303**, 823 (2004).

[141] S. K. Sukumaran, G. S. Grest, K. Kremer, and R. Everaers, *Identifying the primitive path mesh in entangled polymer liquids*, Journal of Polymer Science Part B: Polymer Physics **43**, 917 (2005).

[142] M. Kröger, J. D. Dietz, R. S. Hoy, and C. Luap, *The Z1+ package: Shortest multiple disconnected path for the analysis of entanglements in macromolecular systems*, Computer Physics Communications **283**, 108567 (2023).

[143] R. S. Hoy, K. Foteinopoulou, and M. Kröger, *Topological analysis of polymeric melts: Chain-length effects and fast-converging estimators for entanglement length*, Physical Review E **80**, 031803 (2009).

[144] D. Breoni, M. Schmiedeberg, and H. Löwen, *Active Brownian and inertial particles in disordered environments: Short-time expansion of the mean-square displacement*, Physical Review E **102**, 062604 (2020).

[145] F. J. Sevilla, R. F. Rodríguez, and J. R. Gomez-Solano, *Generalized Ornstein-Uhlenbeck model for active motion*, Physical Review E **100**, 032123 (2019).

[146] L. Caprini, A. R. Sprenger, H. Löwen, and R. Wittmann, *The parental active model: A unifying stochastic description of self-propulsion*, The Journal of Chemical Physics **156**, 071102 (2022).

[147] S. Liu, S. Shankar, M. C. Marchetti, and Y. Wu, *Viscoelastic control of spatiotemporal order in bacterial active matter*, Nature **590**, 80 (2021).

[148] A. Geiseler, P. Hänggi, and F. Marchesoni, *Self-Polarizing Microswimmers in Active Density Waves*, Scientific Reports **7**, 41884 (2017).

[149] D. Breoni, H. Löwen, and R. Blossey, *Active noise-driven particles under space-dependent friction in one dimension*, Physical Review E **103**, 052602 (2021).

[150] L. L. Gutierrez-Martinez and M. Sandoval, *Inertial effects on trapped active matter*, The Journal of Chemical Physics **153**, 044906 (2020).

[151] L. Caprini, R. Kumar Gupta, and H. Löwen, *Role of rotational inertia for collective phenomena in active matter*, Physical Chemistry Chemical Physics **24**, 24910 (2022).

[152] W. R. Schneider and R. N. Doetsch, *Effect of Viscosity on Bacterial Motility*, Journal of Bacteriology **117**, 696 (1974).

[153] C. J. Miles, A. A. Evans, M. J. Shelley, and S. E. Spagnolie, *Active matter invasion of a viscous fluid: Unstable sheets and a no-flow theorem*, Physical Review Letters **122**, 098002 (2019).

[154] D. Breoni, R. Blossey, and H. Löwen, *Brownian particles driven by spatially periodic noise*, The European Physical Journal E **45**, 18 (2022).

[155] M. P. N. Juniper, A. V. Straube, R. Besseling, D. G. A. L. Aarts, and R. P. A. Dullens, *Microscopic dynamics of synchronization in driven colloids*, Nature Communications **6**, 7187 (2015).

[156] S. Coppola and V. Kantsler, *Green algae scatter off sharp viscosity gradients*, Scientific Reports **11**, 399 (2021).

[157] M. A. Fernandez-Rodriguez, F. Grillo, L. Alvarez, M. Rathlef, I. Buttinoni, G. Volpe, and L. Isa, *Feedback-controlled active brownian colloids with space-dependent rotational dynamics*, Nature Communications **11**, 4223 (2020).

[158] D. Breoni, F. J. Schwarzendahl, R. Blossey, and H. Löwen, *A one-dimensional three-state run-and-tumble model with a 'cell cycle'*, The European Physical Journal E **45**, 83 (2022).

[159] C. W. Shebelut, J. M. Guberman, S. van Teeffelen, A. A. Yakhnina, and Z. Gitai, *Caulobacter chromosome segregation is an ordered multistep process*, Proceedings of the National Academy of Sciences **107**, 14194 (2010).

[160] A. Frandi, F. Pini, W. Beroual, A. Bianchetti, A. Chiodi, E. Mascolo, L. Miano, G. Petazzoni, E. G. Biondi, and M. Brilli, in *Cell Cycle Regulation and Development in Alphaproteobacteria*, edited by E. Biondi (Springer International Publishing, Cham, 2022).

[161] C. J. Sherr, *Cancer Cell Cycles*, Science **274**, 1672 (1996).

[162] E. H. Harris, *The Chlamydomonas Sourcebook: Introduction to Chlamydomonas and Its Laboratory Use: Volume 1* (Academic Press, 2009).

[163] M. M. Genkin, A. Sokolov, O. D. Lavrentovich, and I. S. Aranson, *Topological Defects in a Living Nematic Ensnare Swimming Bacteria*, Physical Review X **7**, 011029 (2017).

[164] A. Doostmohammadi, J. Ignés-Mullol, J. M. Yeomans, and F. Sagués, *Active nematics*, Nature Communications **9**, 3246 (2018).

[165] R. Stocker, *Reverse and flick: Hybrid locomotion in bacteria*, Proceedings of the National Academy of Sciences **108**, 2635 (2011).

[166] G. Jacucci, D. Breoni, S. Heijnen, J. Palomo, P. Jones, H. Löwen, G. Volpe, and S. Gigan. *Patchy landscapes promote stability of small groups*, (2023). arXiv:2310.01620 [cond-mat, physics:physics].

[167] S. Bianchi, R. Pruner, G. Vizsnyiczai, C. Maggi, and R. Di Leonardo, *Active dynamics of colloidal particles in time-varying laser speckle patterns*, Scientific Reports **6**, 27681 (2016).

[168] D. Breoni, C. Kurzthaler, B. Liebchen, H. Löwen, and S. Mandal. *Giant Activity-Induced Stress Plateau in Entangled Polymer Solutions*, (2023). arXiv:2310.02929 [cond-mat, physics:physics].

[169] D. Saintillan, M. J. Shelley, and A. Zidovska, *Extensile motor activity drives coherent motions in a model of interphase chromatin*, Proceedings of the National Academy of Sciences **115**, 11442 (2018).

[170] A. Bacanu, J. F. Pelletier, Y. Jung, and N. Fakhri, *Inferring scale-dependent non-equilibrium activity using carbon nanotubes*, Nature Nanotechnology **18**, 905 (2023).

[171] J. C. Blain and J. W. Szostak, *Progress Toward Synthetic Cells*, Annual Review of Biochemistry **83**, 615 (2014).

[172] K. A. Ganzinger and P. Schwille, *More from less – bottom-up reconstitution of cell biology*, Journal of Cell Science **132**, jcs227488 (2019).